

ÉCOLE DOCTORALE SCIENCES ET MÉTIERS DE L'INGÉNIEUR
Laboratoire PIMM - Campus de Paris

THÈSE

présentée par : **Guilherme MALACRIDA ALVES**
soutenue le : **29 janvier 2025**

pour obtenir le grade de : **Docteur d'HESAM Université**

préparée à : **École Nationale Supérieure d'Arts et Métiers**
spécialité : **Génie Mécanique**

**Experimental modal analysis of time varying non-linear
systems. Application to brake squeal**

THÈSE dirigée par :
M Etienne BALMES

co-encadrée par :
M Eric MONTEIRO

et encadrement industriel par :
M Guillaume MARTIN

Jury

M. Jean-Luc DION

M. Frank MASSA

M. Gaël CHEVALLIER

M. Etienne BALMES

M. Guillaume MARTIN

Professeur, ISAE-Supmeca, Quartz

Professeur, Université Polytechnique
Hauts-de-France, LAMIH

Professeur, Ecole de l'Air et de l'Espace

Professeur, Arts et métiers science et tech-
nologies, PIMM

Docteur, SDTools

Président

Rapporteur

Rapporteur

Examineur

Examineur

**T
H
È
S
E**

Contents

List of tables	5
List of figures	7
Abstract	19
Résumé	21
Introduction	23
Industrial Context	23
Parameter varying characteristics of brake squeal tests	24
Outline and contributions	27
1 Functional models of squeal	31
1.1 Introduction	32
1.2 Defining a functional model for squeal	33
1.3 Frequency domain stability analysis using Complex Eigenvalue Analysis (CEA)	36
1.3.1 Classical CEA linearized around sliding state	36
1.3.2 Influence of static load : LPV evolution	37
1.3.3 Introducing an amplitude dependence to the CEA	38
1.3.4 Amplitude dependent root locus	42
1.4 Limit cycle characteristics from time simulations	44
1.4.1 Limit cycle for constant static load	45
1.4.2 Tracking stability boundary with slow static load ramp	46
1.4.3 Intermittent squeal due to static load oscillations	48
1.4.4 Estimation of a time decay rate and relation to root locus	50
1.4.5 Evolution of limit cycle shape with operating condition	51
1.5 Conclusion	53

2	Analyzing the dynamic response of time varying systems	55
2.1	Introduction	56
2.2	Defining a signal model for squeal: Harmonic Balance Vector (HBV) signal model . .	57
2.2.1	Motivation and definition of the HBV signal model	57
2.2.2	Single channel estimation	61
2.2.3	Estimation with multiple channels	70
2.3	Parametric modal analysis	72
2.3.1	Description of a simple parametric contact test bench	73
2.3.2	EMA at fixed system parameters (Classical H1 transfer estimation)	75
2.3.3	Describing the phase resonance mode tracking strategy	77
2.3.4	Applying phase resonance tracking to the contact test bench	81
2.4	Detailed shapes of fundamental and higher harmonics	84
2.5	Using the HBV signal to describe nonlinear behavior: instant stiffness and harmonic modulation	88
2.5.1	Using higher harmonics to define instant stiffness and harmonic modulation . .	89
2.5.2	Harmonic modulation in 3D-SLDV measurements	92
2.6	Conclusion	95
3	Full scale brake tests	97
3.1	Motivation and context of full scale brake tests	98
3.2	Describing the full scale test campaign	99
3.2.1	Parametric testing of brake squeal	99
3.2.2	Measurement setup for full scale test campaign	102
3.3	Tracking influence of pressure on squeal frequency, amplitude and shapes	108
3.3.1	Design of experiment and overview using time frequency analysis	108
3.3.2	Definitions of vibration amplitude and decay rate	109
3.3.3	Tracking/clustering squeal occurrences for a stepped pressure evolution	113
3.4	Parametric EMA in operating condition	117
3.4.1	Motivation for EMA in operating condition	117
3.4.2	Transfer function estimation and coherence analysis	119
3.4.3	Identification of poles for selected pressure values	124
3.5	Detailed shape characterization using 3D-SLDV	132
3.5.1	3D-SLDV Measurement setup	133
3.5.2	ODS estimation using Short Time Fourier Transform	134
3.5.3	Using an HBV signal and demodulation to build operational deflection shapes	136
3.5.4	Sample results	138

CONTENTS

3.6 Conclusion	141
Conclusion	143
A Résumé long (in french)	147
A.1 Introduction	147
A.2 Modèle de signal pour le crissement	149
A.2.1 Définition du modèle de signal HBV (Harmonic Balance Vector)	149
A.2.2 Extraction des composantes du signal HBV	152
A.3 Modèle fonctionnel pour le crissement	154
A.3.1 Construction du modèle fonctionnel	154
A.3.2 Analyse aux valeurs propres dépendant de l'amplitude	157
A.3.3 Comparaison entre les domaines temporel et fréquentiel	160
A.4 Essais sur banc complet	163
A.4.1 Mesures de crissement paramétrique	163
A.4.2 Analyse modale en condition opérationnelle	166
A.4.3 Mesure de forme détaillé par vibromètre laser	169
A.5 Conclusion	171
Bibliography	173

CONTENTS

List of Tables

1.1	Functional model requirements (left) and solutions (right)	34
1.2	Parameters chosen for the functional squeal model	36
3.1	Groups of sweep events selected for a more detailed analysis	125
A.1	Caractéristiques du modèle fonctionnel (à gauche) et solutions (à droite)	155
A.2	Paramètres choisis pour le modèle de crissement fonctionnel	157

LIST OF TABLES

List of Figures

1	Classification of different brake noise according to their approximate spectral content, as proposed by Akay [1]	23
2	Example of spectrogram of full scale squeal acceleration measurement under a slow varying pressure. 3s buffer length with Hanning window and 90% overlap.	25
3	a) Spectrogram of an squeal measurement between 65 and 80s, 1.5s buffer length, Hanning window and 90% overlap. b) Spectrogram of the same measurement between 75 and 80s, 0.15s buffer length, Hanning window and 90% overlap. c) Estimated instant frequency of the signal between 75s and 80s (color indicating amplitude)	26
4	Comparison of the characteristic times of the different parameter variations and the squeal vibration. Arrows indicate the separation between the fast and slow timescales.	27
1.1	Lumped elements diagram of the proposed 2-DOF functional model	34
1.2	Evolution of the linearized system poles as a function of the static load F_{pres} . Left: natural frequency. Right: damping coefficient. Color indicates normalized contact stiffness.	38
1.3	Example of imposed contact overclosure g (Left) and the corresponding contact pressure P_c (Right)	40
1.4	Extracted harmonic 0 and 1 from the imposed contact displacement (Left) and the corresponding contact pressure (Right)	40
1.5	Left: Comparison between the linearized forces corresponding to harmonic 1 stiffness $K_{c,1}$ and tangent stiffness for an arbitrary exponential contact law and trajectory defined by g_0, g_1 . Right: Equivalent stiffness evolution with the static load F_{pres} and first harmonic amplitude g_1	41
1.6	Poles obtained from (1.11) for different values of contact stiffness K_c (Root Locus). Pairs of poles corresponding to the crossing of the $\zeta = 0$ line (limit cycles) are indicated by L1/L2 and R1/R2.	42
1.7	Damping coefficient of the unstable mode ζ_2 evolution with the static load F_{Pres} and first harmonic amplitude g_1 . LPV stability boundary shown as black line. Vertical white line indicating $F_{Pres} = 400N$	43
1.8	Evolution of the MAC between mode shapes of the stable and unstable poles as a function first harmonic amplitude g_1 for $F_{Pres} = 400N$ with ζ indicated as color. Vertical line indicate the amplitude corresponding to $\zeta_2 = 0$ (limit cycle).	44

LIST OF FIGURES

1.9	Left: Constant static load F_{Pres} profile and stability frontier. Right: Modal amplitudes evolution over time	45
1.10	Evolution of $g_1(t)$ extracted from the transient simulation described in figure 1.9 using demodulation (-) compared to the limit cycle amplitude predicted using amplitude dependent CEA (- -).	46
1.11	Left: Slow ramp static load F_{Pres} profile and stability frontier. Right: First harmonic component of the overclosure $g_1(t)$ extracted using demodulation (blue) and stability boundary obtained from the amplitude dependent CEA (black) as a function of F_{Pres}	47
1.12	Left: Spectrogram of the overclosure g at the contact interface. Right: Evolution of the natural frequency of poles interpolated from figure 1.6 using the trajectory of F_{Pres}, g_1 from the transient simulation.	48
1.13	Left: Oscillating static load profile F_{Pres} profile and stability frontier. Right: Overclosure g and contact pressure P_c evolution over time.	49
1.14	Evolution of the first harmonic of the overclosure g_1 as a function of applied pressure F_{Pres} and time (color) compared to the stability boundary obtained from the amplitude dependent CEA (black). Arrows (A,B,C) indicate the sense of time evolution. Left: complete simulation. Right: first 5 s.	49
1.15	Decay ratio as a function of instantaneous frequency with amplitude as color (-). Root Locus estimated in using complex eigenvalue analysis (- -)	51
1.16	Evolution of the generalized coordinate associated with the two principal shapes	52
1.17	Left: Amplitude of q_{1R} as a function of the relative phase between q_{2R} and q_{1R} with decay rate as color. Right: Decay rate as a function of the relative phase between q_{2R} and q_{1R} with the amplitude of q_{1R} as color. Vertical dashed line indicates 90°	52
2.1	Sample spectrogram of full scale squeal measurement under a slowly varying pressure. 3s buffer length with Hanning window and 90% overlap.	58
2.2	Spectrogram of an squeal measurement with different time widows and buffer lengths, both use a Hanning window and 90% overlap. Left: Between 65 and 80s, 1.5s buffer length. Right: Between 75 and 80s, 0.15s buffer length.	59
2.3	Comparison of the characteristic times of the different parameter variations and the squeal vibration. Arrows indicate the separation between the fast and slow timescales.	59
2.4	Diagram showing the Synchronous demodulation algorithm	61
2.5	Application of synchronous demodulation in a simple test signal.	62
2.6	Demodulation results in presence of a frequency error. Left: constant error. Right: modulated frequency.	63
2.7	Frequency correction after first demodulation for a signal with different frequency errors (zero, constant, modulated). Estimated frequency (solid line) and true frequency (dashed line)	64
2.8	Diagram showing the 3-step demodulation algorithm for a single channel signal	65
2.9	Spectrogram of a microphone measurement from a full scale brake test used as example for the demodulation algorithm.	66

LIST OF FIGURES

2.10	Instant frequency obtained when the first cutoff frequency is too low (estimated signal amplitude as color). Initial frequency for demodulation 3350 Hz, first demodulation cutoff 20 Hz.	67
2.11	Instant frequency estimated in the demodulation algorithm without conditioning (Left) and with 30Hz low pass filter conditioning (Right), with amplitude of the estimated signal as color. Initial frequency for demodulation 3350 Hz, first demodulation cutoff 150 Hz.	67
2.12	Estimated instant frequency superposed over the measurement spectrogram. Left: entire signal. Right: region between 2.1 and 4.8s.	68
2.13	Rest of the identification obtained with different values of the second demodulation cutoff frequency 30 Hz (Left), 80 Hz (Center), and 150 Hz (Right). Initial frequency for demodulation 3350 Hz, first demodulation cutoff 150 Hz, frequency conditioning low pass 30 Hz.	68
2.14	Spectrogram of full signal, rest and HBV show in three separate intervals.	69
2.15	Left: $2\omega(t)$ superposed over the measurement spectrogram around the second harmonic. Right: $3\omega(t)$ superposed over the measurement spectrogram around the third harmonic.	70
2.16	Diagram showing the 3-step demodulation algorithm for a signal with multiple measured channels	71
2.17	Left: Estimate instantaneous frequency for different sensor sets. Right: Principal amplitudes $ q_{jR} $ associated with the first 5 principal shapes $\{u_j\}$	72
2.18	First design of the contact test bench	73
2.19	Second design of the contact test bench on the ground (left) and suspended (right)	74
2.20	Placement of the triaxial accelerometers sensors (yellow) and shaker input (red) on the second design	75
2.21	Left: pressure and input force applied to the test bench. Right: transfer functions corresponding to different pressure levels	76
2.22	Identified natural frequency (left) and damping coefficient (right) evolution with pressure using swept sine excitation at fixed pressure.	77
2.23	Example of the phase resonance estimation from the linear interpolation of phase for two neighboring frequencies.	78
2.24	Parametric evolution of natural frequency (Left) and damping (Right)	79
2.25	Input frequency (Left) and response phase lag (Right) as a function of external parameter for a 1DoF parametric system. Excitation frequency profiles: identical to phase resonance (Blue), piece-wise cubic (Red), and Linear (Yellow).	79
2.26	Re-estimation of phase resonance frequency and damping coefficient in a 1DoF system	80
2.27	Pressure and frequency profiles used in the parametric sine tests. Learning points indicated by \blacklozenge and vertical lines.	82
2.28	Left: complex amplitude of the first harmonic in different accelerometers in a single measurement. Right: generalized coordinate associated with the first principal shape for different measurements with and without frequency offset	82

LIST OF FIGURES

2.29 Estimated evolution of natural frequency and damping with time. Learning points indicated by \blacklozenge and vertical lines. Gray bars highlight the regions where estimation fails. 83

2.30 3D-SLDV measurement mesh superposed with the camera view of the measurement system. Left: front view. Right: back view. 84

2.31 Fixed reference accelerometer measurement corresponding to three sequentially measured laser points. 85

2.32 Frame of the extracted complex shape of the response to a sine excitation at the resonance frequency for mode 3 at 4 bar (Left) and 15 bar (Right). Red square highlights the portion of the mesh corresponding to the piston and red arrow indicating the same point in space. 86

2.33 Pressure paper measurement of the contact pressure between piston and backplate on the contact test bench at an hydraulic pressure of 4 and 15 bar 87

2.34 Frames of the extracted complex shape of the response to a sine excitation at the resonance frequency for mode 1. a) First harmonic front view b) First harmonic back view c) Second harmonic front view d) Second harmonic back view e) Third harmonic front view f) Third harmonic back view 88

2.35 Left : force as function of reduced time ($1=1/4$ period). Right : corresponding harmonic modulation ($q^a(t)$ blue) and first harmonic (q^1 red). 90

2.36 Left : force / displacement curve with 2 levels of pre-stress, 2 amplitudes and 3 frequencies. Right : corresponding instant stiffness (2.28) / displacement curves. Hyperelastic force/tangent stiffness is shown as a black dotted line. 91

2.37 Acceleration measurement and rest after harmonic extraction as function of reduced time ($1=1/4$ period). 92

2.38 Left: Harmonic modulation and harmonic 1 coefficient over reduced time ($1=1/4$ period). Right: Harmonic modulation and harmonic 1 coefficient over harmonic 1 trajectory. 93

2.39 Trajectory of the harmonic 1 shape over reduced time ($1=1/4$ period) 94

2.40 Harmonic perturbation over reduced time ($1=1/4$ period) 94

3.1 Spectrogram of a squeal measurement under slow varying pressure showing the parametric effect of pressure on squeal limit cycle. 100

3.2 Left: Spectrogram of a squeal measurement under fixed pressure and velocity showing the periodic fluctuations introduced by wheel rotation (angular position effect). Right: Normal displacement of a point on the disk under braking as a function of the wheel position WP ($1=1/4$ of a revolution) and temperature 101

3.3 Left : measured torque (**Pres4** run) , right : spectrogram of measured torque. 102

3.4 Brake system mounted in the test bench, 2023 setup. 103

3.5 Placement of sensors in the test bench Left: pad temperature sensor. Center: tachometer. Right: pressure sensor. 104

3.6 Accelerometer placement superposed with the finite element geometry of the brake system used in the full scale test setup 105

LIST OF FIGURES

3.7	Electrodynamic shaker placement in the full scale test setup	105
3.8	Placement of the 3D laser Doppler vibrometer with respect to the brake system in the full scale test setup	106
3.9	Left : raw time signal measured at 51.2 kHz sampling rate (Pres2 run), Right : 0-20kHz lowpass and 2.7-3kHz band pass filtered signals (blue and red respectively). Vertical dotted lines indicate a fixed wheel position.	107
3.10	Brake system mounted in the test bench, 2024 setup.	107
3.11	Left : measured pressure steps. Right : pressure profiles as a function of induced temperature.	108
3.12	Spectrogram using 1 wheel turn buffers of runs a) Pres1 , b) Pres2 , c) Pres4 . Text indicates harmonics of limit cycles that will be discussed later.	109
3.13	Left : Acceleration associated with the first 3 singular vectors $\alpha_j(t)$ obtained by band-pass and spatial filtering. Right : Generalized amplitudes associated with the first 2 singular vectors obtained from demodulation q_{jR} and obtained by band-pass and spatial filtering a_{mj}	111
3.14	Left : intermittent growth events of the first three principal amplitudes. Right : amplitude associated to the first singular vector q_{1R} as a function of frequency (time shown as color).	112
3.15	Left: Spectrogram of a squeal measurement under stepped pressure on the 2024 setup. Right: Decay rate versus instant frequency (experimental root locus)	113
3.16	Left : spectrogram for run pres2 for full test. Center: instant frequency over time with amplitude coded as color and transparency. Right: amplitude over instant frequency with applied pressure as color.	114
3.17	Evolution of the generalized amplitudes q_{jR} associated with the first three principal shapes for the pres2 measurement.	114
3.18	Left: spectrogram of pres4 test focusing of the limit cycle. Right : MAC with respected to shape at picked instants indicated by diamond marker.	115
3.19	Frequency amplitude tracking. Dotted line raw, colored line low pass filtered. Left : pres4 test. Right : pres2	116
3.20	Amplitude q_{1R} evolution showing intermittent squeal with instant frequency as color.	117
3.21	Reproducibility of transfer function obtained from measurements in different conditions: Static with 0 Nm torque (top left) static with 100Nm torque (top right) static with 200Nm torque (bottom left) and sliding (bottom right). Extracted from [17]	118
3.22	Left: spectrogram of the applied load in the parametric sweep test over the entire measurement with indications of pressure and temperature. Right: Evolution of the applied pressure with indication of high amplitude squeal areas (gray areas) and selected pressure points for identification in section 3.4.3 (dots).	119
3.23	Spectrogram of the acceleration measured in the brake knuckle. Left: first 100s wide frequency view. Left: first 30s focused frequency view.	120

LIST OF FIGURES

3.24	H1 Transfer function describing the response to the sweep excitation constructed using windows starting at 6.89, 9.88 and 21.92s.	120
3.25	Response to a sweep excitation at an accelerometer placed in the brake knuckle. Left: Transfer function constructed using H1 averaged sliding windows starting at 6.89, 9.88 and 21.92s. Right: Corresponding coherence values.	121
3.26	Response to a sweep excitation at the drive point accelerometer. Left: Transfer function constructed using H1 averaged sliding windows starting at 100, 200 and 240s. Right: Corresponding coherence values.	122
3.27	Coherence drops computed using a sliding window for the acceleration response measured at the brake knuckle (left) and drive point (right)	123
3.28	Selected pressure points for identification (dots) overlapped with the applied pressure profile (blue). Gray areas indicate high squeal levels.	124
3.29	Superposition of the transfer functions describing the system response for the selected sweep events indicated in figure 3.28	125
3.30	Superposition of the transfer functions describing the system response for the selected sweep events of group 1. Gray areas indicate regions where low coherence was detected in at least one measurement.	126
3.31	Comparison between the measured transfer functions and the ones reconstructed from the identification results for the selected sweep events of group 1. a) 6.7 bar b) 6.5 bar c) 6.3 bar d) 6.2 bar e) 6.1 bar	127
3.32	Evolution of the identified poles for the sweep transfer function of group 1. Gray areas indicate regions where low coherence was detected in at least one measurement.	128
3.33	Evolution of the MAC between the shapes of identified poles for the sweep transfer function of group 1	129
3.34	Superposition of the transfer functions describing the system response for the selected sweep events of group 2. Gray areas indicate regions where low coherence was detected in at least one measurement.	129
3.35	Comparison between the measured and identified transfer functions for group 2 events a) 5.4 bar b) 5.3 bar c) 5.1 bar d) 4.9 bar	130
3.36	Evolution of the identified poles for the sweep transfer function of group 2. Gray areas indicate regions where low coherence was detected in at least one measurement.	131
3.37	Evolution of the MAC between the shapes of identified poles for the sweep transfer function of group 2	131
3.38	Superposition of the transfer functions describing the system response for the selected sweep events of group 3. Gray areas indicate regions where low coherence was detected in at least one measurement.	132
3.39	Brake system with front and mirror views indicated	133
3.40	Sample ODS (FastScan measurement) combining front and mirror meshes	134
3.41	Sample 10ms buffer of the 3D-SLDV.	135

LIST OF FIGURES

3.42	ODS extracted from a 3D-SLDV measurement using H1 transmissibility. Left: real part. Right: imaginary part. Color indicates displacement normal to the disk.	135
3.43	MAC between the ODS extracted from a 3D-SLDV measurement with different references	136
3.44	Example of 3D-SLDV measurement for a single point in x,y and z directions (Left) and the corresponding demodulation with two filter setups as function of instant phase $\varphi = \int_0^t \omega(t)dt$ (Right).	137
3.45	ODS extracted from a 3D-SLDV measurement using the HVD signal model and demodulation. Left: real part. Right: imaginary part. Color indicates displacement normal to the disk.	138
3.46	Animation frames of Polytec FastScan STFFT shape	139
3.47	Animation frames from HBV signal shape obtained via demodulation	139
3.48	Frames from the animation showing the second harmonic shape obtained from HBV signal	140
3.49	Frames from the animation showing the third harmonic shape obtained from HBV signal	140
3.50	Frames from the animation showing the fifth harmonic shape obtained from HBV signal	141
A.1	Classification des différents types de bruit de freinage en fonction de leur contenu spectral, proposé par Akay [1]	147
A.2	Exemple de spectrogramme d'une mesure de crissement sur frein complet avec pression lentement variable. Longueur de buffer 3 secondes avec fenêtre de Hanning et overlap de 90 %.	150
A.3	Spectrogramme d'une mesure de crissement avec différentes fenêtres temporelles et longueurs de buffer, toutes deux utilisant une fenêtre de Hanning et un overlap de 90%. Gauche : entre 65 et 80s, longueur du buffer 1,5s. Droite : Entre 75 et 80s, longueur du buffer 0,15s.	151
A.4	Comparaison des temps caractéristiques des différentes variations paramétriques et de la vibration du crissement. Les flèches indiquent la séparation entre les échelles de temps rapides et lentes.	151
A.5	Diagramme schématisant l'algorithme de démodulation synchrone	152
A.6	Diagramme montrant l'algorithme d'estimation d'un signal HBV en 3 étapes (notations pour une mesure à un seul capteur)	153
A.7	Schéma du modèle fonctionnel à 2-DDL.	155
A.8	Evolution des pôles du système linéarisé en fonction de la charge statique F_{pres} . A gauche : fréquence modale. A droite : coefficient d'amortissement modal. La couleur indique la rigidité de contact normalisée K_c/K_x	158
A.9	Gauche: Évolution de la rigidité équivalente en fonction de la charge statique F_{pres} et de l'amplitude de la première harmonique g_1 . Droite: Pôles obtenus à partir de (1.11) pour différentes valeurs de la rigidité de contact K_c (Root Locus). Les paires de pôles correspondant au passage de la ligne $\zeta = 0$ (cycles limites) sont indiquées par L1/L2 et R1/R2.	159

LIST OF FIGURES

A.10 Coefficient d’amortissement de l’évolution du mode instable ζ_2 en fonction de la charge statique F_{Pres} et de l’amplitude de la première harmonique g_1 . La limite de stabilité LPV est représentée par la ligne noire. 160

A.11 A gauche : Profil de charge statique constante F_{Pres} et frontière de stabilité. A droite : Évolution des amplitudes modales au cours du temps 161

A.12 Évolution de $g_1(t)$ extraite de la simulation transitoire décrite dans la figure 1.9 utilisant la démodulation (-) comparée à l’amplitude du cycle limite prédite en utilisant la CEA dépendante de l’amplitude (- -). 162

A.13 A gauche : Profil de charge statique F_{Pres} de la rampe lente et frontières de stabilité. A droite : Première composante harmonique de l’interpénétration $g_1(t)$ extraite à l’aide de la démodulation (bleu) et limite de stabilité obtenue à partir de la CEA dépendante de l’amplitude (noir) en fonction de F_{Pres} 162

A.14 Système de freinage sur le banc d’essai, setup 2023. 163

A.15 A gauche : rampes de pression. A droite : profils de pression en fonction de la température. 164

A.16 Spectrogramme utilisant des buffers de temps de 1 tour de roue pour les essais a) **Pres1**, b) **Pres2**, c) **Pres4**. Le texte indique les harmoniques des cycles limites qui seront examinés. 165

A.17 A gauche : spectrogramme pour l’essai **pres2**. Au milieu : fréquence instantanée en fonction du temps et de l’amplitude globale (en couleur et transparence). A droite : amplitude globale en fonction de la fréquence instantanée et de la pression (en couleur). 166

A.18 Gauche : spectrogramme de l’effort appliqué dans l’essai de balayage paramétrique sur toute la durée de la mesure, avec indication de la pression et de la température. Droite : Évolution de la pression appliquée avec indication des zones de crissement de forte amplitude (zones grises) et des points de pression sélectionnés pour l’analyse modale expérimentale dans la section 3.4.3 (points). 167

A.19 Superposition des fonctions de transfert décrivant la réponse du système pour les événements de balayage sélectionnés du groupe 1. Les zones grises indiquent les régions où une faible cohérence a été détectée dans au moins une mesure. 168

A.20 Évolution des pôles identifiés pour la fonction de transfert du groupe 1. Les zones grises indiquent les régions où une faible cohérence a été détectée dans au moins une mesure. 169

A.21 Système de frein avec vues frontale et miroir indiquées. 169

A.22 Images de l’animation montrant la forme de la première harmonique obtenue à partir du signal du VHB 170

A.23 Images de l’animation montrant la forme de la seconde harmonique obtenue à partir du signal du VHB 171

A.24 Images de l’animation montrant la forme de la troisième harmonique obtenue à partir du signal du VHB 171

LIST OF FIGURES

LIST OF FIGURES

Abstract

Brake squeal is a complex phenomenon resulting from a mode coupling instability. Despite being a subject of study for many years, no robust design method exists for its prevention and correcting measures are heavily based on prototyping and validation, which is time-consuming and expensive. Squeal testing can be separated into three main activities: classification of squeal occurrences based on acoustic levels, detailed spatial characterization of limit cycles, and modal characterization of components and assemblies. This work thus seeks to propose and analyze the usefulness of different methodological changes to testing methods.

A specificity of squeal is that vibration depends on multiple operating parameters pressure, wheel speed, temperature, ... which vary in time relatively slowly compared to the frequencies of squeal limit cycles. It is thus necessary to take this specificity into consideration to design testing methods and analyze their results.

As a mean to gain further insight on the effects of slowly changing operating conditions, a new functional model for squeal is proposed based on the well-known Hoffmann model. The novelty lies in replacing the variable friction assumption by a nonlinear contact law, which introduces a sensitivity to the applied pressure (as the static-state is modified), and amplitude (through its effect on the mean pressure). Analyzing and comparing the response of this model in frequency and time domain provides a path to understanding the relations between squeal limit cycle vibration and parameters.

The definition of a Harmonic Balance Vector (HBV) signal model and the use of demodulation for its estimation, then allows tracking of quasi-periodic squeal signals without resolution limitations of the Fourier transform. For parametric squeal tests, this method improved occurrence classification by extracting the evolutions of features such as instantaneous frequency, global vibration amplitude, generalized coordinates and shape.

For the detailed shape analysis using 3D-SLDV measurements, the HBV signal estimates led to results improved over current methods based on short time Fourier transforms. Applications are illustrated in a contact test bench to obtain the evolution of shapes with pressure, and in a full scale brake tests to obtain the limit cycle shapes.

The HBV signal estimation can also extract spatially detailed shapes for higher harmonics. Two indicators (harmonic modulation and harmonic perturbation) are then proposed, based on the notion of instant stiffness, as a mean of evaluating where in a period the system is stiffer or softer.

Finally, for in operation parametric Experimental Modal Analysis (EMA), full scale tests showed that modes away from squeal can be consistently identified and tracked. Near squeal, however, the presence of a coherence loss indicates that other methods are required such as the feedforward phase resonance tracking proposed in the analysis of the simplified contact test bench.

Keywords : Brake squeal, Nonlinear vibrations, Limit cycle, Parameter-varying systems, Signal model, Experimental modal analysis, 3D-SLDV, Instant stiffness, clustering.

ABSTRACT

Résumé

Le crissement des freins est un phénomène complexe résultat d'une instabilité induite par couplage de modes. Bien qu'il fasse l'objet d'études depuis de nombreuses années, il n'existe pas de méthode de conception robuste pour le prévenir et les mesures correctives reposent largement sur le prototypage et la validation, ce qui est long et coûteux. Les essais de crissement peuvent être séparés en trois activités principales : la classification des occurrences de crissement en fonction des niveaux acoustiques, la caractérisation spatiale détaillée des cycles limites et la caractérisation modale des composants et des assemblages. Ce travail a donc cherché à proposer et à analyser l'utilité de différents changements méthodologiques dans les méthodes d'essai.

Une spécificité du crissement est que la vibration dépend de multiples paramètres de fonctionnement : pression, vitesse de roue, température, ... qui varient dans le temps relativement lentement par rapport aux fréquences des cycles limites de crissement. Il est donc nécessaire de tenir compte de cette spécificité pour concevoir des méthodes d'essai et analyser leurs résultats.

Afin de mieux comprendre les effets des conditions de fonctionnement qui changent lentement, un nouveau modèle fonctionnel pour le crissement est proposé sur la base du modèle d'Hoffmann bien connu. La nouveauté réside dans le remplacement de l'hypothèse de frottement variable par une loi de contact non linéaire, qui introduit une sensibilité à la pression appliquée (car l'état statique est modifié) et à l'amplitude (par son effet sur la pression moyenne). L'analyse et la comparaison de la réponse de ce modèle dans le domaine fréquentiel et temporel permettent de comprendre les relations entre les vibrations et les paramètres du cycle limite de crissement.

La définition d'un modèle de signal de balance harmonique vectoriel (HBV) et l'utilisation de la démodulation pour son estimation permettent ensuite de suivre les signaux quasi-périodiques issus du crissement sans les limites de résolution de la transformée de Fourier. Pour les tests de crissement paramétriques, cette méthode a amélioré la classification des événements en extrayant les évolutions des caractéristiques telles que la fréquence instantanée, l'amplitude globale de la vibration, les coordonnées généralisées et la forme.

Pour l'analyse détaillée de la forme à l'aide de mesures 3D-SLDV, les estimations du signal HBV ont permis d'améliorer les résultats par rapport aux méthodes actuelles basées sur les transformées de Fourier à court terme. Les applications sont illustrées dans un banc d'essai de contact pour obtenir l'évolution des formes en fonction de la pression, et dans des essais de freinage sur frein complet pour obtenir les formes du cycle limite. L'estimation du signal HBV peut également extraire des formes spatialement détaillées pour les harmoniques supérieures. Deux indicateurs (modulation harmonique et perturbation harmonique) sont ensuite proposés, sur la base de la notion de rigidité instantanée, comme moyen d'évaluer à quel moment d'une période le système est plus ou moins rigide.

Enfin, pour l'analyse modale expérimentale (EMA) paramétrique en fonctionnement, les essais en vraie grandeur ont montré que les modes éloignés du crissement peuvent être identifiés et suivis de manière cohérente. À proximité du crissement, cependant, la présence d'une perte de cohérence indique que d'autres méthodes sont nécessaires, telles que le suivi de la résonance de phase par anticipation proposé dans l'analyse du banc d'essai de contact simplifié.

Mots-clés : Crissement de frein, Vibrations non-linéaires, Cycle limite, Systèmes à paramètre variable, Modèle de signal, Analyse modale expérimentale, 3D-SLDV, Raideur instantanée, Clustering.

RESUME

Introduction

Industrial Context

Friction has long been used as a way of dissipating the kinetic energy of moving objects. It is one of the most versatile dissipation mechanisms and is extensively used in brake systems. Be it cars, trains, or planes, most of them use a friction-based brake system for service braking. Friction is, however, a known source of noise in mechanical systems. A wide variety of noises can be produced by brake systems with vastly different frequencies, duration, evolution and modulation. Using these characteristics Akay [1] constructs a series of categories to classify the different noise occurrences, reproduced in figure 1.

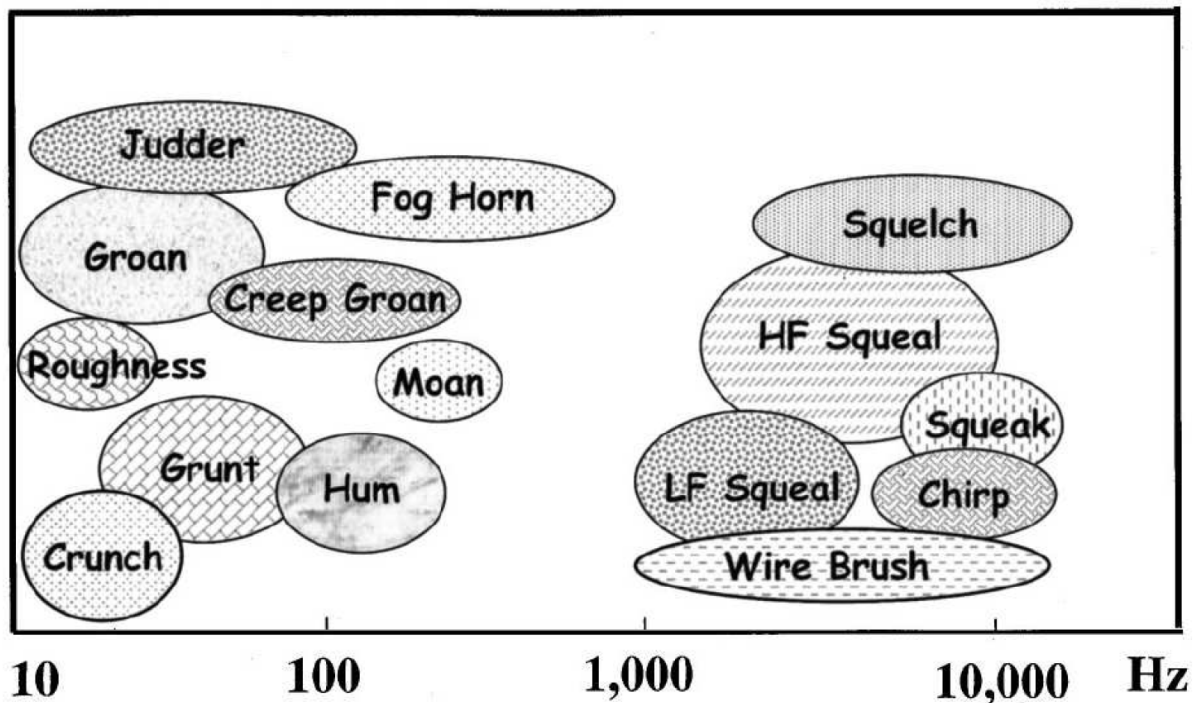


Figure 1: Classification of different brake noise according to their approximate spectral content, as proposed by Akay [1]

Among these noise types, squeal is a frequent problem faced by braking systems manufacturers such as Hitachi Astemo France, the industrial partner of this project. Characterized by the presence of self-excited response between 1kHz and 10kHz squeal vibration reach significant amplitude levels resulting in noise emission up to 120dB. Squeal is not only a problem to the final user of the product but also a notable source of acoustic pollution. Therefore, economic penalties are imposed on suppliers if noise requirements are not met. Recent changes in technology and requirements in brake systems have led to an increase in friction coefficient and a reduction of component mass. As a result brake squeal has become a more frequent issue.

Brake squeal has been a subject of study for many years going back to the early 60's with the works of Spurr [2]. What is commonly named squeal is a mode lock-in theorized [3, 4, 5] as a Hopf-Bifurcation for a system showing parametric instability. Sample experimental studies are [6, 7].

When the presence of squeal leads to unacceptable levels of noise, one can seek to propose corrective measures by analyzing one of three types of data: experimental test data, FEM simulation data, test/FEM correlation data.

Using the experimental test data, one is able to ensure the exact behavior of the physical system is considered. However, this approach requires iterative prototyping and validation, making it a long and expensive process. Using experimental data without expansion also limits the propositions of structural modification to the sensor locations. Experimental studies of squeal analyze acoustic fields [8], deflection shapes [9, 10], equilibrium positions [11], or temperature distributions [12], ...

Using FEM simulations, the complete geometry of the system can be taken into consideration to propose corrective measures. This method is can be faster than building prototypes of proposed modifications. The challenge of this approach lies in making sure the numerical model represents the physical system. This has motivated a number of studies seeking to obtain better numerical models for squeal [13, 14, 15, 16]

A middle ground between the two approaches can be obtained with methods combining test and FEM. The basic idea is that, by using the results of the measurements in combination with the FEM model, it is possible to update the model [17] and/or generate a hybrid test/FEM approximation [18] and thus propose better corrective measures.

In this project, our main goal is to improve the characterization of parametric effects in experimental approaches by detailing the relation between system parameters, stability and limit cycle characteristics.

Parameter varying characteristics of brake squeal tests

Since squeal only occurs under certain parametric conditions, understanding how parameters evolve in time and influence the possible transition to/from a squeal limit cycle is the general objective of tests.

Parameters routinely considered by industry are the applied hydraulic pressure [9], the loading profile [19], the temperature [12], the wheel speed, ... The wheel angular position is also known to be important [7, 20, 8, 17, 21].

Computations indicate that these parameters affect pressure distributions in contact surfaces, which have a direct effect on the occurrence and amplitude of squeal [13]. In addition to pressure, the dependence of stiffness and damping on amplitude is well documented for jointed structures [22], turbine friction dampers [23], to cite just a few studies.

Other studies have sought to include more details on the modeling by describing the relation between system parameters and stability [24], the effects of equilibrium positions on the friction forces [11, 16], or even to describe squeal as a chaotic vibration [25, 26, 27].

Now as a motivating example let us take a look at a squeal measurement. This measurement is part of the full scale experimental campaign described in chapter 3. The brake system used had all its viscoelastic patches removed, friction material composition and contact shape were also changed to increase the probability of squeal occurrence. Figure 2 shows the spectrogram of the self excited vibration resulting of a pressure profile increasing step by step from $p = 1.5bar$ to $p = 9bar$. In this figure it is possible to notice four different regions of squeal at different times of the measurement with fundamental frequencies around 1560, 6440, 1900, 2950 Hz , showing that changes in applied pressure have a direct effect on the limit cycle fundamental frequency.

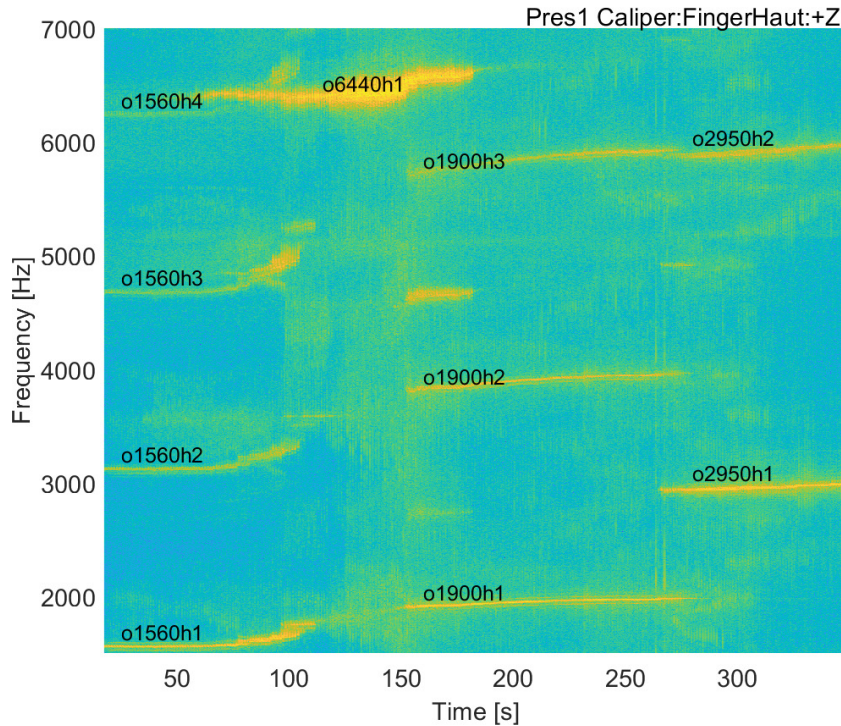


Figure 2: Example of spectrogram of full scale squeal acceleration measurement under a slow varying pressure. 3s buffer length with Hanning window and 90% overlap.

Figure 3a shows a new spectrogram that focuses the analysis on the time band [65 – 80]s around the first harmonic. In this figure, it is possible to see the presence of a main peak near 1570 Hz, this is the limit cycle frequency. This peak shows a slow variation with the pressure steps taken every 5s and some periodic fluctuations that match the period of wheel rotation. In addition, two sidebands at $\pm 30Hz$ can be seen around the limit cycle indicating a frequency modulation. This modulation

INTRODUCTION

matches the frequency of torque fluctuation induced by a torsion mode on the system axle. The observed characteristics illustrate the effect of operating conditions in the limit cycle.

However, since the buffer length used in the spectrogram from figure 3a is close to the wheel revolution period, it is difficult to characterize the frequency fluctuations that happen in a full wheel revolution. To improve this analysis figure 3b reduces the buffer length used in the spectrogram from 1.5s to 0.15s in a reduced time band [75 – 80]s. In this even more focused window the periodic fluctuations of the squeal frequency with wheel rotation can be clearly seen.

A new difficulty arises in this case, by reducing the buffer length to be more descriptive of the time variations the frequency resolution is negatively affected. In an ideal case it would be desirable to have the squeal frequency value at all times like what is shown in figure 3c. In this figure it is possible to see the combination of all different parametric effects including the periodic effect of wheel rotation and the 30Hz fluctuations caused by the torsion mode.

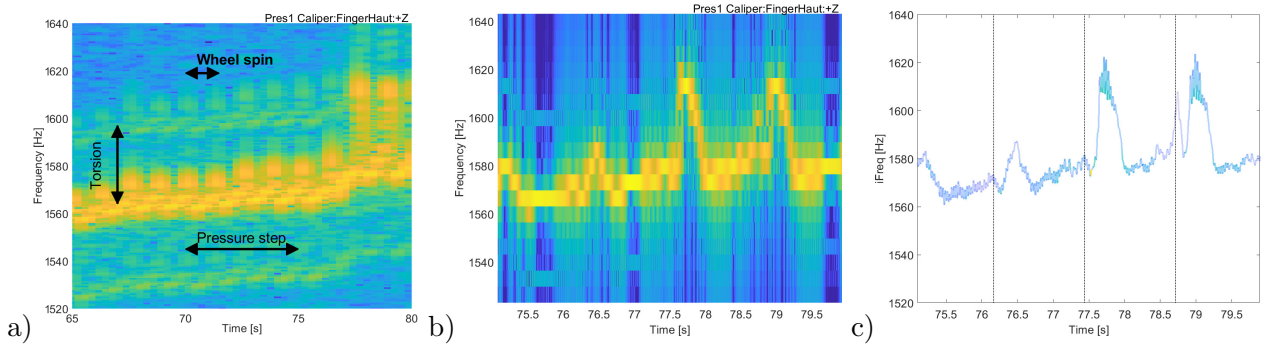


Figure 3: a) Spectrogram of an squeal measurement between 65 and 80s, 1.5s buffer length, Hanning window and 90% overlap. b) Spectrogram of the same measurement between 75 and 80s, 0.15s buffer length, Hanning window and 90% overlap. c) Estimated instant frequency of the signal between 75s and 80s (color indicating amplitude)

Looking again at figures 2 and 3, one clearly notice that parameter induced changes on the system are slow compared to the squeal vibration. This timescale separation is highlighted in figure 4 which compares the characteristic times (or frequencies) of the different parameter with the squeal vibration.

Starting with the pressure, the test in figure 3 change pressure in steps that happen approximately every 5s. The wheel rotation period is around 1.3s (for a velocity of 6km/h). The torsion mode induce fluctuations at 30Hz(period of 0.03s). The changes due to the temperature are much slower, for the sake of example, let us consider its characteristic time as 20s. With the squeal vibration at 1580Hz (period of 0.63ms), there are almost two orders of magnitude separating the vibration (indicated by the t arrow) from the parametric effects (indicated by the t_{slow} arrow).

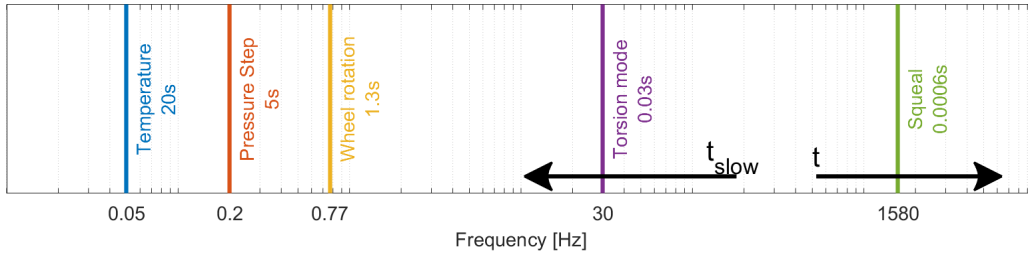


Figure 4: Comparison of the characteristic times of the different parameter variations and the squeal vibration. Arrows indicate the separation between the fast and slow timescales.

One of the consequences of the timescale separation is that it is possible to consider that the vibration characteristics are locally constant. More specifically this means that two different time values are considered, a fast time t and a slow time t_{slow} . The fast time t represents the variations that occur with a period, or a few periods, which can be described by the harmonics of the limit cycle frequency. While the slow time t_{slow} describes how these characteristics change with the operating parameters. This type separation between slow and fast dynamics can be seen in some application of the analytic signal formulation [28].

From the overall context and this quick analysis, we can determine that the main characteristics of a brake squeal vibration are:

- Fundamental frequency of dynamics between 1kHz and 10kHz (based on the overall classification in figure 1)
- Presence of integer harmonics of the fundamental frequency (as shown in figure 2)
- Common instantaneous frequency to all measured channels as they are part of the same system.
- Modulation due to parametric effects at a maximum frequency of 50Hz (30Hz is the maximum observed in the experiments in chapter 3) allow timescale separation
- Limit cycle vibration is principally contained in a low dimensional subspace [17, 21, 25].

These characteristics served as a guideline for the different analysis made during this project.

Outline and contributions

Even though it is a frequent problem, there is no robust design method to prevent squeal. Defining corrective measures is an iterative process heavily based on testing, which is an expensive and time-consuming solution.

Squeal testing can be separated in three main activities : classification of squeal occurrences based on acoustic or vibration levels, detailed spatial characterization limit cycles, and modal characterization of components and assemblies. As discussed in the previous section, squeal vibration depends on multiple operating parameters such as pressure, wheel speed, temperature, ... which vary in time relatively slowly compared to the frequencies of squeal limit cycles.

The main goal of this project is thus to revisit the main brake squeal testing activities, propose and analyze the usefulness of different methodological changes in their ability to characterize dependence of brake vibrations on parameters.

Chapter 1 begins the analysis by proposing a functional model for squeal that represents the parametric effect of the applied loading (pressure) and vibration amplitude in the initiation of squeal and the resulting limit cycle. The proposed model is inspired by the well known Hoffmann model [4] and represents squeal mode lock-in using a 2-DOF nonlinear model. As a **first contribution** to this thesis, a series of analysis in frequency and time domain are made in order to evaluate the parametric effects on the limit cycle. The results presented in this chapter were the subject of a conference presentation [29].

Section 1.3 addresses the frequency domain stability analysis of the functional model using the classical Complex Eigenvalue Analysis (CEA). A Linear Parameter-Varying (LPV) perspective is used, in a first moment, to evaluate the effect of pressure on stability. Then an amplitude dependence is added to this analysis, which allow us to estimate the pressures/amplitudes where limit cycle vibration is possible.

Then in section 1.4, nonlinear transient simulations are used to obtain the functional model time response to a series of pressure profiles. These responses are then analyzed in order to extract features that represent the limit cycle vibrations such as amplitude, frequency, and decay rate. These values are then compared with the ones obtained in frequency domain in an analogy to test/FEM correlation strategies.

Chapter 2 then addresses characterization of slowly time/parameter varying non-linear systems with vibrations dominated by quasi-periodic response.

Based on timescale separation assumption, section 2.2 introduces the Harmonic Balance Vector (HBV) signal model as a mean to represent quasi-periodic response. A demodulation algorithm is described and shown to be able to extract the HBV signal parameters. Illustrations are based on the full scale brake squeal measurements from chapter 3.

In addition to squeal, this signal model is of interest in sine, slow sweep or any other type of testing where the period depends on excitation. The combination of the HBV signal model and demodulation algorithm thus make a **second contribution** to the thesis and has been applied in many parts of this thesis, from the functional model to the full scale tests.

Parametric modal testing is then considered as second test case of slowly time/parameter varying non-linear systems. A contact test bench, where properties vary with a continuously changing pressure, is detailed in section 2.3. In this example, the knowledge obtained at a few fixed pressure points in order to construct an approximate relation between pressure and frequency. Then a series of parametric sine measurements are made, where the signal frequency depends on the pressure is applied in order to track phase resonance. From the measurements and using the HBV signal estimation, a continuous relation between pressure, resonance frequency and damping is obtained. This application has been the subject of a conference presentation [30].

Section 2.4 then addresses the use of the HBV signal model to construct spatially detailed vibration shape on the same contact test bench. This is achieved through the measurement of the sine response near system modes resonance frequency using 3D scanning laser vibrometer (3D-SLDV). By comparing

the shapes of harmonic at different pressures it is possible to evaluate the effects of pressure on mode shapes for the first harmonic and non-linearity for higher harmonics. The analysis of the higher harmonics is extended in section 2.5 with a focus on the analysis of the nonlinearity. Inspired by the notion of instant modulus/stiffness proposed in [31], this section uses the combined effect of the harmonics to characterize the nonlinear response of the system. An early version of these results has been presented in [32] using data from rubber identification tests.

Full scale experiments are an essential part of the validation process of the NHV characteristics of brake systems. Chapter 3 describes the application of proposed methods to a full scale test campaign seeking to characterize parametric effects. It corresponds to the **third contribution** to the thesis.

These measurements were performed on an industrial brake system with the anti-squeal features removed. Parameters considered in the test are described in section 3.2.1, followed by a description of the measurement setup in section 3.2.2.

Section 3.3 discusses tracking of squeal limit cycle using the HBV signal model estimated with demodulation. Parametric variations are induced approximating continuous pressure changes by a series of steps. A first analysis focusing on an intermittent squeal occurrence is used to discuss the definition of a global vibration amplitude, followed by the construction of a decay rate comparable to the damping ratio of a complex mode, leading to an experimental root locus. Then, classification (clustering) of squeal occurrences is discussed using frequency/amplitude, generalized coordinates, or shapes. A paper discussing the results presented in this section has been submitted [33].

Section 3.4 then describes the analysis of a parametric Experimental Modal Analysis (EMA). These tests are performed to evaluate how the system modes evolve in operating condition. This measurement allows tracing the evolution of system modes in operating condition with pressure. In addition, the section discusses the difficulties of performing EMA in a system that presents self-excited vibration.

Finally, 3D-SLDV measurements are used to obtain spatially detailed Operational Deflection Shapes (ODS) of the limit cycle. In section 3.5 the challenges of using sequential measurements are discussed. Two different methods for construction of the ODS are considered: the usual transmissibility based on short time Fourier transform, and the HBV demodulation. The shapes obtained for the limit cycle fundamental frequency using the two methods are then compared. Lastly, the shapes corresponding to the higher harmonics of the limit cycle are shown and their differences highlighted.

Functional models of squeal

Content

1.1	Introduction	32
1.2	Defining a functional model for squeal	33
1.3	Frequency domain stability analysis using Complex Eigenvalue Analysis (CEA)	36
1.3.1	Classical CEA linearized around sliding state	36
1.3.2	Influence of static load : LPV evolution	37
1.3.3	Introducing an amplitude dependence to the CEA	38
1.3.4	Amplitude dependent root locus	42
1.4	Limit cycle characteristics from time simulations	44
1.4.1	Limit cycle for constant static load	45
1.4.2	Tracking stability boundary with slow static load ramp	46
1.4.3	Intermittent squeal due to static load oscillations	48
1.4.4	Estimation of a time decay rate and relation to root locus	50
1.4.5	Evolution of limit cycle shape with operating condition	51
1.5	Conclusion	53

1.1 Introduction

Simplified models have been widely used in the literature in order to characterize the mechanisms of brake squeal vibration. Notably, Hoffmann [4] proposed a simple two degree of freedom model that describes the formation of instability. This simple functional model has been used to show how the friction coefficient μ and damping affect the stability of the system.

Following the observations by [25, 26] that brake squeal shows the characteristics of low dimensional irregular deterministic dynamics (chaos), the Hoffmann model was extended in to [27] include the characterization of irregular vibrations.

Alternative functional models have sought to include other effects in the modeling process. In [11, 16], for example, the model considers the presence of multiple static equilibrium positions induced by the combinations of tolerances and nonlinear behavior. On the other hand the model proposed by [34, 24] seeks to combine geometric considerations such as the sprag angle (as defined by [2]) in a stability analysis to determine the conditions for squeal and the limit cycle.

Some studies have focused on bringing more detail to the widely used complex eigenvalue analysis (CEA). A modal reduction of the FEM model is applied using complex interface modes to improve the squeal prediction in reduced models in [14, 35]. While the modal amplitude has been added a parameter in the eigenvalue analysis in [15] by imposing a periodic trajectory to the system with a fixed mode shape. This considers the effect of vibration amplitude on the stability of the system.

Others such as [19, 36] included the parametric effect of loading in the squeal vibration by comparing the transient response of a simplified system with a static and a ramp loading using wavelet transform. The wavelet transform that has also been used in [37] to extract the growth rates in the initiation of squeal.

Our goal in this chapter is to propose a modified version of the Hoffmann functional model [4] that represents the parametric effect of the applied loading (pressure) and vibration amplitude in the initiation of squeal and the resulting limit cycle. The use of a functional model aims to simplify to its maximum the behavior of a system reproducing squeal evolutions found in test. The new functional model, composed of two degree of freedom system subject to contact and friction nonlinearities, is described in section 1.2. By describing the influence of both static pressure and vibration amplitude on the contact (and thus friction) forces, the proposed model is able to represent the effect of operating conditions on the mode coupling instability and limit cycle saturation.

The proposed functional model is first analyzed in frequency domain using the Complex Eigenvalue Analysis (CEA) in section 1.3. In this type of stability analysis the system is linearized around a steady sliding equilibrium, in order to characterize the low amplitude behavior. Using the CEA it is possible to characterize the presence of unstable modes for different operating conditions. However, due to the linearization process, it is not possible to represent the effect of amplitude in the CEA. As a consequence, this method is not capable of estimating limit cycle amplitudes.

In order to counter this limitation, section 1.3.4 introduces a second linearization strategy that takes into consideration both the steady sliding equilibrium and the vibration amplitude. This new linearization, inspired by the Harmonic Balance Method (HBM), strategy seeks to represent the system dynamics as a function of an imposed periodic trajectory restricted to harmonics zero and one. An equivalent stiffness value is then defined by looking at the nonlinear forces resulting from this imposed trajectory. The result is an equivalent stiffness chart that is a function of both the applied pressure and vibration amplitude. This strategy is similar to the one used in [38] to characterize punctual nonlinearities in the sense that vibration amplitude is included into the construction of a stiffness chart without fixating the vibration shape. Using this new linearization the CEA is extended to become an amplitude dependent eigenvalue problem that is capable of estimating limit cycle amplitude. Additionally, this allows for an evaluation of the amplitude effect on the system poles.

The functional model response in time domain is then analyzed using nonlinear transient simulations 1.4. A series of transient simulations are performed representing usual experiments are considered: drag where constant pressure is applied, pressure ramps, and pressure oscillations mimicking the contact changes due to wheel rotation, which is thought to be the source of intermittent squeal occurrences. In addition to analyzing the time response, section 1.4 compares the results obtained in time domain with the results from section 1.3. In this comparison it is possible to see that the transient responses reproduce stability boundaries, limit cycle saturation, sensitivity to pressure estimated in the amplitude dependent eigenvalue analysis.

1.2 Defining a functional model for squeal

In this section, we introduce a functional model for brake squeal. The objective is to represent the mode coupling instability mechanism and its dependency to static load and limit cycle amplitude. The proposed functional model, shown in figure 1.1, tackles many requirements through a number of elements added to the model as listed in table 1.1. The result is a two degree of freedom system with a linear part composed of a mass held by two orthogonal spring-damper pairs. This is meant to represent the two modes interacting in a brake squeal situation. An external load F_{Pres} representing the quasi-static pressure piston pressure is applied to the mass. Contact and friction are introduced by a sliding plane at an angle θ . It couples the two modes through nonlinear force F_{NOR} normal to the sliding plane and friction force (Coulomb's law) F_{TAN} tangent to the sliding plane. In [24] the contact angle θ (also called the sprag angle) is related to a necessary condition for the occurrence of squeal. This necessary condition states that mode coupling squeal is only possible when $0 < \tan(\theta) < \mu$ where μ is the friction coefficient, a condition that is verified in the proposed functional model.

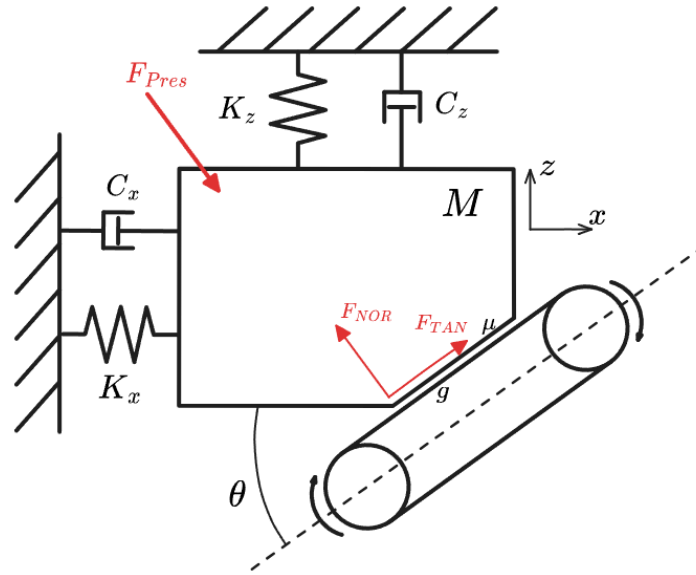


Figure 1.1: Lumped elements diagram of the proposed 2-DOF functional model

Table 1.1: Functional model requirements (left) and solutions (right)

Model requirements	Model elements
Squeal is theorized as a Hopf bifurcation [4, 5] and requires at least two DOF	2 translation DOFs in directions x and z
Tune modal frequencies and dampings	<ul style="list-style-type: none"> • Mass M, common to both DOFs • Spring/damper K_x and C_x between DOF x and the ground • Spring/damper K_z and C_z between DOF z and the ground
Vary (quasi-)static load	External load F_{Pres}
Contact force sensitive to static load and amplitude	Contact force $F_{NOR}(g)$ depends on normal overclosure g in a nonlinear way. Which leads to a linearized stiffness that depends on static load and amplitude.
Mode coupling through sliding friction	<ul style="list-style-type: none"> • $F_{TAN} = \mu F_{NOR}$ (Coulomb's law) • θ : sliding plane rotation with respect to the mass to tune the coupling

The differential equation describing this model is

$$\underbrace{\begin{bmatrix} M & 0 \\ 0 & M \end{bmatrix}}_{[M]} \begin{Bmatrix} \ddot{x} \\ \ddot{z} \end{Bmatrix} + \underbrace{\begin{bmatrix} C_x & 0 \\ 0 & C_z \end{bmatrix}}_{[C]} \begin{Bmatrix} \dot{x} \\ \dot{z} \end{Bmatrix} + \underbrace{\begin{bmatrix} K_x & 0 \\ 0 & K_z \end{bmatrix}}_{[K]} \begin{Bmatrix} x \\ z \end{Bmatrix} + \{ \tilde{F}_{NOR}(x, z) \} + \{ \tilde{F}_{TAN}(x, z) \} - \{ \tilde{F}_{Pres} \} = 0 \quad (1.1)$$

and we will now detail the complete expression of F_{Pres} , F_{NOR} and finally F_{TAN} .

The external load \tilde{F}_{Pres} is applied to represent the pressure applied on the brake system. This force is considered static, or slowly varying (quasi-static) so that it can play the role of operating condition (external parameter).

$$\{ \tilde{F}_{Pres} \} = \begin{bmatrix} \sin(\theta) \\ -\cos(\theta) \end{bmatrix} F_{Pres}(t_{slow}) = [\tilde{b}_{Pres}] F_{Pres}(t_{slow}) \quad (1.2)$$

The force F_{NOR} (normal to the sliding plane) represents contact surface reaction between the pad and the disc. For simplicity, it is considered here that the contact takes place at a single point. In more detailed reduced brake models, a pressure distribution over the contact surface is considered. For a given surface S_{Pad} , F_{NOR} is thus simply related to the contact pressure by $F_{NOR} = P_c(g)S_{Pad}$. $P_c(g)$ is a nonlinear contact law as a function of g the overclosure, penetration, or opposite of the gap between surfaces. g plays the role of contact strain, is linearly related to the model DOFs by the observation equation.

$$g = [\tilde{c}_{NOR}] \{ q \} = \begin{bmatrix} \sin(\theta) & -\cos(\theta) \end{bmatrix} \begin{Bmatrix} x \\ z \end{Bmatrix} \quad (1.3)$$

The key aspect for the contact law is that it is assumed to be amplitude dependent, and thus not piecewise linear, which is verified for surfaces that are not considered ideally flat [23]. In this thesis, the exponential law used by Hitachi Astemo is retained

$$P_c(g) = p_0 e^{\lambda_c(g)} \quad (1.4)$$

The normal contact force F_{NOR} on the model DOFs is thus

$$\{ \tilde{F}_{NOR} \} = \begin{bmatrix} \sin(\theta) \\ -\cos(\theta) \end{bmatrix} F_{NOR} = \begin{bmatrix} \sin(\theta) \\ -\cos(\theta) \end{bmatrix} S_{pad} P_c(g) = [\tilde{b}_{NOR}] P_c(g) \quad (1.5)$$

The force F_{TAN} (tangent to the sliding plane) represents the surface friction under constant sliding. It is modeled using the Coulomb laws and thus linearly related to F_{NOR} through the friction coefficient μ

$$F_{TAN} = \mu F_{NOR} \quad (1.6)$$

μ is sometimes considered to be dependent on sliding speed ([24] for example), but for the scope of this study, it will be considered constant to emphasize the fact that friction dependence is not necessary to explain the limit cycle stabilization mechanism. Similarly to the contact force, F_{TAN} can then be described using observation/command formalism as

1.3. FREQUENCY DOMAIN STABILITY ANALYSIS USING COMPLEX EIGENVALUE ANALYSIS (CEA)

$$\{\tilde{F}_{TAN}\} = \begin{bmatrix} -\cos(\theta) \\ -\sin(\theta) \end{bmatrix} F_{TAN} = - \begin{bmatrix} \cos(\theta) \\ \sin(\theta) \end{bmatrix} \mu S_{pad} P_c(g) = -\mu [\tilde{b}_{TAN}] P_c(g) \quad (1.7)$$

Taking a linear system reference, it is then possible to construct a set of modal coordinates $\{q\} = [\phi] \begin{Bmatrix} x \\ z \end{Bmatrix}$ such that $[\phi]^T [M] [\phi] = [I]$ and $[\phi]^T [K] [\phi] = [\omega_j^2]$. By using the modal coordinate transformation and substituting the expressions of loads (1.2), (1.4) and (1.7) into (1.1), we obtain the nonlinear dynamic equation for the functional model in modal coordinates

$$[I] \{\ddot{q}\} + [2\zeta_j \omega_j] \{\dot{q}\} + [\omega_j^2] \{q\} + [b_{NOR} - \mu b_{TAN}] P_c([c_{NOR}] \{q\}) - [b_{Pres}] F_{Pres} = 0. \quad (1.8)$$

where $[b_{NOR}] = [\phi]^T [\tilde{b}_{NOR}]$, $[c_{NOR}] = [\tilde{c}_{NOR}] [\phi]$, $[b_{TAN}] = [\phi]^T [\tilde{b}_{TAN}]$ and $[b_{Pres}] = [\phi]^T [\tilde{b}_{Pres}]$.

Although the representation of a brake system through a simple functional model may seem restrictive at first glance, a similar development can be applied to a two mode reduced model resulting from the linearization of a full brake finite element model. Difficulties then come from the fact that pressure does not vary uniformly across a surface that may change. Applications were performed by SDTools outside the scope of this thesis.

The values shown in table 1.2 were selected manually to be somewhat close to experimental results.

Table 1.2: Parameters chosen for the functional squeal model

m [kg]	ω_x [kHz]	ω_z [kHz]	ζ_x [%]	ζ_z [%]	p_0 [MPa]	λ_c [mm^{-1}]	θ [$^\circ$]	S_{Pad} [mm^2]
1	1.5	1.45	0.1	0.2	0.01	750	25	20

1.3 Frequency domain stability analysis using Complex Eigenvalue Analysis (CEA)

1.3.1 Classical CEA linearized around sliding state

The first analysis of the proposed functional model is done in frequency domain using the Complex Eigenvalue Analysis (CEA). This type of stability analysis is commonly used to evaluate the presence of squeal in industrial models.

Study of stability in brake systems [39] starts by linearizing the system equations around a steady sliding solution. Poles are then computed from linearized equations (this is typically called Complex Eigenvalue Analysis CEA in squeal applications), and stability is associated with the real part of poles. Changes in operating conditions modify the steady sliding solution, the associated linearization, and poles. CEA must thus be performed for each configuration. Since this is a linearization around small amplitudes, CEA does not depend on amplitude and does not provide a mechanism to predict limit cycles.

1.3. FREQUENCY DOMAIN STABILITY ANALYSIS USING COMPLEX EIGENVALUE ANALYSIS (CEA)

Amplitudes estimation can be performed in the time domain [40, 13] or using approximation methods, such as the Harmonic Balance Method (HBM) to compute nonlinear modes [41, 42, 43], or the normal forms [44]. As less costly alternatives, approached methods emulating pseudo-periodic complex mode based cycles have also been attempted such as the Energy Balance Method [45, 46], the Modal Amplitude Stability Analysis [15], or energy potential indicators [47]. The numerical evaluation of attainable amplitude remains a challenge for industrial models.

Now let us describe the application of CEA to the functional model proposed in 1.2. The first step is linearization around a static sliding conditions, which here depends on the applied pressure F_{Pres} . One thus solves the static problem

$$\left[\omega_j^2 \right] \{q_0\} + [b_{NOR} - \mu b_{TAN}] P_c([c_{NOR}] \{q_0\}) - [b_{Pres}] \{F_{Pres}\} = 0 \quad (1.9)$$

to obtain the static displacement $\{q_0\}$, inducing a static overclosure $g_0 = [c_{NOR}] \{q_0\}$. The nonlinear contact law is then linearized around g_0 using a first order approximation of pressure $P_c(g) \approx K_c(g_0) [c_{NOR}] (\{q\} - \{q_0\})$ where

$$K_c(g_0) = \frac{\partial P_c}{\partial (g)}(g_0) = p_0 \lambda_c e^{\lambda_c g_0} \quad (1.10)$$

By replacing (1.10) into (1.8) the system equation becomes linear and a complex eigenvalue problem dependent on g_0 can be constructed by seeking a solution of the form $\{q\} = \{\psi\} e^{\lambda t}$

$$\left(\lambda^2 [I] + \lambda \left[2\zeta_j \omega_j \right] + \left[\omega_j^2 \right] + [b_{NOR} - \mu b_{TAN}] K_c(g_0) [c_{NOR}] \right) \{\psi\} = 0 \quad (1.11)$$

The modes of this system correspond to non-trivial solutions ($\{\psi_j\} \neq 0$) associated to poles $\lambda_j = -\zeta_j \omega_j + i\omega_j \sqrt{1 - \zeta_j^2}$. A mode is unstable if the pole real part is positive i.e. its damping coefficient ζ_j is negative. In classical Linear Time Invariant (LTI) analysis, the system is considered unstable if at least one pole is unstable.

1.3.2 Influence of static load : LPV evolution

To analyze the modal interaction that leads to unstable system, it is common to vary the friction coefficient μ as in [4]. However, for real systems, the friction coefficient is unlikely to change and, in tests, pressure is the first parameter changed in the system. To emphasize this, we have chosen to consider F_{Pres} as parameter of the following stability study. Changing the static pressure leads to an evolution of the linearized contact stiffness : this parametric study corresponds to a Linear Parameter-Varying (LPV) evolution.

Figure 1.2 shows the evolution of pole frequencies and dampings with F_{Pres} varying from 250N to 550N. The region between vertical bars highlights the static load range [375 – 460]N for which the system is unstable (negative damping).

Color in Figure 1.2 is used to indicate stiffness changes using the ratio $K_c(g_0)/K_x$. In the considered range of F_{Pres} (from 250N to 550N) the value of $K_c(g_0)/K_x$ is between 2 and 20%, while the relative difference $\frac{|K_z - K_x|}{K_x}$ between $K_z = m\omega_z^2$ and K_x is around 6.5%. This shows that the stiffness changes introduced by the contact are signal are larger than the stiffness difference between the two directions.

1.3. FREQUENCY DOMAIN STABILITY ANALYSIS USING COMPLEX EIGENVALUE ANALYSIS (CEA)

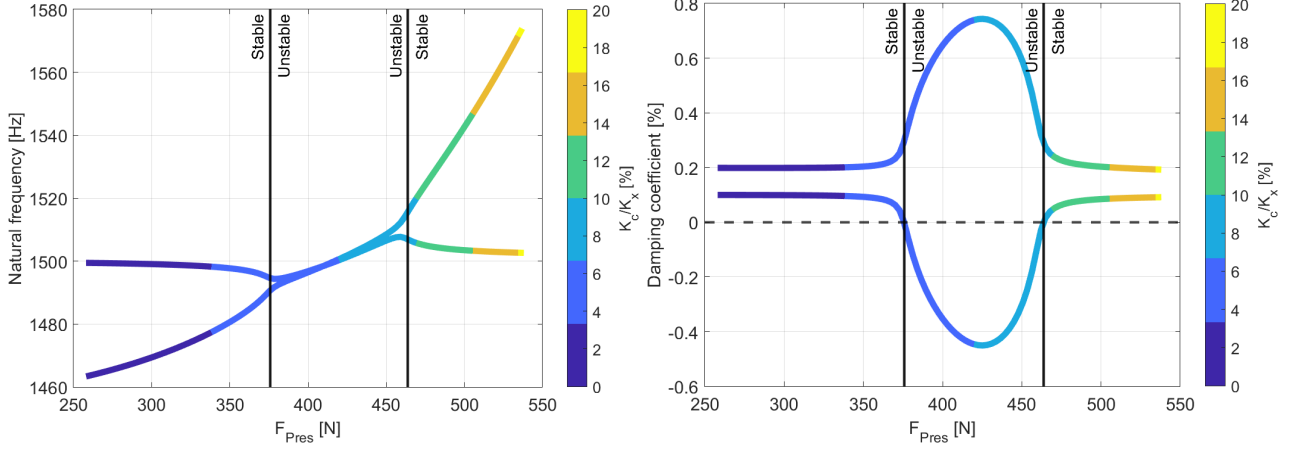


Figure 1.2: Evolution of the linearized system poles as a function of the static load F_{pres} . Left: natural frequency. Right: damping coefficient. Color indicates normalized contact stiffness.

Additionally, in the unstable range of F_{pres} the poles give us information about the expected growth rate at low amplitude. More specifically, the obtained growth rate is representative of the initial vibration growth for a given unstable operating condition, but not the limit cycle vibration (as noted by [37, 24]).

1.3.3 Introducing an amplitude dependence to the CEA

As mentioned previously, the CEA has some limitations. The most notable one being that it only represents the system behavior at low amplitude. In practice, as the vibration amplitude increases, the small amplitude hypothesis used to linearize the model is no longer valid. In order to include the amplitude effect on the CEA, a second linearization strategy is introduced in this section.

Before defining the second linearization strategy, it is important to note that performing a linearization around the steady sliding state or around a point within the limit cycle gives notably different results [13]. In other words, one should distinguish linearization for the objective of predicting the response for a time short compared to the limit cycle period or for a slow timescale, where the response is averaged over multiple periods. Taking the example of two surfaces in intermittent contact [48], for fast time scales contact or separation will lead to very different results, for slow time scales the relevant parameter will be the fraction of the period where contact occurs. The two interpretations can be seen respectively as nonlinear or parametric LTI models.

The effect of amplitude is commonly described using nonlinear normal modes (NNM) [41]. There are however two main definitions for NNM. The first definition initially proposed by Rosenberg [49] considers NNM the periodic motion of a conservative system. The second definition proposed by Shaw and Pierre [50, 51] considers the NNM as invariant manifolds.

In this study, one only assumes periodic motion as in Harmonic Balance Method [41, 42, 43] which corresponds to the invariant manifold definition. As mentioned previously, harmonic balance is one of the computational methods used to estimate limit cycle amplitudes.

A simplified approach to include amplitude in the analysis of limit cycle was developed by [15] by

1.3. FREQUENCY DOMAIN STABILITY ANALYSIS USING COMPLEX EIGENVALUE ANALYSIS (CEA)

imposing a periodic trajectory using the shape of the unstable pole obtained from the CEA at low amplitude. The idea of imposing a periodic trajectory is very interesting and allow for the construction of a pole dependency to amplitude. Nevertheless, by using a fixed complex mode shape, one is not able to include the effect of shape changes in the limit cycle stability. An alternative approach that does not impose fixed mode shapes has been used in [52] to experimentally characterize the step-sine response of well separated modes in nonlinear systems using drive point displacement as an indicator of modal amplitude. This approach relies on a non parametric description of the nonlinear forces as stiffness and damping depending on modal amplitude [38].

The approach considered in this study seeks to characterize the system behavior in terms of periodic trajectories. For this we consider that the vibration characteristics vary slowly with time, and so can be considered constant for a few periods of the limit cycle. It is thus possible to describe a period through its Fourier series

$$\{q(t)\} = \sum_{h=0}^{\infty} Re \left(\{q_h\} e^{ih\omega t} \right) \quad (1.12)$$

where the state vector describing the period is composed of a frequency ω and harmonic vectors $\{q_h\}$. This corresponds to a space-time decomposition of the response and this vector of unknowns used by the Harmonic Balance Method, and the coefficients can be obtained by a simple Fourier decomposition

$$\frac{\omega}{\pi} \int_0^{2\pi/\omega} \{q(t)\} e^{-ih\omega t} dt = \begin{cases} \{q_k\} & \text{if } h \neq 0 \\ 2\{q_0\} & \text{if } h = 0 \end{cases} \quad (1.13)$$

In the case of the 2-DOF functional model proposed in section 1.2, describing the nonlinear behavior means describing contact overclosure (inverse of the gap) and forces. This is done by imposing a periodic trajectory to the contact overclosure $g(g_0, g_1, t) = g_0 + g_1 \cos(\omega t)$. The effect of the static equilibrium is represented by the harmonic 0 component g_0 , and the vibration amplitude by the harmonic 1 component g_1 . Both of these coefficients are related to the system displacement by

$$g_j(t) = [c_{NOR}] \{q_j(t)\} \quad j = 0, 1. \quad (1.14)$$

Using this imposed trajectory and the nonlinear contact law (1.4), it becomes possible to obtain a contact pressure profile. Figure 1.3 illustrates the relation between imposed displacement and contact pressure using arbitrary parameters.

1.3. FREQUENCY DOMAIN STABILITY ANALYSIS USING COMPLEX EIGENVALUE ANALYSIS (CEA)

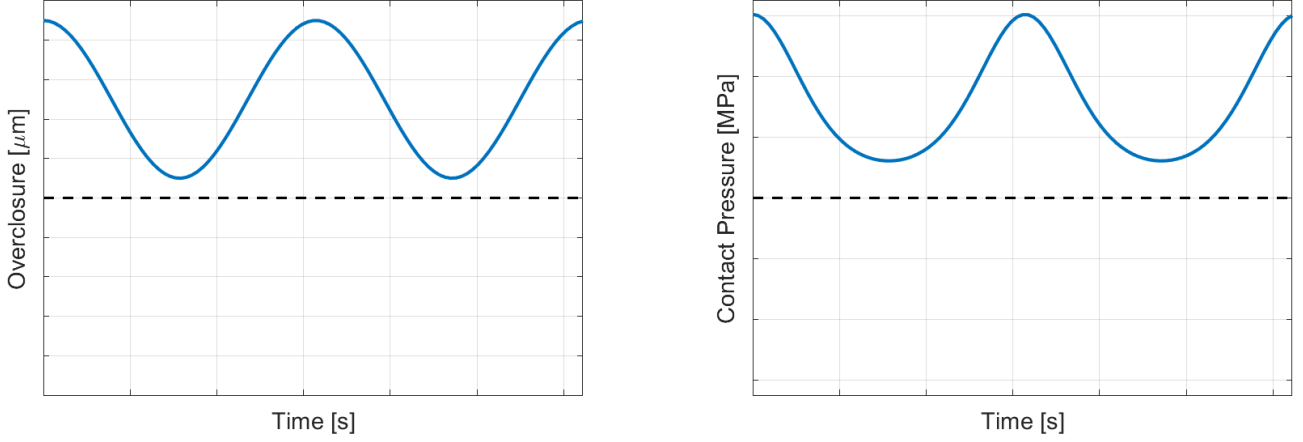


Figure 1.3: Example of imposed contact overclosure g (Left) and the corresponding contact pressure P_c (Right)

Despite imposing a trajectory restricted to harmonics 0 and 1, the resulting contact pressure contains higher harmonics. This can be seen in figure 1.4 which shows the components of the signal corresponding to harmonics 0, 1 and all the others.

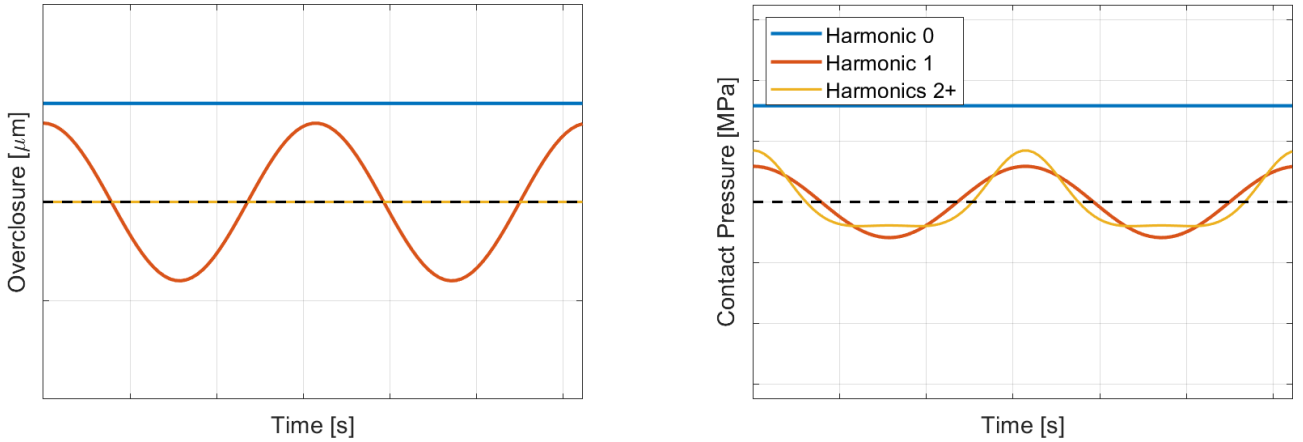


Figure 1.4: Extracted harmonic 0 and 1 from the imposed contact displacement (Left) and the corresponding contact pressure (Right)

For the new linearization strategy, we turn ourselves to the Harmonic Balance Method. In the framework of the HBM, one computes the virtual work over a period of true forces with respect to each of the space-time unknowns (components of $\{q_h\}$ vectors). One thus introduces an equivalent stiffness by comparing the virtual work of the nonlinear pressure and $P_c(t)$ and that of an equivalent linearized force $K_h(g_0, g_1)g(t)$ using

$$\int_0^{2\pi/\omega} P_c(t) e^{-ih\omega t} dt = \int_0^{2\pi/\omega} (K_h(g_0, g_1)g(t)) e^{-ih\omega t} dt. \quad (1.15)$$

1.3. FREQUENCY DOMAIN STABILITY ANALYSIS USING COMPLEX EIGENVALUE ANALYSIS (CEA)

A linear contact stiffness having the same work as the nonlinear harmonic thus verifies

$$K_{c,0}(g_0, g_1) = \frac{P_{c,0}(g_0, g_1)}{g_0} \quad K_{c,1}(g_0, g_1) = \frac{P_{c,1}(g_0, g_1)}{g_1}. \quad (1.16)$$

where $P_c^0(g^0, g^1)$ and $P_c^1(g^0, g^1)$ are virtual work of harmonics 0 and 1 contact pressure, the left part of equation (1.15). Using this definition, one is then able to describe the nonlinear contact pressure as a function of g_0 and g_1 . This approach is similar to the identification process used in [38] to experimentally characterize a nonlinearity.

Figure 1.5 Left shows a comparison of the linearized force corresponding to harmonic 1 stiffness $K_{c,1}$ and the tangent stiffness (1.10). This figure shows that the slope of the linearized force corresponding to $K_{c,1}$ is higher than the one for tangent stiffness, which indicates stiffening with amplitude.

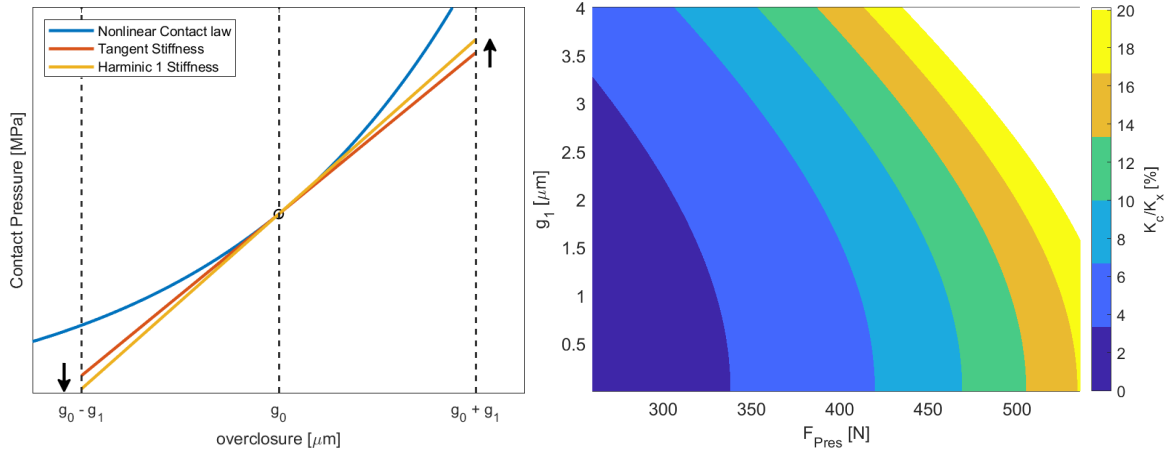


Figure 1.5: Left: Comparison between the linearized forces corresponding to harmonic 1 stiffness $K_{c,1}$ and tangent stiffness for an arbitrary exponential contact law and trajectory defined by g_0, g_1 . Right: Equivalent stiffness evolution with the static load F_{Pres} and first harmonic amplitude g_1 .

Using this definition figure 1.5 shows the evolution of $K_{c,1}(g_0, g_1)/K_x$ as a function of the static load and amplitude. It shows us that the increase in stiffness resulting from amplitude is significant compared to the relative difference $\frac{|K_z - K_x|}{K_x}$ between K_z and K_x , which is around 6.5%. For the sake of simplicity the static load F_{Pres} is related to g_0 by equation (1.9).

This equivalent stiffness can be combined with the equilibrium equations by applying the HBM framework to (1.8), resulting in a pair of parametric equilibrium equations. The equation corresponding to harmonic 0 is a modified version of equation (1.9)

$$\left[\omega_{j\setminus}^2 \right] \{q_0\} + [b_{NOR} - \mu b_{TAN}] K_{c,0}(g_0, g_1) [c_{NOR}] \{q_0\} - [b_{Pres}] \{F_{Pres}\} = 0. \quad (1.17)$$

While the equilibrium for harmonic 1 verifies

$$-\omega^2 [I] \{q_1\} + i\omega \left[2\zeta_j \omega_{j\setminus} \right] \{q_1\} + \left[\omega_{j\setminus}^2 \right] \{q_1\} + [b_{NOR} - \mu b_{TAN}] K_{c,1}(g_0, g_1) [c_{NOR}] \{q_1\} = 0 \quad (1.18)$$

One notices that the solutions for harmonic 0 and 1 are coupled, and both of them must be solved together in order to obtain the response to a given static load one must pass by both (1.17) and (1.18).

1.3. FREQUENCY DOMAIN STABILITY ANALYSIS USING COMPLEX EIGENVALUE ANALYSIS (CEA)

Equation (1.18) can be rewritten as a parametric eigenvalue problem, similar to (1.11)

$$\left(\lambda^2 [I] + \lambda [2\zeta_j \omega_j] + [\omega_j^2] + [b_{NOR} - \mu b_{TAN}] K_c(g_0, g_1) [c_{NOR}] \right) \{\psi\} = 0. \quad (1.19)$$

This amplitude dependent eigenvalue problem allow us to evaluate the pole evolution with both the static load (represented by g_0) and vibration amplitude (represented by g_1).

1.3.4 Amplitude dependent root locus

Using the eigenvalue problem from (1.19) it is possible to characterize the poles of the system for given values of g_0 and g_1 . While g_1 is a good amplitude indicator, it is more practical to describe the static operating conditions as function of experimentally controllable parameters such as the applied pressure F_{Pres} . For simplicity equation (1.9) was used a bijective transposition between g_0 and F_{Pres} as an aid for visualization.

Figure 1.6 displays the system root locus as a function of K_c/K_x . As the equivalent stiffness is a scalar value, the path of the poles in figure 1.6 is the same as the one displayed in figure 1.2. The difference is that the root locus is now a function of two variables F_{pres} and g_1 , related to $K_{c,1}$ by (1.16) as illustrated by figure 1.5 Right.

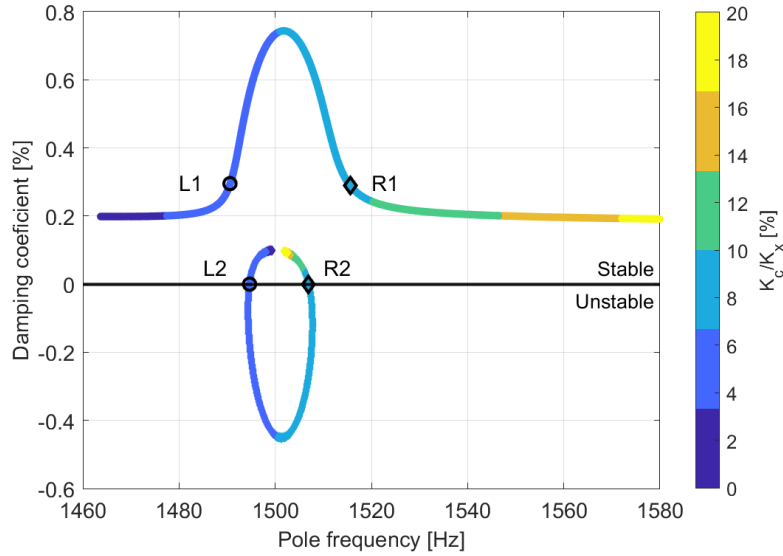


Figure 1.6: Poles obtained from (1.11) for different values of contact stiffness K_c (Root Locus). Pairs of poles corresponding to the crossing of the $\zeta = 0$ line (limit cycles) are indicated by L1/L2 and R1/R2.

From the obtained poles, it is then possible to trace the evolution of ζ for the unstable pole in the g_0, g_1 parametric space, as shown in figure 1.7. The regions in red left and right indicate positive damping. These are the stable zones where vibration is attenuated. In the middle, a blue region corresponds to a negative damping (instability) that leads to amplitude growth. On the frontier between the stable and unstable regions, the limit cycles can be found. Their location at the boundary

1.3. FREQUENCY DOMAIN STABILITY ANALYSIS USING COMPLEX EIGENVALUE ANALYSIS (CEA)

means that all possible limit cycles can be found by tracking the regions, where damping equals zero (black lines in figure 1.7). If the proposed equivalent stiffness is pertinent, one expects to have limit cycles of different amplitude for variable static pressure. This will be illustrated by transient simulations in section 1.4.

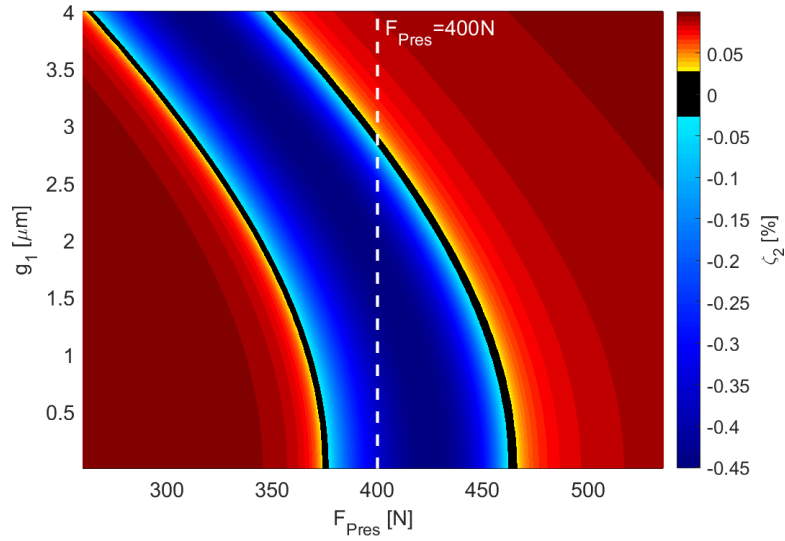


Figure 1.7: Damping coefficient of the unstable mode ζ_2 evolution with the static load F_{Pres} and first harmonic amplitude g_1 . LPV stability boundary shown as black line. Vertical white line indicating $F_{Pres} = 400N$.

In order to take a closer look at the saturation mechanism, in figure 1.8 we analyze the evolution of the mode shapes $\{\psi_j(g_0, g_1)\}$ obtained from (1.19) with g_1 for a fixed static load $F_{pres} = 400N$ using the Modal Assurance Criterion (MAC) [53]

$$MAC(\psi(g_0, 0), \psi(g_0, g_1)) = \frac{|\psi(g_0, 0)^T \psi(g_0, g_1)|^2}{\|\psi(g_0, 0)\|^2 \|\psi(g_0, g_1)\|^2}. \quad (1.20)$$

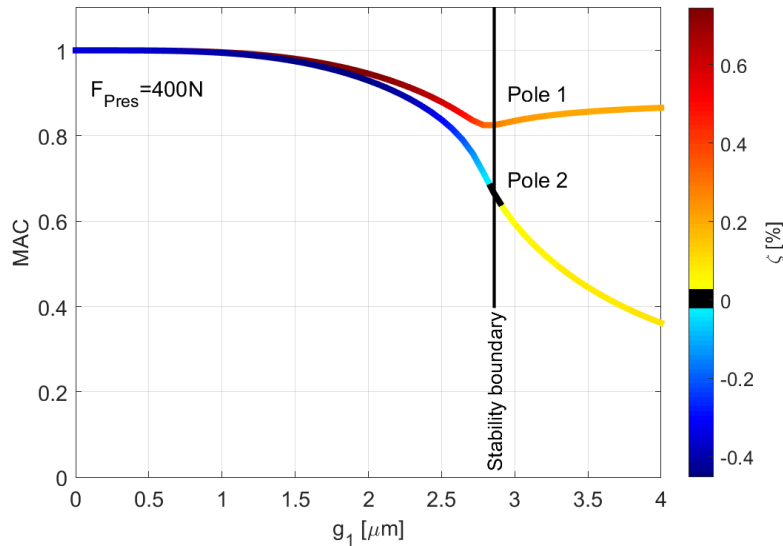


Figure 1.8: Evolution of the MAC between mode shapes of the stable and unstable poles as a function of first harmonic amplitude g_1 for $F_{Pres} = 400N$ with ζ indicated as color. Vertical line indicates the amplitude corresponding to $\zeta_2 = 0$ (limit cycle).

In figure 1.8 it is noticeable that as amplitude g_1 increases the mode shapes of both the stable and unstable mode slowly change resulting in a decreasing MAC value until reaching the stability boundary. The g_1 value at the stability boundary represents the first harmonic amplitude where a limit cycle vibration is possible for the chosen $F_{Pres} = 400N$. Further increasing the amplitude g_1 results in the MAC for the stable pole increasing, while for the unstable pole it continues to decrease. The main conclusion is the complex harmonic shape associated with sliding linearization and limit cycle should be different, a result that has been observed on the analysis of time simulations in section 1.4.5.

In particular, this implies that methods that use a fixed vibration shape in order to evaluate the amplitude effect on squeal (such as the Energy Balance Method [45, 46] and Modal Amplitude Stability Analysis [15]) are not adapted to estimate squeal limit cycle amplitudes.

1.4 Limit cycle characteristics from time simulations

In the previous section, two different linearization strategies were considered and allowed analysis of squeal through the study of parametric variations of poles with pressure and amplitude. This corresponds to CEA analyzes of brakes performed in design phases of development.

In this section, the focus is on the time domain responses like the ones observed in real brake tests. The time domain responses of the functional model are obtained using a modal Newmark nonlinear integration scheme [54].

A series of slowly varying pressure F_{Pres} profiles are considered, emulating the parametric tests performed in a full scale brake system (see chapter 3 for details). First a constant pressure is applied, representing drag tests, followed by pressure ramps, and pressure oscillations mimicking the contact

1.4. LIMIT CYCLE CHARACTERISTICS FROM TIME SIMULATIONS

changes due to wheel rotation (which is thought to be the source of intermittent squeal occurrences). A small background noise is added to represent the background noise present in real tests, such as the passage of irregularities under the pads.

The goal of this section is then to extract representative characteristics from time data and compare them with the results from the eigenvalue analysis in section 1.3.

Section 1.4.1 starts by comparing the harmonic 1 amplitude of the limit cycle for a constant pressure value. The stability boundary is then evaluated using pressure ramps in section 1.4.2 and oscillating pressure in 1.4.3. A comparison of the growth phase during intermittent squeal with the root locus is discussed in section 1.4.4 using the decay rate. Finally, section 1.4.5 analyses the relation between growth and shape.

1.4.1 Limit cycle for constant static load

Using CEA results as a guideline, one first considers an applied pressure F_{Pres} . As depicted in figure 1.9 left F_{Pres} slowly raises from zero until $370N$ close to the unstable region (see figure 1.7), stabilizes for $0.4s$ to limit remaining transient effects from the initial loading and then increases to $385N$ triggering the instability. Figure 1.9 right shows the static response slowly evolving with small noise induced vibration until the system enters the unstable region, where the vibration amplitude suddenly increases and quickly reaches a limit cycle that remains stable until the end of the simulation. This shows that the proposed model is capable of reproducing the mechanisms responsible for unstable growth and limit cycle formation.

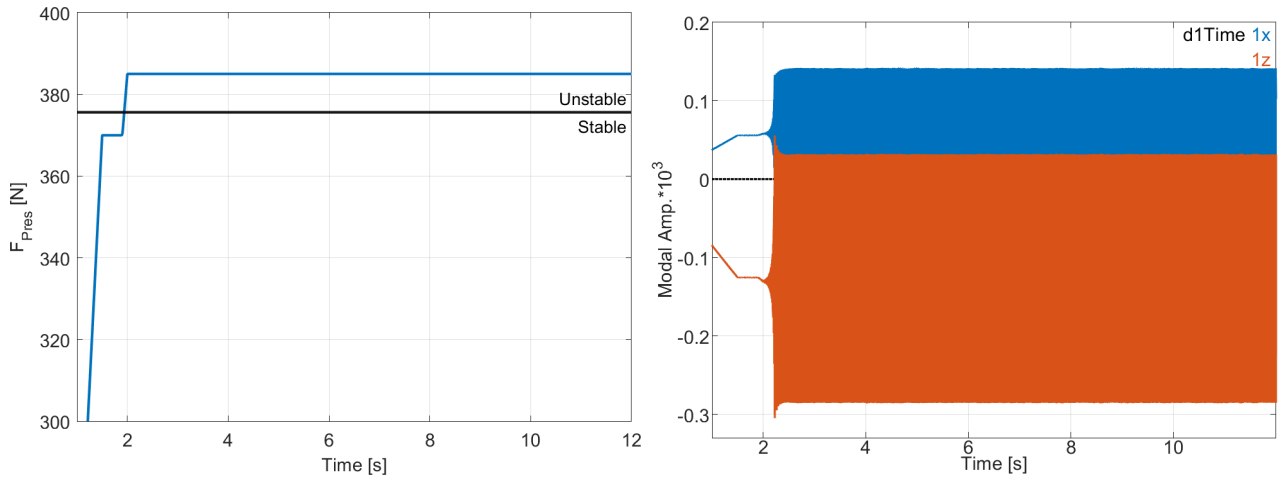


Figure 1.9: Left: Constant static load F_{Pres} profile and stability frontier. Right: Modal amplitudes evolution over time

1.4. LIMIT CYCLE CHARACTERISTICS FROM TIME SIMULATIONS

In the amplitude dependent eigenvalue analysis of the functional model detailed in 1.3.4, we have considered that the system behavior can be described by the trajectory of the contact, more specifically the amplitudes of harmonics 0 and 1 of the overclosure g_0 and g_1 respectively. Both of these values can be extracted from the overclosure $g(t)$ using the HBV signal model and demodulation strategy detailed in section (1.12).

Figure 1.10 compares the limit cycle first harmonic amplitude g_1 extracted from time simulation and its expected value from the Amplitude dependent CEA with $F_{pres} = 385N$. The prediction obtained from the CEA is very close to the values obtained in the nonlinear time simulation, despite the fact that the CEA only considers harmonics 0 and 1 to estimate limit cycle.

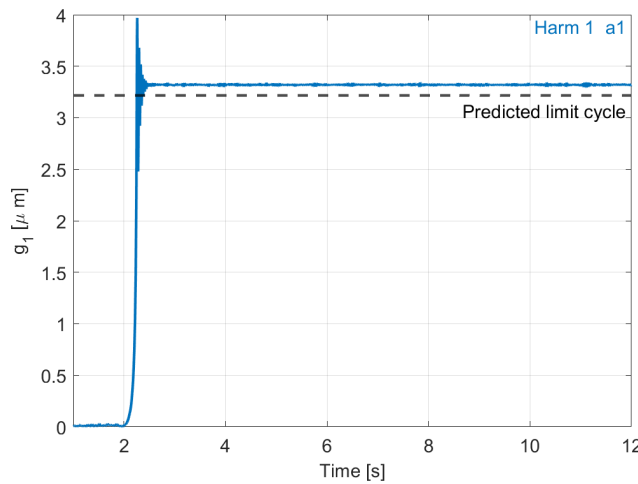


Figure 1.10: Evolution of $g_1(t)$ extracted from the transient simulation described in figure 1.9 using demodulation (-) compared to the limit cycle amplitude predicted using amplitude dependent CEA (-).

1.4.2 Tracking stability boundary with slow static load ramp

In this analysis the limit cycle dependence to the applied pressure is evaluated by slowly increasing the applied pressure using the profile described in figure 1.11. Such pressure ramps are considered in real tests. This force profile was constructed to pass through the unstable region estimated using CEA in section 1.3. The value of $g_1(t)$ is then extracted using the same demodulation strategy as the test case with a constant pressure described above.

1.4. LIMIT CYCLE CHARACTERISTICS FROM TIME SIMULATIONS

By plotting the evolution of $g_1(t)$ with F_{pres} against the predicted stability obtained in the eigenvalue analysis, it is very clear that as soon as the system enters in unstable range the overclosure vibration amplitude rapidly increases. As amplitude increases, the influence of the system nonlinearities increases inducing a saturation near the upper stability boundary. From this point onward the limit cycle amplitude follows closely the predicted limit cycle until the end of the unstable zone. This superposition shows that using the first harmonic extracted from the transient response is comparable to amplitude dependent eigenvalue results from 1.3.4.

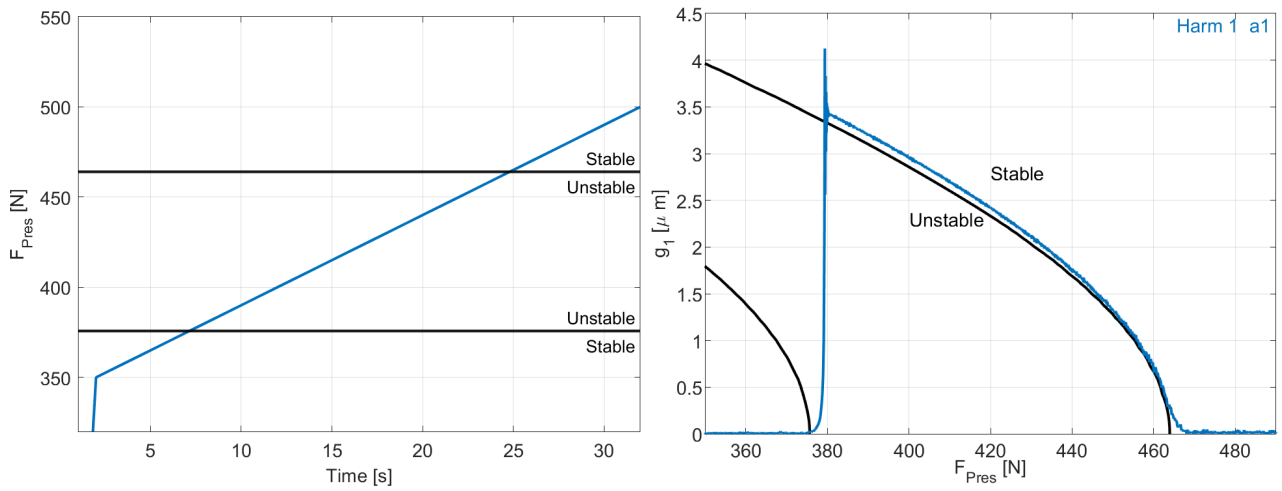


Figure 1.11: Left: Slow ramp static load F_{Pres} profile and stability frontier. Right: First harmonic component of the overclosure $g_1(t)$ extracted using demodulation (blue) and stability boundary obtained from the amplitude dependent CEA (black) as a function of F_{Pres} .

The fact that it is possible to compare the limit cycle estimated in frequency and time domain in itself is very encouraging.

1.4. LIMIT CYCLE CHARACTERISTICS FROM TIME SIMULATIONS

Now looking at frequencies, figure 1.12 compares the vibration frequencies obtained in the transient simulation with the poles from section 1.3.4. For the transient, frequencies are assessed directly using a spectrogram of the overclosure g (figure 1.12 left). Obtaining a direct comparison from the eigenvalue results is not as straightforward, since a pair of poles is obtained for every g_1, F_{pres} pair without any notion of time. The simplest way of obtaining a good comparison is to take the slow time evolution of $g_1(t_{slow}), F_{pres}(t_{slow})$ and seek the corresponding contact stiffness and poles in the eigenvalue results 1.6 as a look-up table. The frequencies obtained are displayed in figure 1.12 right. The comparison between the spectrogram and pole frequencies show that the limit cycle frequency matches that predicted in the eigenvalue analysis (pole R2 in figure 1.6).

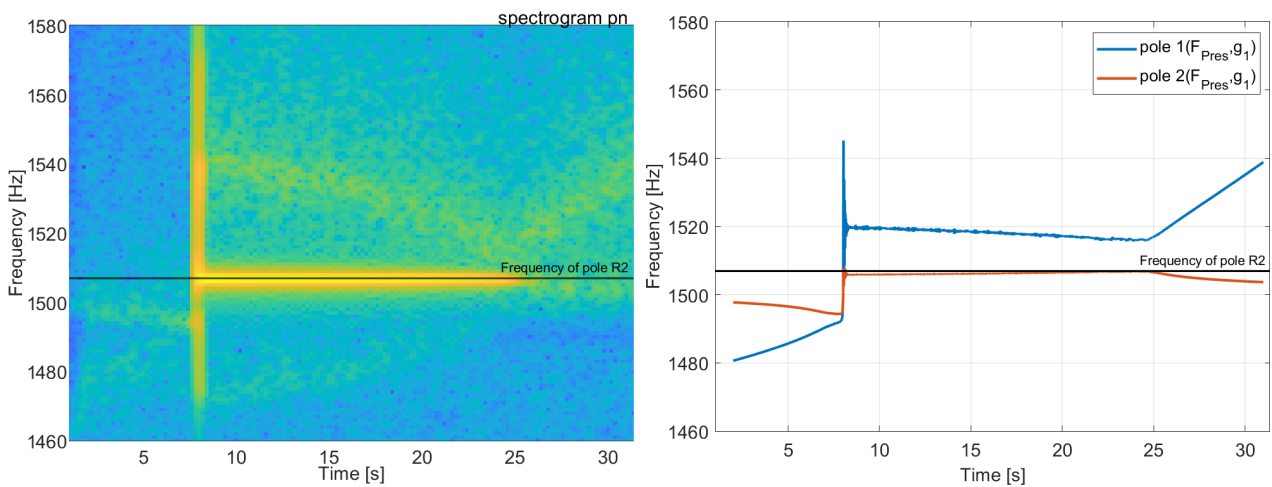


Figure 1.12: Left: Spectrogram of the overclosure g at the contact interface. Right: Evolution of the natural frequency of poles interpolated from figure 1.6 using the trajectory of F_{Pres}, g_1 from the transient simulation.

As a small level of noise is added in the transient simulation, it is also possible to see system modes in the spectrogram before and after the unstable region. The spectrogram also shows the presence of sidebands around the limit cycle that starts at around twice the frequency difference between estimated poles. This, as well as the amplitude difference between limit cycle amplitude and stability boundary (figure 1.11) are notable differences between time and LPV analysis.

1.4.3 Intermittent squeal due to static load oscillations

Then, by using an oscillating external force shown in figure 1.13, an intermittent squeal is induced in the system. This imitates the periodic parametric variations induced for example by changes related to the angular position that is observed in practical cases [21].

1.4. LIMIT CYCLE CHARACTERISTICS FROM TIME SIMULATIONS

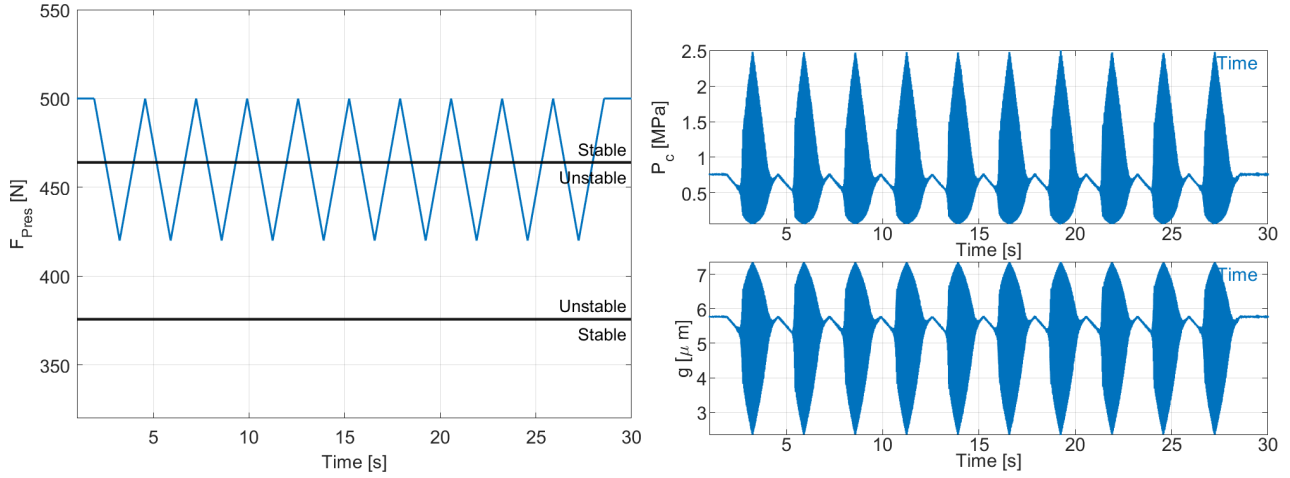


Figure 1.13: Left: Oscillating static load profile F_{Pres} profile and stability frontier. Right: Overclosure g and contact pressure P_c evolution over time.

Figure 1.14 once again tracks the extracted first harmonic g_1 as function of F_{Pres} and compares it with the CEA stability boundary. Two different time windows are used in to showcase the intermittent vibration behavior. Looking at the entire simulation (figure 1.14 left) shows that the extracted characteristics are consistent and repeatable over time. The superposition of curves, however, makes it difficult to analyze the time evolution of these characteristics in the chosen axes.

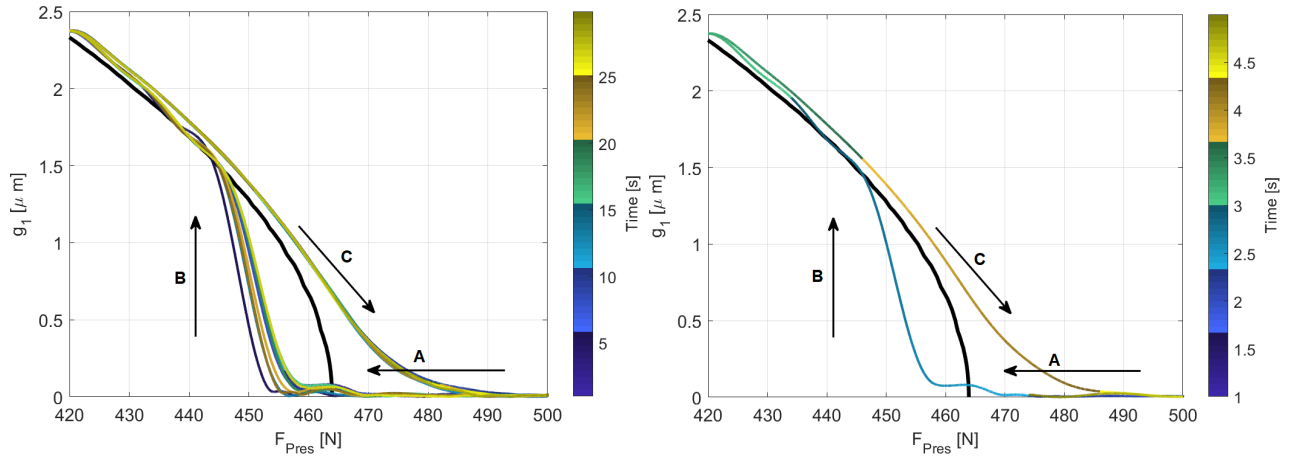


Figure 1.14: Evolution of the first harmonic of the overclosure g_1 as a function of applied pressure F_{Pres} and time (color) compared to the stability boundary obtained from the amplitude dependent CEA (black). Arrows (A,B,C) indicate the sense of time evolution. Left: complete simulation. Right: first 5 s.

In order track how the amplitude changes during the pressure trajectory, figure 1.14 right limits the time window to the first 5s of the simulation, corresponding to the first pressure oscillation. As the applied pressure reduces from its starting point at $F_{Pres} = 500N$ (arrow A), the value of g_1 remains near zero until it reaches the stability boundary around $F_{Pres} = 465N$. After crossing the

1.4. LIMIT CYCLE CHARACTERISTICS FROM TIME SIMULATIONS

stability boundary, the vibration rapidly gets amplified and meets the stability line once again near $g_1 = 1.5\mu m$ (end of arrow B). The vibration amplitude then follows the estimated frontier as pressure decreases to $F_{Pres} = 420N$ and subsequently increases. The value of g_1 remains close to the predicted stability boundary until around $F_{Pres} = 460N$ (arrow C). At this point, the decay rate of the stability boundary, for the chosen static pressure rate, is faster than the decay rate of the time simulation. Resulting in a decay of amplitude that reaches zero as pressure goes back to its initial value.

The presence of transient behavior when crossing the stability boundary indicates that parametric studies using transient simulations or experimental measurements should be careful to ensure the parametric changes are sufficiently slow in order to accurately characterize parametric effects.

1.4.4 Estimation of a time decay rate and relation to root locus

For a given unstable pole λ_j , growth depends on the pole real part and can be described by an instant frequency and negative damping value by $Re(\lambda_j) = -\omega_j\zeta_j$. This implies that one may trace a parallel between growth phase of a time simulation to the natural frequency ω_j and damping coefficient ζ_j of the amplitude dependent CEA poles (the root locus).

In order to establish this comparison, the signal instant frequency $\hat{\omega}(t)$ and amplitude $A(t)$ are extracted using a demodulation strategy (detailed in section 2.2). Then, a decay rate $\hat{\zeta}(t)$ is computed from the amplitude using

$$\hat{\zeta}(A, t) = \frac{-1}{\omega} \frac{d}{dt} (\log(A(t))). \quad (1.21)$$

Using one of the signal channels from the intermittent squeal, figure 1.15 shows the comparison of the damping ratio and instant frequency with the root locus from the amplitude dependent CEA. This comparison shows that, during a squeal event, the relation between instant frequency and decay ratio follows the same overall behavior predicted by the root locus.

The intermittent nature of the considered squeal events imply that in figure 1.15 the extracted frequency/decay ratio follow a clear trajectory. When the system enters an unstable region, the trajectory starts at the bottom of the figure where amplitude is low and the decay rate is negative. Maximum amplitude is reached when $\hat{\zeta} \approx 0$ where it stays until the system exits the unstable region. The decay rate then becomes positive and the response decays back to low amplitude.

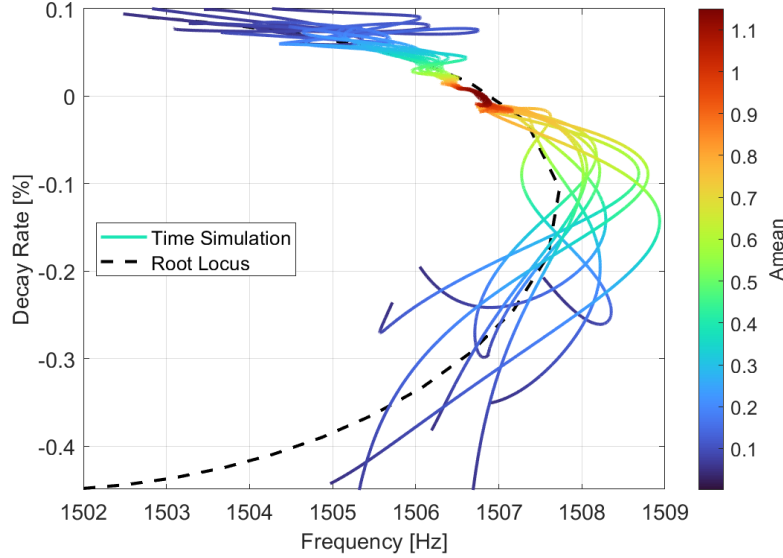


Figure 1.15: Decay ratio as a function of instantaneous frequency with amplitude as color (-). Root Locus estimated in using complex eigenvalue analysis (- -)

One may also notice a significant level of spread on the extracted frequency/decay ratio present at lower amplitudes. This spread is a result of the added background noise, and can also be seen in the F_{pres}, g_1 trajectories shown in figure 1.14 Left. This effect will be minimized in the next section by taking vibration shape into account.

1.4.5 Evolution of limit cycle shape with operating condition

In the construction of the proposed functional model (section 1.2) we considered that mode lock-in is the main mechanism behind brake squeal. This indicates that the response of the system must be contained in a two-dimensional subspace. Although evident in the 2-DoF functional model, this characteristic has been observed in squeal measurements of full scale systems [55].

With this in mind, one seeks to describe the vibrations from the functional model using real shapes with complex amplitudes varying with operating condition. To obtain real shapes, N_T snapshots of the harmonic 1 complex vector $\{q_1\} = \{q_{1c}\} + i\{q_{1s}\}$ is reordered as $\left[\{q_{1c}\} \quad \{q_{1s}\}\right]_{N_S \times (2N_T)}$ matrix, and the Singular Value Decomposition (SVD) is used to build an ordered set of contributions

$$\left[\{q_{1c}(t)\} \quad \{q_{1s}(t)\}\right]_{N_S \times (2N_T)} = \sum_j \{u_j\}_{N_S \times 1} \left(\sigma_j \begin{Bmatrix} v_{jc}^T & v_{js}^T \end{Bmatrix}\right)_{1 \times 2N_T} \quad (1.22)$$

The complex generalized coordinates $q_{jR}(t)$ associated with the principal shapes $\{u_j\}$ are then obtained by recombining real and imaginary parts of the right singular vectors

$$\sum_j \{u_j\}_{N_S \times 1} \{q_{jR}(t)\}_{1 \times N_T} = \sum_j \{u_j\} \sigma_j \left(\begin{Bmatrix} v_{jc}^T & v_{js}^T \end{Bmatrix}^T + i \right) = \{q_1(t)\}_{N_S \times N_T} \quad (1.23)$$

which is a decomposition of the full complex signal $\{q_1(t)\}$. Further uses of this decomposition will be discussed in section 2.2.

1.4. LIMIT CYCLE CHARACTERISTICS FROM TIME SIMULATIONS

Applying this to the transient simulation of the functional model (figure 1.16) shows that the vibration is dominated by the first principal shape with a relatively small participation of the second shape. However, it can be seen that there is a significant evolution of the relative phase between them.

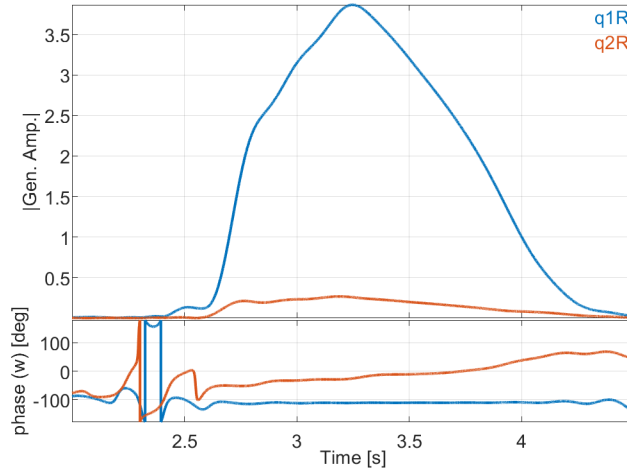


Figure 1.16: Evolution of the generalized coordinate associated with the two principal shapes

Knowing that there is a relation between the relative phase between the principal shapes and the limit cycle we seek to evaluate how it relates to other significant information about the limit cycle: the amplitude associated to the first principal shape $|q_{1R}|$ and the decay rate. Figure 1.17 illustrates this relation in two different points of view. This shows in particular that the growth or decay of the vibration is directly related to the relative phase between q_{2R} and q_{1R} , indicating a growth tendency when the phase is smaller than 90° and a decay tendency when greater than 90° . This is particularly interesting considering the continuous system evolution induced by the changes in applied pressure. It is also possible to infer that the phase between principal shapes is related to the formation of brake squeal.

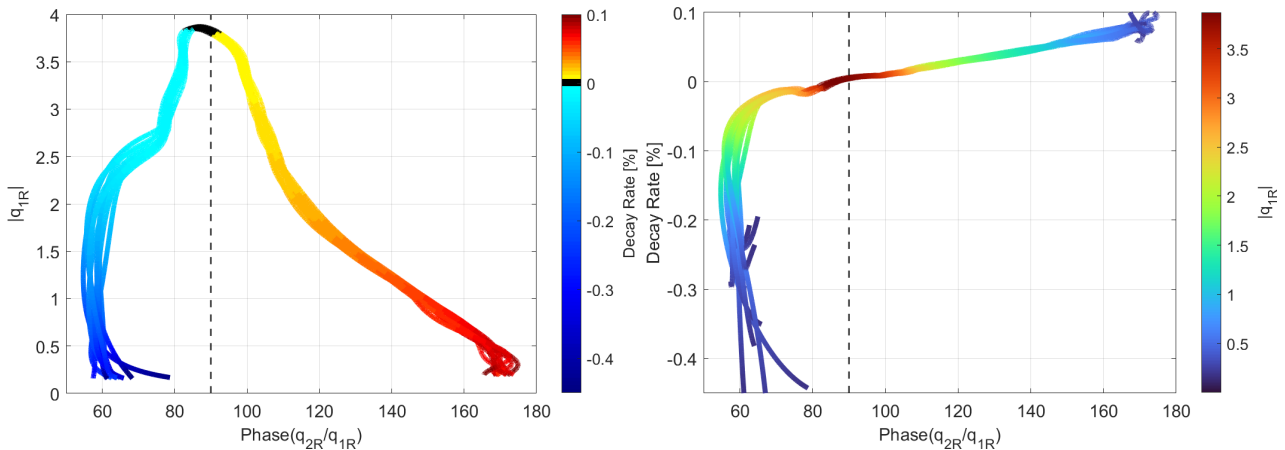


Figure 1.17: Left: Amplitude of q_{1R} as a function of the relative phase between q_{2R} and q_{1R} with decay rate as color. Right: Decay rate as a function of the relative phase between q_{2R} and q_{1R} with the amplitude of q_{1R} as color. Vertical dashed line indicates 90°

1.5 Conclusion

In this chapter we proposed a new functional model for squeal that represents the effect of slow pressure variations representative of experimental parametric measurements. In a first moment, the functional model is analyzed in frequency domain with Complex Eigenvalue Analysis (CEA), evaluating the linearized response of the model for different pressure values. This Linear Parameter-Varying (LPV) strategy is then extended by including amplitude as an additional parameter to the linearization. Using this amplitude dependent CEA it is then possible to estimate limit cycle amplitude evolution with pressure.

The functional model is then analyzed in time domain by replicating a series of usual experiments such as: drag where constant pressure is applied, pressure ramps, and pressure oscillations mimicking the contact changes due to wheel rotation. Using the HBV signal model and demodulation (described later in section (1.12)) the results of transient simulations are decomposed to extract the amplitude associated to the first harmonic, which is then compared to the eigenvalue results.

The combination of the transient analysis with the amplitude dependent CEA provides a basis for designing experimental strategies used to characterize the parametric dependencies of brake squeal on operating condition. Additionally, these ideas may serve as a guideline for the development of model updating strategies that correlate measured and estimated parametric changes leading to the construction of better predictive reduced industrial models.

In full models, a large number of contact points are present in the contact interface, implying that a model reduction technique such as hyper-reduction [56] or contact interface modes [14, 35] should be used, but this is out of the scope of this thesis.

1.5. CONCLUSION

Analyzing the dynamic response of time varying systems

Content

2.1	Introduction	56
2.2	Defining a signal model for squeal: Harmonic Balance Vector (HBV) signal model	57
2.2.1	Motivation and definition of the HBV signal model	57
2.2.2	Single channel estimation	61
2.2.3	Estimation with multiple channels	70
2.3	Parametric modal analysis	72
2.3.1	Description of a simple parametric contact test bench	73
2.3.2	EMA at fixed system parameters (Classical H1 transfer estimation)	75
2.3.3	Describing the phase resonance mode tracking strategy	77
2.3.4	Applying phase resonance tracking to the contact test bench	81
2.4	Detailed shapes of fundamental and higher harmonics	84
2.5	Using the HBV signal to describe nonlinear behavior: instant stiffness and harmonic modulation	88
2.5.1	Using higher harmonics to define instant stiffness and harmonic modulation	89
2.5.2	Harmonic modulation in 3D-SLDV measurements	92
2.6	Conclusion	95

2.1 Introduction

The dynamic behavior of brake systems is subject to the effects of multiple parameters. Some parameters can be controlled such as applied pressure and wheel velocity. Other parameters such as temperature and angular position, however, cannot be controlled and are constantly changing over time during experimental measurements. These parameter variations have an effect on the system nonlinearities and directly affect its dynamics.

Since the characteristic times of the parametric changes are much slower than the nonlinear effects, it is possible to consider that for a few periods the parametric conditions are constant. This suggests the presence of two characteristic times for squeal: a fast time associated to the nonlinear intra-period effects, and a slow time associated to the effects of parametric changes.

With this in mind, the goal of this chapter is to provide a basis for analyzing the nonlinear dynamics of systems under the influence of slow parameter variations.

Section 2.2 defines a Harmonic Balance Vector (HBV) signal model adapted to the analysis of quasi-periodic vibrations. Target applications are squeal limit cycles, stepped sine and slow sine sweep test. This signal model takes into consideration the expected characteristics of a squeal vibration to better represent a given measurement.

The HBV signal properties are estimated using a demodulation algorithm that identifies the slow evolution of both frequency and amplitude. Section 2.2.2 describes the application on the case of a measurement with a single channel. Then section 2.2.3 discusses the application to measurements with multiple channels, while keeping a common instantaneous frequency estimation. Having been identified as a simple and robust way of extracting signal components, the demodulation algorithm was widely used during this project from the functional model in section 1.4, to a simplified test bench in sections 2.3,2.4 and full scale measurements in chapter 3.

Section 2.3 then discusses the parametric modal testing for systems with slowly varying parameters. A contact test bench, where properties depend on the applied pressure, is used as illustration.

A first approximation of the relation between pressure and resonance frequency is done using traditional Experimental Modal Analysis (EMA) at a few fixed pressure points. However, this discrete characterization lacks accuracy.

Then, a procedure to obtain a continuous tracking of the modal properties with pressure is then proposed based on the phase resonance concept. In this procedure, the modal properties evolution with parameter is obtained using a series of parametric sine measurements, where the signal frequency depends on the pressure, are made near the target mode resonance frequency. This was constructed as a feedforward version of closed loop phase resonance methods [57, 58, 59, 60], the final intent being to apply it in the full scale model to track modes near instability. The application of this method to the contact test bench was presented in the Survishno conference [30].

The HBV signal is then applied to the construction of spatially detailed vibration shapes in section 2.4. This is achieved through the measurement at different pressures of the sine response near system modes resonance frequency using 3D scanning laser vibrometer (3D-SLDV). The effect of pressure on the vibration shapes is then evaluated by comparing the shapes obtained for the first harmonic at

2.2. DEFINING A SIGNAL MODEL FOR SQUEAL: HARMONIC BALANCE VECTOR (HBV) SIGNAL MODEL

different pressures.

In addition to the first harmonic, the HBV signal modes gives us access to the shapes of higher harmonics. These shapes provide and insight on how each harmonic interacts with the nonlinear contact surface.

Finally, section 2.5 details a way to exploit the higher harmonic information contained in the HBV signal model. Inspired by the construction of instant modulus to characterize nonlinear behavior in viscoelastic materials [31], two indicators are proposed to describe the system behavior around the harmonic 1 response: the harmonic modulation and the harmonic perturbation. These indicators are used to evaluate the changes of the dynamic system within a single period, highlighting where it is softer or stiffer. An early version of these results was presented at the ISMA conference [32] using data from rubber identification tests.

2.2 Defining a signal model for squeal: Harmonic Balance Vector (HBV) signal model

Brake squeal is known to be sensitive to multiple operating parameters that are time varying and some of which are uncontrollable. This introduces an additional complexity to the analysis of squeal measurements that must take into consideration the time varying nature of the system dynamics.

With this in mind, this section aims to describe a signal model that represents the expected characteristics of a brake squeal measurement. A discussion on the characteristics of squeal is done in 2.2.1, followed by the construction of the Harmonic Balance Vector (HBV) signal model.

A demodulation algorithm is then proposed as a mean of estimating the parameters of the HBV signal model. Section 2.2.2 starts with the simple case of estimating the first harmonic of signal with a single channel. This is later extended to multiple channels in 2.2.3, where a brief discussion is made on the extraction of higher harmonics.

2.2.1 Motivation and definition of the HBV signal model

As a motivation for defining the proposed HBV signal, let us take a closer look at the expected characteristics of a squeal measurement.

Figure 2.1 shows the spectrogram of a squeal measurement under variable pressure. This is one of the full scale squeal measurements detailed in chapter 3. It shows the evolution of squeal when the applied pressure is slowly increased step by step from $p = 1.5bar$ to $p = 9bar$. It is possible to notice four different regions of squeal at different times of the measurement with fundamental frequencies around 1560, 6440, 1900, 2950Hz, showing that changes in applied pressure have a major effect on squeal.

It is important to note that the brake system used in this measurement had all its viscoelastic patches removed, friction material composition and contact shape were also changed to increase the probability of squeal occurrence.

2.2. DEFINING A SIGNAL MODEL FOR SQUEAL: HARMONIC BALANCE VECTOR (HBV) SIGNAL MODEL

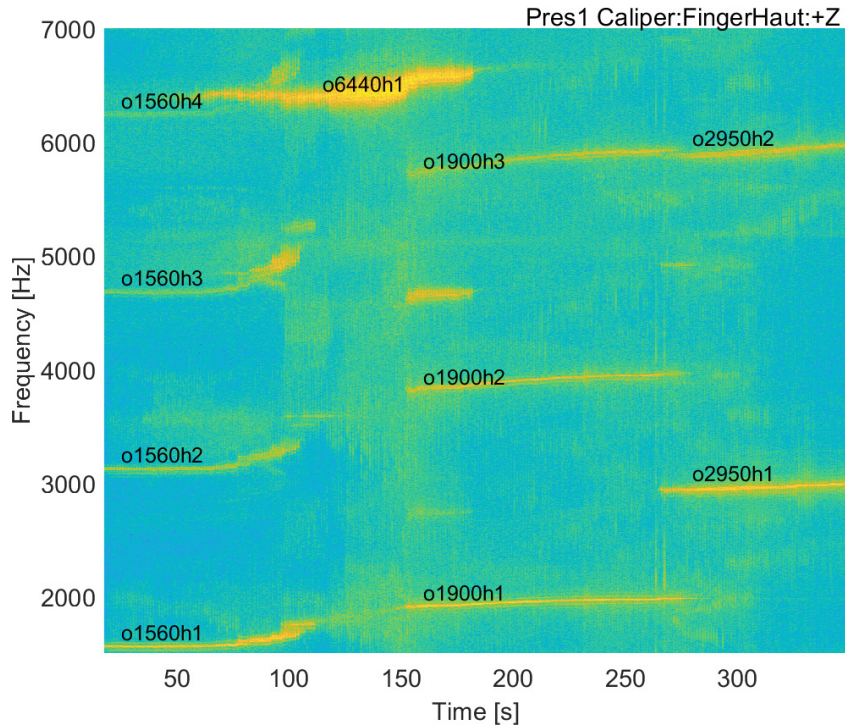


Figure 2.1: Sample spectrogram of full scale squeal measurement under a slowly varying pressure. 3s buffer length with Hanning window and 90% overlap.

However, pressure is not the only effect that must be taken into consideration. Figure 2.2 Left show this clearly by focusing the analysis on the first harmonic of the vibration between 65 and 80s. In this figure, two other parametric effects are visible spectrogram in addition to the pressure steps. One effect takes the form of periodic fluctuations, with a period that matches the wheel revolution. The other effect is seen by the presence of two sidebands at $\pm 30Hz$ around the squeal limit cycle frequency. This modulation matches the frequency of torque fluctuation induced by a torsion mode on the system axle.

In order to improve the time resolution of the analysis, figure 2.2 Right reduces the spectrogram buffer length from 1.5s to 0.15s and the time band to the interval between 75 and 80s. In this timescale the periodic fluctuations due to the wheel rotation are even more visible as the buffer length is small compared to characteristic times of variation. The 30Hz modulation, on the other hand, is much less visible as the frequency resolution is too poor.

2.2. DEFINING A SIGNAL MODEL FOR SQUEAL: HARMONIC BALANCE VECTOR (HBV) SIGNAL MODEL

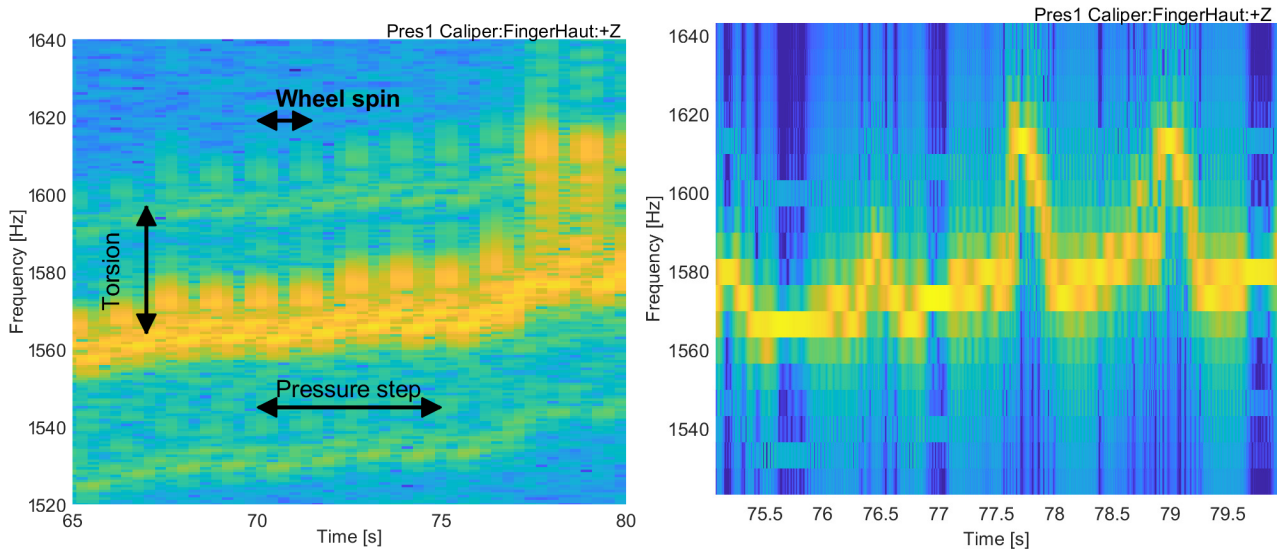


Figure 2.2: Spectrogram of an squeal measurement with different time widows and buffer lengths, both use a Hanning window and 90% overlap. Left: Between 65 and 80s, 1.5s buffer length. Right: Between 75 and 80s, 0.15s buffer length.

Figure 2.3 illustrates timescales of effects present in the system. Temperature changes very slowly (arbitrarily set here to a characteristic time of 20s). Pressure steps were performed with an interval of approximately 5s. The wheel rotation period is around 1.3s (for a velocity of 6km/h). The torsion mode in the system drive mechanism induces fluctuations near 30Hz (period of 0.03s). Finally, squeal generates quasi-periodic oscillations, above 1.5kHz here.

There is almost two orders of magnitude separating the lowest limit cycle frequency from the fastest parametric effect.

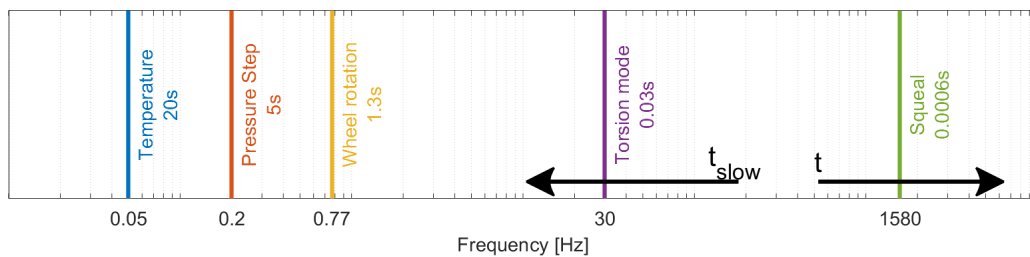


Figure 2.3: Comparison of the characteristic times of the different parameter variations and the squeal vibration. Arrows indicate the separation between the fast and slow timescales.

With these characteristic times in mind, one notices that the buffer lengths used for the two spectrogram in figure 2.2 (1.5s and 0.15s) do not respect the time separation between parametric effects and limit cycle. On the left figure the 1.5s buffer length is not able to track neither the evolution with the wheel rotation, nor the evolution of the torsion mode. In exchange a lower frequency evolution the right figure reduces the buffer length to 0.15s, which is able to represent the evolution induced by rotation but not the torsion mode (seen by the presence of sidebands at $\pm 30Hz$).

2.2. DEFINING A SIGNAL MODEL FOR SQUEAL: HARMONIC BALANCE VECTOR (HBV) SIGNAL MODEL

In order to represent the torque induced modulations, the buffer length must be smaller than the modulation period of 0.03s. Doing so would result in a very poor frequency resolution. Consider for example a buffer length of 0.01s, which respects the timescale separation indicated in figure 2.3, implies a frequency resolution of 100Hz. This resolution would be too coarse to effectively track the variations with wheel position visible in figure 2.2 right.

The use of time-frequency representations, implicitly assumes a separation of timescales. For each buffer, the signal is analyzed as a frequency response and thus in general as a constant system. If the system is not constant over the buffer length, the frequency response is modified as illustrated by the sidebands due to drive torsion.

This type separation between slow parameter variations and higher frequency (fast) dynamics is present in studies about analytic signals [28] and will be the starting point for the proposed HBV signal model.

Starting with the analytic signal formulation, we describe a vibration with an instantaneous frequency $\omega(t_{slow})$ with amplitude and phase given by the complex amplitude $q(t_{slow})$. The vibration frequency ω is considered to be sufficiently separated (faster) than the parametric variations described by t_{slow} to consider, that for a few periods, the vibration frequency is constant

$$q_A(t) = Re \left(q(t_{slow}) e^{i \int_0^t \omega(t_{slow}) dt} \right). \quad (2.1)$$

In the analytic signal formulation [28], each signal channel is considered independently with an instantaneous frequency for each one. However since all signals come from measurements of the same system at the same time, it is natural to consider that the instantaneous frequency of vibration is the same in all channels. For this, we introduce a shape vector $\{q(t_{slow})\}$ leading to an analytic vector signal

$$\{q_{AV}(t)\} = Re \left(\{q(t_{slow})\} e^{i \int_0^t \omega(t_{slow}) dt} \right) \quad (2.2)$$

Another characteristic is that the response is quasi-periodic, so that it is meaningful to describe periods using their Fourier series (1.12). This can be achieved by introducing a shape $\{q_h(t_{slow})\}$ for each harmonic h resulting in the following signal model we call *Harmonic Balance Vector (HBV) signal model*

$$\{q_{HBV}(t)\} = Re \left(\sum_h \{q_h(t_{slow})\} e^{ih \int_0^t \omega(t_{slow}) dt} \right). \quad (2.3)$$

Using this signal model one is now able to represent both the slow parametric changes and the nonlinear coupling with higher harmonics.

A demodulation algorithm used to identify an HBV signal from a test measurement is discussed in sections 2.2.2 and 2.2.3.

Test data, however, is subject to a number of perturbations that do not correspond to squeal and are not represented by the HBV signal model. The most notable perturbations include harmonics of the electrical signal, broadband noise introduced by the friction contact, and sensor saturation. This implies that an identification rest can be found after extracting the HBV signal from a measurement.

$$\{q_{Test}\} = \{q_{HBV}\} + \{q_{Rest}\} \quad (2.4)$$

2.2.2 Single channel estimation

Having defined the HBV signal model (2.3), let us now to discuss how estimate its parameters from a measured signal. Considering that the HBV signal model is combination of analytic signals that verify vector and harmonic constraints (frequency common to multiple sensors and harmonics), it is natural to consider that the algorithms used to estimate an analytic signal can also be used for a HBV signal. There are a number of different algorithms used to extract sine components in the literature such as FFT, extended Kalman filters [61], synchro-squeezing transform [62], ESPRIT [63, 64] and others. Among these methods the one chosen for this study is the synchronous demodulation.

Synchronous demodulation [28] is a widespread and robust method for estimating analytic signal, the most notable applications of demodulation certainly being the extraction of frequency and amplitude modulations in FM and AM radio respectively. In the domain of mechanics, the use of demodulation can be found for example in the phase locked loop controllers used for experimental characterization of nonlinear systems [59].

Inspired by these application, this section describes the use of synchronous demodulation to extract the different components of the HBV signal model (2.3).

The main idea behind the demodulation is that by knowing beforehand the frequency of a signal, the amplitude of the corresponding oscillation can be obtained by multiplying the original signal by a pair of reference signals in phase quadrature.

Consider a analytic signal $y_A(t)$ with a slowly varying instant frequency $\omega(t)$ of the form

$$\begin{aligned} y_A(t) &= \text{Re} \left((y_c + y_s i) e^{i \int_0^t \omega(\tau) d\tau} \right) = \text{Re} \left(y_1 e^{i \int_0^t \omega(\tau) d\tau} \right) \\ &= y_c \cos \left(\int_0^t \omega(\tau) d\tau \right) - y_s \sin \left(\int_0^t \omega(\tau) d\tau \right). \end{aligned} \quad (2.5)$$

It is possible to extract the cosine y_c and sine y_s components by multiplying $y_A(t)$ by $\cos(\omega t)$ and $-\sin(\omega t)$. These products results in

$$\begin{aligned} (y_c \cos(\omega t) - y_s \sin(\omega t)) * 2 \cos(\omega t) &= y_c + y_c \cos(2\omega t) - y_s \sin(2\omega t) \\ (y_c \cos(\omega t) - y_s \sin(\omega t)) * -2 \sin(\omega t) &= y_s - y_s \cos(2\omega t) - y_c \sin(2\omega t). \end{aligned} \quad (2.6)$$

Both products have a static component proportional to the amplitude of the reference signal in $y_A(t)$ and an oscillating part at frequency $2\omega t$. It is then possible to obtain y_c and y_s by removed the 2ω component using a low pass filter, as described by the diagram in figure 2.4.

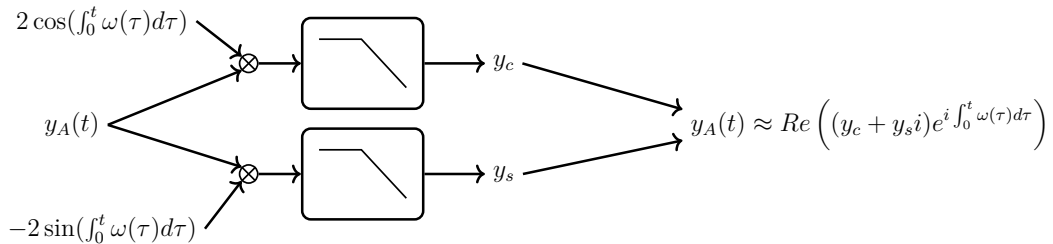


Figure 2.4: Diagram showing the Synchronous demodulation algorithm

2.2. DEFINING A SIGNAL MODEL FOR SQUEAL: HARMONIC BALANCE VECTOR (HBV) SIGNAL MODEL

As a first example, figure 2.5 illustrated the synchronous demodulation applied to a signal $y_A(t)$ with a complex amplitude $y_c + iy_s = (1 + i)/\sqrt{2}$ and a constant frequency $\frac{\omega}{2\pi} = 1kHz$. In this example the low pass filter used is a 8th order Butterworth filter with 500Hz cutoff frequency applied forward and backward. The use of a forward and backward filter helps to minimize the phase errors introduced by the filtering process.

One correctly find the amplitude of 1 and phase of 45° , after some stabilization period. Using this filter configuration the stabilization periods are 0.015s long on both sides, which is small compared to the total signal length of 0.1s.

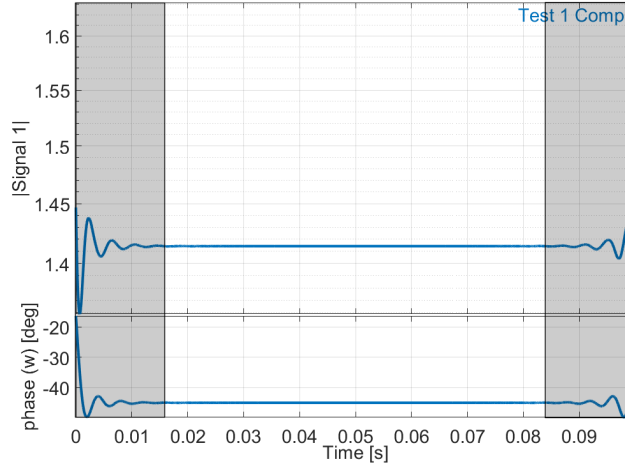


Figure 2.5: Application of synchronous demodulation in a simple test signal.

In practice, however, as brake squeal is a self-excited vibration under a slow modulation due to parameter variations, it is not possible to know the vibration frequency beforehand. It is thus necessary to consider the effects of an error in the frequency used for demodulation.

Let us consider the test signal $y_A(t)$ with an added frequency error $\delta\omega$ that is small compared to ω , it can be written as

$$y_A(t) = \text{Re} \left((y_c + y_s i) e^{i(\omega + \delta\omega)t} \right) = \text{Re} \left(y_1 e^{i(\omega + \delta\omega)t} \right) \quad (2.7)$$

If demodulation is applied using ω as input the product between $y(t)$ and the reference signals from equation (2.6) becomes

$$\begin{aligned} (y_c \cos(\omega t + \delta\omega t) - y_s \sin(\omega t + \delta\omega t)) * \cos(\omega t) &= \\ \frac{1}{2} (y_c \cos(\delta\omega t) - y_s \sin(\delta\omega t) + y_c \cos(2\omega t + \delta\omega t) - y_s \sin(2\omega t + \delta\omega t)) & \\ (y_c \cos(\omega t + \delta\omega t) - y_s \sin(\omega t + \delta\omega t)) * -\sin(\omega t) &= \\ \frac{1}{2} (y_c \sin(\delta\omega t) + y_s \cos(\delta\omega t) - y_c \sin(2\omega t + \delta\omega t) - y_s \cos(2\omega t + \delta\omega t)) & \end{aligned} \quad (2.8)$$

The static component from (2.6) now becomes a slow oscillation with frequency $\delta\omega$. Provided that the cutoff frequency for the demodulation low pass filter is larger than $\delta\omega$ the estimated sine \hat{y}_s and cosine \hat{y}_c components turn into

$$\begin{aligned} \hat{y}_c &= y_c \cos(\delta\omega t) - y_s \sin(\delta\omega t) \\ \hat{y}_s &= y_c \sin(\delta\omega t) + y_s \cos(\delta\omega t) \end{aligned} \quad (2.9)$$

2.2. DEFINING A SIGNAL MODEL FOR SQUEAL: HARMONIC BALANCE VECTOR (HBV) SIGNAL MODEL

From the combination of \hat{y}_c and \hat{y}_s an estimated analytic signal \hat{y}_A is obtained. This signal is characterized by a frequency ω and a complex amplitude $\hat{y}_1 = \hat{y}_c + \hat{y}_s i$.

$$\hat{y}_A(t) = \text{Re}((\hat{y}_c + \hat{y}_s i)e^{i\omega t}) = \text{Re}(\hat{y}_1 e^{i\omega t}) \quad (2.10)$$

The complex amplitude \hat{y}_1 can also be split into amplitude $|\hat{y}_1|$ and phase $\hat{\varphi} = \text{angle}(\hat{y}_1) = \arctan\left(\frac{\hat{y}_s}{\hat{y}_c}\right)$, as seen before in figure 2.5. Equation (2.11) show us that amplitude is not affected by small frequency errors $\delta\omega$.

$$|\hat{y}_1| = |\hat{y}_c + \hat{y}_s i| = \hat{y}_c^2 + \hat{y}_s^2 = y_c^2 + y_s^2 \quad (2.11)$$

The effect of a frequency error is more noticeable on the phase. The estimated phase $\hat{\varphi}$ shows a drift over time with a rate equal to $\delta\omega$. This means that it is possible to estimate $\delta\omega$ simply by

$$\delta\omega = \frac{\partial\hat{\varphi}}{\partial t} = \frac{\partial \arctan\left(\frac{\hat{y}_s}{\hat{y}_c}\right)}{\partial t} \quad (2.12)$$

and obtain an updated frequency

$$\omega(t) = \omega_0 + \delta\omega(t). \quad (2.13)$$

As an example, figure 2.6 shows the the effect of two different frequency errors:

- constant frequency error : $\delta\omega = -30$ Hz
- frequency error of ± 30 Hz modulated at 50Hz : $\delta\omega = 30\sin(2\pi * 50t)$

On the left, the constant frequency error leads to a constant phase drift. In the case of oscillating frequency around the demodulation frequency, the right part of figure 2.6 shows an oscillating phase drift.

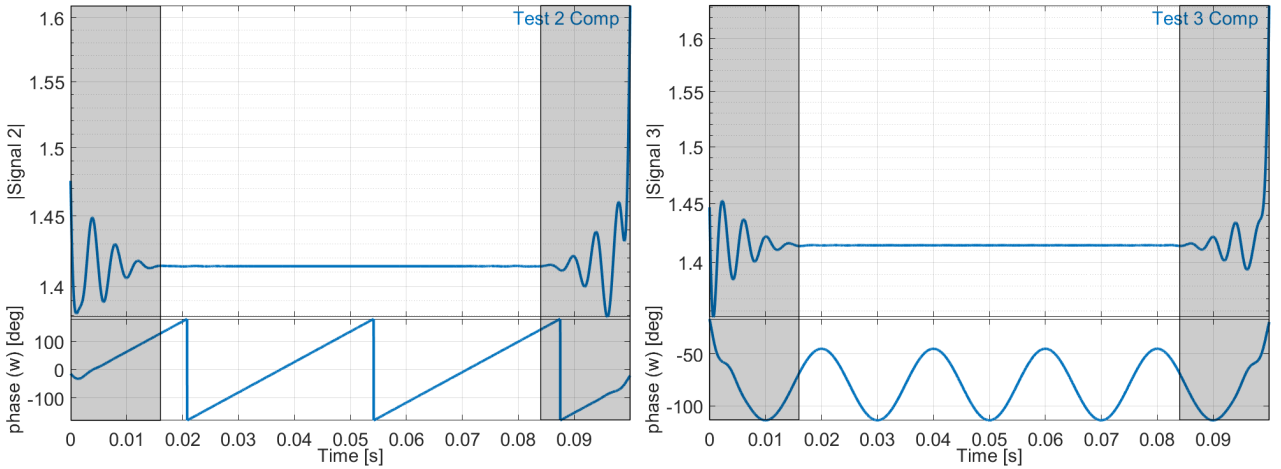


Figure 2.6: Demodulation results in presence of a frequency error. Left: constant error. Right: modulated frequency.

2.2. DEFINING A SIGNAL MODEL FOR SQUEAL: HARMONIC BALANCE VECTOR (HBV) SIGNAL MODEL

Using (A.6), a frequency correction step can be constructed in order to obtain the instantaneous frequency from the phase drift obtained in the demodulation. Figure 2.7 shows the application of frequency correction in the three signals shown in figure 2.5 and 2.6. Aside from the filter convergence regions on the borders shown as grayed areas, there is a good match between the extracted (solid line) and real (dashed line) frequencies.

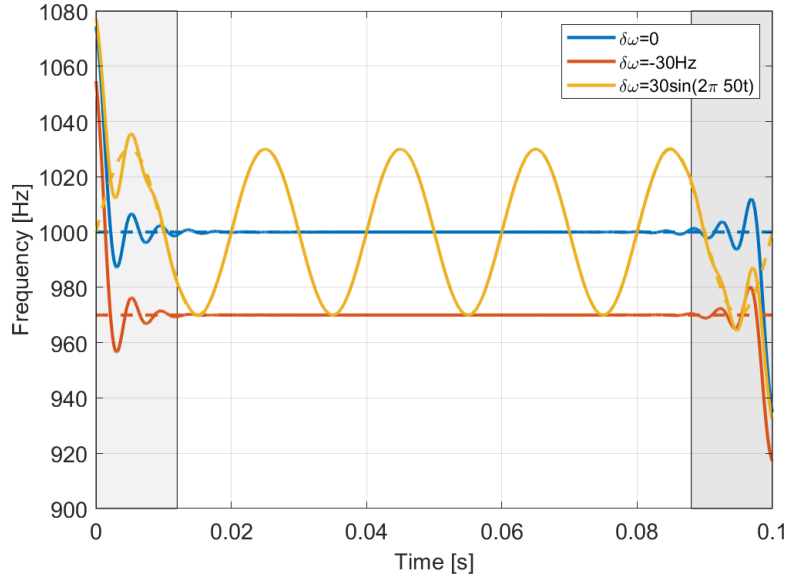


Figure 2.7: Frequency correction after first demodulation for a signal with different frequency errors (zero, constant, modulated). Estimated frequency (solid line) and true frequency (dashed line)

In some applications, such as the extraction of sine components resulting from impact testing [65], the convergence time may be an issue. However, in most applications considered in this work, the measurements are sufficiently long for the convergence times on the borders not to be a problem. Take the example measurements shown in figure 2.9, the measurement is around 10s long while convergence in the example 2.8 is achieved in less than 0.02s.

The particular case of short time sequential laser Doppler vibrometer measurements will be discussed in 3.5, along with a discussion on how initial conditions can minimize the convergence time.

In practice the frequency correction must take into account all measured channels at once, which is achieved using principal coordinates as discussed in section 2.2.3. This tends to stabilize the values, but the phase derivative in (A.5) is expected to be noisy.

The noise introduced by the phase derivative may result in a instant frequency of poor quality. A low pass filter is then applied to condition $\delta\omega$ and ensure that the estimated frequency is slowly varying.

2.2. DEFINING A SIGNAL MODEL FOR SQUEAL: HARMONIC BALANCE VECTOR (HBV) SIGNAL MODEL

Combining the demodulation with this frequency correction results in a three-step demodulation strategy :

1. First demodulation from rough instantaneous frequency guess
2. Instantaneous frequency correction from phase drift + LP filtering
3. Second demodulation using updated frequency to obtain amplitude

This algorithm illustrated in figure 2.8 is able to estimate both the instantaneous frequency and amplitudes from a HBV signal. Similar strategies have been used in the estimation of the instantaneous angular velocity of rotating machinery through the application of demodulation in order tracking [66, 67].

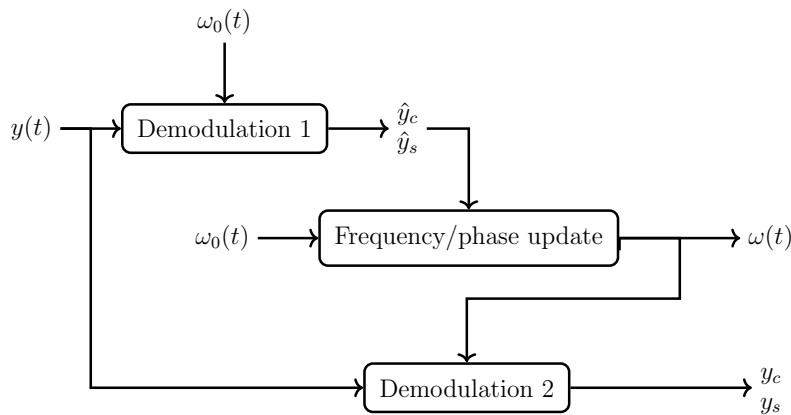


Figure 2.8: Diagram showing the 3-step demodulation algorithm for a single channel signal

The tuning of this algorithm consists in setting the three low pass filters: for the first demodulation, after frequency correction, and for the second demodulation. In this study the chosen filters are 8th order Butterworth filter, known to have no gain ripples and a sufficiently fast cutoff. This leaves only the three cutoff frequencies as parameters to be set in the tuning of the proposed demodulation algorithm.

As each of these cutoff frequencies has an intuitive effect on the extracted signal, the tuning process of the demodulation algorithm is very simple. As an illustration, let us consider the microphone measurement obtained from a full scale brake test shown in the spectrogram in figure 2.9. This measurement shows the response of the system to a slowly varying pressure.

2.2. DEFINING A SIGNAL MODEL FOR SQUEAL: HARMONIC BALANCE VECTOR (HBV) SIGNAL MODEL

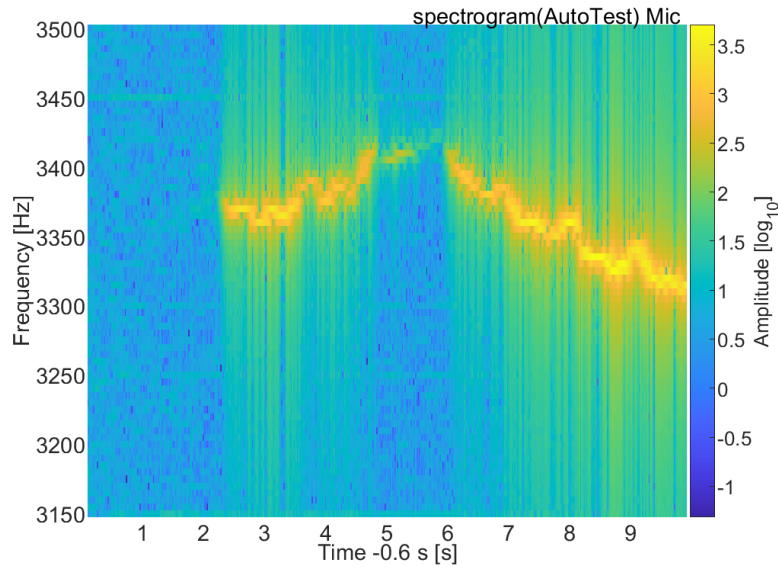


Figure 2.9: Spectrogram of a microphone measurement from a full scale brake test used as example for the demodulation algorithm.

The first parameter (cutoff frequency of the first demodulation) controls the tolerance of frequency error. With a larger cutoff frequency the algorithm is able to track larger frequency modulations, working as a sort of tolerance band around the initial frequency used for the demodulation.

In the case the first low pass cutoff being set too low the algorithm will not be able to track the instantaneous frequency. For example, the frequency changes in figure 2.9 are in the range [3300-3430 Hz]. Setting the first demodulation cutoff to 20Hz with an initial frequency guess of 3350 Hz means that the selected frequency range is only [3330-3370 Hz], which does not cover the entire signal frequency range and fails as shown in figure 2.10. Note that without the second filter set at 30 Hz, the figure would show strong excursions of the estimated frequency for low vibration levels.

A correct estimation of the instant frequency requires a cutoff frequency such that the demodulation band covers the entire signal frequency range. This is the case of the instant frequency shown in figure 2.11, which sets the first demodulation cutoff to 150 Hz with 3350 Hz as initial frequency. This results in a target frequency range [3200-3500 Hz] that covers the signal frequency range.

2.2. DEFINING A SIGNAL MODEL FOR SQUEAL: HARMONIC BALANCE VECTOR (HBV) SIGNAL MODEL

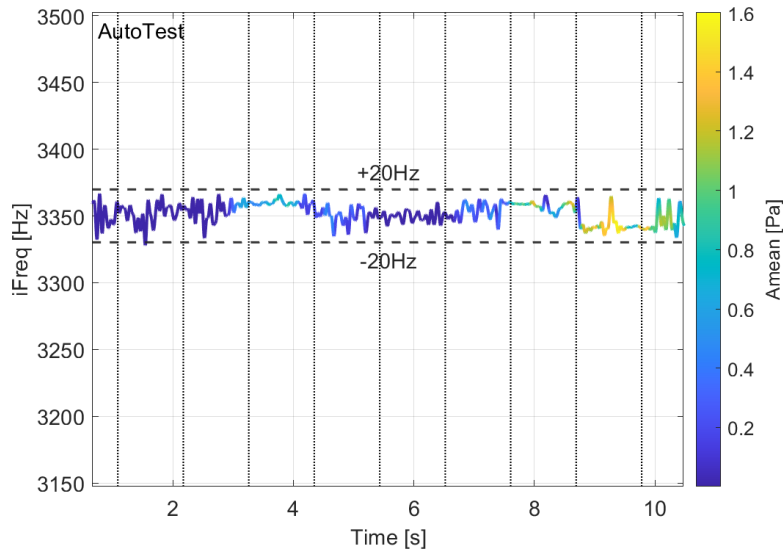


Figure 2.10: Instant frequency obtained when the first cutoff frequency is too low (estimated signal amplitude as color). Initial frequency for demodulation 3350 Hz, first demodulation cutoff 20 Hz.

The second parameter is the bandwidth limitation of instant frequency changes. In other words, it guarantees that the instant frequency is slowly varying. Figure 2.11 left shows the instant frequency obtained without low pass filtering and right using a 30Hz low pass filter. Without filtering, a significant level of noise arises when the signal amplitude is low, sometimes resulting in undesirable frequency spikes. Filtering eliminates this issue. On the regions with significant amplitude both estimations follow the same trends.

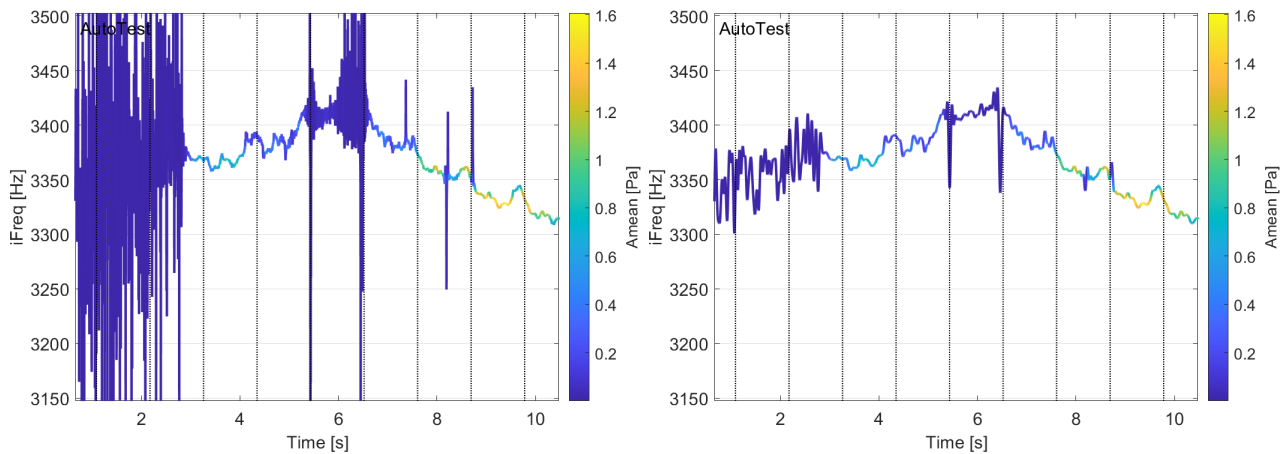


Figure 2.11: Instant frequency estimated in the demodulation algorithm without conditioning (Left) and with 30Hz low pass filter conditioning (Right), with amplitude of the estimated signal as color. Initial frequency for demodulation 3350 Hz, first demodulation cutoff 150 Hz.

By superposing both estimated frequencies with the spectrogram, figure 2.12 Left confirms that the estimated frequencies follow the squeal evolution very closely. The regions where the unfiltered frequency shows larger fluctuations match the regions where the signal is dominated by background

2.2. DEFINING A SIGNAL MODEL FOR SQUEAL: HARMONIC BALANCE VECTOR (HBV) SIGNAL MODEL

noise.

The right figure shows that a smoothing of frequency fluctuations also occurs in high amplitude areas. If the timescale separation is set correctly, this occurs without losing the ability to extract the signal as will be shown by the analysis of a rest signal next.

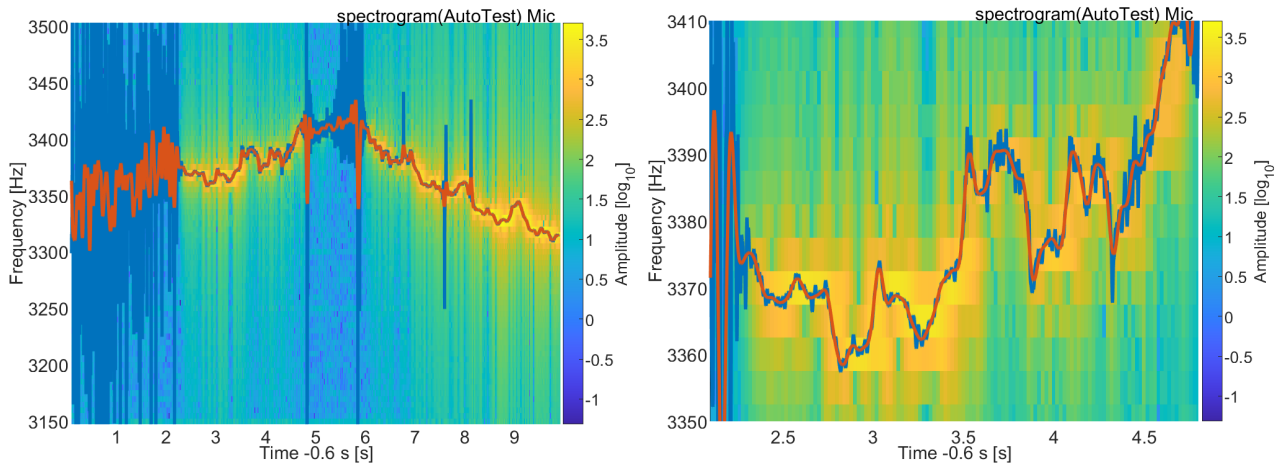


Figure 2.12: Estimated instant frequency superposed over the measurement spectrogram. Left: entire signal. Right: region between 2.1 and 4.8s.

Using the instant frequency as input, the second demodulation then tracks the evolution of amplitude. This is where the final parameter (cutoff frequency of the second demodulation) is used.

Figure 2.13 illustrates that the parameter controls a band in which one seeks to reproduce the signal using a characteristic time for amplitude modulation. The figure represents the spectrogram of the rest : difference (2.4) between raw signal and HBV estimation. Going from left to right, a 30 Hz band does not capture all the signal and significant levels appear close to the band. A 80 Hz band at the center seems correct. Further increasing to 150 Hz, will only capture additional noise and perturbations.

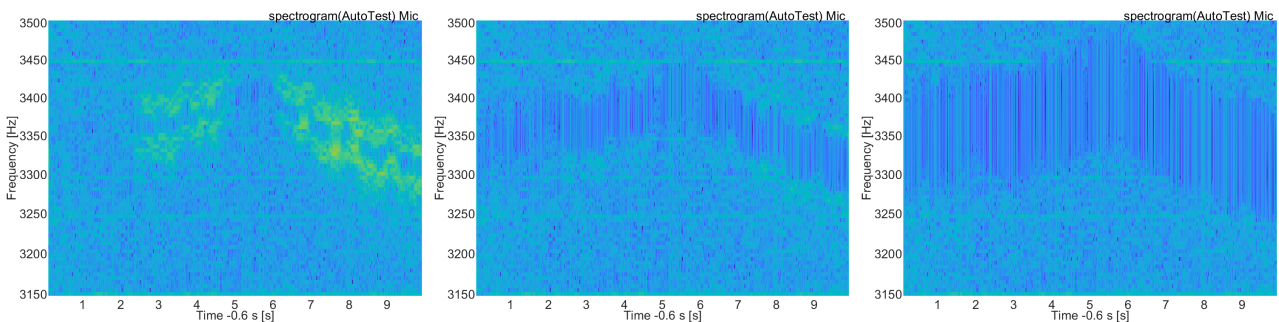


Figure 2.13: Rest of the identification obtained with different values of the second demodulation cutoff frequency 30 Hz (Left), 80 Hz (Center), and 150 Hz (Right). Initial frequency for demodulation 3350 Hz, first demodulation cutoff 150 Hz, frequency conditioning low pass 30 Hz.

2.2. DEFINING A SIGNAL MODEL FOR SQUEAL: HARMONIC BALANCE VECTOR (HBV) SIGNAL MODEL

One also notices that the vertical lines present in the measured signal spectrogram in figure 2.9 are not present in the spectrogram of the rest in figure 2.13. The presence of vertical lines in figure 2.9 is caused by the fact that squeal signal is non-periodic due to the variations of frequency and amplitude. These lines disappear in the rest signal because the non-periodic squeal signal has been removed leaving mostly noise and the electric network harmonics. This is made even clearer in figure 2.14 by showing three sections with full signal up to 5s, rest up to 8.5 s and spectrogram of HBV signal later.

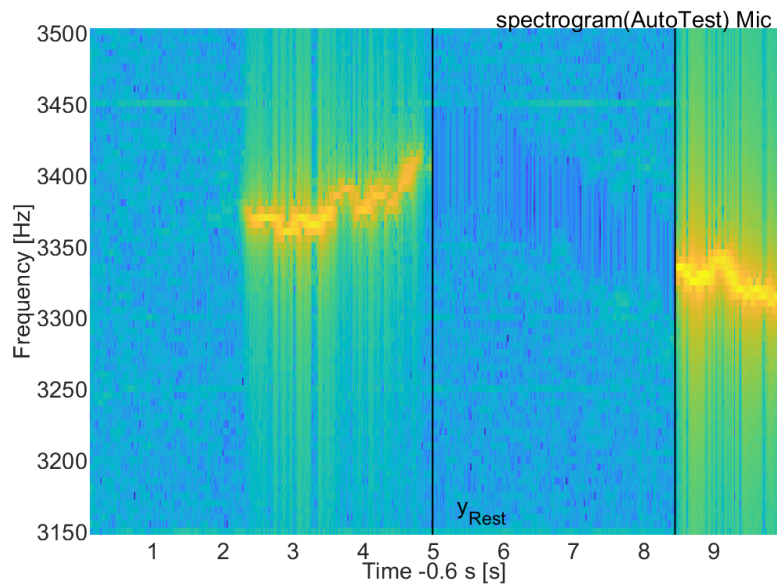


Figure 2.14: Spectrogram of full signal, rest and HBV show in three separate intervals.

With this example we have now covered the effect of all three tuning parameters on the proposed demodulation algorithm. In practice, tuning the first low pass filter with a larger cutoff than the other two gave satisfying results.

After estimating the component corresponding to the first harmonic, extending the estimation to higher harmonics is rather simple. Since the instant frequency of the first harmonic has already been estimated, the amplitudes corresponding to higher harmonics can be obtained by simply applying the second demodulation at multiples of the first harmonic instant frequency $\omega(t)$. Figure 2.15 confirms that integer multiples of $\omega(t)$ match the harmonics 2 and 3 of the measurement shown in 2.9.

2.2. DEFINING A SIGNAL MODEL FOR SQUEAL: HARMONIC BALANCE VECTOR (HBV) SIGNAL MODEL

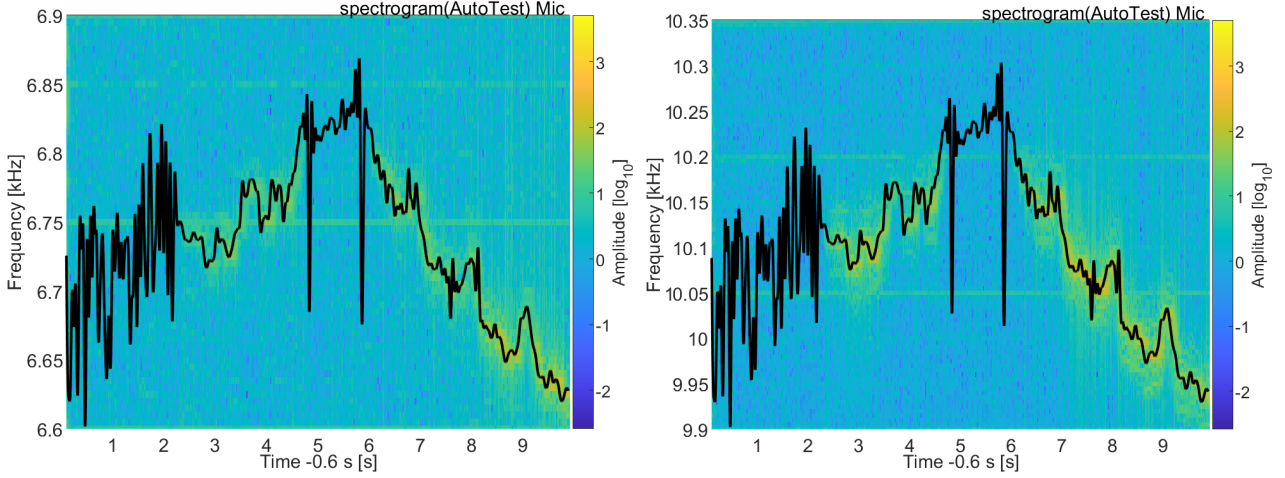


Figure 2.15: Left: $2\omega(t)$ superposed over the measurement spectrogram around the second harmonic. Right: $3\omega(t)$ superposed over the measurement spectrogram around the third harmonic.

2.2.3 Estimation with multiple channels

In practice, one often seeks to analyze a system response of multiple measurement channels at once. Looking at the demodulation algorithm described in the previous section, one quickly notices that it only considers one channel at once. With this in mind, this section discusses what needs to be added so that the algorithm is able to handle measurements with multiple channels.

Independently applying the demodulation to all channels would result in as many frequency estimations as measured channels. It is thus necessary to adapt the frequency correction step in order to impose the same instantaneous frequency to all channels. The most straightforward approach to impose this restriction is to select one channel as reference and impose the resulting frequency to all other channels. This choice of a reference channel is not always easy, in particular for self excited vibrations where there is no controlled input signal that could serve as a natural reference.

Instead of choosing a single channel as reference, the approach taken in this study is to create a linear combination of all channels as reference for the frequency correction step. This can be achieved by using a Singular Value Decomposition (SVD) to obtain an ordered set of principal complex amplitudes associated to real vibration shapes, like in the analysis of the functional model in section 1.4.5.

The measurement signal can be written as a vector combining all channels $\{q(t)\}_{N_C \times N_T}$, where N_C is the number of channels and N_T the number of time frames.

The first demodulation step gives a vector of complex amplitudes $\{\hat{q}_1\} = \{\hat{y}_c(t)\} + \{\hat{q}_s(t)\}i$ from which we want to extract main real shapes associated to complex amplitude time evolution. A Singular Value Decomposition (SVD) is thus performed on the grouping of real and imaginary part

$$\begin{bmatrix} \{\hat{q}_c(t)\} & \{\hat{q}_s(t)\} \end{bmatrix}_{N_C \times (2N_T)} = \sum_j \{u_j\}_{N_C \times 1} \left(\sigma_j \begin{bmatrix} v_{jc}^T(t) & v_{js}^T(t) \end{bmatrix} \right)_{1 \times 2N_T} \quad (2.14)$$

in which the $\{u_j\}$ are principal shapes constant over the selected time interval, and the singular value

2.2. DEFINING A SIGNAL MODEL FOR SQUEAL: HARMONIC BALANCE VECTOR (HBV) SIGNAL MODEL

and right singular vector can be rewritten as a complex generalized coordinate

$$\hat{q}_{1R}(t) = \sigma_1 \left(v_{1c}(t) + v_{1s}(t)i \right) \quad (2.15)$$

The demodulation 2.8 is thus modified by using the amplitude $q_{1R}(t)$ associated to the first principal shape for the frequency correction. The updated algorithm is shown in figure 2.16. This choice ensures that a large part of the vibration energy over the whole structure is considered for the estimation of the frequency/phase update. The same SVD may also be applied to the results of the second demodulation to generate principal coordinates, that will be analyzed in figure 2.17 for example.

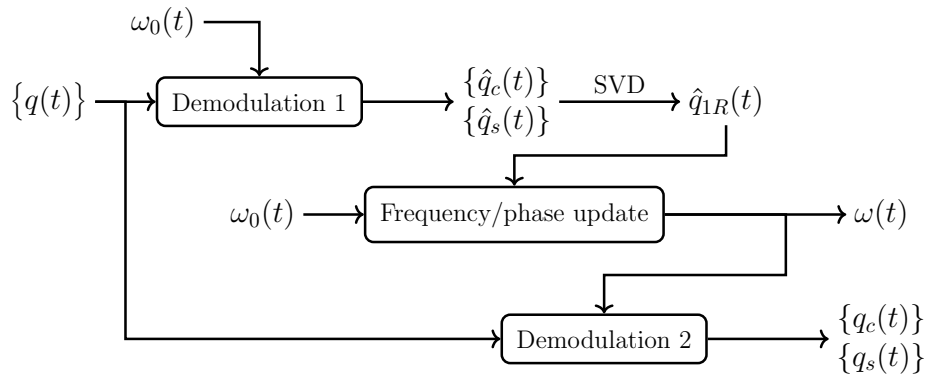


Figure 2.16: Diagram showing the 3-step demodulation algorithm for a signal with multiple measured channels

As an illustration of this instant frequency estimation using multiple sensors, let us use a squeal occurrence that will be further detailed section 3.3. One naturally expects that the instantaneous frequency estimation show some dependency to the choice of sensors used. In order to evaluate this, Figure 2.17 Left compares the estimated frequency for different sets of sensors :

- Ku (sensors on knuckle)
- Bra (sensors on bracket)
- Cal (sensors on caliper)
- All sensors

In parallel to the instant frequency, figure 2.17 Right shows the amplitudes $|q_{jR}|$ associated with the first 5 principal shapes $\{u_j\}$. In this figure it is possible to see that the amplitude of the first two shapes (thick lines) are dominant over the other shapes (thin lines). This indicates that the measured squeal is contained in low dimensional subspace, similar to what has been observed by [17, 21].

Looking at frequency and amplitude side by side, it is noticeable that instantaneous frequency estimates are very consistent when the amplitude is high (near 61 and 62.5s). On the contrary, when amplitudes are low (near 61.5 or 63 s), a notable spread of frequencies is found for different sensor set selections. The use of the largest number of sensors gives the best result unless some of those have problems, in which case they should be discarded.

2.3. PARAMETRIC MODAL ANALYSIS

Using the vertical dotted lines that indicate fixed wheel positions, the periodic effect of the wheel position can be clearly seen in the extracted frequency. An additional small fluctuation can be seen, showing that the 30Hz modulation associated to the torsion mode can be extracted using a 65 HZ cutoff frequency for the second demodulation.

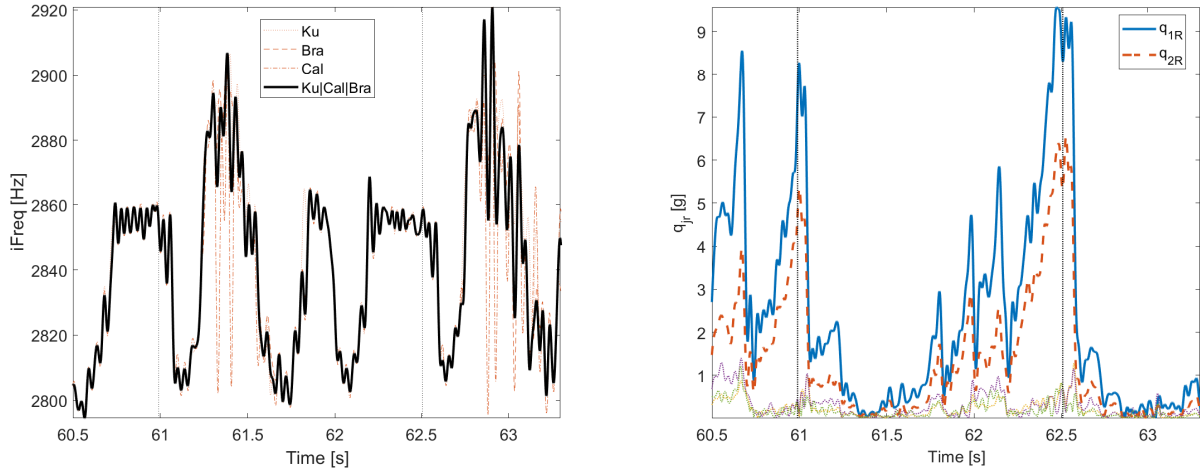


Figure 2.17: Left: Estimate instantaneous frequency for different sensor sets. Right: Principal amplitudes $|q_{jR}|$ associated with the first 5 principal shapes $\{u_j\}$.

This HBV estimation methodology has proven to be very robust. The applications included the extraction of squeal characteristics in the functional model 1.4 and full scale measurements 3.3, the tracking of sine responses with variable frequency in a simplified test bench 2.3.4, as well as the analysis of laser vibrometer measurements 2.4 and 3.5.

2.3 Parametric modal analysis

Brakes are complex systems in which some operating parameters cannot be fully controlled (temperature, wheel turn, ...). One then asks the question: how to perform modal analysis on a parameter varying system?

In order to test strategies on a fully controllable system, a simplified contact test bench is used. This test bench, described in section 2.3.1, was originally designed to characterize the effects of pressure on the contact between piston and the backplate of a brake pad.

Then section 2.3.2 shows the characterization of the contact test bench using EMA at fixed parameter values. In order to handle the continuous parameter variation, section 2.3.3 describes an algorithm for tracking phase resonance. This algorithm is then applied to the test bench in section 2.3.4.

2.3.1 Description of a simple parametric contact test bench

The simplified contact test bench was designed to evaluate the contact between piston and the backplate of a brake pad. It is composed of a brake caliper that was cut in half with a piston that presses the back-plate of a brake pad against a support base. The caliper is held in place by two guide columns connected to the base and pressure is applied via voltage controlled pressure generator. The dynamics of this test bench is affected by the nonlinearities present in the contact between different parts and the viscoelasticity of the rubber seal that closes the pressure chamber and holds the piston in place. All of these nonlinearities are directly affected by changes in applied pressure.

On the first design iteration, shown in figure 2.18, some problems were noticed in the first round of tests. A difference in height between the columns caused the piston to be inclined inside the caliper and touch the chamber, affecting the contact pressure distribution. Additionally, the visibility of the piston and backplate was low, leading to difficulties in measured with the 3D-SLDV.

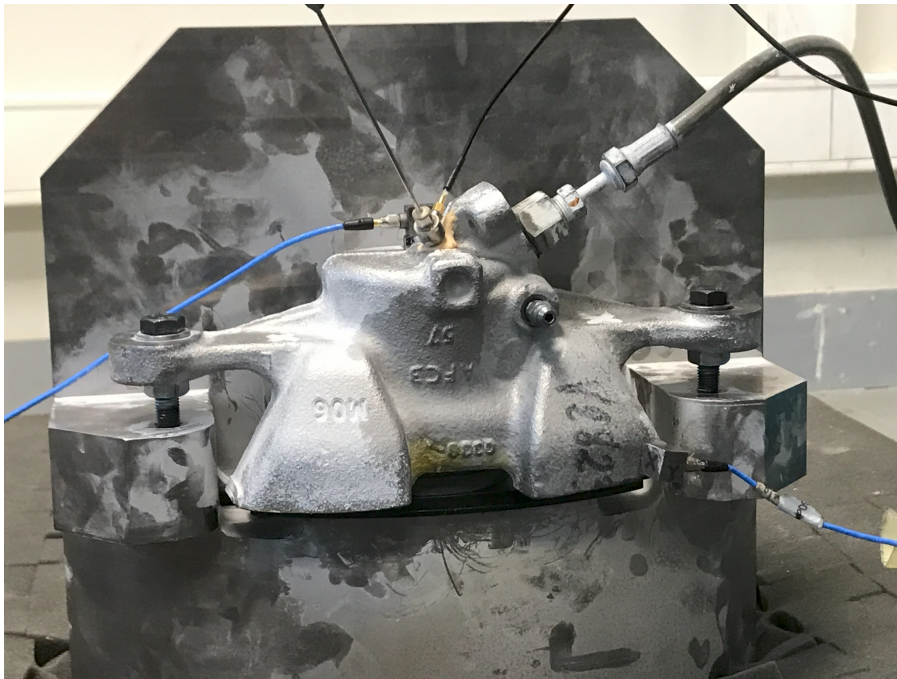


Figure 2.18: First design of the contact test bench

To improve on the previously mentioned difficulties, a second version of the test bench was tested as shown in figure 2.19. The support columns, previously consisting of standard bolts, were replaced by the guide columns used in the brake system to hold the caliper. The height of the columns was carefully set to prevent the piston to be inclined inside the caliper. An additional nut has been placed for the caliper weight to be held without pressing into the backplate. Finally, the bottom of the caliper was trimmed and an opening added to the back of the support base in order to improve visibility for the 3D-SLDV measurements.

2.3. PARAMETRIC MODAL ANALYSIS



Figure 2.19: Second design of the contact test bench on the ground (left) and suspended (right)

This test bench is used to answer three questions before application to full brake systems.

- *Can we identify evolution of modal properties with pressure ?*

Sweep tests are performed for sequential fixed pressure values and standard Experimental Modal Analysis is discussed in section 2.3.2

- *Can we identify modal properties under slow continuous parameter variation ?*

A feed-forward approach is used to construct parametric sine tests where excitation frequency and applied pressure evolve simultaneously in section 2.3.4.

- *How to obtain a more detailed shape than using only few accelerometers?*

A detailed characterization of the shape in response to the sine excitation of the system is obtained using a 3D scanning laser Doppler vibrometer (3D-SLDV) in section 2.4.

Both the sweep and parametric sine measurements are made using the same setup illustrated in figure 2.20. The bench was equipped with 2 tri-axial accelerometers and excited via a electrodynamic shaker connected to a power amplifier. The applied load was assessed using a load cell and a conditioning amplifier. Measurements were made using a NI cDAQ modular acquisition system with 2 analog output and 8 analog inputs. The position and orientation of the sensors is indicated in figure 2.20.

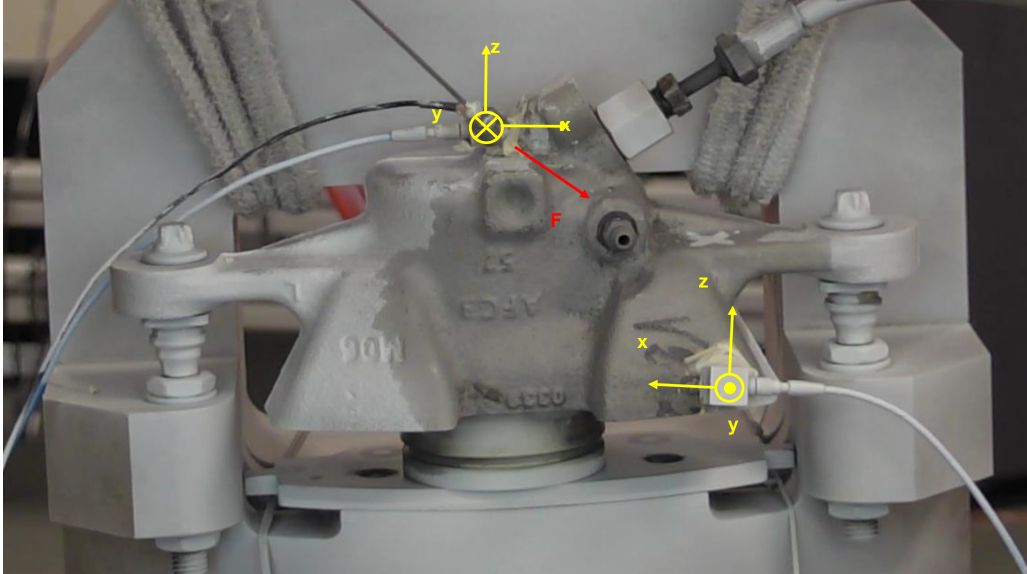


Figure 2.20: Placement of the triaxial accelerometers sensors (yellow) and shaker input (red) on the second design

For the 3D-SLDV measurement, the test bench was suspended as shown in 2.19 where the same setup of shaker and accelerometers is combined with a 3D-SLDV measurement system (polytec PSV500). Details of the 3D-SLDV measurements such as the choice of measurement points will be discussed later in section 2.4.

2.3.2 EMA at fixed system parameters (Classical H1 transfer estimation)

In this first test campaign, we seek to obtain a characterization of the effects of pressure on the test bench using traditional modal analysis techniques. More specifically, through a series of swept sine measurements (between 100 and 3000Hz in 20 seconds), we trace the evolution of the system poles with increasing pressure. The system response is evaluated for a total of 8 equally spaced pressure values from 2 to 16 bar.

Figure 2.21 left shows the measured input force sine sweeps (blue) and applied pressure (red) where it is possible to see that the excitation level is not constant, possibly due to an interaction between the shaker and test bench.

These measurements are then used to construct a series of transfer functions using a simple H1 estimator [68]

$$H_1(\omega) = \frac{G_{XF}(\omega)}{G_{FF}(\omega)}. \quad (2.16)$$

The obtained transfer functions describe the effect of pressure on the system. Focusing on the first mode, figure 2.21 right shows a progressive increase in the peak frequency with applied pressure. An additional perturbation can be seen in the transfer functions at multiples of 50Hz, indicating a problem with the electrical grounding of the test bench.

2.3. PARAMETRIC MODAL ANALYSIS

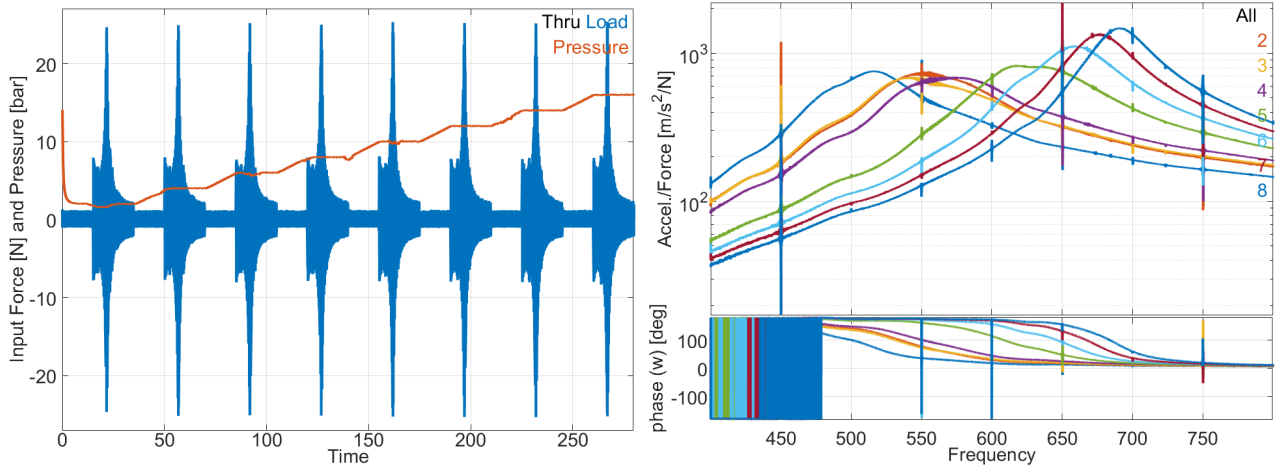


Figure 2.21: Left: pressure and input force applied to the test bench. Right: transfer functions corresponding to different pressure levels

The system poles are then obtained for each pressure using the modal identification interface from the SDT MATLAB toolbox [54]. The applied identification uses a pole-residue model with residual terms

$$H(s) = \sum_j^{N_p} \left(\frac{[R_j]}{s - \lambda_j} + \frac{\overline{[R_j]}}{s - \overline{\lambda_j}} \right) + [E] + \frac{[F]}{s^2}. \quad (2.17)$$

Poles are initialized using a narrowband around the resonance peak, and possibly optimized using a gradient based algorithm. Residues (the shape information associated with each mode) and residual terms are obtained as solution of a linear least squares problem at every iteration. A more detailed explanation on the algorithms used for modal analysis can be found in [54, 17].

By increasing the applied pressure, we expect a growth of the contact stiffness. This would lead to an increase in resonance frequency and damping evolution, both of which can be observed in Figure 2.22. Between 4 and 8 bar, the evolution of frequency is not growing regularly. This is attributed to a modal interaction which was a limitation of the test bench. Doing slow parametric changes would allow having intermediate points making the analysis easier.

Using the strategy described above requires the system parameters to be kept constant during a measurement, which is not possible in the case of brake systems in operating condition. It is then necessary to work on experimental strategies that can be applied to identify the system while it is slowly changing. Section 2.3.3 will describe the principles of the proposed methodology and section 2.3.4 the application.

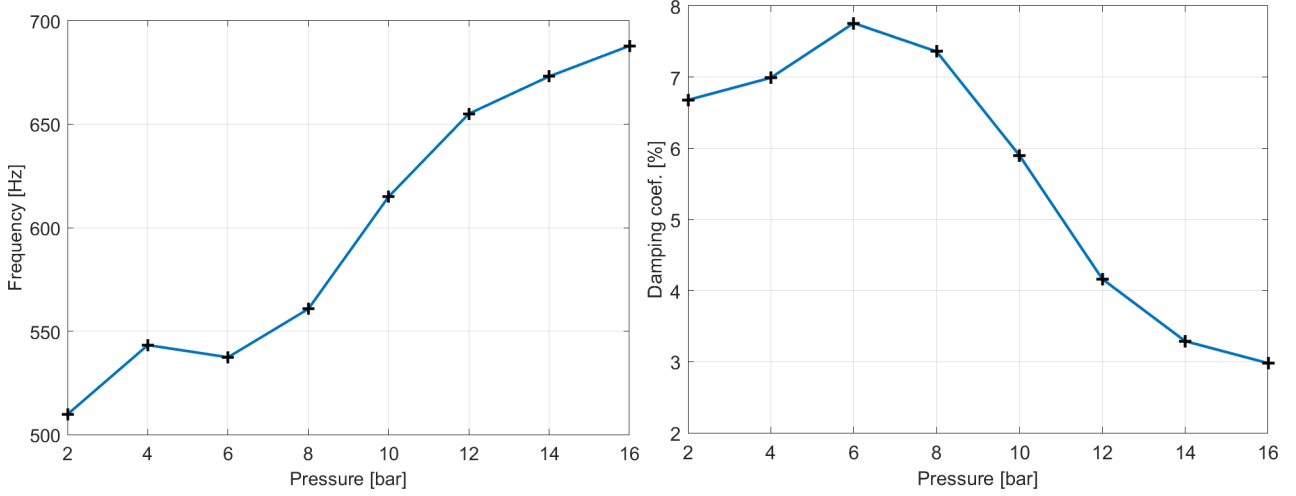


Figure 2.22: Identified natural frequency (left) and damping coefficient (right) evolution with pressure using swept sine excitation at fixed pressure.

2.3.3 Describing the phase resonance mode tracking strategy

The objective of this section is to characterize the evolution of modes for a continuous pressure variation. This is thought important as full brake tests are sensitive to continuously varying possibly uncontrollable parameters. The principle retained for continuous tracking is to use phase resonance. Originally introduced in force appropriation techniques [57], the phase resonance has been applied to characterize the evolution of modal properties with amplitude since the 60's. Recent applications are combination with feedback techniques such as phase-locked-loop (PLL) [59, 60] and autoresonance [69]. Extensions of the phase resonance concept are discussed in [70].

To motivate the methodology, let us consider a one degree of freedom linear parameter-varying (LPV) system with natural frequency ω_n and damping coefficient ζ dependent on a slowly varying external parameter p leading to the transfer

$$H(\omega, p) = \frac{X}{F}(\omega, p) = \frac{1}{-\omega^2 + 2i\zeta(p)\omega_n(p)\omega + \omega_n^2(p)} = |H(\omega, p)|e^{i\varphi(\omega, p)} \quad (2.18)$$

From this expression, one can get the phase between displacement and force

$$\varphi(\omega, p) = \text{phase}(H(\omega, p)) = \tan^{-1} \left(\frac{-2\zeta(p)\omega_n(p)\omega}{\omega_n^2(p) - \omega^2} \right) \quad (2.19)$$

which is a function of the excitation frequency ω and external parameter p .

Phase resonance in the case of 1DoF linear time invariant systems is defined as the frequency for which phase φ equals -90° between displacement and excitation force. The question now is how to track the phase resonance of a parametric system.

From an a priori known relation between the resonance frequency and the varying parameter $\omega_{n0}(p)$ (this will for example be obtained from figure 2.22), we propose to perform two sequential sine measurements at frequencies $\omega_{n0}(p)$ and $\omega_{n0}(p) + \delta\omega_0$. Comparing these two responses will allow

2.3. PARAMETRIC MODAL ANALYSIS

to estimate the phase resonance. For each value of p , we thus have two points marked by a star in figure 2.23 that relates the phase between displacement and force at both excitation frequencies. If these two points are reasonably close to the phase resonance, the linear interpolation between them can be directly compared to the first order development of the phase around -90°

$$\left(\varphi(p, \omega) - \frac{\pi}{2}\right) = -\frac{1}{\omega_n(p)\zeta(p)}(\omega - \omega_n(p)) + O((\omega - \omega_n(p))^2) \quad (2.20)$$

From this, one can readily see that the frequency at which the interpolation crosses -90° gives the phase resonance frequency $\omega_{n1}(p)$, and that the interpolation slope is directly related to the damping $\zeta_1(p)$ by

$$\zeta(p) = \left(-\frac{1}{\omega_n(p)}\right) \frac{\omega - \omega_n(p)}{\varphi(p, \omega) - \pi/2} \quad (2.21)$$

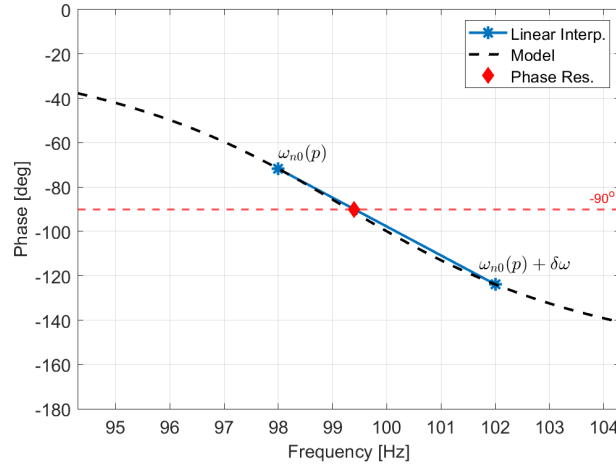


Figure 2.23: Example of the phase resonance estimation from the linear interpolation of phase for two neighboring frequencies.

This is very comparable to the force appropriation and PLL approaches [57, 60] with the major difference that an iterative feed-forward strategy is used instead of feed-back. The advantage sought proceeding that way is that the process is inherently stable, leading to testing times known in advance.

As a verification example, let us consider the evolution of natural frequency and damping ratio illustrated in figure 2.24 and test the proposed strategy. This evolution was created by interpolating between a set of four arbitrarily chosen key points.

2.3. PARAMETRIC MODAL ANALYSIS

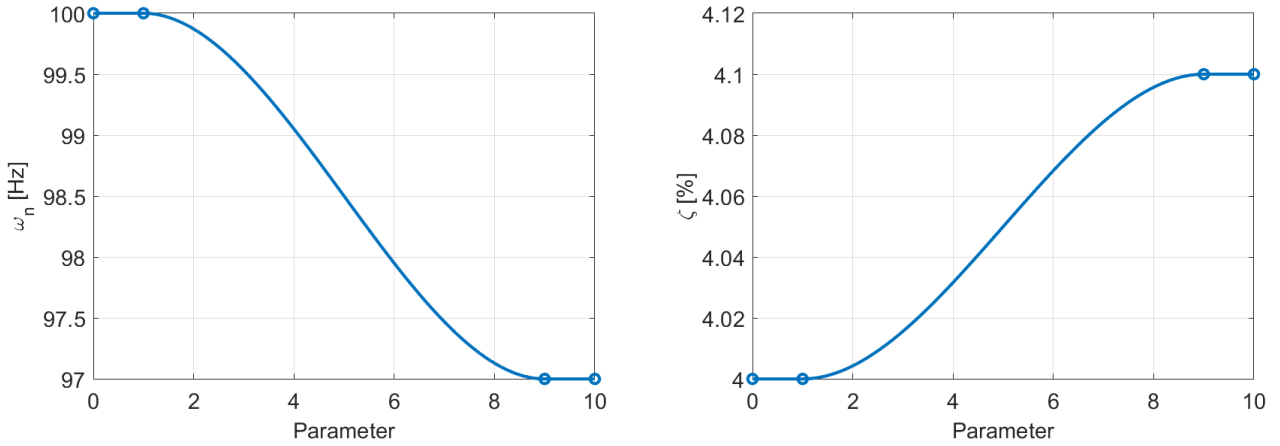


Figure 2.24: Parametric evolution of natural frequency (Left) and damping (Right)

Three excitation profiles (a priori estimation) linking parameter p and excitation frequency $\omega_{n0}(p)$ are considered in figure 2.25 left. The first profile is the true $\omega_n(p)$ (blue), while the other two are respectively piece-wise cubic and linear interpolations of the key-points from figure 2.24 (red and yellow). The offset profiles are also displayed in figure 2.25 left with the excitation frequency shift $\delta\omega = -1Hz$. The resulting phase in response to each input profile is obtained directly from equation (2.19) and shown in figure 2.25 right.

For perfect tracking of phase resonance, the $\omega_{n0}(p)$ phase line will be constant and the $\omega_{n0}(p) + \delta\omega$ line will present a small level of variation due to the damping coefficient changes. For approximate frequencies (shown in red and yellow), some oscillations will be visible and these can be used to correct the estimated frequency and damping.

The value of $\omega_{n1}(p)$ is then found by the $\varphi = -90^\circ$ crossing in (2.20), and $\zeta_1(p)$ by using (2.21).

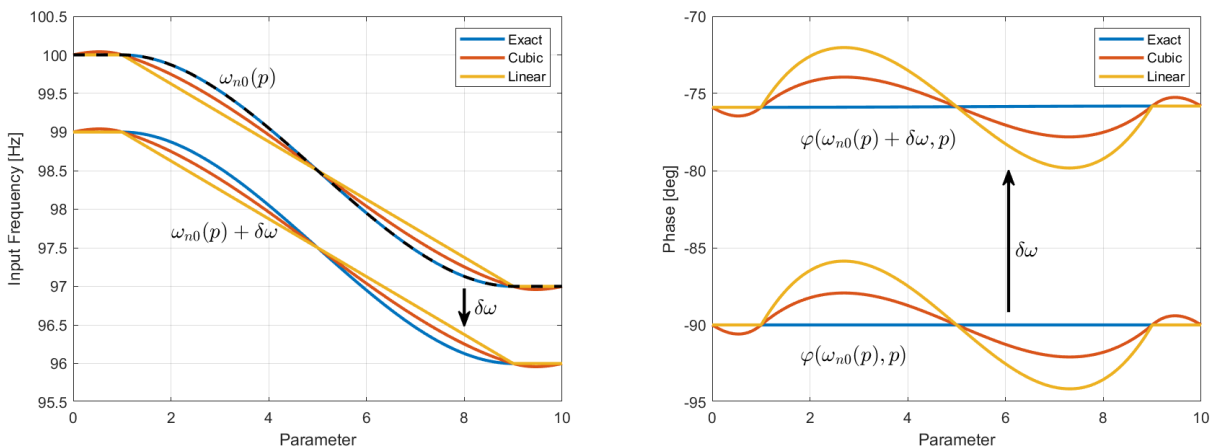


Figure 2.25: Input frequency (Left) and response phase lag (Right) as a function of external parameter for a 1DoF parametric system. Excitation frequency profiles: identical to phase resonance (Blue), piece-wise cubic (Red), and Linear (Yellow).

2.3. PARAMETRIC MODAL ANALYSIS

Figure 2.26 shows that while the natural frequency estimations superpose with the model values, damping has a tendency to be overestimated as a limitation of the first order approximation (2.20). In this example a $1Hz$ frequency offset resulted in a 1.5% damping bias (from $\zeta = 4\%$ to $\zeta = 4.062\%$). Reducing the offset to $0.5Hz$, the bias would be reduced to around 0.3% (from $\zeta = 4\%$ to $\zeta = 4.011\%$), which we deem acceptable. For future applications to real brakes, such analyses should be adapted.

In order to improve this estimation, one could try to have both frequency/phase points closer to the $-\frac{\pi}{2}$ lag. Alternatively we could increase the number of frequency offsets $\delta\omega_i$ and then obtain for each value of p a higher number of points $[\dots (\omega_{n0}(p) + \delta f_i, \varphi(\omega_{n0}(p) + \delta f_i, p)) \dots]$ allowing for a better estimation of $\omega_n(p)$ and $\zeta(p)$.

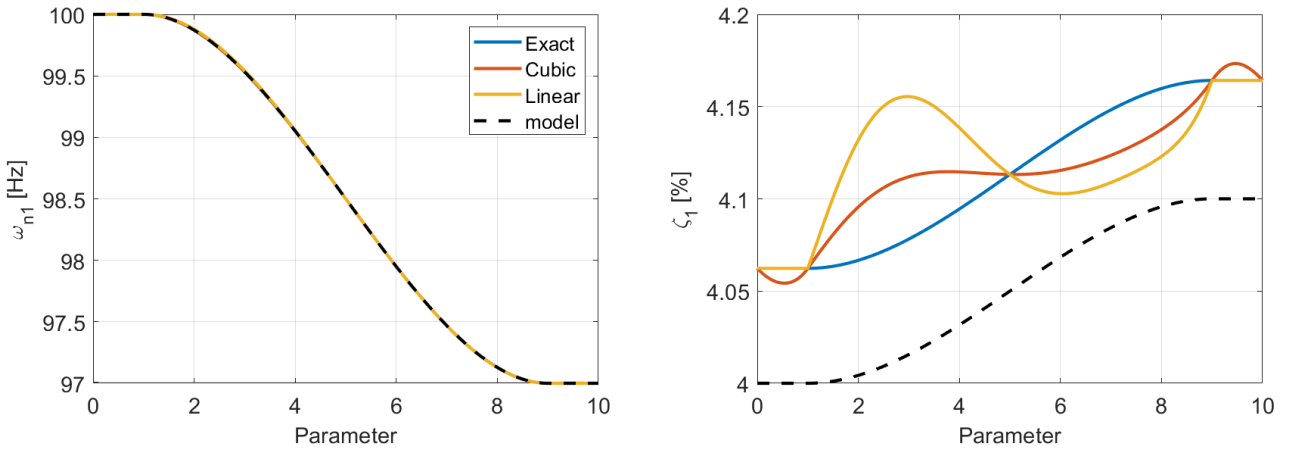


Figure 2.26: Re-estimation of phase resonance frequency and damping coefficient in a 1DoF system

In the case of systems with multiple degrees of freedom, the definition of phase resonance requires some additional steps since multiple modes are present in the response and non-proportional damping can lead to complex modes [71]. The notion of phase resonance is then classically defined for force appropriation [72, 57] or the nonlinear normal mode methodologies [70, 59].

One possibility to define phase resonance in a multiple degree of freedom system is to use the concept of modal coordinates. Let us consider for example a multiple degree of freedom system excited by a force $[b] \{u\}$ and a set of measurements $\{y\} = [c] \{q\}$. The frequency response of this type of system can be represented by the combined response of all N_m modes of the system.

$$[H(\omega)] = \sum_{j=1}^{N_m} \frac{[c] \{\phi_j\} \{\phi_j\}^T [b]}{\omega_j^2 - \omega^2 + 2i\zeta_j\omega_j\omega} \quad (2.22)$$

Using this formulation it is possible to define a set of generalized amplitudes called modal coordinates that represent the amplitude of the structure vibration associated to a given mode shape [73, 71].

$$\{q\} = \sum_{j=1}^{N_m} \{\phi_j\} x_j \quad (2.23)$$

2.3. PARAMETRIC MODAL ANALYSIS

Using the mass orthogonality property of the mode shapes of a mechanical system, it is possible to create a linear combination of the structural degrees of freedom to obtain the modal coordinates [74, 69]

$$[\Phi] = [\dots \{\phi_j\} \dots] \quad \left([\Phi]^T [M] \right) [\Phi] = [I] \quad \{x(t)\} = \left[\Phi^T M \right] \{q\} \quad (2.24)$$

creating a modal filter [75]. Modal filtering has shown its usefulness in a number of different applications such as mode selection in autoresonance feedback excitation [69] and nonlinear modal testing [60].

One may however notice at this point that formulation (2.24) of a perfect modal filter considers all degrees of freedom of the model. To apply a similar approach to measurements, some adaptations need to be made. Measurements consist of the observation of the system at a finite number of sensors.

$$\{y\} = [c] \{q\} = \sum_{j=1}^{N_j} \{c\phi_j\} x_j \quad (2.25)$$

and while mode shapes $[\Phi]$ are mass orthogonal, the observed mode shapes $[c\Phi]$ are not. In order to estimate the modal amplitudes, it is thus necessary to build a modal observation matrix using a pseudo inverse

$$\{x\} \approx [c\Phi]^+ \{y\} \quad (2.26)$$

where $[c\Phi]^+$ is such that $[c\Phi]^+ [c\Phi] \approx [I]$. A good sensor placement is essential in order to allow the observation of all modal coordinates: for a further discussion on the subject refer to [76, 77].

2.3.4 Applying phase resonance tracking to the contact test bench

The proposed phase resonance tracking methodology was applied to the contact test bench.

The first step is thus to construct an a priori relation between mode frequency and parameter : $\omega_{n0}(p)$. This is done by interpolating the mode frequencies previously identified from the swept sine measurements, performed at several fixed pressure values (figure 2.22). The pressure profile $p(t)$ is simply a slow ramp from the lowest pressure (2 bar) to the highest pressure (16 bar), then back down again in the opposite direction. Figure 2.27 right illustrates the sweep excitation profiles used to track the modes : $\omega_{n0}(p(t))$ measured once and $\omega_{n0}(p(t)) + 10Hz$ measured 4 times. Repetitions of the first sweep were not kept due to an operational mistake.

Figure 2.27 left shows the 5 measurements of the pressure profile. (figure 2.27 right). One can notice a pressure transient in the first 20s of the measurement without frequency offset as it converges to the input profile. Also, irregular drops in pressure can be seen in the descent phase suggesting some stick-slip motion of the piston or irregularities on the pressure generator.

2.3. PARAMETRIC MODAL ANALYSIS

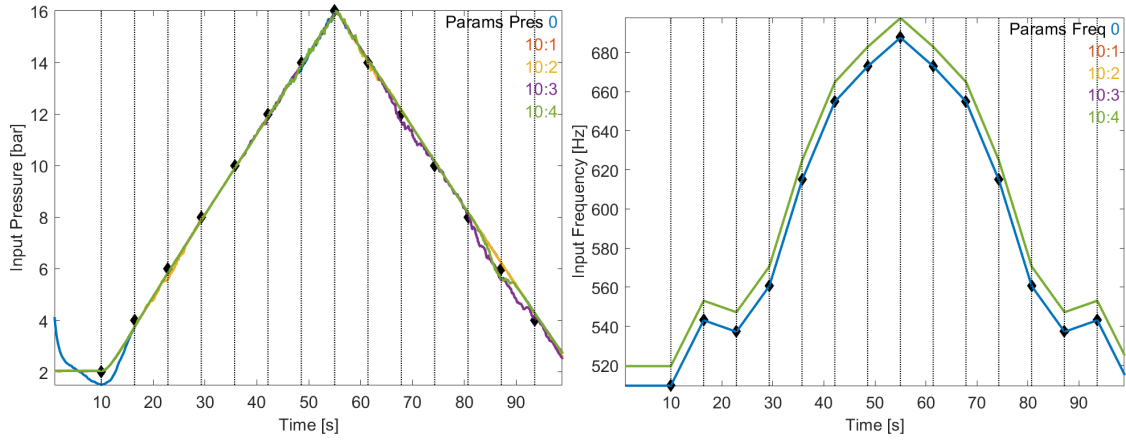


Figure 2.27: Pressure and frequency profiles used in the parametric sine tests. Learning points indicated by \blacklozenge and vertical lines.

Applying the demodulation strategy described in section 2.2, the complex amplitude of each sensor is extracted. Figure 2.28 left shows the complex amplitude extracted for all 6 channels in the measurement with 0 Hz offset. It is possible to see that the sensors with higher amplitudes follow the same overall trend. This confirms the expected behavior that response close to the resonance frequency is dominated by a single principal shape.

Using this idea, a generalized coordinate is constructed with the first principal shape (see section 2.2.3 for more details) obtained from the first sweep. The other measurements are then projected onto the same principal shapes resulting in the evolution shown in figure 2.28 right.

It is noticeable that the extracted generalized amplitude in the four measurements with a +10Hz offset is consistently repeatable, presenting only some level of error at moments where pressure fluctuations are seen in figure 2.27. It is also very clear that for the measurement without offset, the first 20s present large phase variations which can be associated to the pressure drop that is not present in the other measurements.

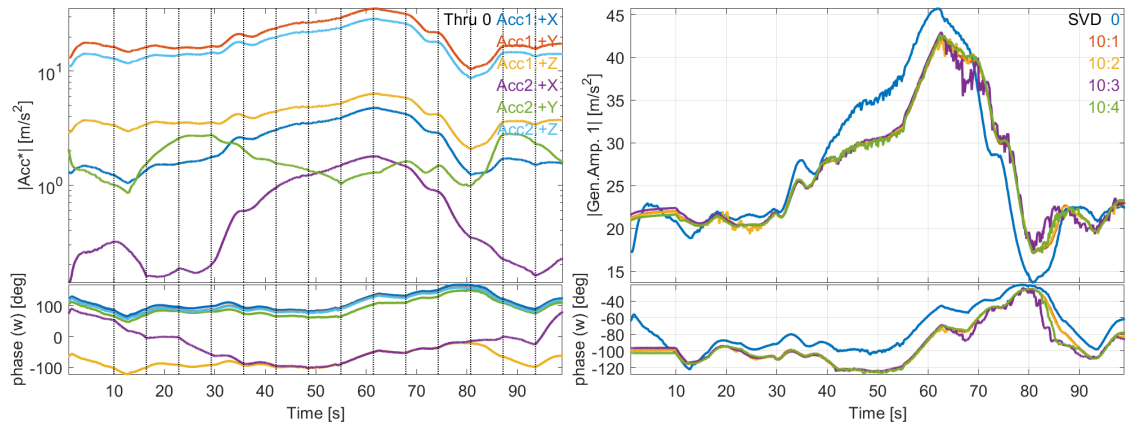


Figure 2.28: Left: complex amplitude of the first harmonic in different accelerometers in a single measurement. Right: generalized coordinate associated with the first principal shape for different measurements with and without frequency offset

2.3. PARAMETRIC MODAL ANALYSIS

From the measured phase difference in 2.28, phase resonance frequency and damping can be estimated leading to figure 2.29.

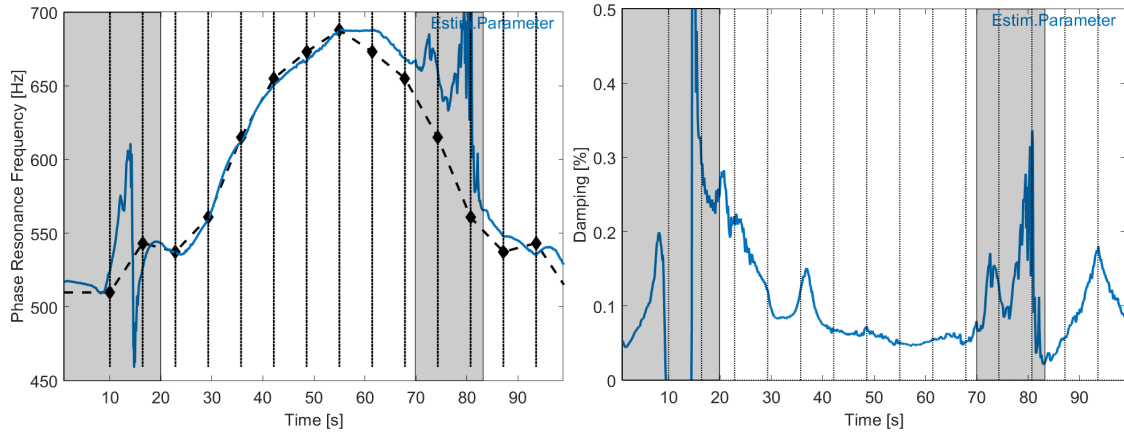


Figure 2.29: Estimated evolution of natural frequency and damping with time. Learning points indicated by \blacklozenge and vertical lines. Gray bars highlight the regions where estimation fails.

- 00s - 20s** For the first 20s the applied pressure was not yet stable in the measurement without offset (as shown in figure 2.27 left). This results in a poor estimation visible in the first gray area in figure 2.29.
- 20s - 55s** The estimated natural frequency follows the same overall trend as the original estimated profile.
- 55s - 70s** An interesting behavior can then be observed in the pressure descent phase after 55s, natural frequency remains constant for a while before starting to decrease. This suggests some level of hysteresis in the pressure dependence and motivates the proposed idea of iterating refinement of tests.
- 70s - 83s** Finally, between 70 and 83s some level of fluctuation in the estimated parameters can be seen in figure 2.28 (second gray bar). This can be related to the fact that phase values are further in figure 2.28 right away from -90° , and thus the linear approximation of the frequency/phase relation is no longer valid.

When frequency is not properly estimated, between 0s and 20s and between 70s and 80s, damping estimates are quite different and thus probably biased (figure 2.29). In other regions, damping values are found to be much lower than those extracted with large band signals dropping from values around 5% in figure 2.22 to values around 0.2% in figure 2.29. It is clear that both tests have notably different variations of the excitation levels with time (mostly constant in the sine test, variable in the sweep as shown in figure 2.22). It is thus expected that the contact state averaged over a period may differ significantly, and this can generate apparent damping [48]. An additional analysis of the evolution of higher harmonics during the measurement [32] may provide some insight into the origins of the observed differences.

The results obtained are quite encouraging and demonstrate how the proposed strategy gives a good understanding of parametric dependence and limitations in the parameter control of the test

2.4. DETAILED SHAPES OF FUNDAMENTAL AND HIGHER HARMONICS

bench. This strategy was designed with the goal of tracking the system modes near instability in full scale brake tests. A second iteration of this experiment was not performed due to time constraints before the full scale brake tests.

In order to improve this estimation strategy future tests should do a comparison between this feedforward and feedback [57, 58, 59, 60] approaches should provide some insight in terms of robustness to perturbations in the system parameters.

2.4 Detailed shapes of fundamental and higher harmonics

Let us now discuss the 3D scanning laser Doppler vibrometer measurements. In these measurements the setup used in the two previous sections is suspended to allow measurement using 3D-SLDV (shown previously in figure 2.19). The positions of the shaker and accelerometers are the same ones used for measurements in the previous section. A problem with the load cell, however, meant that the applied force data had to be discarded in this set of measurements.

Using this setup a series of stable sine excitation is applied at the resonance frequency of the three first modes of the system at 5 different pressure levels (4,6,8,10 and 15 bar). The resonance frequencies for each pressure value are obtained by extracting the maximum amplitude frequencies in the response to a wideband excitation.

Each measurement is done from two different points of view (front and back) allowing measurements that give a good representation of the vibrations at the caliper, piston, backplate, support columns and base. The measurement points on the two views is shown in figure 2.30 superposed with a camera view from the 3D-SLDV measurement system.

In order to keep the same position of the laser measurement system all measures on the front side are made before starting the back view. This implies that the brake pressure is relaxed and reapplied between the front and back view measurement at the same pressure level, which results in small differences between the system characteristics between sides. To minimize this effect on the measured shapes the resonance frequency is re-estimated for the back view measurements.

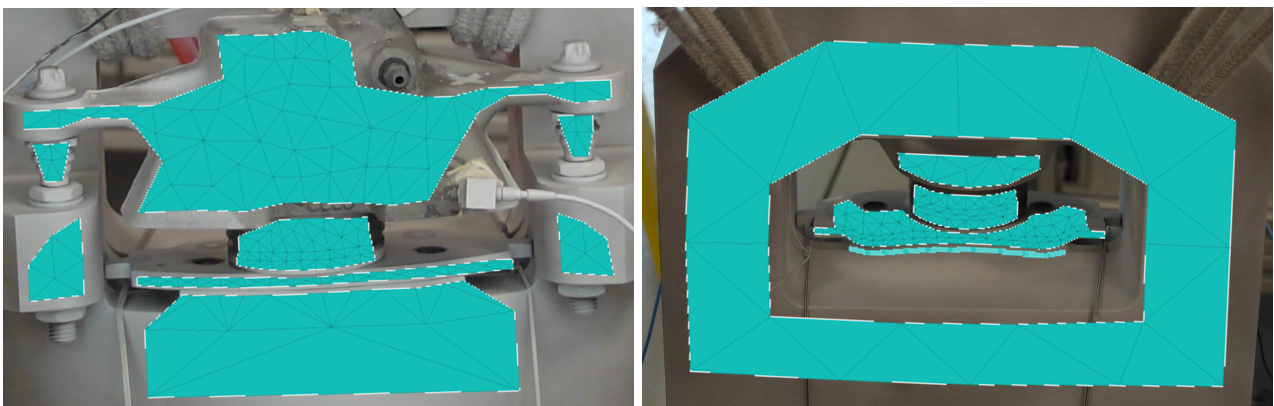


Figure 2.30: 3D-SLDV measurement mesh superposed with the camera view of the measurement system. Left: front view. Right: back view.

2.4. DETAILED SHAPES OF FUNDAMENTAL AND HIGHER HARMONICS

In these measurements the 3D velocity is sequentially measured for each point together with the reference accelerometers. As no triggering is performed, the initial phase differs as illustrated for the reference accelerometer measurement in figure 2.31, where the maximum amplitudes or passage at zero occur with a delay.

The vibration shape at each point is then extracted the demodulation algorithm proposed in 2.2 and then aggregated using the reference sensors (using the method detailed in section 3.5.3). The aggregation of the shapes at each point gives a complex vibration shape for the whole structure and here for each mode and pressure.

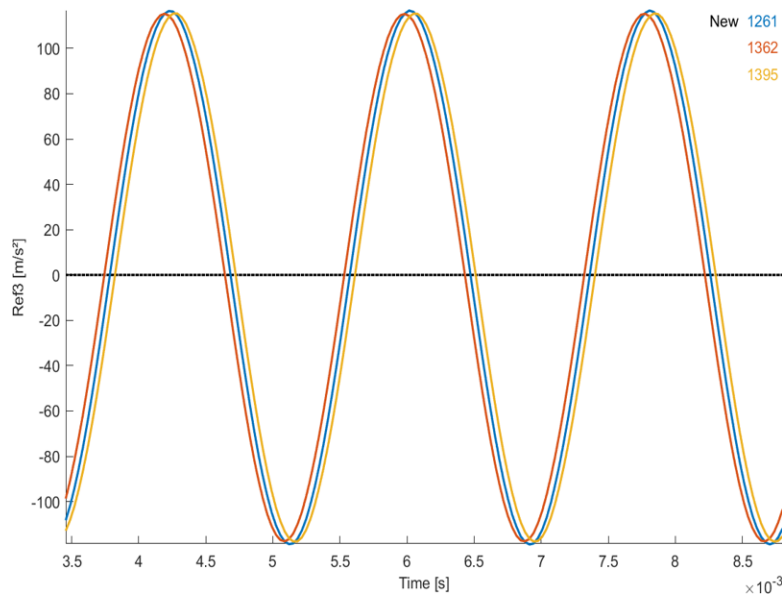


Figure 2.31: Fixed reference accelerometer measurement corresponding to three sequentially measured laser points.

Note that the usual way to display a complex shape in space would be with an animation, which is not adapted to be printed. So in order to obtain a good comparison between shapes at different pressures in figure 2.32, we manually set each shapes to a similar phase. Note that this could be automated using a least squares problem. In this figure the third mode extracted at 4 bar and 15 bar are displayed. The most notable change between them can be seen at the contact between the piston and the backplate, on the region indicated by a red square. Comparing the mesh displacement relative to the point indicated by a red arrow, it is possible to see that at 4 bar the the entire piston seems to move relative to the backplate, while at 15 bar only part of the piston moves relative to the backplate (dark blue region does not move). This shows that at higher pressures the contact between piston is more rigid and does not move while there is some sliding on the contact at lower pressure. A more precise localization of the differences between shapes could be achieved by using methods such as the MACCo described in [78] which determine which sensors have the greatest impact on the difference between shapes.

2.4. DETAILED SHAPES OF FUNDAMENTAL AND HIGHER HARMONICS

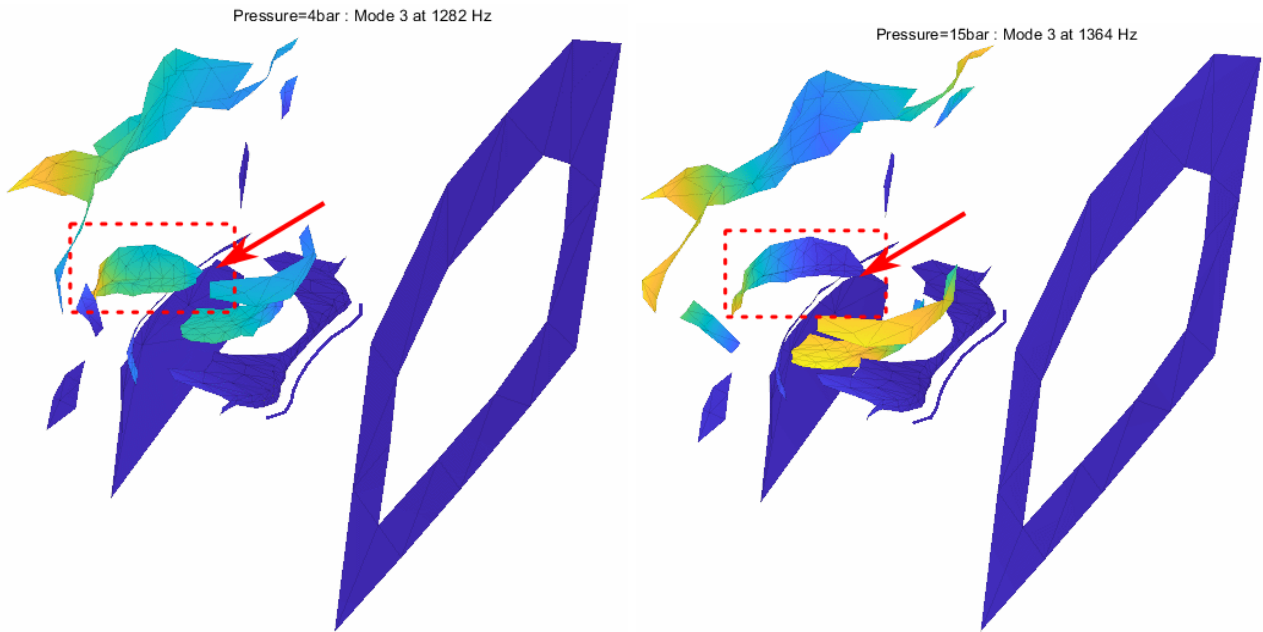


Figure 2.32: Frame of the extracted complex shape of the response to a sine excitation at the resonance frequency for mode 3 at 4 bar (Left) and 15 bar (Right). Red square highlights the portion of the mesh corresponding to the piston and red arrow indicating the same point in space.

One also notices that the displacement of the piston at 15 bar in figure 2.32 is predominantly at one side of the piston. This indicates that the contact pressure is also predominantly on a single side of the piston. This has motivated a measurement of the pressure distribution using calibrated pressure paper.

If the contact pressure was homogeneous the pressure paper would reproduce the ring shape of the piston contact. Figure 2.33, however, shows that the piston only presses against the backplate on one side. Thus confirming the observation made from the shapes in figure 2.32. The probable cause of this is that the support columns are not perfectly aligned, tilting the piston slightly to one side. Note that this type of problem would not occur in a full brake system with floating caliper design such as the one that served as basis for this test bench. In a full brake system the columns used as support in here can slide to balance the loads which would naturally correct the height difference induced here by bolting to a support base.

2.4. DETAILED SHAPES OF FUNDAMENTAL AND HIGHER HARMONICS

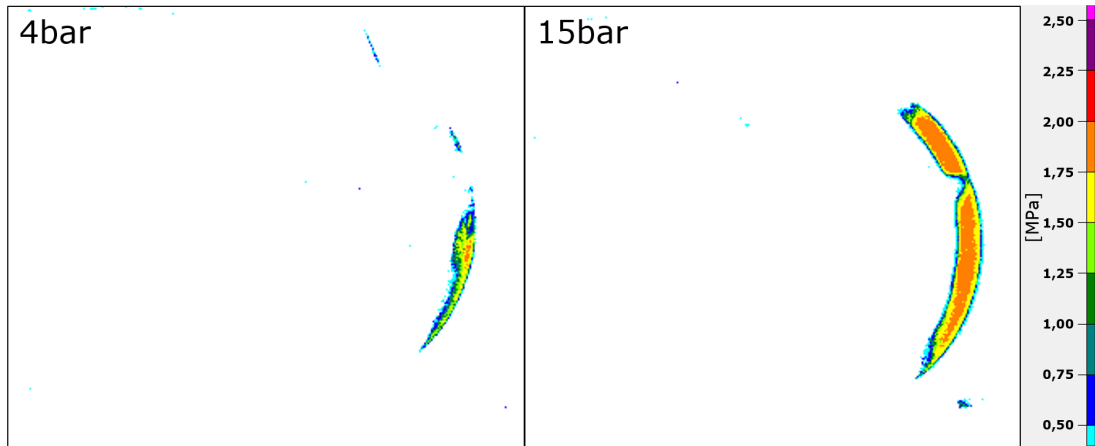


Figure 2.33: Pressure paper measurement of the contact pressure between piston and backplate on the contact test bench at an hydraulic pressure of 4 and 15 bar

Now, let us analyze the shapes obtained from the response to a sine excitation at the first mode resonance frequency. Here one assumes to be sufficiently close to phase resonance for the first harmonic shape to correspond to the mode shape (see figure 2.34a-b). Higher harmonics can also be animated : two in 2.34c-d and three in e-f.

The associated shapes to each harmonic are quite different. The first harmonic shows a forward and backward rocking motion of the caliper. The second harmonic show a more predominant vertical displacement of the caliper and piston with flexing of the arms. The third again show a flexing of the arms, but this time with an increase in lateral movement and deformation of the piston and backplate.

This figure illustrates that since the shapes differ, the nonlinearity of contact interfaces is probably excited differently for each harmonic. Computational methods, that do not allow such shape changes, are thus likely to give less accurate results.

2.5. USING THE HBV SIGNAL TO DESCRIBE NONLINEAR BEHAVIOR: INSTANT STIFFNESS AND HARMONIC MODULATION

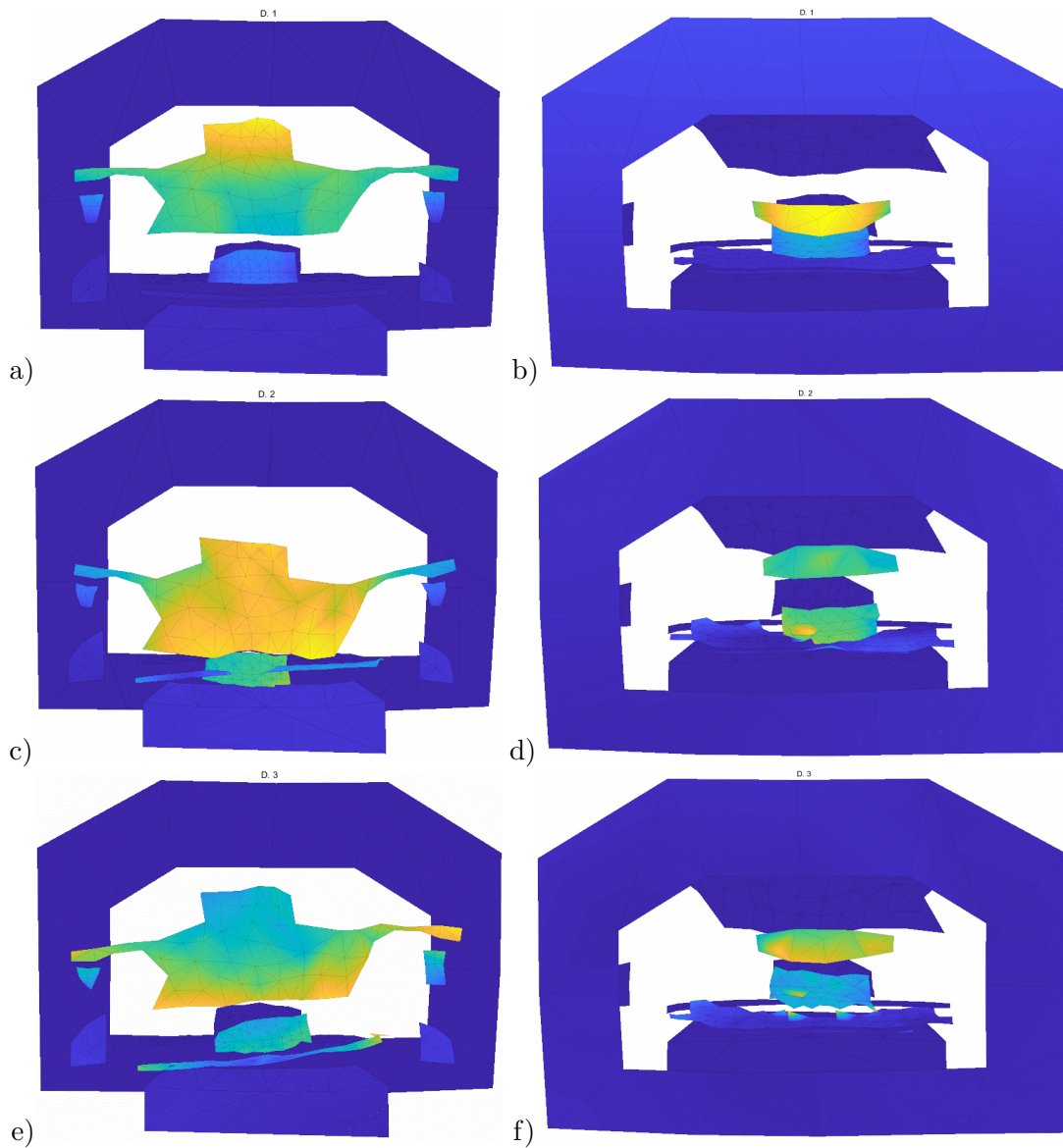


Figure 2.34: Frames of the extracted complex shape of the response to a sine excitation at the resonance frequency for mode 1. a) First harmonic front view b) First harmonic back view c) Second harmonic front view d) Second harmonic back view e) Third harmonic front view f) Third harmonic back view

2.5 Using the HBV signal to describe nonlinear behavior: instant stiffness and harmonic modulation

As mentioned in section 2.2, the HBV signal model considers that the system vibrations and parametric variations happen in two different timescales. Up until this point, the applications of the HBV signal model focused mainly on the slowly varying portion of the signal.

One will seek to analyze system evolution within a period, and thus through the associated har-

2.5. USING THE HBV SIGNAL TO DESCRIBE NONLINEAR BEHAVIOR: INSTANT STIFFNESS AND HARMONIC MODULATION

monics, with higher harmonics being related to nonlinearity. This point of view will assume the slow evolution of harmonics from period to period.

Section 2.5.1 uses the HBV signal to clarify the idea of instant modulus/stiffness first proposed in [31]. Nonlinear viscoelastic behavior examples are used and were used in conference paper [32]. An application to the contact test bench data is then detailed in section 2.5.2.

2.5.1 Using higher harmonics to define instant stiffness and harmonic modulation

In order to better understand the idea of instant stiffness, let us take a look at the context in which the idea of instant stiffness/modulus was introduced. Typical rubber tests use uni-axial shear or compression tests with imposed sinusoidal displacement in order to extract the constitutive laws of the material. In this type of test, one expects the input displacements to be composed of a static displacement plus a single harmonic $q(t) = q_0 + Re(q_1 e^{i\omega t})$ with a periodic multi-harmonic output force $F(t) = Re(\sum_h F_h e^{ih\omega t})$.

Rubber is a material that presents viscoelastic behavior. In this case, the classical approach to its behavior is to ignore higher harmonics and use a complex stiffness/modulus [79] given by

$$[K_1] = \frac{F_1}{q_1} = [K_1]' (1 + i\eta) \quad (2.27)$$

The nonlinearity is only viewed for very low frequencies and analyzed either as rate independent contributions or through an amplitude dependence called Payne effect.

The instant complex modulus proposed in [31] seeks to improve on this by representing nonlinear effects as time varying instead. In this project, this notion is combined with the proposed HBV signal model in order to answer a simple question : *where in the period and how much does the nonlinear response deviate the linear sinusoidal response ?*.

The answer here is given by an instant stiffness indicator that replaces the one initially proposed in [31]

$$[K_t(t, q_0, q_1, \omega)] = \frac{\sum_{h>=1} \{F_h\} e^{i(h-1)\omega t}}{q_1}. \quad (2.28)$$

It is quite obvious that this indicator is constant for a linear system and the instant stiffness is then equal to the complex modulus (2.27). The instant stiffness (2.28) is also clearly periodic, with mean K_1 , thus providing indications that characterize nonlinearity within the period and a clear definition of *weakly nonlinear* as the case where the time dependence is small compared to the mean.

As an illustration, let us consider the same hyper-viscoelastic model used as example in [31, 32]. This model contains a hyperelastic portion interpolated using piecewise cubic polynomials, and a series of 6 branches. The first three branches are associated with slow relaxation times, and are considered purely hysteretic/friction. The other three have faster relaxation times and are considered viscoelastic. For further details on the construction of nonlinear viscoelastic models check [80].

Imposing a displacement containing harmonics 0 and 1 to this nonlinear model, generates the force shown in figure 2.35 Left (large cycle at 0.5 Hz) and zero static displacement in figure 2.36). In the time

2.5. USING THE HBV SIGNAL TO DESCRIBE NONLINEAR BEHAVIOR: INSTANT STIFFNESS AND HARMONIC MODULATION

response, it is possible to see harmonic 0 of the force is non-zero and that deviations from harmonic 1 (in red) are visible.

In the right plot, the instant stiffness (2.27) is shown in blue fluctuating around the harmonic 1 estimate. In compression (corresponding to the $TR = [1\ 3]$ interval), instant stiffness is up to 12% higher than the harmonic 1 stiffness, while in traction it is up to -8% lower.

This imposed displacement strategy is similar to the one used in section 1.3.4 to construct an amplitude dependent eigenvalue analysis for the 2-DOF functional model. The focus is, however, quite different since in section 1.3.4 the stiffness variations were considered at the scale of multiple periods instead of inside a period.

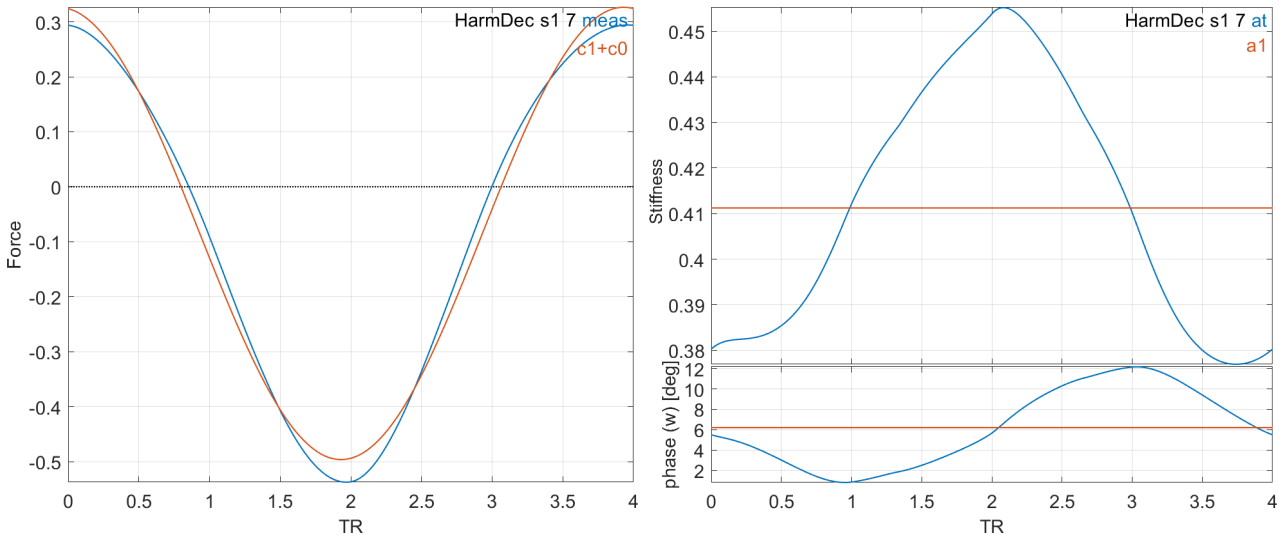


Figure 2.35: Left : force as function of reduced time ($1=1/4$ period). Right : corresponding harmonic modulation ($q^a(t)$ blue) and first harmonic (q^1 red).

The instant stiffness phase δ is typically interpreted as a loss factor $\eta = \tan(\delta)$. The phase deviation is also a clear indication of asymmetry of the loading and unloading phases. When instant force/stiffness is increasing the harmonic modulation phase is below that of harmonic 1. The fact strain energy increases faster than expected can be interpreted as a smaller loss factor. On the contrary when the strain energy decreases faster than what the linear model would say, energy is lost which is seen as a higher than average loss factor.

In figure 2.36 left, the classical force displacement response is shown for different values of frequency, static load, and amplitude. The hyperelastic behavior is visible as global slope changes and the Payne effect in the fact that the slope of small cycles is higher than that of large cycles.

2.5. USING THE HBV SIGNAL TO DESCRIBE NONLINEAR BEHAVIOR: INSTANT STIFFNESS AND HARMONIC MODULATION

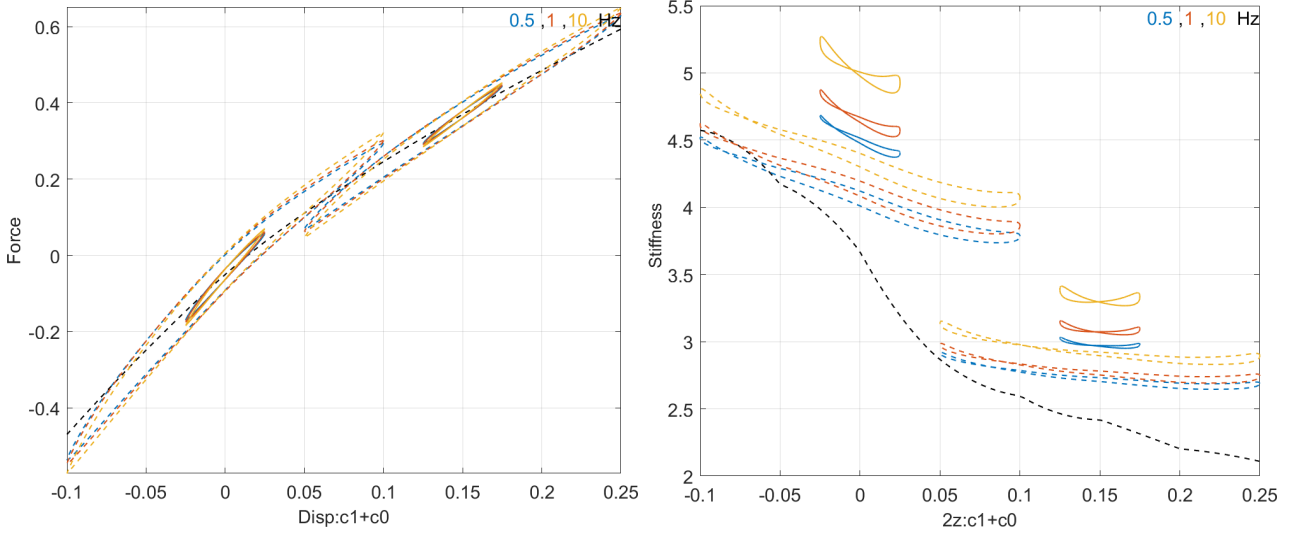


Figure 2.36: Left : force / displacement curve with 2 levels of pre-stress, 2 amplitudes and 3 frequencies. Right : corresponding instant stiffness (2.28) / displacement curves. Hyperelastic force/tangent stiffness is shown as a black dotted line.

Figure 2.36 right illustrates how instant stiffness displacement curves are much more readable than the force displacement ones. The evolution with frequency is readily seen as an increase of modulus with frequency (as expected [31]). The coupling with hyperelasticity is also visible as the fact that the overall instant stiffness trajectories show higher values for higher hyperelastic stiffness.

The Payne effect also clearly appears as the fact that for higher amplitudes the instant stiffness is lower at all instants of the period. This corresponds to the fact that for large amplitudes low frequency relaxation cells reach saturation and thus have a decreased amplitude. At the center of the period (displacement equal to static component), the stiffness is however still higher than the hyperelastic stiffness shown in black. This is consistent with the choice of adding nonlinear viscoelastic cells to a base hyperelastic behavior.

In the rubber application, defining a stiffness in (2.28) where the response is normalized by the harmonic 1 amplitude q_1 was relevant. It is also possible to simply analyze the response by defining an *harmonic modulation*

$$\{q_a(t)\} = \sum_{h>=1} \{q_h\} e^{i(h-1)\omega t} \quad (2.29)$$

2.5. USING THE HBV SIGNAL TO DESCRIBE NONLINEAR BEHAVIOR: INSTANT STIFFNESS AND HARMONIC MODULATION

2.5.2 Harmonic modulation in 3D-SLDV measurements

The measured responses from the stable sine tests of section 2.4 offer a good example for testing the proposed harmonic modulation indicator. In addition to being a periodic response, in figure 2.34 it is possible to see that the extracted higher harmonics carry relevant information. By using the harmonic modulation indicator our goal is to improve the interpretation of the extracted harmonics.

As a starting example, figure 2.37 shows the measured acceleration signal from one of the sine tests (blue line). This measurement corresponds to the vertical direction of the accelerometer seen in figure 2.30. The components corresponding to harmonics 1 to 5 of this signal are estimated, and the rest of this estimation (red line) show us that the system response is completely contained in the extracted components.

In order to simplify the reading of the different phases of the periodic cycle, the time data was replaced by a reduced time TR value such that for a full period $TR = 4$. Additionally, a series of markers were added for every quarter period following the sequence $\diamond, \nabla, \square, \triangle$.

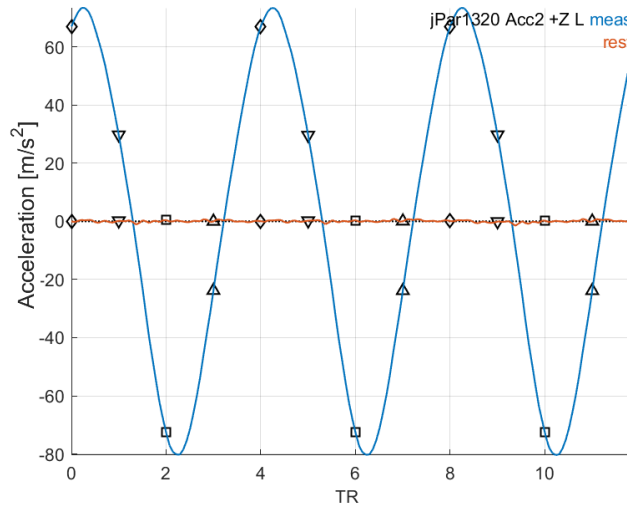


Figure 2.37: Acceleration measurement and rest after harmonic extraction as function of reduced time ($1=1/4$ period).

The measured signal shows some non-symmetry between the above and below zero portions of the signal. This non-symmetry is more easily seen in the harmonic modulation shown in figure 2.38 left. For positive acceleration (markers \diamond, ∇), acceleration evolves more slowly than the linear response (harmonic modulation is smaller than harmonic 1). For negative acceleration (markers \square, \triangle), the evolution is faster (harmonic modulation is larger than harmonic 1).

2.5. USING THE HBV SIGNAL TO DESCRIBE NONLINEAR BEHAVIOR: INSTANT STIFFNESS AND HARMONIC MODULATION

This behavior is highlighted even more in figure 2.38 right, where the harmonic modulation is shown as a function of the first harmonic trajectory. This view also indicates that this characteristic is repeatable between cycles.

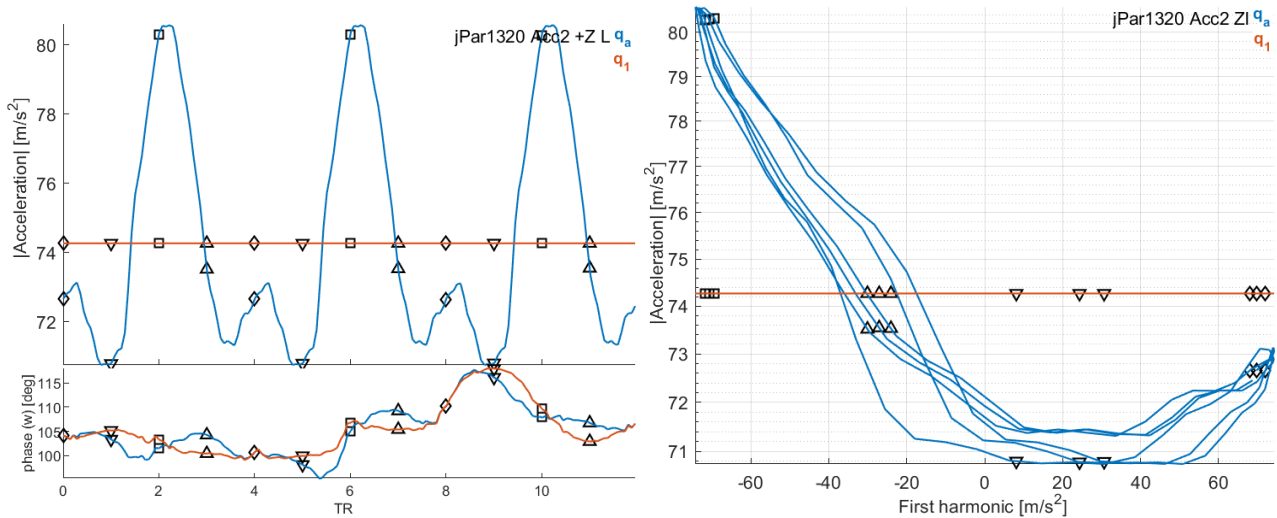


Figure 2.38: Left: Harmonic modulation and harmonic 1 coefficient over reduced time ($1=1/4$ period). Right: Harmonic modulation and harmonic 1 coefficient over harmonic 1 trajectory.

A certain fluctuation on the phase can be seen in the extracted harmonic modulation in figure 2.38 left. It originates from the fact that, since the excitation frequency was known, the extraction of components did not use the instant frequency estimation from the demodulation algorithm described in section 2.2.

Considering that $q_a(t)$ increases at the instants of maximum displacement (same as acceleration), it is possible to relate marked instants with specific positions of the components. The harmonic 1 trajectory over a period obtained from 3D-SLDV measurements shows in figure 2.39 that the predominant motion of the system is a back and forth rocking motion of the caliper and piston. Matching the markers in figures 2.37 and 2.38 with instants in figure 2.39 provides the necessary insight to understand the harmonic modulation.

Marker \diamond corresponds to $t = 0$ in figure 2.39. The contact is opened in the front (the piston presses less on the backplate). This is expected to lead to a decrease of stiffness coherent with a slower evolution seen in the harmonic modulation in figure 2.38. Marker \square corresponds to $t = 2$ in figure 2.39. In this case the contact in the front is closed (the piston presses more on the backplate), which is expected to lead to an increase in stiffness coherent with a faster evolution of the harmonic modulation. Markers ∇, \triangle corresponds to the transition phases, where the contact transitions from the back to the front.

2.5. USING THE HBV SIGNAL TO DESCRIBE NONLINEAR BEHAVIOR: INSTANT STIFFNESS AND HARMONIC MODULATION

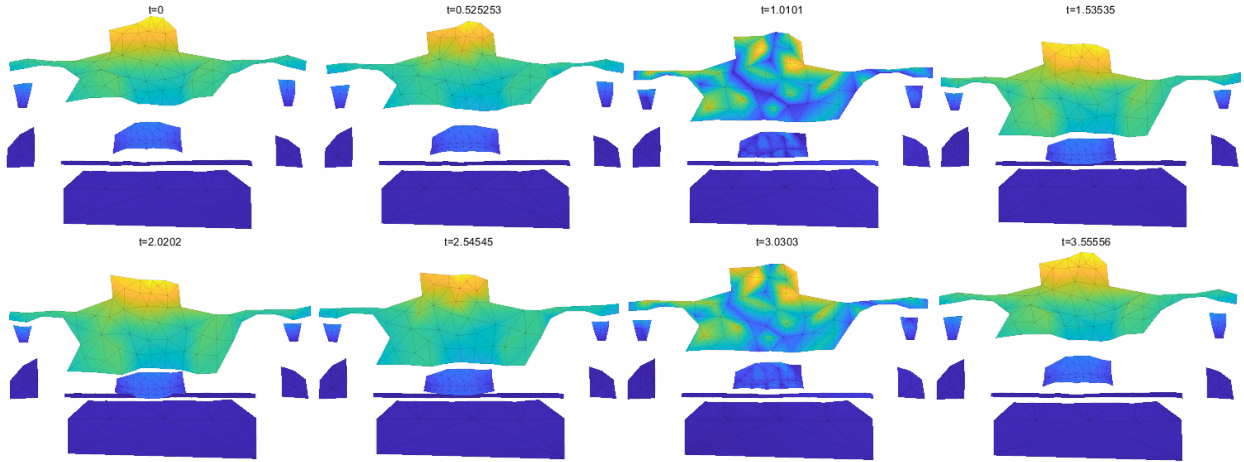


Figure 2.39: Trajectory of the harmonic 1 shape over reduced time ($1=1/4$ period)

Visualizing this over a mesh is not as straightforward as for a single point due to the smaller variations over a larger mean value. In order to visualize how the combined harmonic behave over a cycle, an harmonic perturbation is defined by removing harmonic 1 from the harmonic modulation

$$\{q_a(t)\} - \{q_1\} = \sum_{h>1} \{q_h\} e^{i(h-1)\omega t}. \quad (2.30)$$

This new value only contains the effects of higher harmonics and describes the trajectory followed around the first harmonic shape.

For harmonic 1 in figure 2.39, closing of the piston occurs between $t = 1.5$ and $t = 2.5$. In the harmonic perturbation in figure 2.40, the opposite trend is found as the piston tends to open.

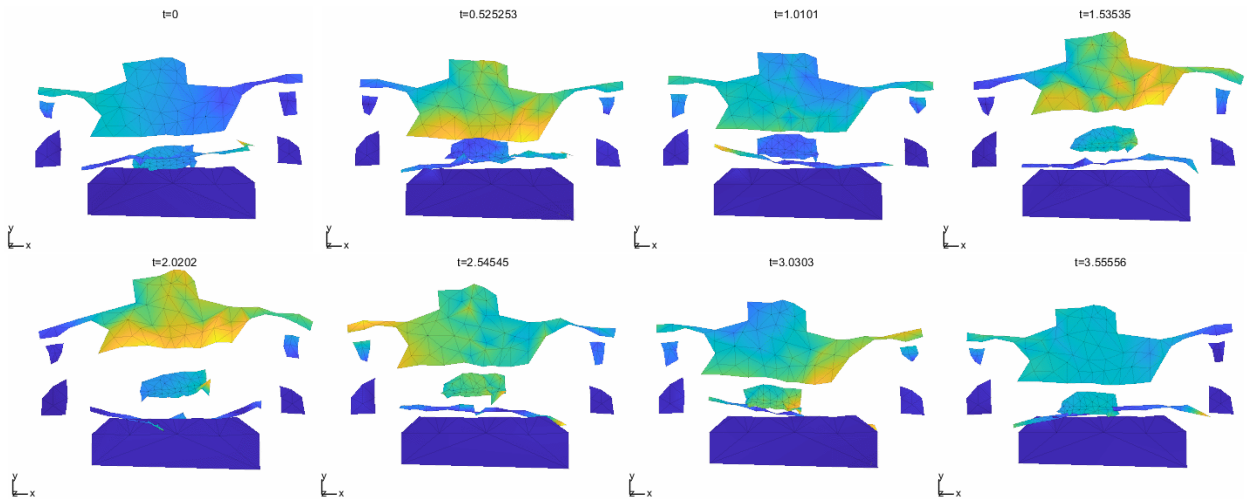


Figure 2.40: Harmonic perturbation over reduced time ($1=1/4$ period)

This confirms that the spatial relation between harmonic shapes and contact nonlinearity can be analyzed using measured shapes. Future work could seek to use this information to characterize the

contact nonlinearity.

2.6 Conclusion

The dynamic behavior of brake squeal is subject to the effect of multiple operating parameters, some of which are not controllable. With this in mind, this chapter discusses how these characteristics can be taken into account on the analysis of squeal tests, on the parametric identification of modal properties, and on the spatially detailed characterization of vibration shapes.

Section 2.2 shows that, due to the effect of slowly varying parameters, the measure of a squeal occurrence is quasi-periodic with two characteristic timescales. A fast timescale that describes the quasi-periodic behavior through the Fourier series representation of a period leading to the presence of harmonics, as in the Harmonic Balance Method, and a slow timescale that describes changes of period and harmonic vector components over multiple periods.

Through the definition of the HBV signal model, one is then able to represent the vibration characteristic of squeal tests. In addition to squeal, this description is of interest in sine, slow sweep or any other type of testing where the period slowly evolves over time.

The properties of the HBV signal model are then estimated using a demodulation algorithm that tracks the slow evolution of both frequency and amplitude for all measurement channels. Its applications throughout this project have shown that this algorithm is robust and easy to tune.

Section 2.3 then describes a process to track the parametric evolution of modal properties. A sample application is detailed using a contact characterization test bench. Experimental Modal Analysis (EMA) at a few fixed pressure points provides an approximate relation between pressure and resonance frequency. The resulting discrete characterization lacks accuracy.

In order to obtain a continuous tracking of the modal properties a phase resonance method is proposed as a feedforward approximation of closed loop methods [57, 58, 59, 60]. This procedure has shown relevant result which were presented at the Survishno conference [30]. In the single application attempt, parameter perturbations created problems and damping estimations differed from broadband excitation, which is expected for a nonlinear system. Thus, despite obvious need for further work, the procedure seems promising.

Using a series of sine tests near the resonance frequency for different pressure values, the HBV signal representing the fundamental and its harmonics is then estimated in section 2.4 to obtain spatially detailed vibration shapes from 3D-SLDV measurements. The evolution of the fundamental harmonic shape highlights the effect of applied pressure on the contact nonlinearity.

In order to exploit higher harmonic data, section 2.5 defines two indicators, the harmonic modulation and harmonic perturbation, based on the notion of instant stiffness/modulus proposed in [31]. These indicators are able to describe, around the harmonic 1 response, where the system is softer or stiffer giving a more precise understanding of the nonlinearity. An early version of these results was presented at the ISMA conference [32] using data from rubber identification tests.

2.6. CONCLUSION

Full scale brake tests

Content

3.1	Motivation and context of full scale brake tests	98
3.2	Describing the full scale test campaign	99
3.2.1	Parametric testing of brake squeal	99
3.2.2	Measurement setup for full scale test campaign	102
3.3	Tracking influence of pressure on squeal frequency, amplitude and shapes	108
3.3.1	Design of experiment and overview using time frequency analysis	108
3.3.2	Definitions of vibration amplitude and decay rate	109
3.3.3	Tracking/clustering squeal occurrences for a stepped pressure evolution	113
3.4	Parametric EMA in operating condition	117
3.4.1	Motivation for EMA in operating condition	117
3.4.2	Transfer function estimation and coherence analysis	119
3.4.3	Identification of poles for selected pressure values	124
3.5	Detailed shape characterization using 3D-SLDV	132
3.5.1	3D-SLDV Measurement setup	133
3.5.2	ODS estimation using Short Time Fourier Transform	134
3.5.3	Using an HBV signal and demodulation to build operational deflection shapes	136
3.5.4	Sample results	138
3.6	Conclusion	141

3.1 Motivation and context of full scale brake tests

Brake squeal limit cycle frequencies and amplitudes are known to be very sensitive to operating parameters (pressure, temperature, wheel position, friction coefficient). Full scale brake tests are an essential tool to characterize brake squeal noise. In industry, test matrices representative of the overall brake operating conditions are applied to the full brake system using a dynamometer test bench. They are often used to evaluate or validate the NVH quality of a brake design and lead to clusters of squeal occurrences that link operating conditions to squeal frequency and noise level.

When corrective measures are necessary due to the presence of an unacceptable level of noise, one can seek to propose structural modifications by using one of three types of data: experimental test data, FEM simulation data, test/FEM correlation data.

The main advantage of using experimental data to propose corrective measures is that it contains the exact behavior of the physical system. However, this approach requires iterative prototyping and validation, which is a long and expensive process. Using only experimental data also limits the propositions of structural modification to the sensor locations. Experimental studies of squeal analyze acoustic fields [8], deflection shapes [9, 10], equilibrium positions [11], or temperature distributions [12], ...

Using FEM simulations to propose corrective measures, one is able to propose structural modifications without the same spatial limitation as the experimental case, since they allow access to the movements of the entire structure. This method is also faster than the experimental one, due to the simple fact that it does not require prototyping. The main challenge of using FEM to propose structural modification lies in ensuring that the numerical model represents the physical system. This has motivated a number of studies seeking to obtain better numerical models for squeal [13, 14, 15, 16]

In order to obtain a balance between the positive aspects of both test and simulation, it is ideal to employ test/FEM correlation techniques. The basic idea is that, by using the results of the measurements in combination with the FEM model, it is possible to update the model [17] and/or generate a hybrid test/FEM approximation [18] and thus propose better corrective measures.

This chapter will analyze a series of tests performed to characterize parametric dependency of brake squeal with a particular focus on slow parameter variations. Section 3.2.1 discusses the different operating parameters that influence brake squeal and their characteristic timescale, while highlighting those that can be used to design parametric tests. Then section 3.2.2 describes the experimental setup used in the test campaign. The analysis of test results is divided in three parts each a type of measurement.

The first type of measurement considered in section 3.3 are squeal occurrences. Standard test matrices seek to identify squeal occurrences based on the acoustic levels for a range of pressure, wheel speed, temperature, and other parameters. This section illustrates how the HBV signal strategy (described in section 2.2) can be used to extract the evolution of signal features such as instantaneous frequency, instantaneous amplitude and shape. Intermittent squeal occurrences are used to discuss amplitude and frequency evolution seeking to obtain experimental root locus as done for the functional model in chapter 1. Variable pressure tests are then used to improve the classification of squeal occurrences and seek characteristic features.

The second type of measurement, discussed in section 3.4, are parametric modal analyzes in operating condition. Using a series of swept sine measurements, the evolution of the system frequency response with pressure is characterized near squeal. The presence of coherence drops near the squeal frequencies makes identification in this region trickier, but is shown to have the potential to track squeal before the appearance of large amplitude limit cycles.

Finally, section 3.5 focuses on the use of 3D Scanning Laser Doppler vibrometer (3D-SLDV) to extract spatially detailed characterizations of squeal vibration shapes. This section seeks to improve results of the current FastScan process, which is based on short time Fourier transform (STFT), by extracting HBV signal components using demodulations to construct shapes. Using demodulation offers an advantage over the usual Fourier method as it takes the quasi-periodic nature of squeal into consideration and can handle noise more efficiently. In addition, the use of the HBV signal allows us to define and extract spatially detailed shapes corresponding to the higher harmonics.

3.2 Describing the full scale test campaign

3.2.1 Parametric testing of brake squeal

As mentioned previously brake systems in operating condition are subject to the effect of multiple parameters. Understanding these parameters and their effect is an essential part of the experimental characterization and classification of squeal occurrences.

This section lists the principal effects and discuss their use in the design of parametric tests. We can divide the parameters that affect a brake squeal measurement in three different categories according to our ability to control and measure the parameter.

The first type are the parameters that can be directly controlled and measured : applied pressure and disk velocity. This characteristic motivated the use of pressure as a reference parameter in the functional model from chapter 1 and the simple parametric test bench in 2.3. Following the same trend, the design of the experiments in this chapter will also consider pressure as the first focus of parametric tests.

As an illustration of the pressure effect figure 3.1 shows one of the measurements from the parametric tests without excitation described in section 3.3. Slowly changing pressure modifies the limit cycle vibration, even introducing a jump in the associated frequency around 70s.

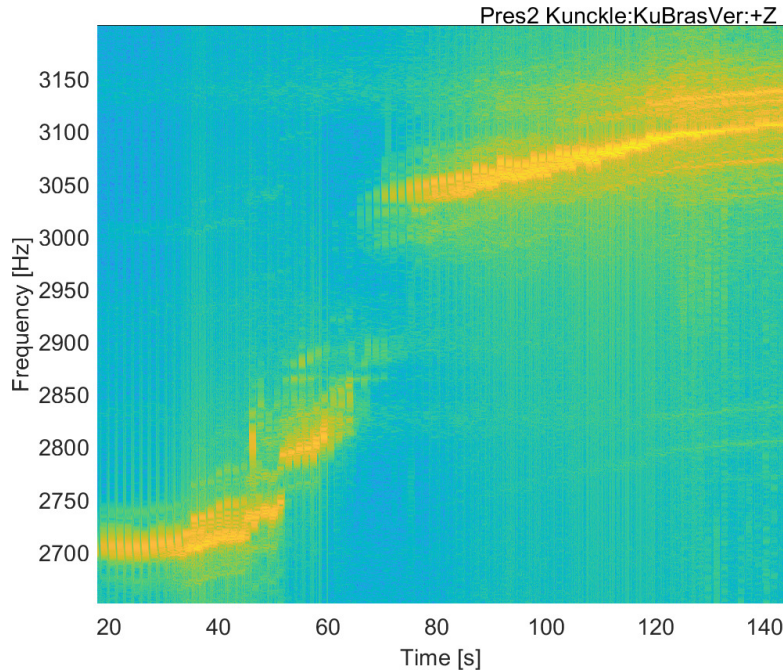


Figure 3.1: Spectrogram of a squeal measurement under slow varying pressure showing the parametric effect of pressure on squeal limit cycle.

The second type of parameter measured but not directly controlled are temperature, angular position and applied torque. Each of these parameters has a characteristic that makes it hard to set them to a specific value. Meaning that the tracking of the parameter effect on the system relies more on following the evolution of these parameters during a measurement than setting the system to a value. Let us now take a closer look into the three parameters of this type.

In the case of temperature obtaining a measurement is very straightforward, one only needs to add a thermocouple to the system at the brake pad or disk. However, tracing the effect of temperature remains a subject of study, some of them focusing on how temperature evolves inside the friction material [12]. The main challenge in the handling of temperature is controlling it since the brake system constantly heats up while braking making it impossible to have a fixed temperature in longer measurements. The initial temperature is typically raised by successive braking and lowered by waiting. This makes it impractical to test multiple temperatures in non-automated procedures such as the ones considered in this work.

One of the main trends visible throughout the campaign, and confirming previous studies [7, 20, 8, 55, 17], is that vibration levels vary during a short part of the wheel turn (intermittent squeal). This indicates that the parametric variation introduced by the wheel angular position have a significant effect on squeal. Figure 3.2 Left illustrates the frequency fluctuations in a measurement where pressure and velocity are kept constant.

The 2024 test, shown in figure 3.10, introduced a sensor to measure the relative position between disk and caliper. The result shown in 3.2 Right, is not perfect as wheel position is estimated by integrating velocity (and not using an encoder) and thus shows a horizontal drift, and as the sensor is sensitive to temperature inducing a vertical drift. But the key result is that distance is not constant

3.2. DESCRIBING THE FULL SCALE TEST CAMPAIGN

during the revolution and one thus expects a change in contact pressures which chapter 1 showed to impact the system properties and thus squeal levels.

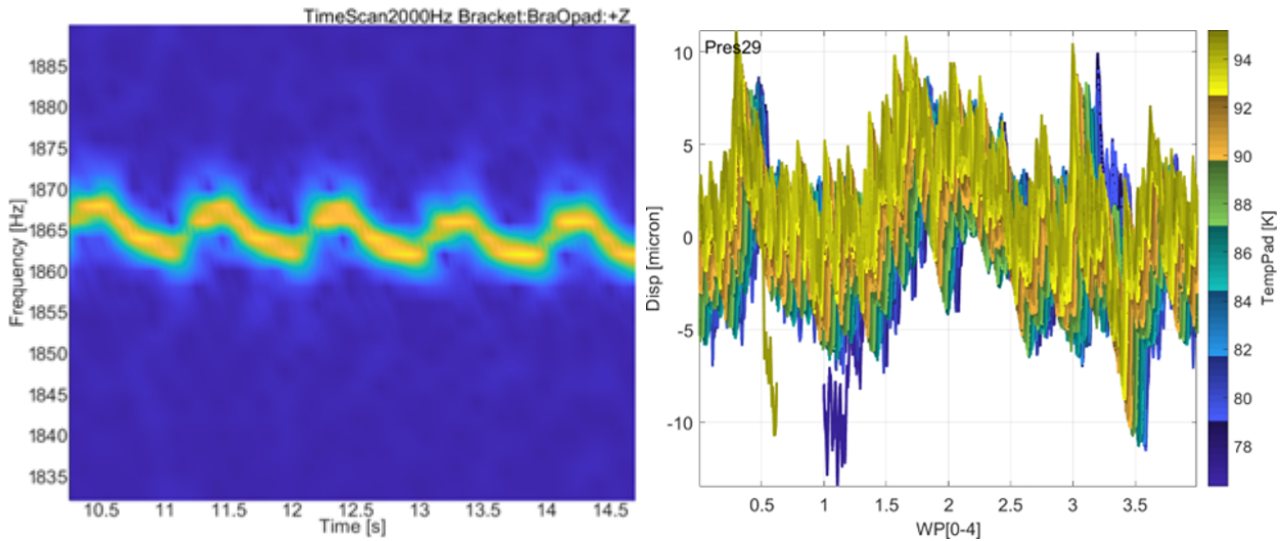


Figure 3.2: Left: Spectrogram of a squeal measurement under fixed pressure and velocity showing the periodic fluctuations introduced by wheel rotation (angular position effect). Right: Normal displacement of a point on the disk under braking as a function of the wheel position WP (1=1/4 of a revolution) and temperature

Initially one might think that the applied torque is a controllable parameter, however the test bench uses torque to control wheel velocity in a feedback loop. This makes torque a parameter that cannot be fixed without releasing the restraint on wheel velocity. In addition to the expected variations, large fluctuations of the torque have been observed. One example of these fluctuations is shown in figure 3.3, where variations above $\pm 50\%$ of the mean value at a frequency of near 30Hz can be seen. The most likely one being a torsion mode of the long shaft used to flip the brake orientation and thus have most parts visible from a 3D scanning laser. In the parametric tests without excitation a fluctuation of the squeal instantaneous frequency at the same frequency near 30Hz showing that the significant torque variations introduce nonlinear changes to the system.

3.2. DESCRIBING THE FULL SCALE TEST CAMPAIGN

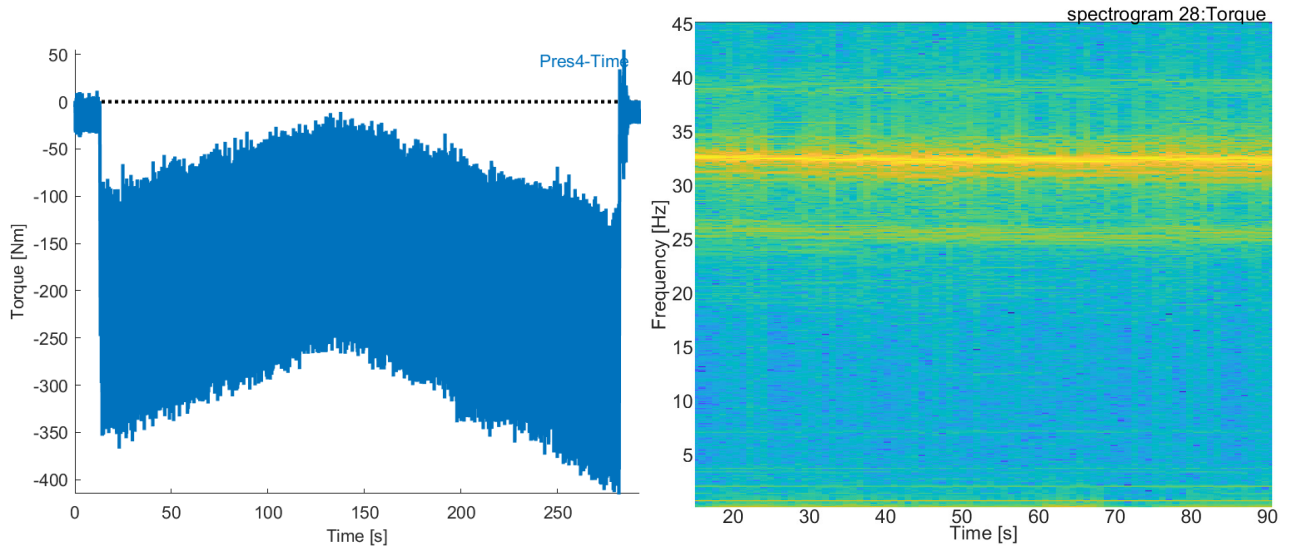


Figure 3.3: Left : measured torque (Pres4 run) , right : spectrogram of measured torque.

Finally, some characteristics of the system and its components cannot be precisely tracked during an experimental campaign. These are the third type of parameter, the ones that cannot be controlled or measured without disassembly. Pad wear is a good example of this type of parameter that has been considered in [81]. During a test campaign wear is taken into account only by the braking history of the pad, and a pre-wear is commonly performed on new pads prior to squeal testing.

Note that the presence or not of anti-noise features such as viscoelastic patches on the back of brake pads have a significant effect on the presence and intensity of squeal events. These anti-noise features were removed to ease the measurement of squeal vibration in the tests discussed here.

3.2.2 Measurement setup for full scale test campaign

Tests were conducted on a Hitachi Astemo inertial test bench using a modified brake system. All viscoelastic patches were removed and friction material composition and contact shape were changed to increase the probability of squeal occurrence. The brake system was held in place using the true vehicle suspension and connected to the test bench by a shaft connected to the inner side of the brake. This leaves the front part of the disk facing outwards as shown in figure 3.4.



Figure 3.4: Brake system mounted in the test bench, 2023 setup.

The inertial test bench also provides the control of the applied pressure and wheel velocity, via an interface, where these parameters were manually set and monitored together with other environmental parameters.

The responses are recorded using a Siemens SCADAS acquisition system sampling at 51.2kHz. The sensors used can be divided into the ones that measure the operating parameters and the ones that measure the vibration and acoustic response. The total list of sensors placed in the system is:

- Operating parameter sensors
 - Pad temperature (figure 3.5 left)
 - Pressure (figure 3.5 right)
 - Tachometer (figure 3.5 center)
 - Torque (from test bench)
- Vibration sensors
 - Microphone (from test bench)
 - Acceleration (6 triaxial accelerometers and 10 monoaxial accelerometers) positions shown in figure 3.6.
 - Collocated force and acceleration on shaker drive point shown in figure 3.7
 - 3D laser Doppler vibrometer (placement shown in 3.8)

The applied torque and the microphone measurements are directly taken from the test bench internal sensors to the acquisition system.

3.2. DESCRIBING THE FULL SCALE TEST CAMPAIGN

The pad temperature is measured using a thermocouple placed inside the pad friction material as seen in the left part of figure 3.5. This is the same sensor used by the test bench for monitoring, but the signal is split into a separate conditioner to provide the measurements. The signal conditioner provided a temperature signal with a 0.5° resolution, which introduced some steps in the measured temperature. Since the temperature evolutions during a measurement are significantly larger the resolution and there is no need for a highly precise temperature value, a simple low pass filter is enough to smooth out the signal.

The velocity measurements are made using a tachometer shown in the center of figure 3.5 which provides, in addition to the wheel velocity, an indication of full rotation that gives us a reference angular position.

For the applied pressure a (Kistler 601CAA) pressure sensor was placed in the location of the purge valve of the piston chamber as shown in the right of figure 3.5. The pressure signal was then conditioned by a charge amplifier, before being sent to the acquisition system. To prevent a bias effect on the pressure measurements, the zero pressure value is recalibrated before each measurement.



Figure 3.5: Placement of sensors in the test bench Left: pad temperature sensor. Center: tachometer. Right: pressure sensor.

In order to allow continuous monitoring of shapes with the objective of grouping squeal instants into clusters associated with regions of the parametric space being tested, six triaxial accelerometers and ten monoaxial accelerometers placed on the brake system and its support arms. A preliminary numerical analysis of the test system was used to gain some insight on the expected vibration shapes of the brake system. Since there is a level of uncertainty in the shapes estimated numerically, they are taken as guidelines for sensor placement instead of using a precise placement algorithm such as [76, 77]. The resulting placement of the accelerometers is shown in figure 3.6.

3.2. DESCRIBING THE FULL SCALE TEST CAMPAIGN

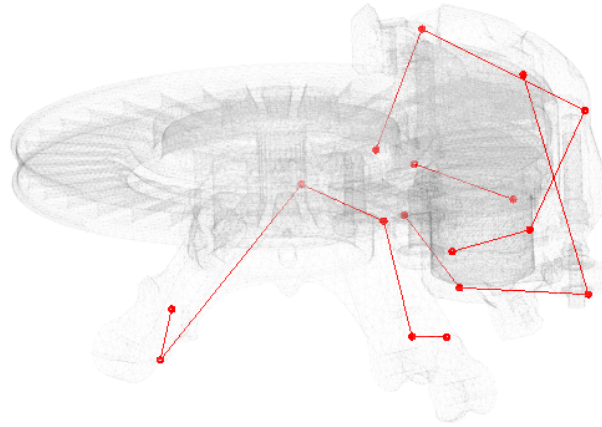


Figure 3.6: Accelerometer placement superposed with the finite element geometry of the brake system used in the full scale test setup

For the parametric tests with excitation, in addition to the accelerometers, it is also necessary to apply force on the system. An electrodynamic shaker, a power amplifier and an impedance head that measures the collocated force and acceleration are used. Their placement is shown in figure 3.7. In order to control the applied excitation a NI cDAQ with an analog output module and an analog input module is used.

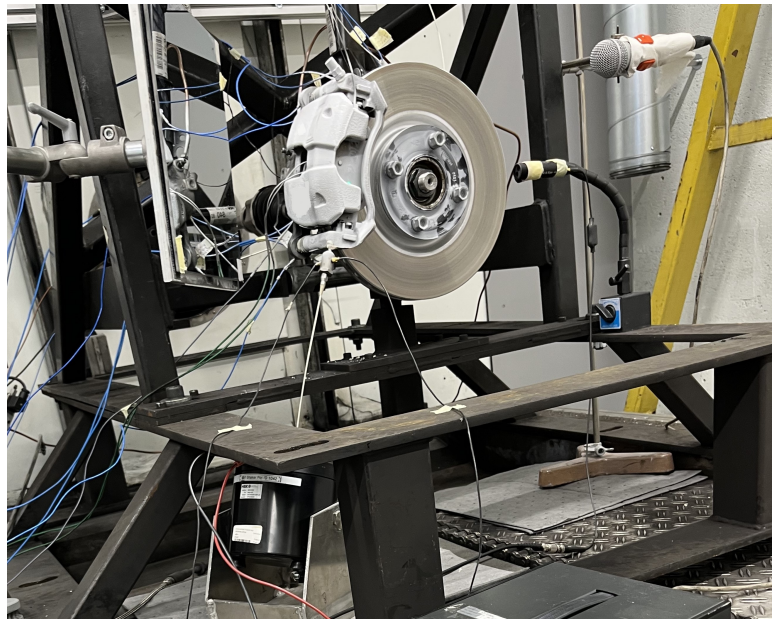


Figure 3.7: Electrodynamic shaker placement in the full scale test setup

3.2. DESCRIBING THE FULL SCALE TEST CAMPAIGN

For the 3D laser Doppler vibrometer (Polytec PSV-500) used in the measurements of limit cycle shapes shown in section 3.5 is placed according to the picture 3.8. This setup is used to sequentially record the 3D velocity in a series of points in two different views, front and mirror. This is the same measurement system that was used to extract the detailed shapes on the simplified test bench in section 2.4.

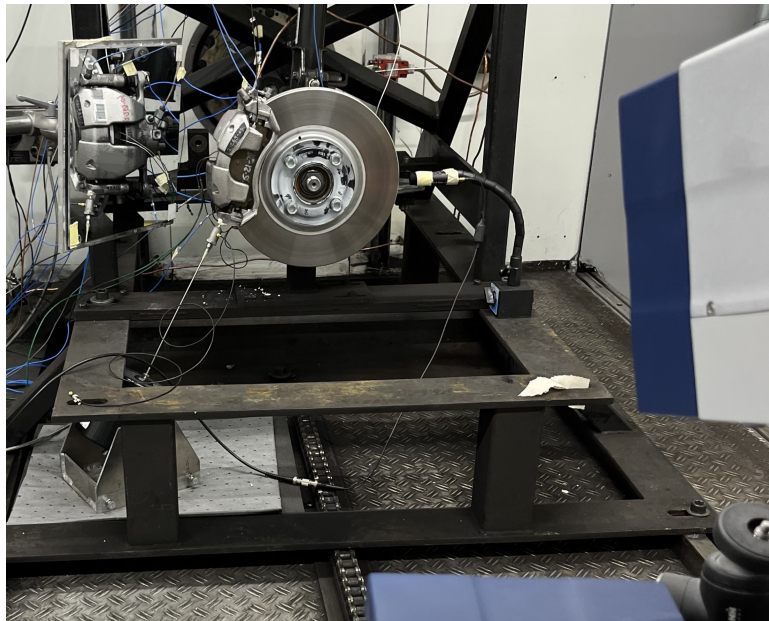


Figure 3.8: Placement of the 3D laser Doppler vibrometer with respect to the brake system in the full scale test setup

During the measurements a significant level of noise was observed above 20kHz during brake events. The sampling frequency on these measurements is set to 51.2kHz, however the accelerometer used for the measurements are only graded with a $\pm 5\%$ accuracy up to 14kHz or 10kHz, so that 20 kHz probably correspond to the mechanical resonance of the accelerometer. In figure 3.9 left response is dominated by content above 20 kHz, so that filtering is necessary to see the actual vibration levels in the right plot. In the right plot, one sees a growth event every wheel period (marked by the vertical dotted lines at 62.5 and 64 s corresponding to measured full rotation marker). Focusing of on the frequency band of interest for this time window ($[2700 - 3000]$ Hz) actually shows multiple growth events within one wheel rotation.

3.2. DESCRIBING THE FULL SCALE TEST CAMPAIGN

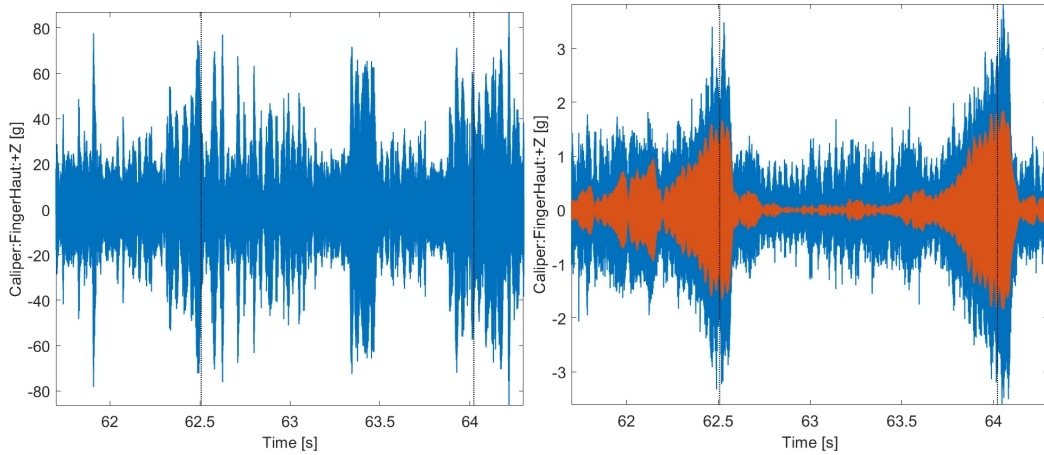


Figure 3.9: Left : raw time signal measured at 51.2 kHz sampling rate (**Pres2** run), Right : 0-20kHz lowpass and 2.7-3kHz band pass filtered signals (blue and red respectively). Vertical dotted lines indicate a fixed wheel position.

Looking at this sample measurement shows us that, in order to analyze squeal measurements, one must be able to extract the slow varying signal on the band of interest while rejecting the noise. These characteristics have motivated the use of the HBV signal model and the demodulation algorithm described in section 2.2 to represent the characteristics of the squeal parametric variation.

A second test campaign was performed in 2024 using a similar brake but changing the test bench and the positioning of the system illustrated in figure 3.10. This eliminated the strong torque modulations of the 2023 test and improved the overall results. However, due to time constraints only a few results are used in this manuscript.

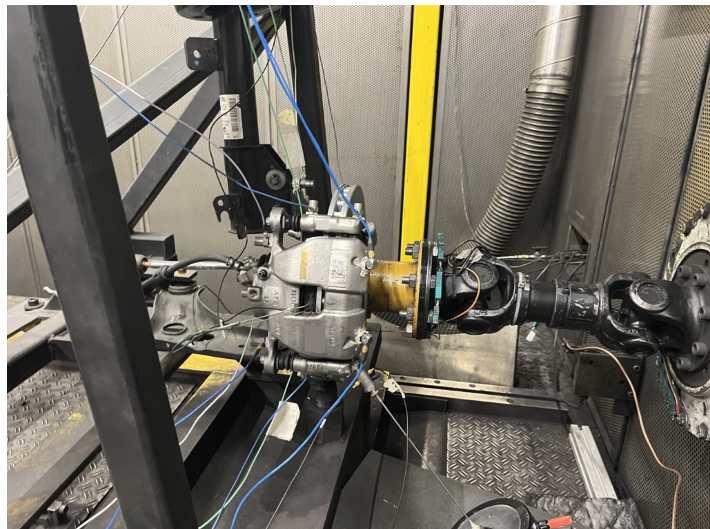


Figure 3.10: Brake system mounted in the test bench, 2024 setup.

3.3 Tracking influence of pressure on squeal frequency, amplitude and shapes

3.3.1 Design of experiment and overview using time frequency analysis

In the parametric tests without excitation our goal is to illustrate the sensitivity of squeal to operating parameters and describe their effect in the limit cycle vibration. Pressure was slowly increased step by step at a constant wheel velocity to characterize its effects. Three of these measurements are analyzed in this section with the applied pressure profiles shown in figure 3.11 left. Temperature, shown in figure 3.11 right, changes slowly under continuous braking. This is an uncontrolled parameter that raises due to energy dissipation, as mentioned in section 3.2.1. Other unintended parameter variations are wheel position and drive train torsion that will be discussed later.

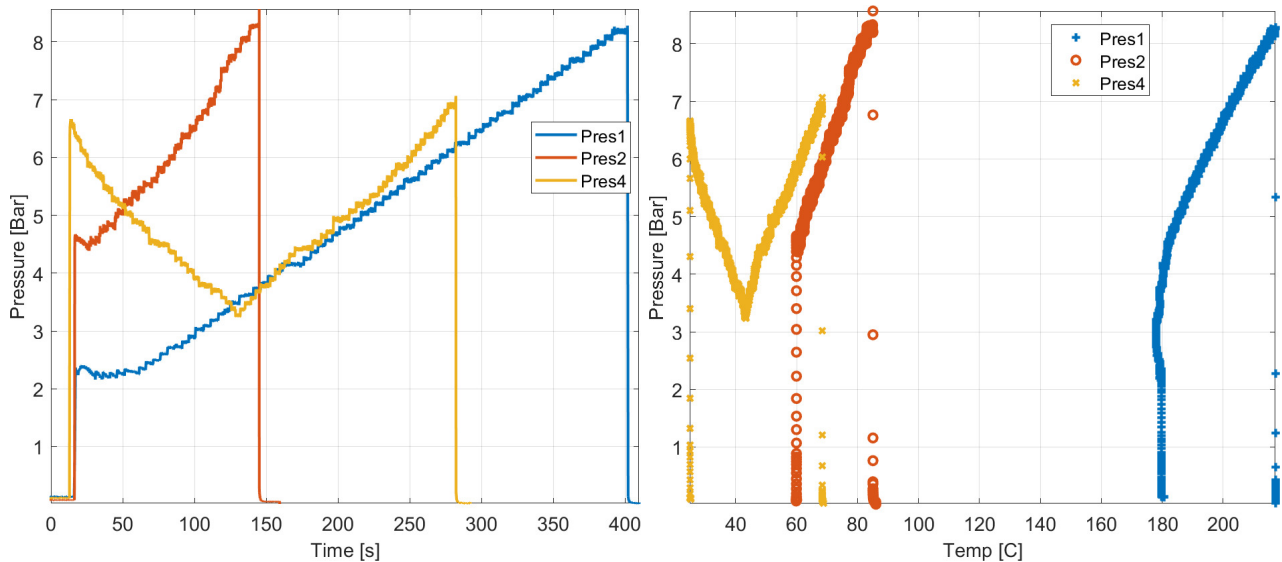


Figure 3.11: Left : measured pressure steps. Right : pressure profiles as a function of induced temperature.

As intended in this experiment, squeals occurs very easily and the gradual pressure change allows tracking of parametric dependence. The first run, labeled **Pres1** in figure 3.11 left, was performed at 6km/h with a pressure increasing from 1.5 to 9bar . The spectrogram in figure 3.12 illustrates at least 3 major operating ranges. Up 100s (3 Bar) an instability occurs near 1560 Hz, with 4 visible harmonics labeled **o1560hi** in the plot. A second instability then develops near 6440 Hz, with both instabilities seeming to coincide for the selected buffer length of 1.5s. Close to 6 bar (280s), another transition occurs and the limit cycle frequency is close to 3 kHz.

The second run **Pres2**, is a partial repeat with slightly different conditions. Wheel speed corresponds to 5km/h and pressure is increased from 4 to 9bar . The focus is on the 3 kHz limit cycle and a transition appears more precisely near 5.5 bar (65s). The question asked in this test is whether **o2710h1** continuously changes to **o3050h1** or if this occurs with a notable change in modal interactions. In other words should this be considered as one squeal occurrence or should different clusters be defined ? The answer that will be given in figures 3.17, 3.18, 3.19 is that three clusters exist.

3.3. TRACKING INFLUENCE OF PRESSURE ON SQUEAL FREQUENCY, AMPLITUDE AND SHAPES

The last run **Pres4** at 5 km/h seeks to study parametric reproducibility, when increasing and decreasing pressure. High amplitude limit cycles are indeed found both when decreasing and reincreasing pressure at similar frequencies. As for the **Pres2** run, transitions between distinct frequencies near 3 kHz. A number of features are of interest: what is constant in the two **o2710h1** occurrences which mostly differ by temperature (continuous increase shown in figure 3.11 right)? Should **o2710h1** and **o2900h1** be considered different? Can we study the interaction between **o2710h2** near 5420 Hz and the **o5200h1** occurrence? Are these two limit cycles occurring at the same time?

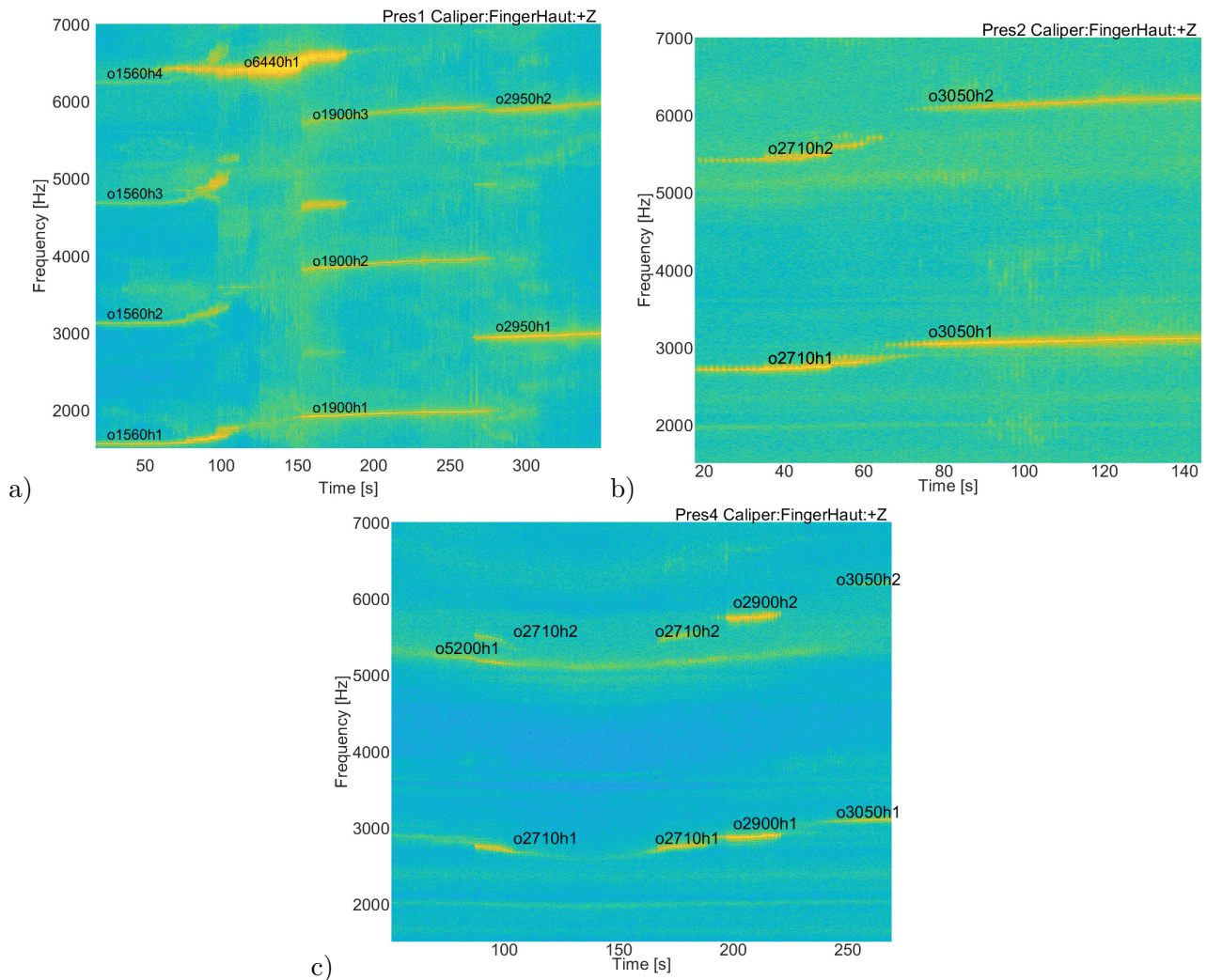


Figure 3.12: Spectrogram using 1 wheel turn buffers of runs a) **Pres1**, b) **Pres2**, c) **Pres4**. Text indicates harmonics of limit cycles that will be discussed later.

3.3.2 Definitions of vibration amplitude and decay rate

The analysis of the functional mode in chapter 1 showed that obtaining an amplitude definition is essential in order to characterize the parametric evolutions of squeal. The question asked in this section is then: how to define a good vibration amplitude for squeal measurements ?

3.3. TRACKING INFLUENCE OF PRESSURE ON SQUEAL FREQUENCY, AMPLITUDE AND SHAPES

Focusing on the fundamental harmonic, the HBV signal model (2.3) provides a common instantaneous frequency $\omega(t_{slow})$ a vector of amplitudes $\{q_1(t_{slow})\}$. If one now considers the results indicating that squeal is contained in a low dimensional subspace [17, 21, 25], it is possible to define amplitude using coordinates associated with principal shapes.

From the complex amplitudes of the first harmonic $\{q_1(t_{slow})\}$, principal real shapes are obtained from the singular value decomposition

$$\begin{bmatrix} Re(\{q_1(t)\}) & Im(\{q_1(t)\}) \end{bmatrix}_{N_S \times (2N_T)} = \sum_j \{u_j\}_{N_S \times 1} \left(\sigma_j \begin{bmatrix} v_{jr}^T(t) & v_{ji}^T(t) \end{bmatrix} \right)_{1 \times 2N_T} \quad (3.1)$$

in which the $\{u_j\}$ are principal shapes constant over the selected time interval, and the singular value and right singular vector can be rewritten as a complex generalized coordinate

$$q_{jR}(t) = \sigma_j (v_{jc}(t) + v_{js}(t)i) \quad (3.2)$$

Note that the phase of this generalized coordinate in (2.14) was used to estimate the instantaneous frequency in the demodulation strategy.

Using the principal shapes $\{u_j\}$ it is also possible to construct a spatial filter that constructs an approximation of the modal coordinates

$$\alpha_j = \{u_j\}^T \{q(t)\}. \quad (3.3)$$

From this modal coordinate it is possible to obtain an estimation of the energy of the modal amplitude signal by

$$E_{mj}(t_{slow}) = \frac{1}{2} \left(\dot{\alpha}_j(t)^2 + \omega_j^2 \alpha_j(t)^2 \right). \quad (3.4)$$

This notion has been used in earlier studies [74, 82] in simulations to describe the amplitude effect on nonlinear systems. Since an energy unit is not directly comparable with the amplitudes extracted using demodulation, it was found useful to introduce a modal amplitude having displacement units as

$$a_{mj}(t_{slow}) = \sqrt{\frac{2E_{mj}(t_{slow})}{\omega_j^2}} = \sqrt{\frac{\dot{\alpha}_j(t)^2}{\omega_j^2} + \alpha_j(t)^2} \quad (3.5)$$

By using either q_{jR} or a_{mj} one obtains a definition of an amplitude using a generalized coordinate seems much more appropriate than the selection of a single reference sensor often considered in nonlinear testing (for example [22, 52, 59]).

In order to illustrate these definitions, figure 3.13 left shows the evolution of the modal coordinates α_j obtained from measurement [Pres2](#) with a band pass filter between 2800 and 3200 Hz. This figure illustrates growth/decay events similar to the ones observed using a single channel in 3.9 right. The figure also shows that the vibration is dominated by the two first principal shapes with the third having a much smaller participation, confirming the idea that squeal can be represented in a low dimensional subspace.

Then, figure 3.13 right compares the amplitudes q_{jR} obtained from (3.2) and a_{mj} obtained from (3.5). Both coincide quite well and the a_{mj} is shown to be a slow varying property even when kinetic $\dot{\alpha}_j(t)^2$ and strain energies $\omega_j^2 \alpha_j(t)^2$ oscillate rapidly.

3.3. TRACKING INFLUENCE OF PRESSURE ON SQUEAL FREQUENCY, AMPLITUDE AND SHAPES

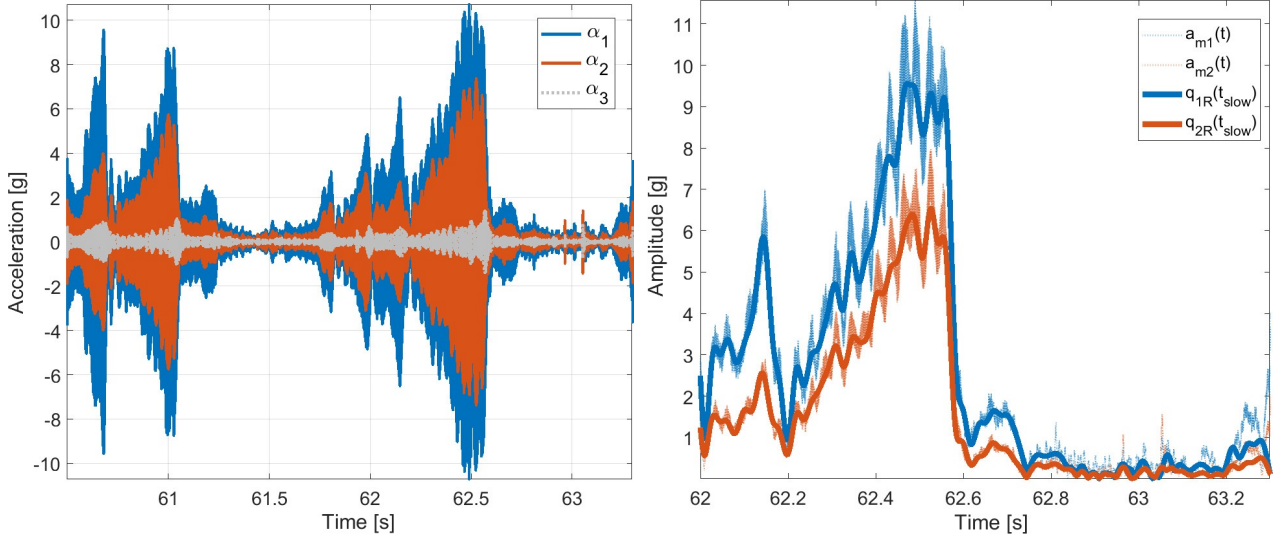


Figure 3.13: Left : Acceleration associated with the first 3 singular vectors $\alpha_j(t)$ obtained by band-pass and spatial filtering. Right : Generalized amplitudes associated with the first 2 singular vectors obtained from demodulation q_{jR} and obtained by band-pass and spatial filtering a_{mj} .

Using the extracted generalized amplitudes it is possible to better analyze the growth events. Figure 3.14 left shows the growth events between 60 and 65s in a log scale. By using this representation we seek to compare the growth and decay events with the expected behavior of a linearized system. In the Linear Time Invariant (LTI) complex mode analysis, the growth/decay of system vibrations are described by a series of poles λ . For lightly damped poles, vibration amplitude changes with $e^{Re(\lambda)t}$, growth and decay being indicated by the sign of $Re(\lambda)$ (the real part of λ) being positive and negative respectively. Just like for the functional model in (1.21), one defines a decay rate that would correspond to the positive damping ratio in the case of linear time invariant system as

$$\hat{\zeta}(A, t) = \frac{-1}{\omega} \frac{d}{dt} (\log(A(t))) \quad (3.6)$$

While noise and the 30 Hz modulation make the interpretation difficult, the figure seems to indicate that these growth and decay events measured show a behavior that can be represented by the poles of a LTI system. Looking at the growth between 62.2 and 62.6 s for a limit cycle around 3 kHz the corresponding negative damping ratio is $\hat{\zeta} = -0.03\%$, a small and realistic value. The following decay from 9g to 2g in 0.032s corresponds to $\hat{\zeta} = 1.7\%$ which again is a value quite usual for brakes.

3.3. TRACKING INFLUENCE OF PRESSURE ON SQUEAL FREQUENCY, AMPLITUDE AND SHAPES

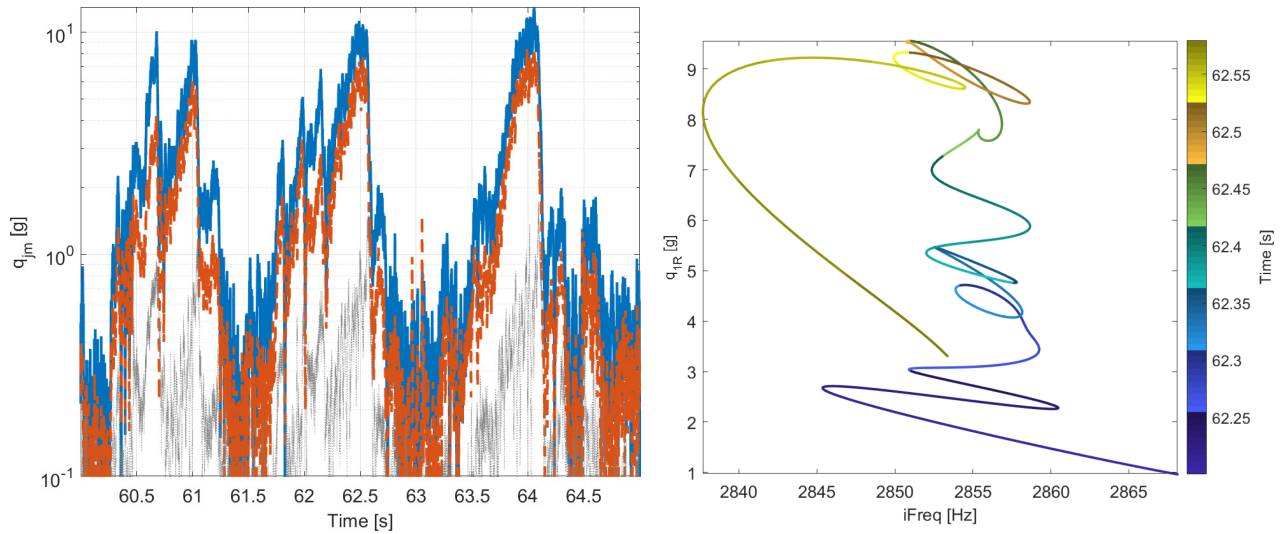


Figure 3.14: Left : intermittent growth events of the first three principal amplitudes. Right : amplitude associated to the first singular vector q_{1R} as a function of frequency (time shown as color).

Another interesting observation can be made when looking simultaneously at the evolution of amplitude and instantaneous frequency, illustrated in figure 3.14 right. This figure shows the growth event that occurs around the 62.5s mark, where it is possible to see that amplitude increases around 2855Hz (despite the oscillation is due to the torsion mode which changes loading of the in-plane pad contacts). After reaching the maximum amplitude the instantaneous frequency quickly decreases below 2840Hz and as amplitude starts decaying with the frequency going up again back to near 2855Hz. This confirms that it is possible to obtain a comparison between the measured behavior and the poles obtained in simulation, again similar to what is done for the functional model in 1.4 which could lead to a better understanding of the squal mechanisms. However, since simulations of full scale industrial models are beyond the scope of this project, the extracted growth rates are not compared with the poles of a linearized model.

Much better results were obtained using the 2024 test which does not present torque oscillations. Take the measurement shown in figure 3.15 Left as an example. The spectrogram shows that as pressure evolves the squal frequency drops with two regions showing intermittent behavior at the beginning and the end of the measurement. The presence of intermittent squal shows that the system is in a state where the parametric variations induced by the wheel rotation are sufficient to transition the system to/from instability. Figure 3.15 Right shows an experimental root locus giving decay rate as a function of instant frequency. The transitions to or from low amplitude regions, intermittent behavior, occur with frequency and decay rate coupling forming two crescent (or "c" shape). This coupling corresponds to what was seen for the functional model in frequency (figure 1.6) and time (figure 1.15) analyzes. At high amplitudes the rate of amplitude change is small, and the decay rate remains close to zero.

3.3. TRACKING INFLUENCE OF PRESSURE ON SQUEAL FREQUENCY, AMPLITUDE AND SHAPES

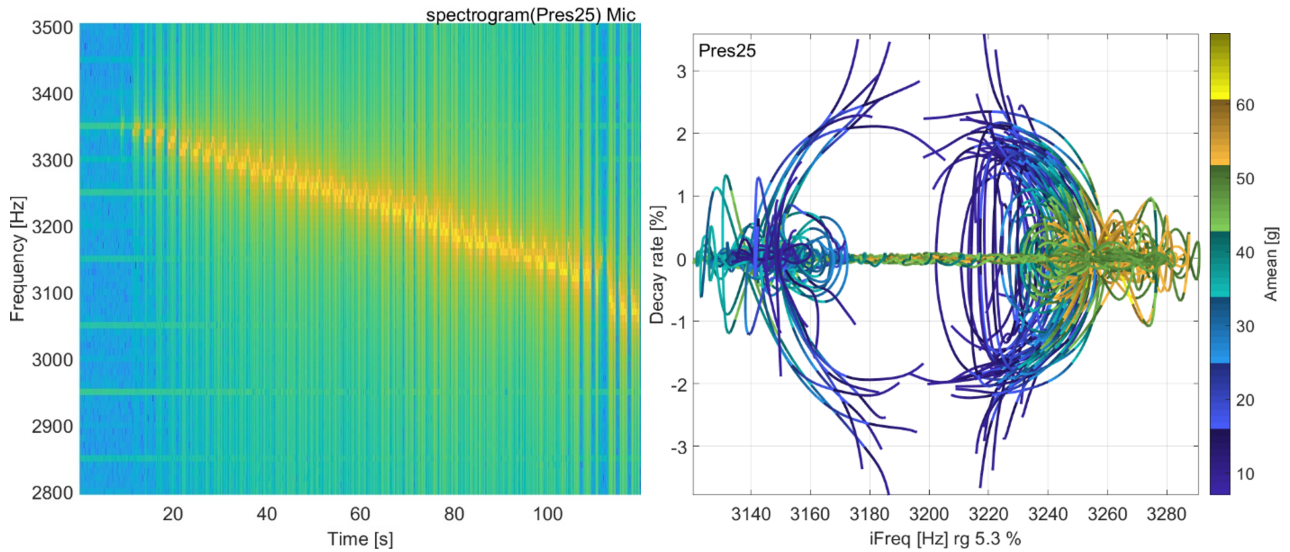


Figure 3.15: Left: Spectrogram of a squeal measurement under stepped pressure on the 2024 setup. Right: Decay rate versus instant frequency (experimental root locus)

3.3.3 Tracking/clustering squeal occurrences for a stepped pressure evolution

As mentioned in the last section, the HBV signal model (2.3) provides an instantaneous frequency $\omega(t_{slow})$ a vector of amplitudes $\{q_1(t_{slow})\}$ at each sensor. This means that, on top of analyzing the global amplitude (q_{1R}) as in the previous section, one could use this additional information to cluster squeal occurrences.

The first technique used to create clusters from a parametric pressure experiment focuses on frequencies and amplitudes. Since distinct frequencies imply different wavelength and thus shapes, tracking the fundamental frequency of a squeal vibration provides insight on the effects of different parameters.

Figure 3.16 left, shows a frequency zoom of the 1.5s buffer spectrogram of the `Pres2` run illustrated in 3.12b. In the spectrogram, there are three distinct high amplitude clusters that slowly evolve with pressure. The HBV signal generates a common frequency to all sensors, as shown in figure 3.16 center, but combined with the global amplitude shown through color and transparency also allows distinction of three clusters (noted A,B and C). Plotting the global amplitude as a function of instant frequency makes the clusters appear as peaks in figure 3.16 right, the addition of pressure as color correlates the clusters with the parametric evolution.

3.3. TRACKING INFLUENCE OF PRESSURE ON SQUEAL FREQUENCY, AMPLITUDE AND SHAPES

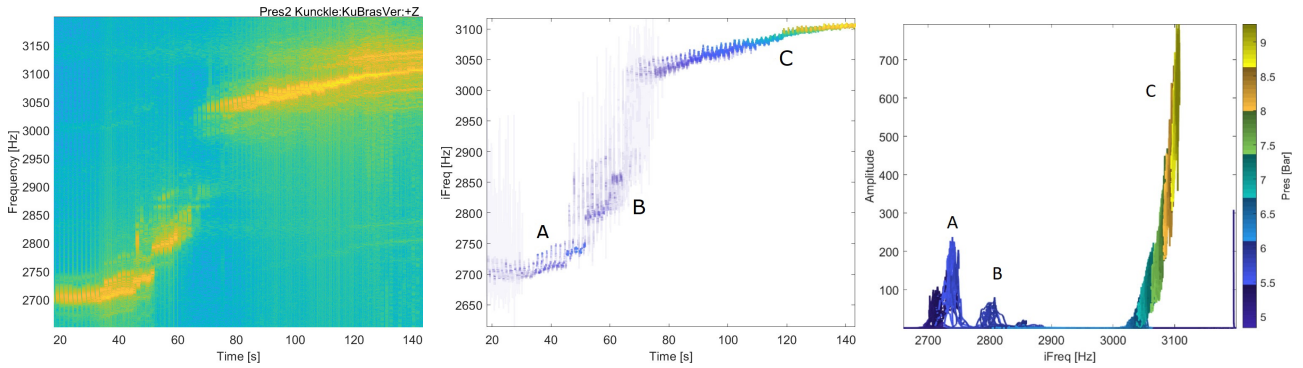


Figure 3.16: Left : spectrogram for run `pres2` for full test. Center: instant frequency over time with amplitude coded as color and transparency. Right: amplitude over instant frequency with applied pressure as color.

This attempt at clustering by amplitude and frequency, does not take shape into account. In order to include the slow variation of shape described in the HBV signal model (2.3), figure 3.17 right shows the evolution of the generalized amplitudes q_{jR} associated with the first three principal shapes in (3.1). The amplitudes associated with the remaining principal shapes are relatively small and are not taken into account.

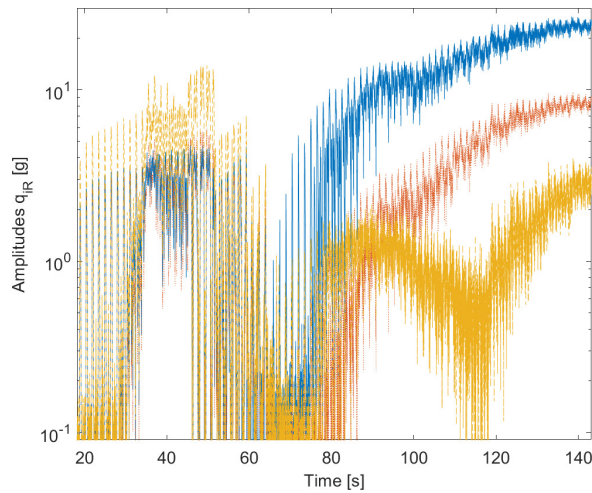


Figure 3.17: Evolution of the generalized amplitudes q_{jR} associated with the first three principal shapes for the `pres2` measurement.

The first (and thus predominant) coordinate shown in figure 3.17 is always large when squeal occurs, this tells that the considered sensor group always sees a common shape. The second and third coordinates have a notably different ratio in different instants. Below 70s both coordinates are mostly equal and of similar value to the first, while above 100s coordinate 1 is larger than 2 that is larger than 3.

In terms of parametric sensitivity, the interpretation is that different real modes get involved at

3.3. TRACKING INFLUENCE OF PRESSURE ON SQUEAL FREQUENCY, AMPLITUDE AND SHAPES

low pressures (before 70s) than high pressures and this is a sensitivity that a FEM model should reproduce to allow detailed design. Additionally, the fact that there are three principal shapes with a significant amplitude level shows an interesting comparison with figure 3.14 left where there are only two shapes with a predominant effect. Since both analyses are made in using the `pres2` measurement, it shows that changing the time window used to construct the principal shapes may affect them if the parametric effects on vibration shapes are sufficiently large.

Reading of figure 3.17 right is difficult since amplitudes change a lot with time. This difficulty is accentuated in the region between 60s and 80s, where squeal is intermittent.

It thus seems desirable to introduce an amplitude independent shape comparison. The correlation coefficient, known as Modal Assurance Criterion (MAC) in the vibration community, serves that purpose. Figure 3.18 illustrates the proposed use of the MAC. Snapshots of three instants corresponding to apparently distinct occurrences are handpicked in run `pres4` and shown as markers in the spectrogram. Shape correlation with these handpicked instants is then computed as a function of time leading to the MAC curves shown right. Distinct areas where the shape is well correlated with the handpicked instant are clearly visible and displayed in the color band shown at the bottom of the spectrogram. This confirms that the same predominant shapes are found for decreasing pressure (before 140s, see figure 3.11) and increasing pressure (after 140s). Note that the 30 Hz torsion modulation induces notable shape fluctuations, so a low pass filter was applied to the shapes before constructing the curves on figure 3.18 right.

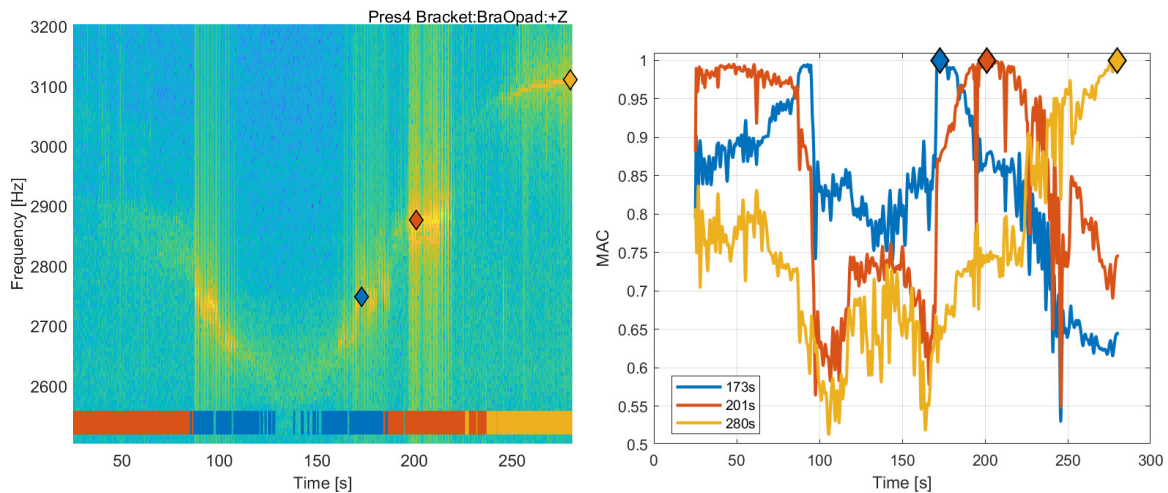


Figure 3.18: Left: spectrogram of `pres4` test focusing of the limit cycle. Right : MAC with respect to shape at picked instants indicated by diamond marker.

To emphasize that the parametric characterization of squeal is essentially met, figure 3.19 comes back to the tests `pres4` and `pres2` that were meant as repetitions of a similar pressure range. Representing the frequency/amplitude dependence of the first generalized coordinate using a log scale and performing low pass filtering of the raw results to highlight the intended slow variations, while ignoring the fluctuations induced by torsion and wheel spin, figure 3.19 shows that limit cycle frequency and amplitude are very correlated with pressures. The very good overlay of results with decreasing and

3.3. TRACKING INFLUENCE OF PRESSURE ON SQUEAL FREQUENCY, AMPLITUDE AND SHAPES

increasing pressure in `pres4` are remarkable. Squeal occurrences appear as peaks, but the transition is continuous. This is compatible with the shape criterion show in figure 3.18 and points to the fact that setting thresholds is necessarily in the classification into clusters of a continuously varying parametric system.

The ability to track limit cycles with nearly 3 orders of magnitude in amplitude is an important result. The first 80s of the `pres4` test would typically be considered a non-squeal condition and the fact that tracking was possible leads to think that parametric testing in non-squeal conditions has a real future. The present campaign considered a very noisy brake without the usual noise reduction treatments, when these are present tracking will be more difficult.

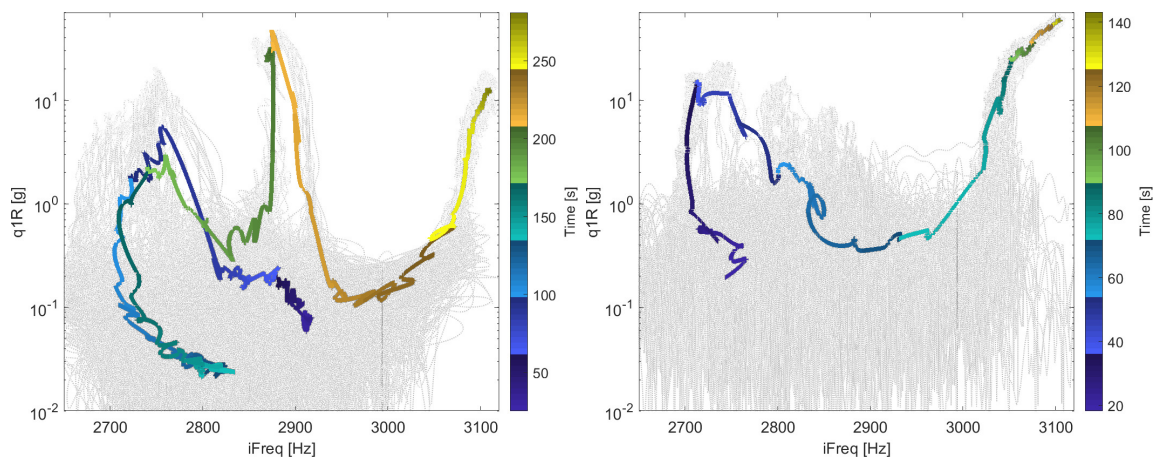


Figure 3.19: Frequency amplitude tracking. Dotted line raw, colored line low pass filtered. Left : `pres4` test. Right : `pres2`

The reproducibility between the two tests, shown with the same scales, is quite good but not perfect. The 2750 and 3100 Hz occurrences have similar frequency/amplitude dependence for varying pressure. The 2900 Hz occurrence seems to be more sensitive to an uncontrolled parameter. This point to the difficulty that will remain of controlling all factors influencing squeal occurrences.

The comparison between the raw and the filtered data gives an important quantification of non-reducible variability. The torsion loading was reduced in 2024, by using another test bench. The variability due to wheel position will always be present, but measuring distances between disk and caliper, as in figure 3.2, showed that geometric effects are likely to be the source of these variations. These geometric effects are also probably the source of intermittent squeal situations. These situations are particularly interesting as the system is sufficiently modified to transition between stable and unstable configurations.

Using the proposed technique one is even able to distinguish two squeal occurrences near each other. This is illustrated in figure 3.20 by showing the presence of two intermittent growth events with distinct frequencies within the same wheel revolution. Using a slow time bandwidth set too low (or a long buffer window), the two events would seem to coincide.

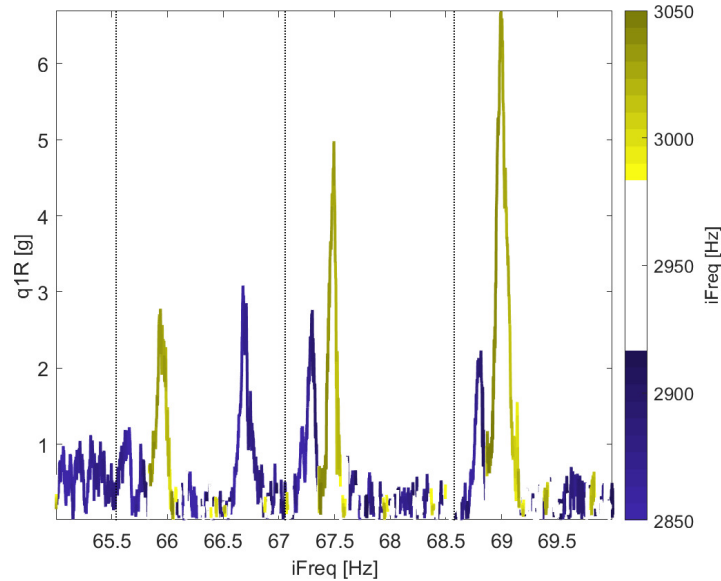


Figure 3.20: Amplitude q_{1R} evolution showing intermittent squeal with instant frequency as color.

3.4 Parametric EMA in operating condition

3.4.1 Motivation for EMA in operating condition

Extracting modal response of a brake system in operating condition (under braking) is a challenge in itself due to the numerous uncontrolled parametric variations and intense background noise. A first attempt to characterize the response of a brake system in static condition (with the wheel rotation blocked) illustrated in figure 3.21, shows strong sensitivity to pressure but poor reproducibility. Measurements in sliding condition (under braking with wheel rotation) show a better reproducibility, but pressure sensitivity was not studied, and the configuration was far from squeal.

3.4. PARAMETRIC EMA IN OPERATING CONDITION

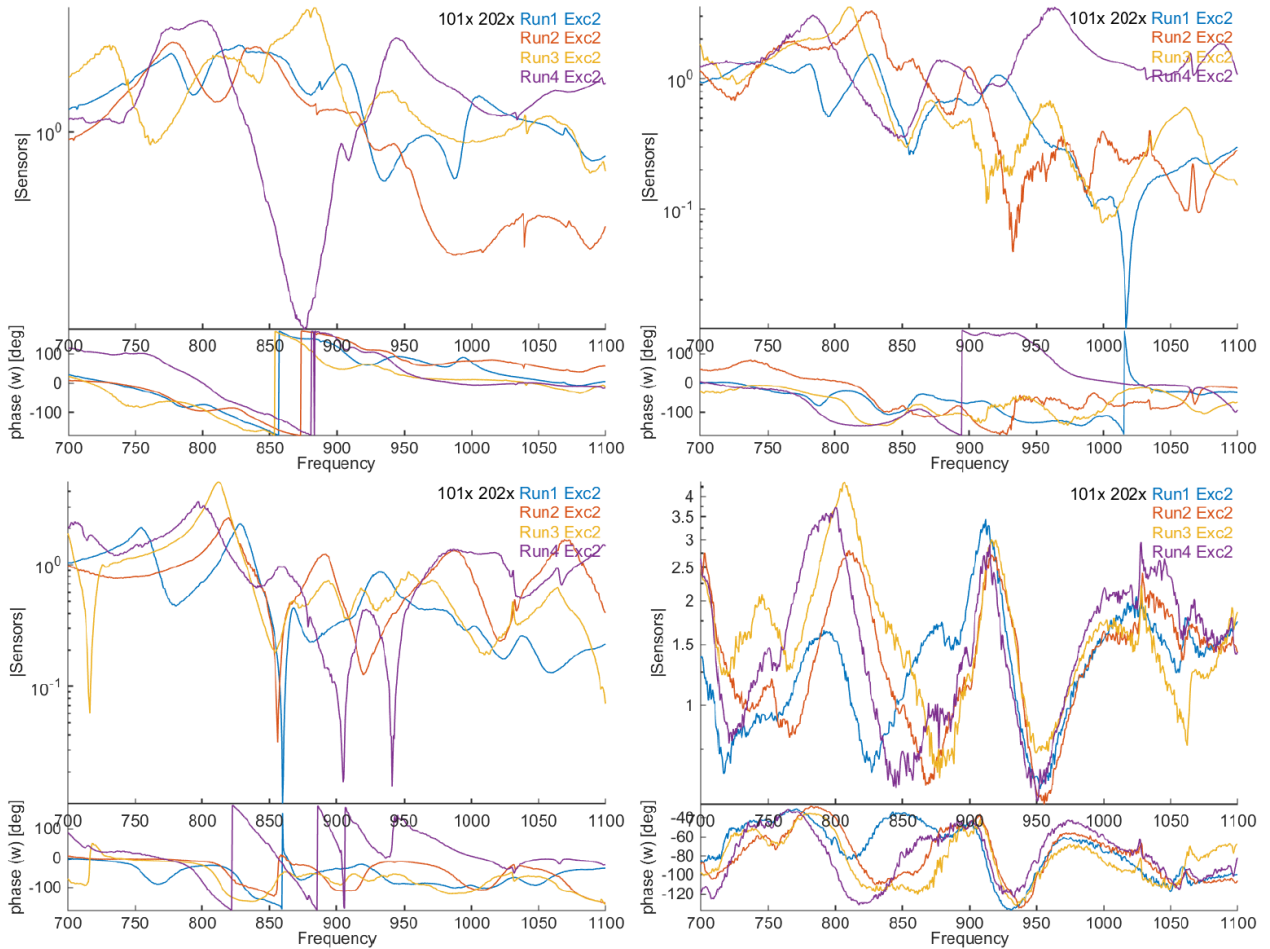


Figure 3.21: Reproducibility of transfer function obtained from measurements in different conditions: Static with 0 Nm torque (top left) static with 100Nm torque (top right) static with 200Nm torque (bottom left) and sliding (bottom right). Extracted from [17]

Thus, in order to obtain a characterization of the system evolution near squeal, this section describes a parametric experimental modal analysis performed in operating (sliding) condition.

As mentioned in section 3.2.2, an electrodynamic shaker is attached to the system for excitation. A swept sine input is used to characterize the system behavior around the expected squeal frequencies at different pressure levels. Seeing that in the runs [pres2](#) and [pres4](#) from section 3.3 squeal happens around 3000Hz, the excitation band used goes from 2500 to 3500 Hz in 2s.

Using sine sweep instead of other excitation provides a good signal-to-noise ratio in the presence of strong background noise. Additionally, by having the excitation passing by each frequency only once we are able to avoid averaging the effect of uncontrollable parameter variations such as the wheel spin. While it is not possible to ensure that the system is exactly the same at the beginning and end of sweep, the system will be approximately the same for neighboring frequencies.

The spectrogram of the applied load can be seen in figure 3.22 together with the evolution of applied pressure. In addition to the diagonal lines of the sweep excitation, one can notice the presence

3.4. PARAMETRIC EMA IN OPERATING CONDITION

of three unexpected patches in the force signal. These patches appear at the same moments and frequencies, where squeal appears, which indicates that at those frequencies the force exerted by the squeal vibration on the shaker is greater than the force the shaker exerts on the system. This combination of effects increases the difficulty of analyzing the measurement since in nonlinear systems the response to a sum of loads is not necessarily the sum of the individual responses to each of these loads.

The gray areas in figure 3.22 indicates the regions where squeal is present over the applied pressure profile. The first region at a higher pressure corresponds to the squeal occurrence near 3100Hz. The second and third regions show that the two occurrences around 2900Hz happen at similar pressure ranges. Dots in figure 3.22 indicate the pressure points used for identification in section 3.4.3, their choice will be detailed later.

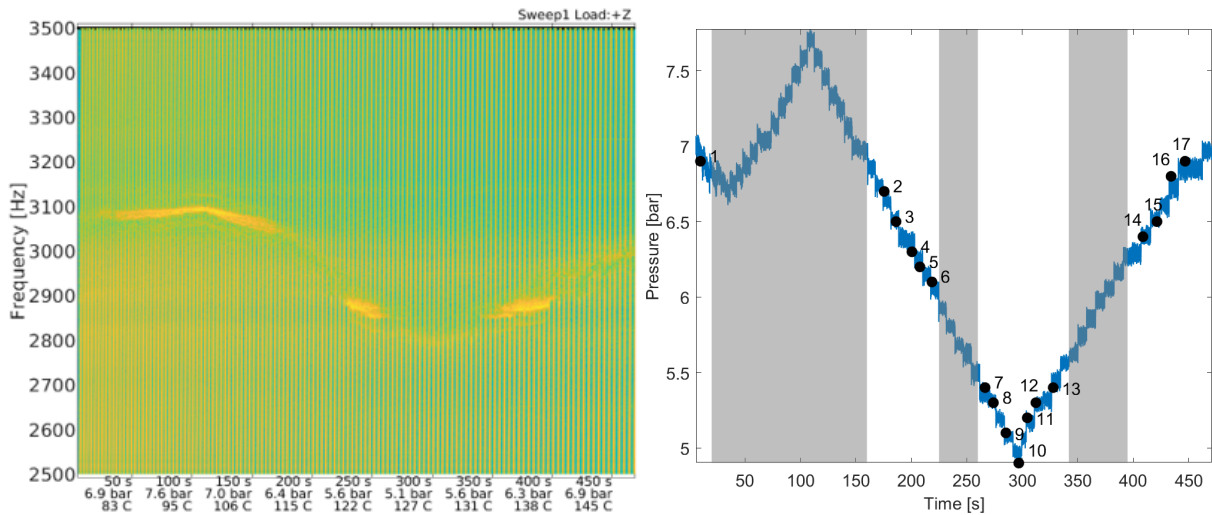


Figure 3.22: Left: spectrogram of the applied load in the parametric sweep test over the entire measurement with indications of pressure and temperature. Right: Evolution of the applied pressure with indication of high amplitude squeal areas (gray areas) and selected pressure points for identification in section 3.4.3 (dots).

3.4.2 Transfer function estimation and coherence analysis

Let us now take a look at the response to this excitation on a fixed accelerometer in figure 3.23 with a particular focus on the beginning of the measurement. Figure 3.23 left shows the first 100s of the measurement with an increased frequency range. We can clearly see the diagonal lines representing the sweep response and the progressive formation of squeal at 3100Hz as pressure evolves.

As in the first 30s of figure 3.23 squeal is not present, the first analysis of the response will be focused on this area. Despite the fact that squeal has low amplitude, it is possible to see an horizontal line, where the squeal will form. One possible explanation for this is that the mode that will become unstable in the squeal has a low damping under these conditions, and its response stands above the noise floor.

3.4. PARAMETRIC EMA IN OPERATING CONDITION

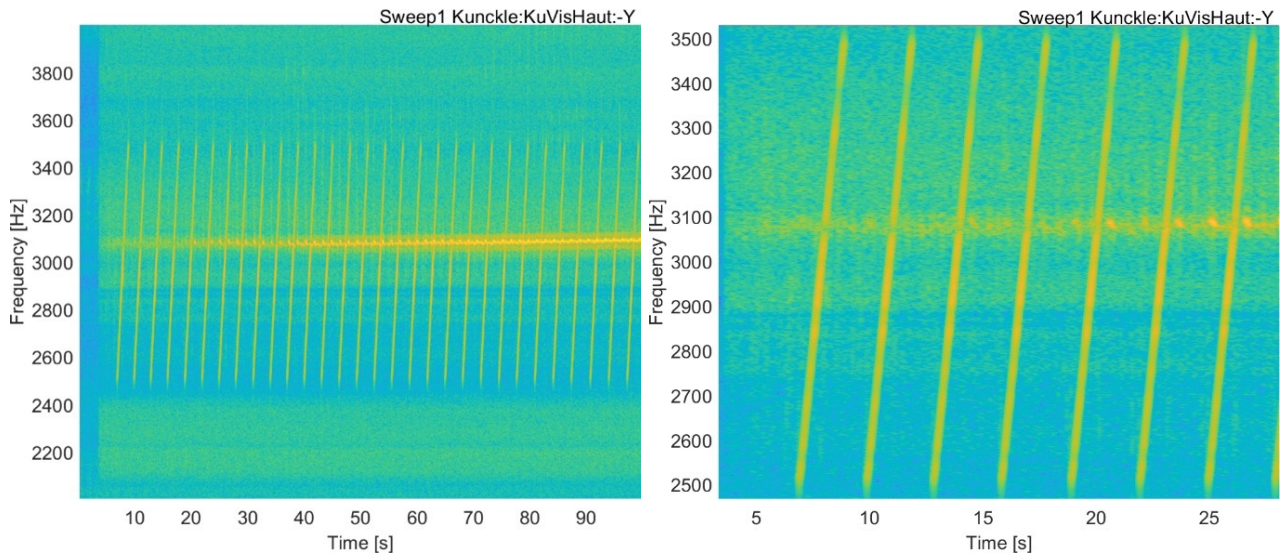


Figure 3.23: Spectrogram of the acceleration measured in the brake knuckle. Left: first 100s wide frequency view. Right: first 30s focused frequency view.

Transfer functions corresponding to the three chosen time windows (starting at 6.89, 9.88 and 21.92s) are first analyzed. The transfer functions are constructed using a simple H1 estimator [68] with a Hanning window around each sweep event. Without averaging, the transfer functions shown in figure 3.24 are quite noisy.

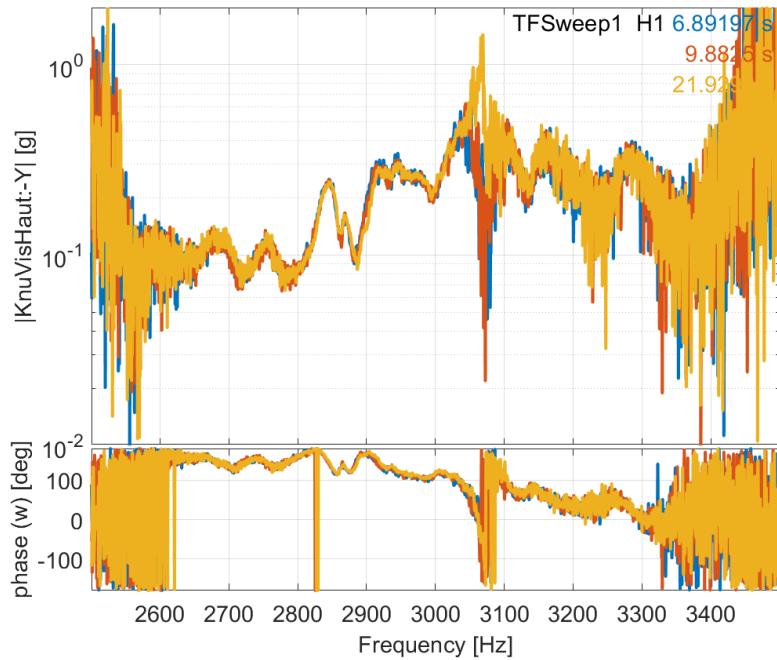


Figure 3.24: H1 Transfer function describing the response to the sweep excitation constructed using windows starting at 6.89, 9.88 and 21.92s.

3.4. PARAMETRIC EMA IN OPERATING CONDITION

Averaging multiple measurements is the usual solution to reduce the effect of uncorrelated noise in a transfer function. Averaging different sweeps is not adapted to our application since it is expected that uncontrolled parameter variations will change the system slightly between each application of the sweep excitation. Averaging thus was performed using a 0.833s window with 90% overlap (15 total windows over 2s). Figure 3.25 left shows that the transfer functions obtained are significantly less noisy than those obtained in figure 3.24. Sliding windows are however normally used for broadband excitation covering the whole spectrum, and their validity for sweep inputs needs further study. Demodulation was also considered but is not detailed due to time constraints.

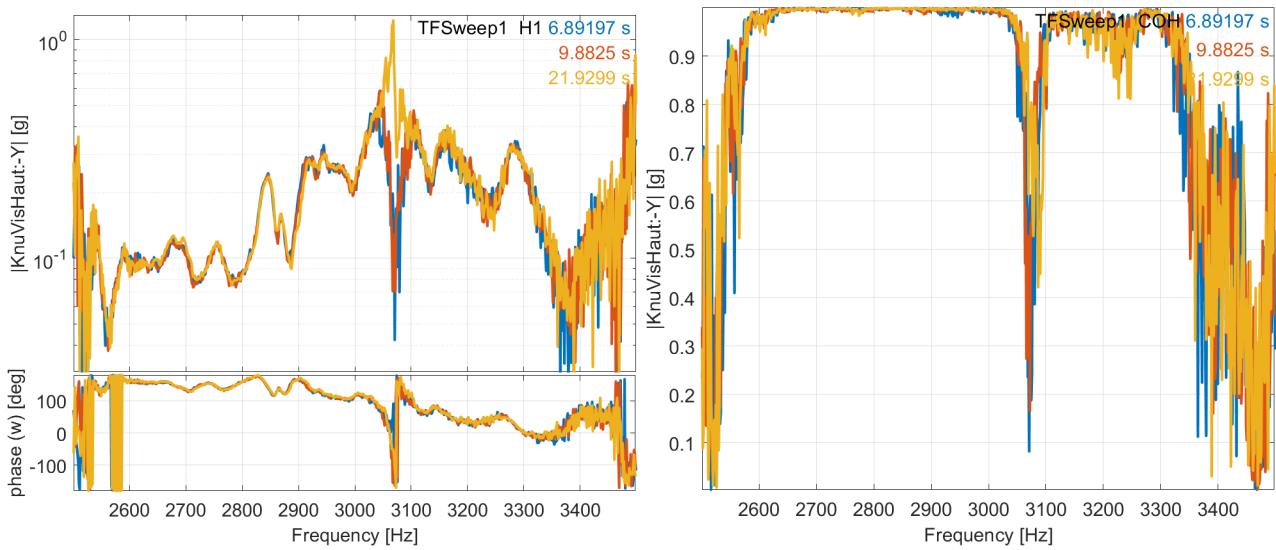


Figure 3.25: Response to a sweep excitation at an accelerometer placed in the brake knuckle. Left: Transfer function constructed using H1 averaged sliding windows starting at 6.89, 9.88 and 21.92s. Right: Corresponding coherence values.

The first two sweeps with start at 6.89 and 9.88s happen at the same pressure (7 bar) very close in time to each another. The close resemblance confirms that a good consistence can be achieved in the measurement of transfer functions in operating condition.

One then compares these two transfer functions to that 6.8 bar (starting at 21.92s). For the most part the transfer function remains unchanged. Differences are concentrated on the two peaks near 3100Hz, where squeal appears later. These two peaks get closer to each other resembling a pair of modes that starts to get coupled. However when looking at the coherence value in figure 3.25 right, we notice a large drop at the frequencies where the squeal will be formed. The loss of coherence makes it difficult to affirm with clear confidence that the two peaks observed are in fact a pair of modes that is getting coupled. Nevertheless, it is possible to conclude that there is a change in the system behavior in the frequency band where squeal will occur.

Seeing that a good overall idea of the system behavior can be obtained using H1 averaged sliding windows, we turn ourselves to larger parameter variations. In the applied load (figure 3.22) it is possible to see two different squeal frequencies with a transition phase between them. With this in mind figure 3.26 shows the transfer function for a sweep applied in the first squeal region (100s 7.6 bar) between squeals (200s 6.3 bar) and in the second squeal region (240s 5.6 bar). The transfer

3.4. PARAMETRIC EMA IN OPERATING CONDITION

functions are constructed using the same H1 averaged sliding windows as the ones from figure 3.25 (0.833s window and 90% overlap), this time looking at the drive point accelerometer response.

In the resulting transfer functions it is possible to see a main peak that moves left as time evolves, following the change in squeal frequency that can be seen in figure 3.22. In the two cases where squeal is present, the peak frequency from the transfer function matches closely the squeal frequency. Additionally, it is noticeable that modes away from squeal are not sensitive to the changes in applied pressure.

Looking at the phase values in the blue and yellow curves (where squeal is present) it is possible to see that near the main peak frequency (around 3100 and 2970Hz respectively) the phase value becomes zero. The reason behind it can be clearly seen when looking at the applied load spectrogram 3.22, in the presence of squeal the vibration reaches a level where the force applied by the system to the shaker is predominant over the force applied by the shaker. The vibration being in phase with the load can then be explained by the fact that it is the vibration that applies a force to the shaker in squeal condition.

The coherence values shown in figure 3.26 right shows that the loss of coherence follows the main peak of the transfer function. In addition to left shift, the coherence drop have a smaller value in the case without squeal than in the two cases with squeal. This highlights the coherence as a possible source of key information about the evolution of instability and presence of squeal.

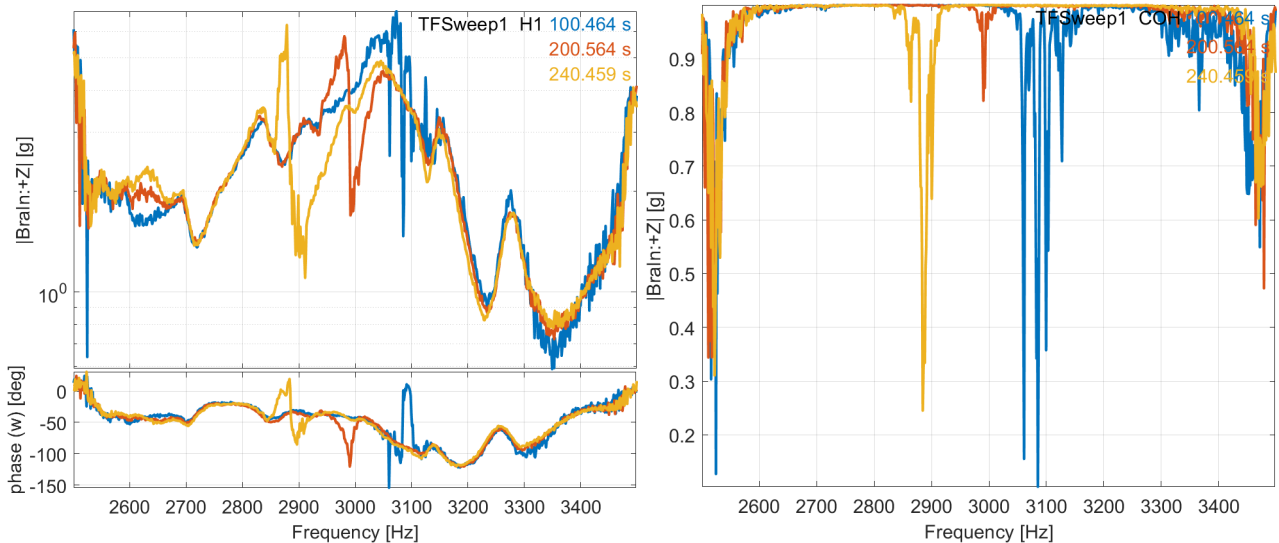


Figure 3.26: Response to a sweep excitation at the drive point accelerometer. Left: Transfer function constructed using H1 averaged sliding windows starting at 100, 200 and 240s. Right: Corresponding coherence values.

Having noted that the coherence drops are closely related to the presence of squeal figure 3.27 takes a look at the evolution of coherence drops over the entire measurement for the two accelerometers considered in figures 3.24 and 3.25. The coherence in this case is constructed using a total of 10 sliding windows with 4s buffer length and 50% overlap (totaling 22s) which smoothes results and avoids problems at sweep transitions. An interesting trend can be seen in the coherence drop shown in both figure 3.27 left and right. In both cases the coherence drops (in red/green) near the squeal

3.4. PARAMETRIC EMA IN OPERATING CONDITION

regions seen in 3.22 and show a continuous variation following the pressure evolution. On the squeal regions however we notice a near perfect correlation (deep blue) between force and vibration, once again related to the fact that vibration is forcing the shaker. The coherence in 3.27 left show two additional drop regions near 2650Hz and 3400Hz that are not present in the drive point accelerometer coherence, possibly showing the effect of other nonlinearities.

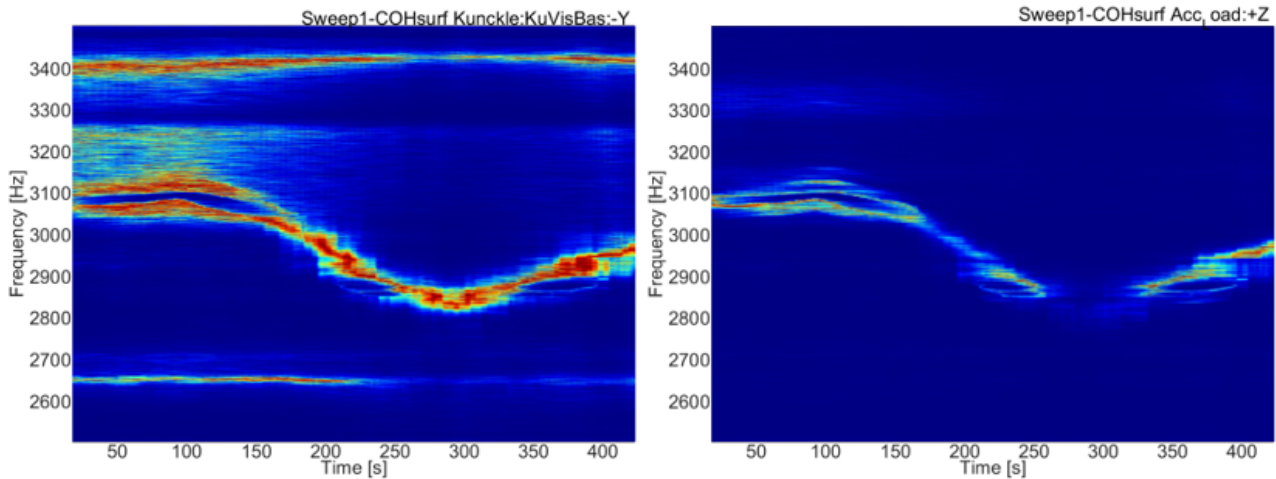


Figure 3.27: Coherence drops computed using a sliding window for the acceleration response measured at the brake knuckle (left) and drive point (right)

Figure 3.27 shows that, through the coherence drops, it is possible to track squeal occurrences before the formation of a limit cycle. This result is particularly interesting as, in a near final brake design, finding a good set of operating conditions to consistently reproduce squeal can be a lengthy process. Using the coherence as an indicator of proximity to squeal, offers the potential to speed up this process.

3.4.3 Identification of poles for selected pressure values

Now that we have discussed some characteristics of the test, let us look into the identification of the obtained transfer functions. In the regions where squeal is present, the superposition between limit cycle and the sweep response have shown to be of difficult interpretation. One of the reasons for this is the vibration inducing a force on the shaker as seen in figure 3.22.

Thus, in order to avoid the possible problems introduced by this superposition of limit cycle and excitation, the identification analysis is restricted to the transfer functions on the regions where squeal is not present. A total of 17 handpicked sweep events in the zones without squeal to identify. The chosen instants are shown in figure 3.28 with respect to the applied pressure profile. The chosen pressure points cover all stable regions of the test and showcase the applied pressure profile.

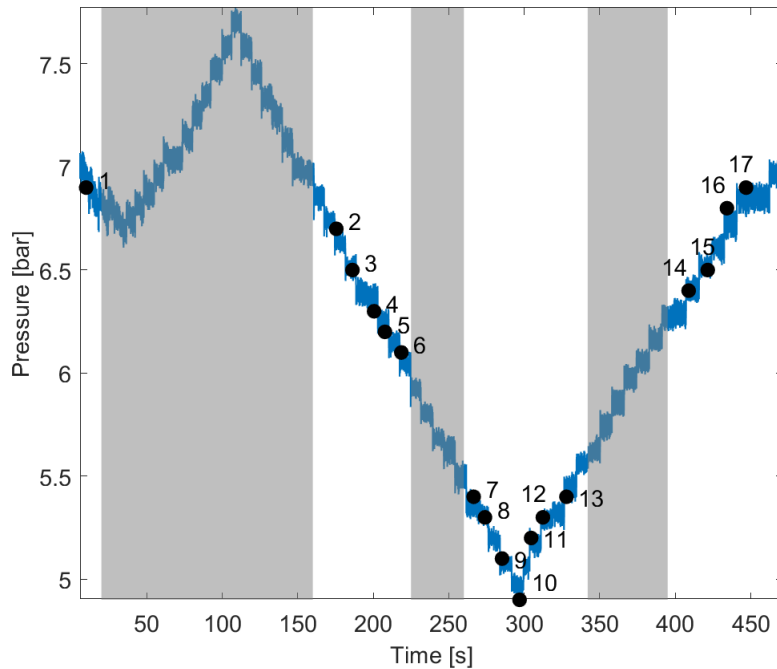


Figure 3.28: Selected pressure points for identification (dots) overlapped with the applied pressure profile (blue). Gray areas indicate high squeal levels.

As in the preliminary analysis, one can analyze parametric effects by superposing transfers associated with different pressures. The superposition for the selected sweep events is shown in figure 3.29. This figure shows that some modes are not very sensitive to pressure variations, most notably those above 3050Hz. The modes below 2900Hz form two groups with different characteristics. The main difficulty of the analysis is on the behavior between 2900 and 3050HZ, where it is difficult to observe any sort of clear trend.

3.4. PARAMETRIC EMA IN OPERATING CONDITION

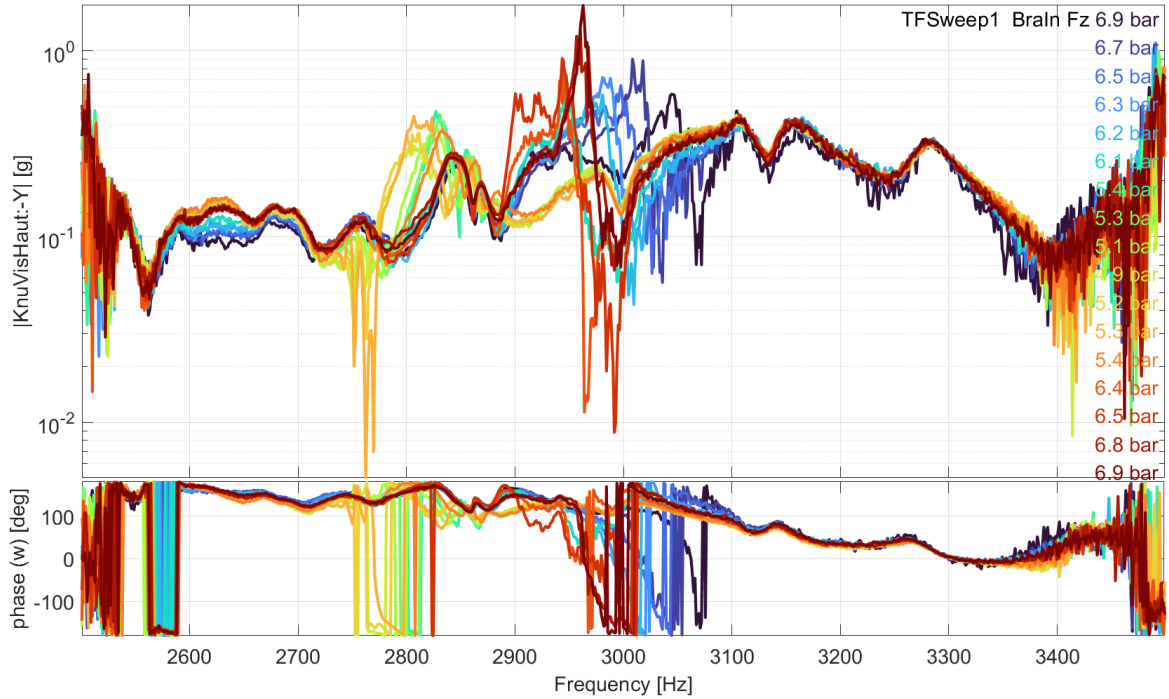


Figure 3.29: Superposition of the transfer functions describing the system response for the selected sweep events indicated in figure 3.28

Two main factors affect our capability of visualizing a sense of progression in figure 3.29: the two senses of pressure variation and the jumps when crossing a squeal occurrence. In order to counter these effects, we divide the analysis into groups of transfer functions that show a monotonic pressure evolution and are not separated by a squeal occurrence. These groups are listed in table 3.1 using the indexes from figure 3.28 and the applied pressure values.

Table 3.1: Groups of sweep events selected for a more detailed analysis

Group	Sweep event indexes	Pressure [bar]
1	2, 3, 4, 5, 6	6.7, 6.5, 6.3, 6.2, 6.1
2	7, 8, 9, 10	5.4, 5.3, 5.1, 4.9
3	14, 15, 16, 17	6.4, 6.5, 6.8, 6.9

The first group of transfer function, shown in figure 3.30, contains the five selected sweeps between the first two squeal occurrences. The peaks, not in the central gray area, between 2900Hz and 3050Hz, are not very sensitive to the pressure variation. In the squeal area in gray, a left shift tendency can be clearly seen as pressure drops. This shifting peak moves between the two squeal occurrences seen in figure 3.22 near 3050Hz for 6.7 bar and near 2900Hz for 6.1 bar. As before, the coherence loss makes analysis of peaks difficult.

3.4. PARAMETRIC EMA IN OPERATING CONDITION

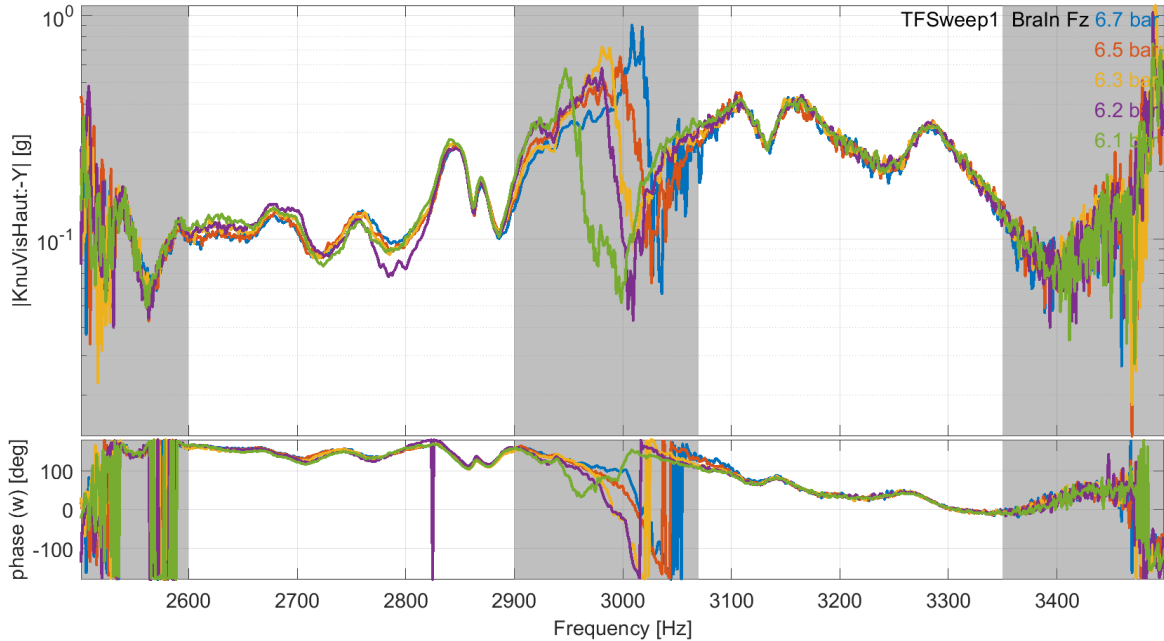


Figure 3.30: Superposition of the transfer functions describing the system response for the selected sweep events of group 1. Gray areas indicate regions where low coherence was detected in at least one measurement.

The system poles are then obtained for each pressure using the modal identification interface from the SDT toolbox [54]. Identification for each pressure was performed by successively applying a local single pole identification algorithm. This algorithm estimates each poles in a narrowband around its corresponding resonance peak. Then, shapes are estimated by fitting a pole-residue model with residual terms in the local bands around each pole.

A couple of different factors make this not a very simple identification. The most notable source of difficulty in this analysis is the presence of contact-friction internal nonlinear forces. These internal forces act as a secondary source of energy and cause the loss of coherence observed previously in figure 3.27. Similar types of problems have been noted in Operational Modal Analysis (OMA) studies of rotating machines, where a combination of random and periodic sources are observed. In the case of [61], an Extended Kalman Filter (EKF) was used to remove the periodic components leaving only the stochastic one. Applying this strategy to the considered modal analysis measurements is not straightforward. The main reason for this being that since a sweep excitation was used both sources are (quasi-)periodic, making it not possible to clearly differentiate them by nature. While an OMA could be a solution, the internal source of energy being about at the same frequencies as the target modes may pose an additional challenge.

The identification difficulties extend to the optimization of pole placement, notably on the regions where coherence drops are observed. Optimization required careful user input in restricting the optimization to a small number of poles at a time, sometimes even to a single pole at a time. As a result optimization of poles using either a gradient based or the IDRC algorithm [54, 83, 84] was a lengthy process. Applying the lengthy optimization to some of the selected transfer functions also showed that the overall results are fundamentally the same as without.

3.4. PARAMETRIC EMA IN OPERATING CONDITION

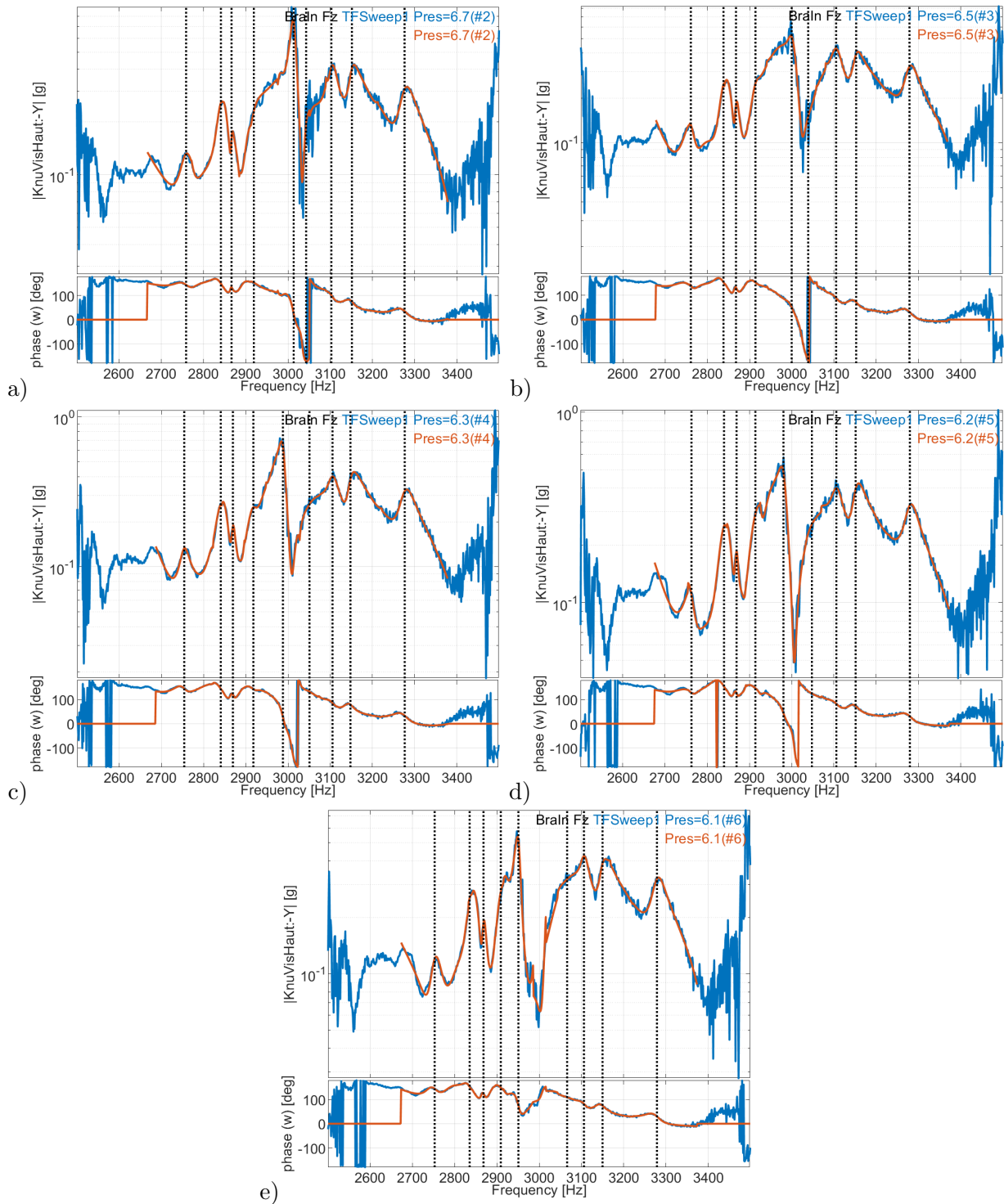


Figure 3.31: Comparison between the measured transfer functions and the ones reconstructed from the identification results for the selected sweep events of group 1. a) 6.7 bar b) 6.5 bar c) 6.3 bar d) 6.2 bar e) 6.1 bar

3.4. PARAMETRIC EMA IN OPERATING CONDITION

Now, in order to have a better idea of how pressure affect the system poles, figure 3.32 shows the evolution of identified poles. Each pole is noted according to its frequency from 1 (lowest frequency) to 9 (highest frequency).

In figure 3.32, it is possible to see that poles on the extremes (poles 1,2,3,7,8 and 9) show a very little variation on both frequency and damping. Poles 4 and 6 show a larger damping then frequency variation. It is however difficult to say if these damping variations are mostly due to uncertainty or to pressure changes. The pressure effects can be much more clearly seen on pole 5 which reproduces the frequency shift previously noted on figure 3.30, suggesting it may be a part of the squeal mode lock-in.

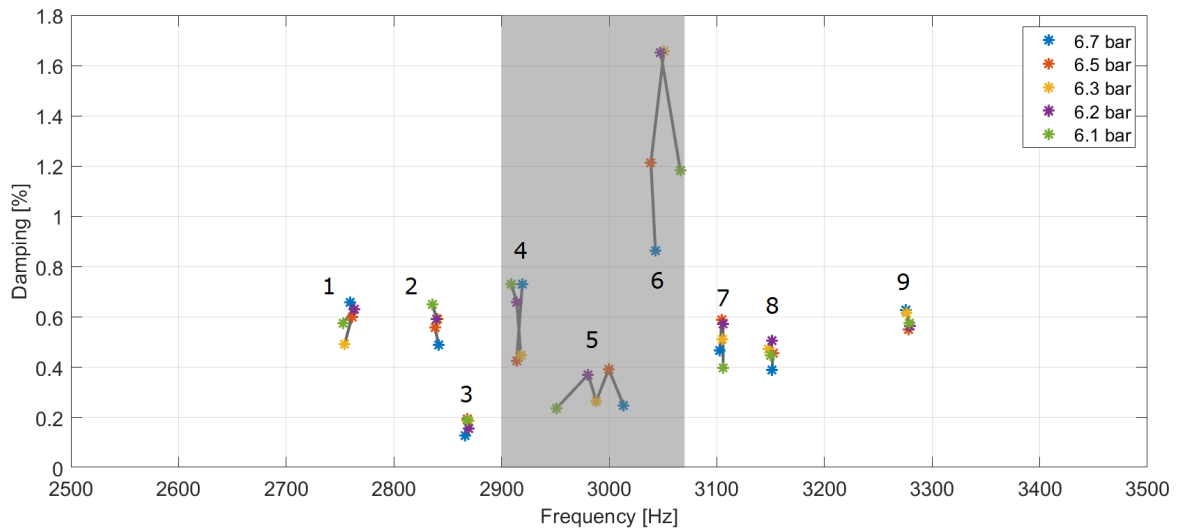


Figure 3.32: Evolution of the identified poles for the sweep transfer function of group 1. Gray areas indicate regions where low coherence was detected in at least one measurement.

After describing the evolution of frequency and damping let us now focus on the shapes. Using the Modal Assurance Criterion (MAC) [53], figure 3.33 compares the mode shapes at 6.7 bar to the mode shapes at other pressures.

In figure 3.33, one first analyzes modes outside the squeal band. Modes 2 and 9 are well identified and show almost no sensibility to pressure range of group 1. For modes 7 and 8, the sensor configuration does not allow clear differentiation. The need to discard some sensors due to saturation in the measurements is probably the source of this difficulty.

The shapes of modes 1 and 3 on the other hand show more variations without any clear pattern. This apparent inconsistency in the shape of modes 1 and 3, while their natural frequency and damping is stable, indicates possible problems with their identification.

Modes 4-6 are within the squeal occurrence band. The frequency of mode 5 is also the most sensitive to pressure, while the shape of mode 5 is reasonably stable. Interaction with modes 4 and 6 whose shape is less stable. This is coherent with the expectation from the previous section : squeal occurrences below 6.1 bar is close to 2900 Hz and above 6.7 close to 3100 Hz. The analysis of operational shapes confirms that these clusters differ both in frequency and shape.

3.4. PARAMETRIC EMA IN OPERATING CONDITION

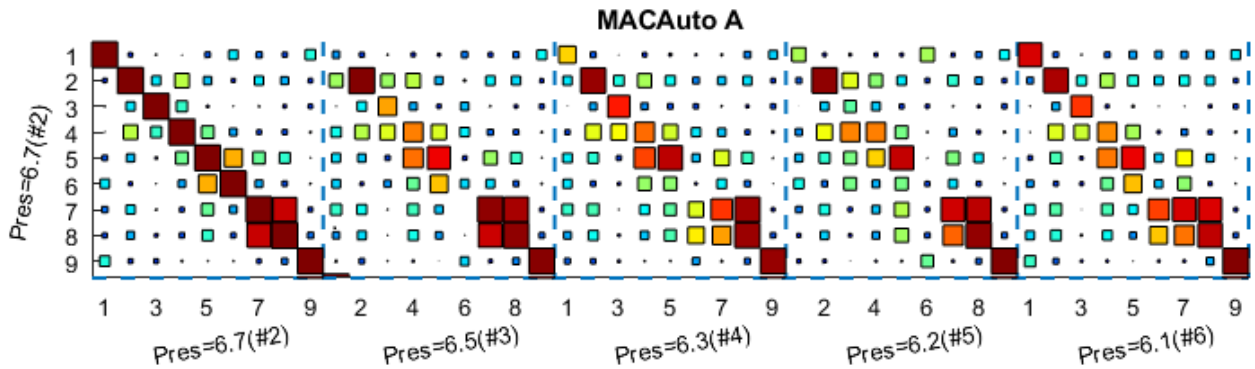


Figure 3.33: Evolution of the MAC between the shapes of identified poles for the sweep transfer function of group 1

Summing up the results for group 1, there are a number of challenges in the identification and analysis of the obtained transfer. Reasons include: presence of internal source of energy, noisy nonlinear measurements, reject sensors difficulty the separation of mode shapes.

The second group of transfer function seeks to describe the evolution after crossing the second instability region. As mentioned previously, sweep events were selected with a constantly decreasing pressure (5.4, 5.3, 5.1 and 4.9 bar) in order to simplify the reading of results. The transfer functions corresponding to group 2 are displayed in figure 3.34.

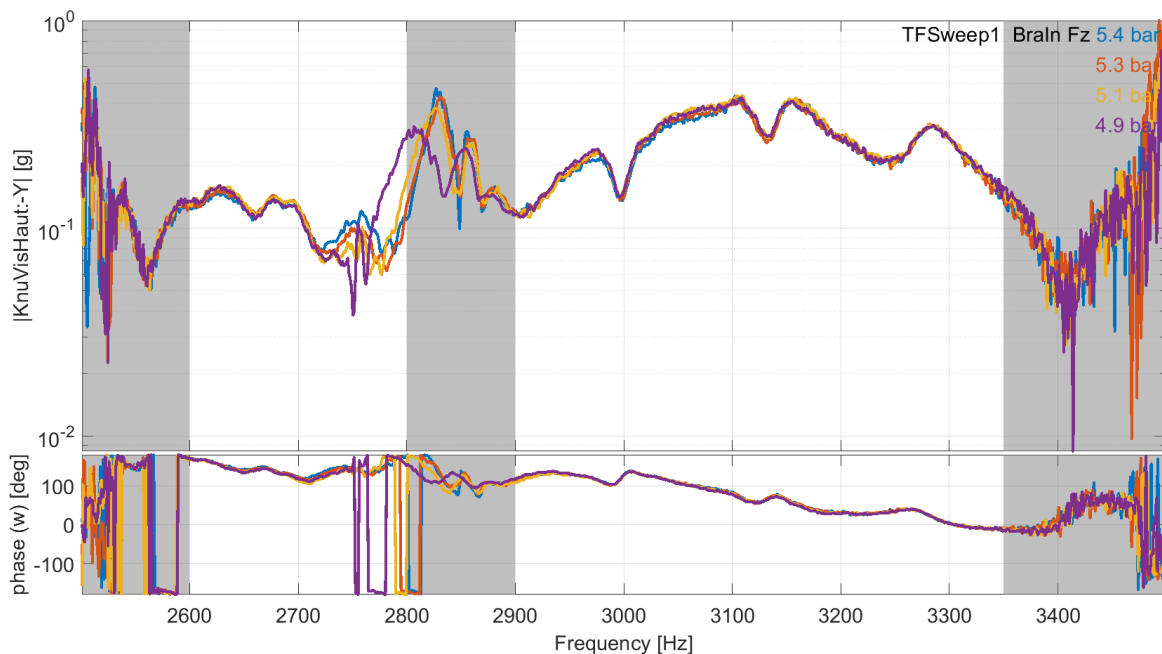


Figure 3.34: Superposition of the transfer functions describing the system response for the selected sweep events of group 2. Gray areas indicate regions where low coherence was detected in at least one measurement.

3.4. PARAMETRIC EMA IN OPERATING CONDITION

Looking at the evolution of peaks, the modes at frequencies higher than 2900Hz seem to be stable, while the ones at lower frequencies show some level of change. This is expected to a degree as the pressure sensitive mode crosses the squeal region near 2900Hz, which is confirmed by a loss of coherence in the 2800 to 2900Hz band. While a left shift can be seen in the highest peak below 2900Hz the changes do not show a clear trend as in group 1.

Identification is performed using the same local single pole identification algorithm than for group 1. One additional challenge faced in this group is how close the first four modes are in frequency. This closeness created some additional difficulties to using a local pole identification. Regardless of the difficulties, figure 3.35 shows that the reconstructed frequency responses overlap with the measured transfer functions.

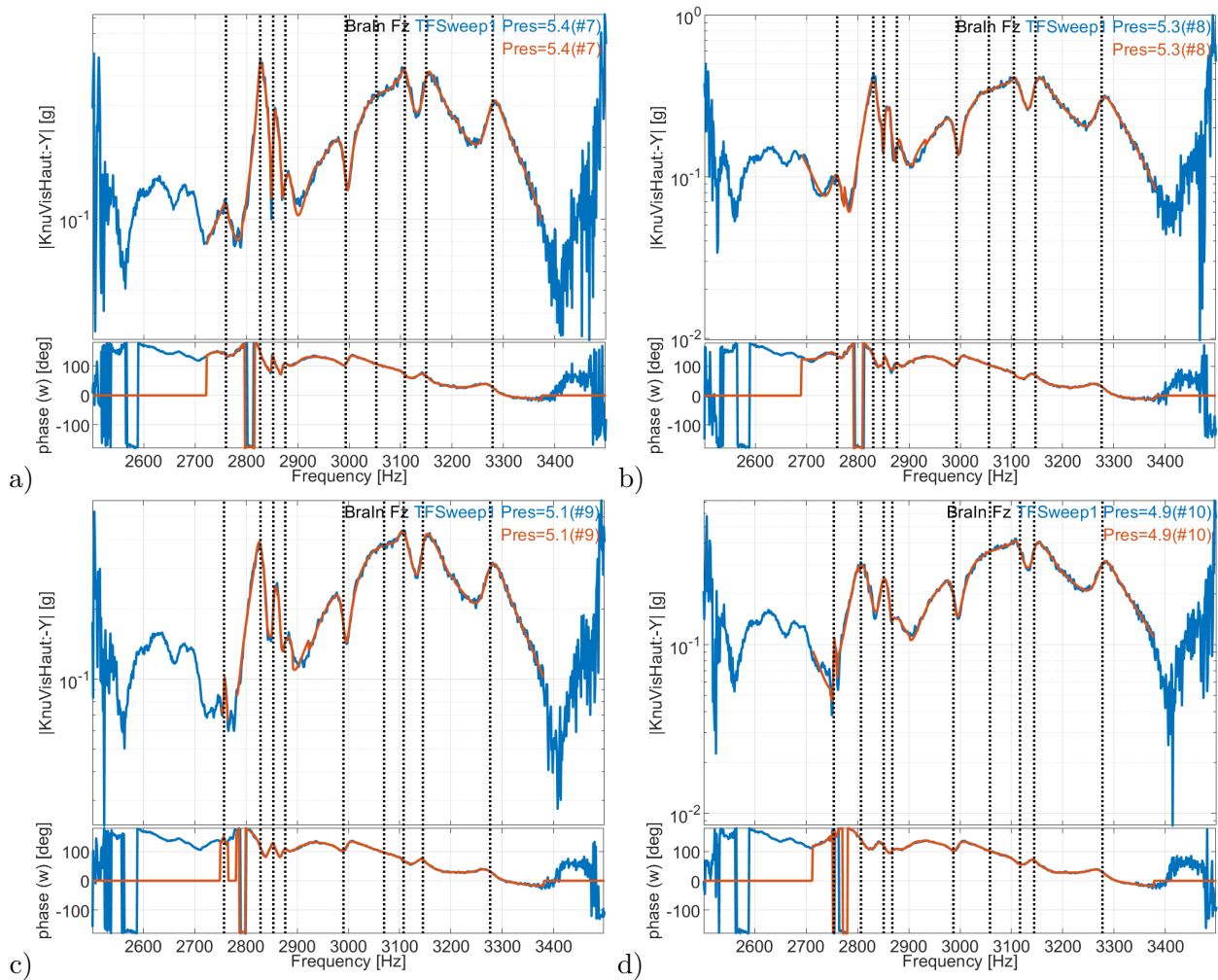


Figure 3.35: Comparison between the measured and identified transfer functions for group 2 events a) 5.4 bar b) 5.3 bar c) 5.1 bar d) 4.9 bar

By tracing the evolution of poles, figure 3.36 confirms that modes 5,6,8 and 9 are reasonably stable in frequency and damping. Mode 7 shows a small damping uncertainty but is stable in frequency. A damping uncertainty is also seen in modes 1,2,3 and 4, which may be related to the difficulty in using

3.4. PARAMETRIC EMA IN OPERATING CONDITION

the single pole identification algorithm.

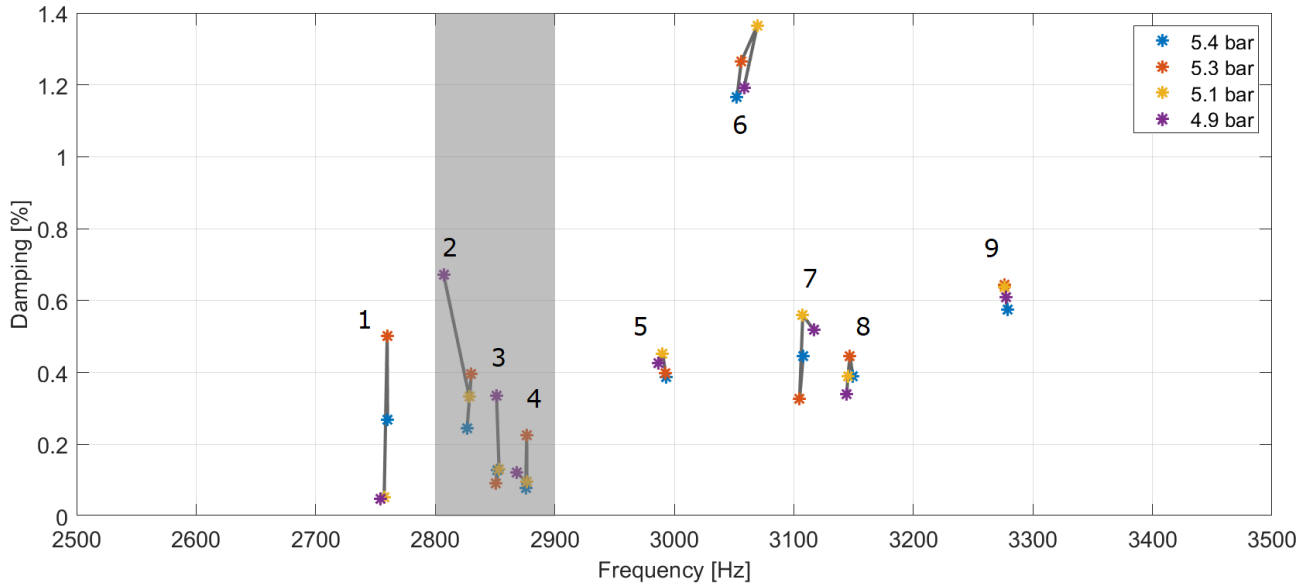


Figure 3.36: Evolution of the identified poles for the sweep transfer function of group 2. Gray areas indicate regions where low coherence was detected in at least one measurement.

Let us now look at the shapes using MAC in figure 3.37. This figure show us that it is difficult to differentiate the shapes from modes 1,2,3 and 4. Which confirms the difficulty in identifying these modes independently for the considered sensor configuration. Modes 5,7,8 and 9 have stable shapes with little variation. Similar to what is observed in group 1, it is not possible to differentiate the shapes of modes 7 and 8. Lastly, the shape of mode 6 do not present a clear trend despite being reasonably stable in frequency and damping.

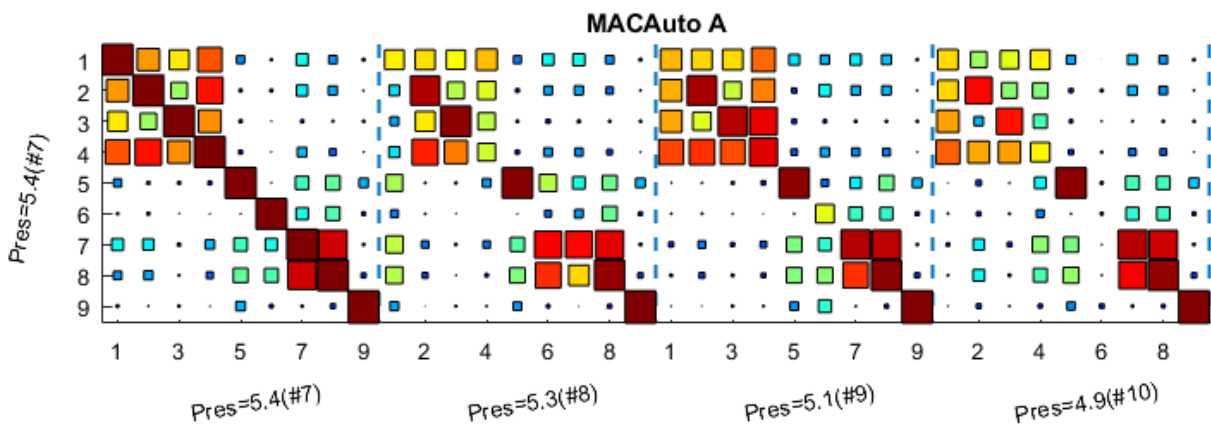


Figure 3.37: Evolution of the MAC between the shapes of identified poles for the sweep transfer function of group 2

3.5. DETAILED SHAPE CHARACTERIZATION USING 3D-SLDV

Finally, group 3 corresponds to the transfer functions after the third squeal occurrence at pressures 6.4, 6.5, 6.8 and 6.9 bar. From the superposition of transfer functions in figure 3.38, it is possible to see that the effect of pressure changes is limited to the frequency band between 2900 and 3050Hz. Outside of this band the modes are reasonably stable and are very similar to the ones seen in group 1 (as displayed in figure 3.30). Considering that the pressure values in group 3 are similar to the ones in group 1, this similarity is a very encouraging result.

Inside the variable frequency band, however, the situation is less clear. Despite an expected right shift on the main peak, the number of modes on the band is inconsistent. This is most visible on the transfer function at 6.5 bar where two additional peaks can be seen between 2900 and 2950Hz.

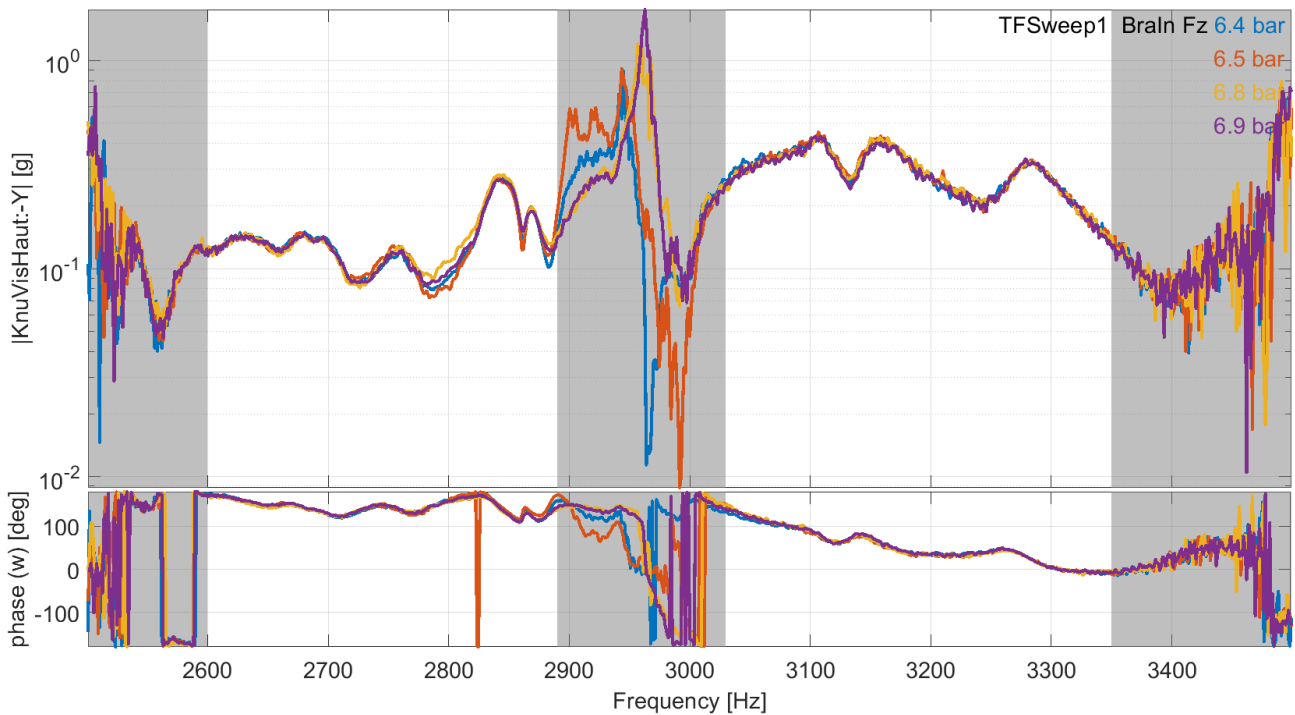


Figure 3.38: Superposition of the transfer functions describing the system response for the selected sweep events of group 3. Gray areas indicate regions where low coherence was detected in at least one measurement.

Due to this apparent variable number of modes identification results were very inconsistent in the band between 2900 and 3050Hz. With this in mind, we decided to limit the analysis of these results and avoid any misinterpretation caused by measurement problems.

3.5 Detailed shape characterization using 3D-SLDV

Finally, this section exploits 3D-SLDV (3D Scanning Laser Doppler Vibrometer) measurements typically used to obtain detailed spatial characterizations of limit cycles. The extraction of detailed limit cycle shapes provides an important basis for proposing corrective measures on a brake design. The current method for extracting shapes from 3D-SLDV measurements is called FastScan and is

3.5. DETAILED SHAPE CHARACTERIZATION USING 3D-SLDV

based on the short time Fourier transform (as detailed in section 3.5.2). The goal of the section is to analyze the relative performance of shape estimation using an HBV signal and Fourier transforms. Section 3.5.3 describes results obtained from the HBV signal model. The comparison between sample results from both methods is shown in section 3.5.4. The section also shows the shapes obtained for higher harmonics. Similar to what is shown in section 2.4 the higher harmonics shapes highlight how the nonlinearities are excited differently for different harmonics.

3.5.1 3D-SLDV Measurement setup

In the 3D-SLDV measurements velocity is sequentially measured for a series of points on the system surface together with some fixed reference accelerometers. Two different views (front and mirror) are used to capture the vibration in a wide area over the brake disk, caliper, bracket, and outer pad. Both views are indicated in figure 3.39 and the combined mesh is showcased in the measurement of figure 3.40.

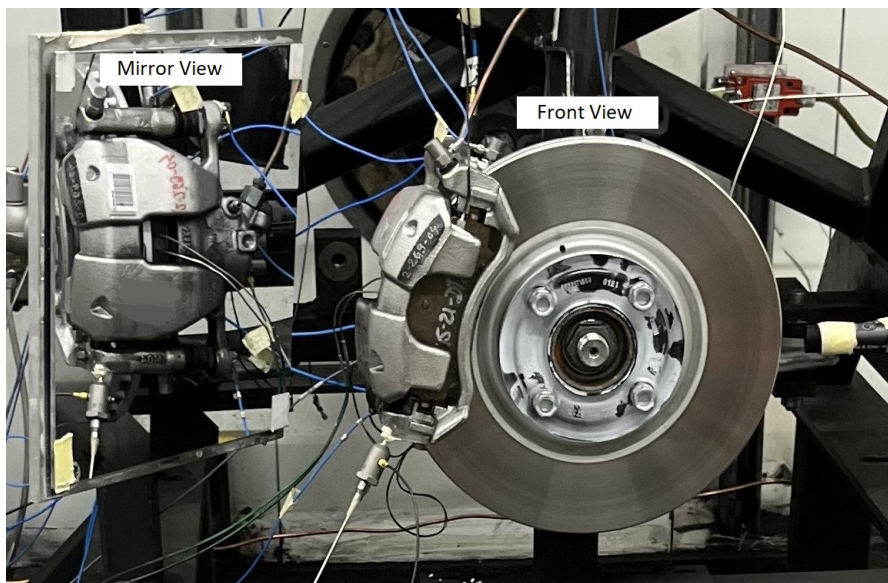


Figure 3.39: Brake system with front and mirror views indicated

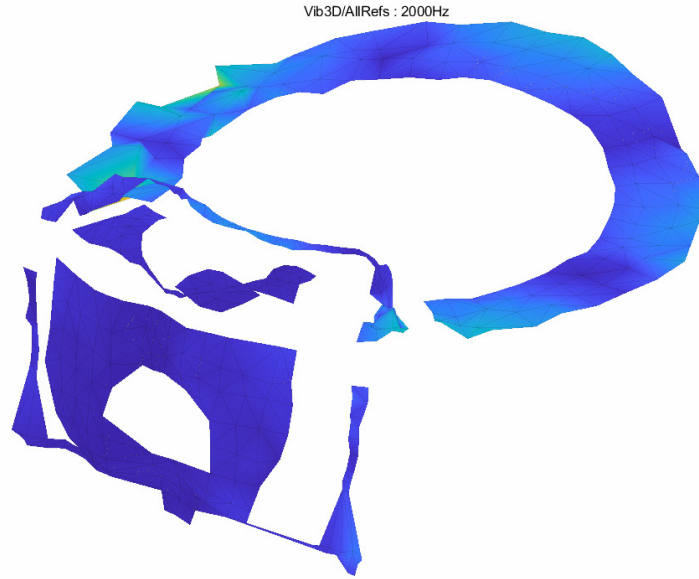


Figure 3.40: Sample ODS (FastScan measurement) combining front and mirror meshes

A big limitation of the 3D-SLDV is that measurements can only be made on visible parts of the structure, making it difficult to apply in cases where the target system is covered by surrounding structures. For example, 3D-SLDV cannot measure a brake system mounted in a car as it is covered by the chassis and wheel. The positioning on the test bench is then a key aspect to be considered in planning this type of measurements.

3.5.2 ODS estimation using Short Time Fourier Transform

The classical approach to extract the squeal ODS from a 3D-SLDV measurement is to use the transmissibility between one of the fixed reference accelerometers and the laser velocity measurement. This is called FASTSCAN in the Polytec acquisition system used here.

With the 3D-SLDV mirrors stabilized at a point, a short time window (typically 10 ms) is measured as shown in figure 3.41. Using multiple measured frames, one of the fixed reference sensors is chosen and an H_1 estimator is used to compute the transmissibility

$$H_1^p(f) = \frac{\sum_{rep} G_{p,ref}}{\sum_{rep} G_{ref,ref}} \quad (3.7)$$

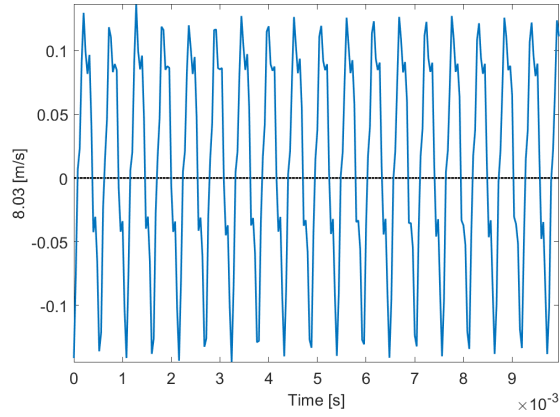


Figure 3.41: Sample 10ms buffer of the 3D-SLDV.

The global ODS shape is then obtained by combining the responses at the maximum frequency of each point

$$\{\Psi\} = \begin{Bmatrix} \Psi^1 \\ \Psi^2 \\ \vdots \end{Bmatrix} = \begin{Bmatrix} H_1^1(f_{max}^1) \\ H_1^2(f_{max}^2) \\ \vdots \end{Bmatrix} \quad (3.8)$$

For the sake of visualization this type of shape will be displayed as a real and a imaginary shape in quadrature $\{\Psi\} = \{Re(\Psi)\} + i\{Im(\Psi)\}$. Figure 3.42 shows an example of this technique applied to a self excited vibration at 1800Hz.



Figure 3.42: ODS extracted from a 3D-SLDV measurement using H1 transmissibility. Left: real part. Right: imaginary part. Color indicates displacement normal to the disk.

Choosing only one reference sensor to combine the sequential measures raises the question of the effect the reference sensor in the resulting shape. In order to evaluate this figure 3.43 compares the vibration shapes using as reference the channels of a triax placed on the bracket. It is possible to see that the shapes show slight variations. Analyzing the noise in estimation for individual points, corresponding to different measurement times, would be necessary to refine analysis of differences.

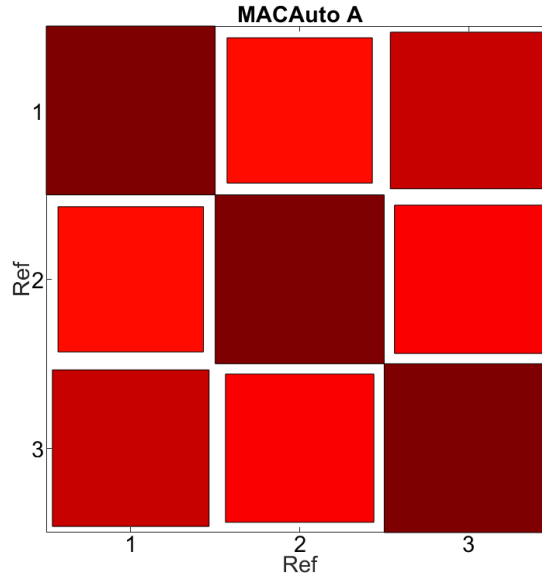


Figure 3.43: MAC between the ODS extracted from a 3D-SLDV measurement with different references

Improvements of the technique require understanding noise issues. The Polytec systems has some built-in techniques to track H1 convergence. Using 10ms windows leads to a frequency resolution of 100 Hz, which is coarse and sensitive to the presence of short high amplitude errors in the signal due to laser signal dropout.

Rather than transmissibility from a single sensor, a more robust approach would be to use a strategy that includes all references in the aggregation like the one proposed in [17].

3.5.3 Using an HBV signal and demodulation to build operational deflection shapes

The HBV signal proposed in section 2.2 can be used to provide a description of complex shapes

$$\{y(t)\} = Re \left(\sum_h \begin{Bmatrix} y_{vib}^h \\ y_{ref}^h \end{Bmatrix} e^{ih\omega t} \right) \quad (3.9)$$

at vibrometer *vib* and reference sensors *ref*.

Since the HBV estimation occurs on a small time window, convergence issues associated with the use of a low pass filter must be addressed. Figure 3.44 shows an example of demodulation. The right plot illustrates that demodulation takes some time to converge and tends to oscillate at the end as low pass filtering cannot be too slow due to the short time window available. For each point, rather than using the $H_1^p(f_{max}^p)$ as in the previous section, one thus select the amplitude at a specific time $y^h(t_p)$ or the average over a short window towards the right in figure 3.44.

In more recent applications, an initial condition for the demodulation is set using a Fourier transform over the entire measurement to speed up the convergence. Multiple passes are used to adapt the estimated instantaneous frequency, which ideally should come from a continuous measurement of references that was not available here.

3.5. DETAILED SHAPE CHARACTERIZATION USING 3D-SLDV

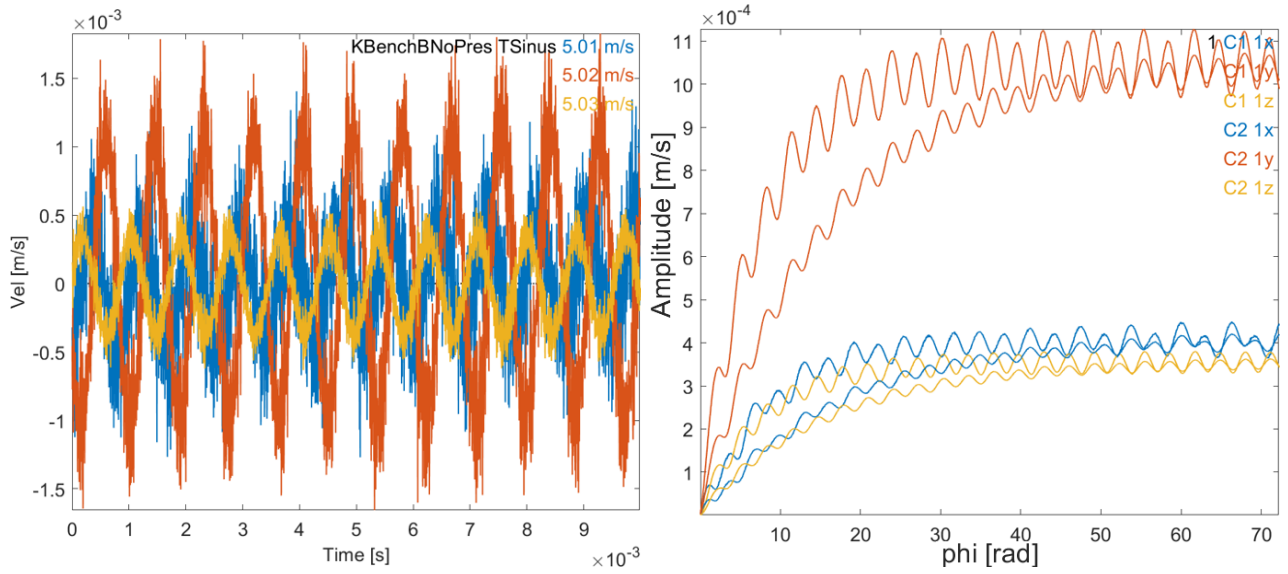


Figure 3.44: Example of 3D-SLDV measurement for a single point in x,y and z directions (Left) and the corresponding demodulation with two filter setups as function of instant phase $\varphi = \int_0^t \omega(t)dt$ (Right).

One must then perform spatial aggregation using the assumption of the previous section: the ratio between motion at the reference sensor and at the laser point is constant. If a single reference is chosen, the equivalent of transmissibility is thus

$$\{y_h\} = \begin{Bmatrix} \vdots \\ y_h^p(t_p) \\ \vdots \end{Bmatrix} = \begin{Bmatrix} \vdots \\ \frac{y_{h,vib}(t_p)}{y_{h,ref}(t_p)} \\ \vdots \end{Bmatrix}. \quad (3.10)$$

The result is a complex shape such as the one displayed in figure 3.45 split into real and imaginary part. In this figure it is possible to see that while the real part is reasonably smooth, the imaginary part show a sudden dip in the left part of the disk. This suggests a problem in this measurement either on the laser vibrometer or the reference sensor during the measurement of this specific point. This should be detected by analysis of signals and lead to either a second measurement or elimination of the point based on noise rather than *strange shape* considerations.

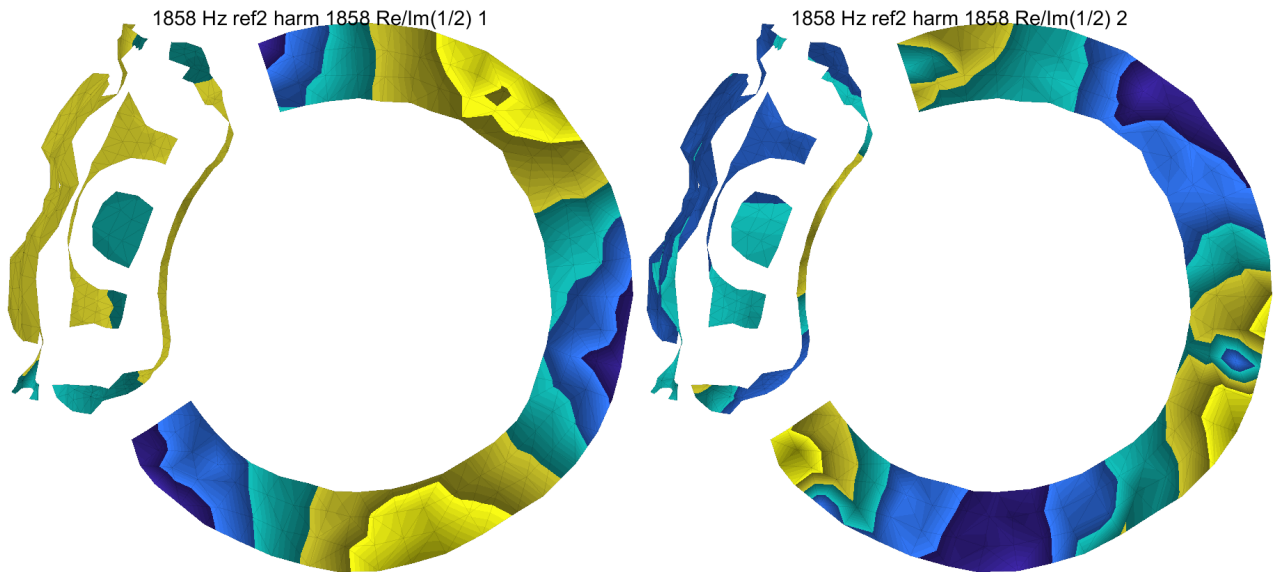


Figure 3.45: ODS extracted from a 3D-SLDV measurement using the HVD signal model and demodulation. Left: real part. Right: imaginary part. Color indicates displacement normal to the disk.

3.5.4 Sample results

When looking at shapes obtained via the STFT 3.42 and demodulation 3.45, one quickly notices that it is rather difficult to compare complex shapes only through their real and imaginary parts. Since they are complex shapes the most natural way of visually comparing them is through the use of animations. Animations, however, cannot be added in a manuscript to be printed such as this one. Leaving us with the option of splitting the animation into a series of frames as a way to better visualize the two complex shapes.

Figures 3.46 and 3.47 show the ODS extracted using transmissibility and demodulation respectively. Both results follow the same overall trend (especially on the normal direction), showing a disk vibration with 3 lobes and a similar caliper deformation. The main difference is the noise level with notably better results for the demodulation. Drawing general conclusions for this specific case should however be avoided even if demodulation is less sensitive to fast impulses associated with laser signal dropouts than FFT.

3.5. DETAILED SHAPE CHARACTERIZATION USING 3D-SLDV



Figure 3.46: Animation frames of Polytec FastScan STFT shape



Figure 3.47: Animation frames from HBV signal shape obtained via demodulation

In addition to improving the estimation of the shape corresponding to the first harmonic, the proposed method gives us access to the shapes of higher harmonics. Figures 3.48 3.49 and 3.50 show the shapes corresponding to the harmonics 2,3 and 5 of the vibration respectively. The obtained shapes are reasonably smooth. It is possible to see that as frequency increases the number of lobes in the disk progressively increases from 4 at the second harmonic to 7 at the fifth harmonic.

3.5. DETAILED SHAPE CHARACTERIZATION USING 3D-SLDV

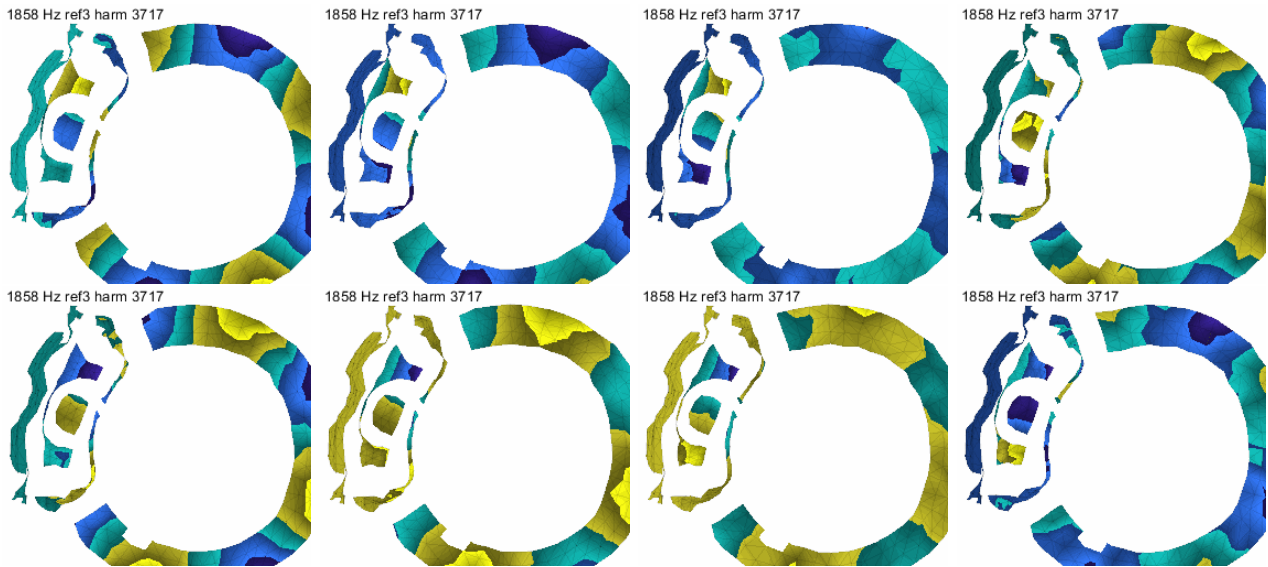


Figure 3.48: Frames from the animation showing the second harmonic shape obtained from HBV signal

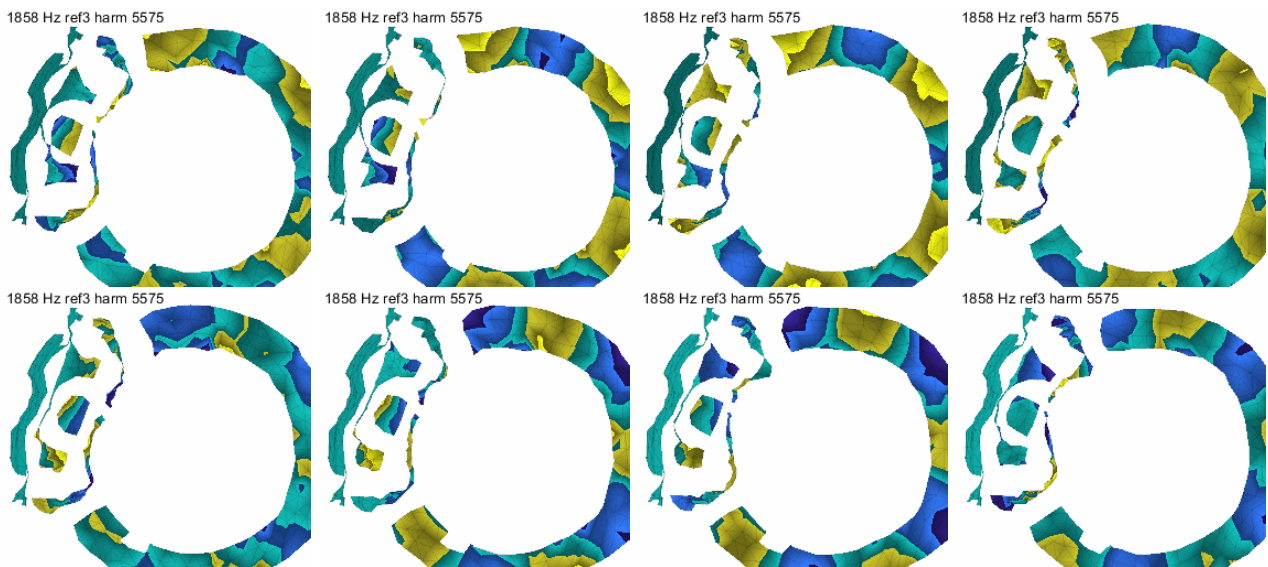


Figure 3.49: Frames from the animation showing the third harmonic shape obtained from HBV signal

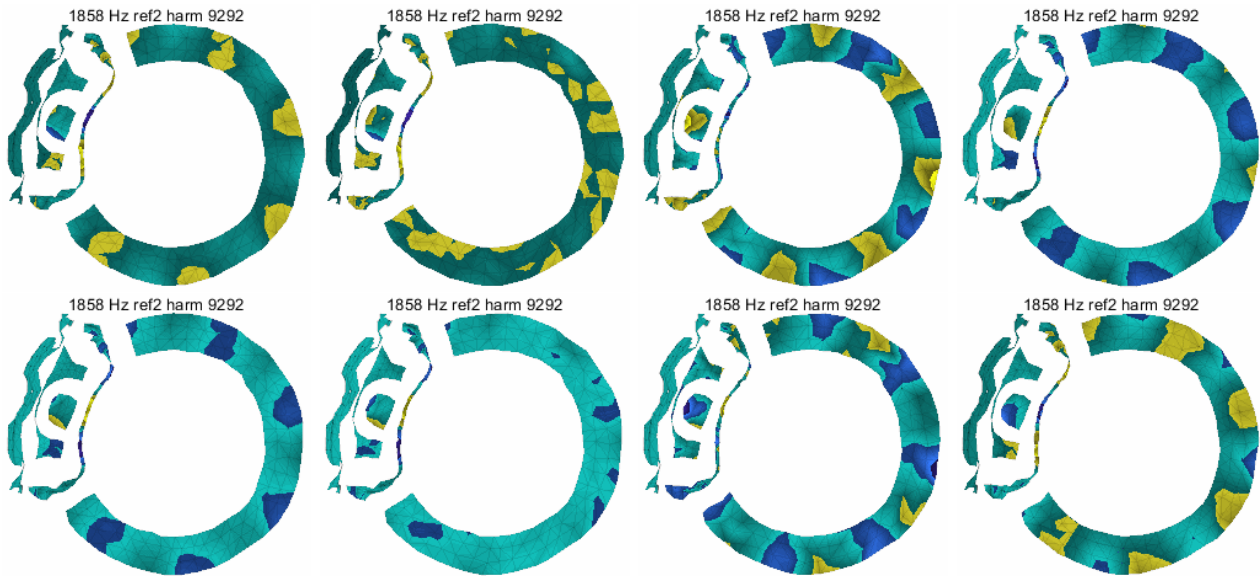


Figure 3.50: Frames from the animation showing the fifth harmonic shape obtained from HBV signal

3.6 Conclusion

In order to improve the parametric characterization of brake squeal, this chapter proposes and analyzes the usefulness of different methodological changes to testing methods. This is done for the three main types experimental brake squeal characterization: classification of squeal occurrences, modal characterization of components and assemblies, and detailed spatial characterization of limit cycles.

In the classification of squeal occurrences, section 3.3 shows that the HBV signal model is a practical tool to analyze squeal tests. Using a series of drag tests as example, a series of features describing the parametric evolution of squeal are extracted.

First a global vibration amplitude is defined to represent the growth/decay events of an intermittent squeal case. From the obtained amplitude it is then possible to define a decay rate for comparisons with complex mode damping ratio. In a parallel to the analysis of the functional model in chapter 1, instant frequency and decay rate are used to construct an experimental root locus that represents the system behavior when crossing the stability boundary.

The classification (clustering) of squeal occurrences is then show using features extracted from the HBV signal model. By tracking the evolution with pressure of frequency/amplitude, generalized coordinate, or shape it is possible to distinguish three clusters that are relatively close in frequency to each other (around 2700, 2800 and 3100Hz). Note that using enough sensors to classify shapes is a proposal of this work that does not correspond to current industrial practice.

In this section a great amount of information has been extracted from the parametric tests without excitation. The remaining question at this point is how to feed this information back to a design process and correlate it with simulation results. Chapter 1 points out a few directions on how to better correlate experimental results and simulation by comparing the stability boundary. In the

3.6. CONCLUSION

present test this boundary is obtained by analyzing the parametric evolution of squeal and with an extent associated with squeal transients used to build the experimental root locus. In the functional model, this was obtained either by transients as in test or by amplitude/pressure dependent CEA (but the second option does not simply generalize to pressure fields).

The realization of a parametric EMA in operating condition, described in section 3.4, shows that it is possible to accurately identify the system modes in regions away from squeal. In the regions near squeal, a loss of coherence indicates that the interpretation of identified poles is difficult beyond saying that the frequencies follow the same trends as the squeal frequencies. In order to characterize these modes, it is thus necessary to use a different approach such as the phase resonance testing discussed in section 2.3.

The presence of a coherence loss that follows the squeal frequency in itself is an interesting result. Since the coherence loss is observed even when the squeal limit cycle is not present, one could seek to use it as a method of early detection to more efficiently track the stability boundaries associated with squeal clusters.

Finally, section 3.5 shows that extracting the HBV signal model to construct vibration shapes is a valid alternative to the current Fourier based method. For the sample measurement HBV method obtained cleaner shapes. Future work should seek to understand the origin of better noise rejection and use a more robust aggregation strategy that includes all references in the aggregation like the one proposed in [17].

In addition to improving the shape obtained for the first harmonic, the HBV signal gives access to spatially detailed shapes of higher harmonics. These shapes provide an insight on how each harmonic interacts with the nonlinearity. Section 2.5 discussed a possible way to exploit this information to analyze the system nonlinearity using harmonic modulation and harmonic perturbation indicators, which are based on the notion of instant stiffness proposed in [31].

A second full scale test campaign was performed in the beginning of 2024 with some updated strategies, but due to time constraints it was not possible to fully discuss the corresponding results in this manuscript.

Conclusion

Brake squeal is a complex phenomenon, which has been a subject of study for many years. Despite this fact, there is no robust design method for preventing it. Correcting measures are heavily based on prototyping and validation, which is time-consuming and expensive. This work thus sought to propose and analyze the usefulness of different methodological changes to testing methods.

Squeal testing can be separated in three main activities : classification of squeal occurrences based on acoustic levels, detailed spatial characterization limit cycles, and modal characterization of components and assemblies. A specificity is that squeal notably depends on parameters pressure, wheel speed, temperature, ... which vary in time relatively slowly compared to the frequencies of squeal limit cycles. It is thus important to ensure that any method is compatible with this specificity.

Occurrence classification seeks to analyze the probability of exceeding a target level, usually acoustic, for variations in pressure, wheel speed, temperature, ... This is oriented towards the certification that a brake system squeals as rarely as possible. However, identifying only the squeal occurrences lacks the details giving the understanding of squeal phenomenon needed to guide choices of correcting measures. Thus as a first overall goal, this project seeks to improve the classification (clustering) and detailed characterization of squeal occurrences. A paper discussing the some of the results obtained on this development has been submitted to MSSP [33].

Due to the slowly varying characteristic of brake squeal, the measure of a squeal occurrence is quasi-periodic with two characteristic time scales. A fast timescale that describes the quasi-periodic behavior in a single period through the presence of harmonics as in the Harmonic Balance Method, and a slow timescale that describes changes of period and harmonic vector components over multiple periods. This HBV (harmonic balance vector) signal model, detailed in section 2.2, differs from analytic signals by the consideration that the period is common to all measurements and all harmonics. As is the case of analytic signals, the HBV is able to represent variations that cannot be captured by STFT because of its buffer length/frequency resolution constraints. In addition to squeal, this description is of interest in sine, slow sweep or any other type of testing where the period depends on excitation.

The estimation of HBV signal properties is done using a demodulation algorithm that estimates the slow evolution of both frequency and amplitude for all measurement channels (which is often separated in global amplitude and shape). This algorithm has been widely used in this project and proven to be robust and easy to tune (see section 2.2.2 for details on tuning).

Illustrations of HBV signal usage in section 3.3 focus on the analysis of drag tests, where squeal is measured under a constant wheel velocity and slowly evolving pressure. Its application is however

CONCLUSION

not limited to this case, with applications possible in other types of squeal tests (such as stop tests that reduce velocity at constant pressure, and deceleration tests that impose a constant deceleration rate) or any other test with a quasi-periodic response (in either nonlinear or time varying systems). It was for example applied to the construction of transfer functions in tests with unbalance excitation in [85].

Definitions of global vibration amplitude (independently of shape) are first discussed for intermittent squeal events. Estimation of a decay rate comparable to complex mode damping ratio is then introduced, showing that the results of the functional model are applicable to real tests. Correlation between amplitude and limit cycle frequencies is hard to illustrate with this test where torque modulation has a strong influence, while the 2024 test gives clear experimental root loci as illustrated in figure 3.15.

Classification (clustering) of squeal occurrences using frequency/amplitude, generalized coordinate, or shape is then discussed. The example chosen, drag with variable pressure, illustrates a case with close frequencies but three different clusters for both clustering techniques. Note that using enough sensors to classify shapes is a proposal of this work does not correspond to current industrial practice.

The application of the HBV signal model to characterize squeal showed to be a robust process capable of handling large datasets in a reasonable time. These characteristics indicate that the proposed strategy could be automated and integrated into industrial procedures.

As a mean to gain further insight on how to better correlate experimental results and simulation, chapter 1 seeks to describe the effects of slowly changing operating conditions using a new functional model for squeal. As in the well known Hoffmann model [4] two translations of a mass allow the representation of squeal as a mode lock-in. The novelty lies in replacing the variable friction assumption by a nonlinear contact law, which introduces a sensitivity to the applied pressure (as the static-state is modified by it), and amplitude (through its effect on the nonlinear contact). The analysis of this model has been presented at the Inter-Noise conference[29].

The analysis of the functional model is done in both frequency and time domain. In frequency domain (section 1.3), the functional model stability is evaluated using a Complex Eigenvalue Analysis (CEA). First, the dynamic equations are linearized around a steady sliding solution to describe the effects of applied pressure. Then an amplitude dependence is added to this analysis by imposing periodic trajectories composed of harmonics 0 and 1 to the contact surface. As a result the effects of both pressure and amplitude are taken into account, thus allowing the characterization of the pressure effect on the limit cycle vibration amplitude.

In time domain (section 1.4), the functional model response to a series of pressure profiles is obtained using nonlinear transient simulations which are analyzed using the HBV signal model also used for real experiments in an effort to verify consistence. The three types of pressure profile considered represent usual experiments: drag where constant pressure is applied, pressure ramps, and pressure oscillations mimicking the contact changes due to wheel rotation, which is thought to be the source of intermittent squeal occurrences. These responses are then analyzed by extracting features that represent the limit cycle vibration and comparing it with the values obtained in frequency domain.

The comparison between frequency and time domain results provides a better understanding the dependence of limit cycle properties on parameters. The ability to compare time and frequency

CONCLUSION

results is however linked to the use of a scalar nonlinearity. Extension to full scale industrial model was performed by SDTools and due to the dependence on pressure fields there is no obvious way to build an equivalent frequency domain model from transient results. It seems however clear that any frequency analysis would require using generalized interface coordinates (for example hyper-reduction [56] or contact interface modes [14, 35]) to avoid using a large number of parameters. This would allow parametric studies, on full scale industrial models, to trace the amplitude/pressure stability boundary and the expected root locus when transitioning to/from instability.

The second test activity, detailed spatial characterization of limit cycles, is typically performed using 3D-SLDV measurements. The extraction of detailed shapes of the limit cycle shape provides an important basis for proposing corrective measures on a brake design. As such, improving the test and analysis of 3D-SLDV measurements is a second overall goal of this thesis.

Seeking to improve results of the current FastScan process, which extracts the fundamental harmonic component in Fourier transforms, is the first point tackled in sections 2.4 and 3.5. The HBV demodulation offers an advantage over the usual Fourier method as it takes the nature of squeal into consideration and can handle noise more efficiently.

For the contact test bench, 3D-SLDV shapes obtained near a resonance for different pressure values provide an insight on how pressure affects the contact nonlinearity. For the full scale brake test, global shapes are obtained using both short time Fourier transform and HBV signals combined using the usual transmissibility method. The comparison shows less noise in HBV derived shapes. Future works should seek to use a more robust aggregation strategy that includes all references in the aggregation like the one proposed in [17].

In addition to improving the shape obtained for the fundamental harmonic, the HBV signal characterizes vibration as a sum of harmonics. This allows us to define and extract spatially detailed shapes corresponding to the higher harmonics. In both the contact bench and full scale measurements these shapes were able to highlight how nonlinearities are excited differently for different harmonics.

Section 2.5 discusses how the higher harmonics can be used to analyze motion within a period as a that of a parameter varying system. Inspired by the notion of instant modulus/stiffness proposed in [31], this section analyzes higher harmonics as harmonic modulation or perturbation around the harmonic 1 response, which highlights positions where the system is stiffer or softer thus giving a more detailed understanding of nonlinearity. Although presented here only for the contact test bench the two proposed indicators could be applied to describe the (quasi-)periodic response of any kind of nonlinear system. An early version of these results was presented at the ISMA conference [32] using data from rubber identification tests.

In a near final brake design, squeal rarely occurs when it does can be difficult to consistently reproduce. This means that the process of finding a good set of operating condition for 3D-SLDV measurements can be very lengthy. A prospect of improvement for speeding up this process is found in the analysis of the coherence form the parametric Experimental Modal Analysis (EMA) (detailed in section 3.4).

Analyzing the system response to a series of 2s sweep measurements showed that, in the close

CONCLUSION

vicinity of the squeal region even if no limit cycle is visible, one observes a strong loss of coherence. The loss of coherence can be interpreted by comparing it with the force spectrogram. In the force spectrogram the occurrence of squeal can be seen as a region where the structure excites the shakes. The loss of coherence is observed around these regions and forming a path between them.

This result suggests that it is possible to track the evolution of the squeal before the appearance of large vibration amplitudes by looking at the coherence. This result could then be used to speed up the search for a good set of operating condition to characterize limit cycle.

The third experimental activity, dialog with FEM prediction of squeal, is performed using modal analysis. A multilevel strategy from component to full brake test in operating conditions was outlined in [17, 21]. Since squeal shows strong parameter dependence, it is however expected that modal properties on the complete system will depend notably on classical operating parameters pressure, temperature, ... in particular when the system is close to squeal. It is thus desirable to improve the modal analysis in operating condition in order to better evaluate parametric effects.

A first discussion on the parametric modal analysis is made in section 2.3 using a contact test bench. Experimental Modal Analysis (EMA) at a few fixed pressure points provides an approximate relation between pressure and resonance frequency, this discrete characterization lacks accuracy. In order to achieve continuous tracking of modal parameter dependence on pressure, it is proposed to use phase resonance. The proposed procedure is shown to provide relevant results which were presented at the Survishno conference [30].

The proposed procedure was meant as feedforward approximation of closed loop phase resonance methods [57, 58, 60] targeting the end application of tracking system modes near instability in full scale brake tests. In the single application attempt, parameter perturbations created problems and damping estimations differed from broadband excitation, which is expected for a nonlinear system. Thus, despite obvious need for further work, the procedure seems promising.

Application to the full scale test bench of Parametric EMA in operating condition is then addressed in section 3.4. Away from the squeal frequency (at least 100 Hz or 3% away, which is still quite close), modes are well identified and not very sensitive to limited pressure changes. This confirms that the proposed use of 2s sweeps is a well adapted strategy for parametric EMA and that similar processes could be used industrially.

In the regions near squeal, the already mentioned loss of coherence indicates that interpretation of peaks or identified poles is difficult beyond saying that the frequencies follow the same trends as the squeal frequencies. This suggests that very close in frequency to squeal occurrences, other methods such as phase resonance testing discussed in section 2.3, are needed.

Résumé long (in french)

A.1 Introduction

Le frottement est depuis longtemps utilisé pour dissiper l'énergie cinétique des objets en mouvement. C'est l'un des mécanismes de dissipation les plus polyvalents et il est largement utilisé dans les systèmes de freinage. Qu'il s'agisse de voitures, de trains ou d'avions, la plupart d'entre eux utilisent la friction dans leurs systèmes de freinage. La friction est cependant une source connue de bruit dans les systèmes mécaniques. Les systèmes de freinage peuvent produire des bruits avec une grande variété de fréquences, durées, évolutions et des modulations. À partir de ces caractéristiques, Akay [1] construit une série de catégories pour classer les différents bruits, comme le montre la figure A.1.

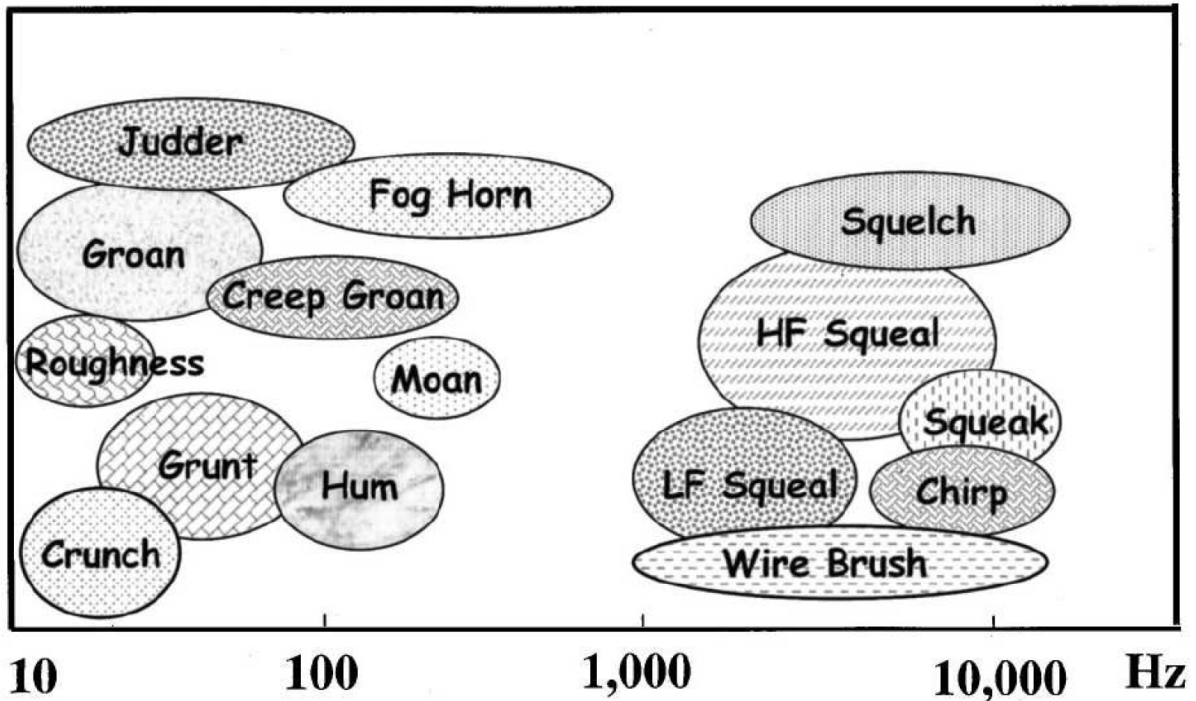


Figure A.1: Classification des différents types de bruit de freinage en fonction de leur contenu spectral, proposé par Akay [1]

Parmi ces types de bruit, le crissement (squeal) est un problème fréquent auquel sont confrontés les fabricants de systèmes de freinage tels que Hitachi Astemo France, le partenaire industriel de ce projet.

Caractérisé par la présence d'une réponse auto-excitée (appelée cycle limite) entre 1kHz et 10kHz, le bruit de crissement atteint des niveaux d'amplitude significatifs entraînant des émissions sonores qui peuvent atteindre jusqu'à 120dB. Le crissement n'est pas seulement un problème pour l'utilisateur final du produit, mais aussi une source notable de pollution acoustique. C'est pourquoi des pénalités économiques sont imposées aux fournisseurs si les exigences en matière de bruit ne sont pas respectées. L'évolution récente de la technologie et des exigences en matière de systèmes de freinage a entraîné une augmentation du coefficient de frottement et une réduction de la masse des composants. En conséquence, le crissement des freins est devenu un problème plus fréquent.

Le crissement de frein est un sujet d'étude depuis de nombreuses années, qui remonte jusqu'au début des années 60 avec les travaux de Spurr [2]. Le crissement est théorisé comme une bifurcation de Hopf induite par un couplage de modes [3, 4, 5]. Les études de crissement abordent à la fois des aspects numériques [13, 14, 15, 16] et expérimentaux. [6, 7, 8, 18].

Dans ce projet de recherche, notre objectif principal est d'améliorer la compréhension de l'impact des paramètres de freinage dans les approches expérimentales. Nous allons chercher à détailler la relation entre les paramètres du système, sa stabilité et les caractéristiques du cycle limite (fréquence, amplitude et forme). Pour atteindre cet objectif, trois objectifs expérimentaux seront poursuivis:

- la classification d'occurrences de crissement (niveau, fréquence, forme, ...)
- l'analyse modal du système de frein en condition opérationnelle non crissante
- la caractérisation spatialement détaillée de la forme du cycle limite

Dans ce résumé, les principales contributions de cette thèse sont rapidement présentées en trois sections. Pour plus de détails merci de consulter les chapitres correspondants.

La section A.2 présente la construction du modèle de signal HBV discuté dans le chapitre 3. Basée sur l'hypothèse de variation lente du système, le modèle de signal HBV (*Harmonic Balance Vector*) est proposé comme une façon de représenter les réponses quasi-périodiques. Un algorithme de démodulation est décrit et montré comme capable d'extraire les paramètres du signal HBV avec illustration dans le cas d'une mesure de crissement sur frein complet.

Ensuite, la section A.3 analyse le modèle fonctionnel proposé dans le chapitre 1. Ce modèle est conçu pour représenter l'effet de la charge appliquée (pression) et de l'amplitude de vibration sur les caractéristiques du cycle limite. Le modèle proposé est inspiré du modèle de Hoffmann [4] et présente un couplage de modes à partir d'un modèle à 2-DDL non-linéaire. Une série d'analyses dans les domaines fréquentiel et temporel sont effectuées afin d'évaluer les effets paramétriques sur le cycle limite.

La section A.4 décrit rapidement les essais réalisés sur frein complet où les concepts développés dans les chapitres précédents sont appliqués (Chapitre 3). Ces mesures ont été effectuées sur un frein industriel dont les dispositifs visant à limiter les occurrences de crissement ont été supprimés. Elles ont été effectuées sur un banc d'essai du partenaire industriel Hitachi Astemo France. Le premier type d'essai présenté est une mesure de crissement à pression variable, où l'estimation du modèle de signal HBV permet l'extraction de l'évolution des caractéristiques du cycle limite. Ces caractéristiques sont alors utilisées pour la classification (clustering) des occurrences de crissement. Ensuite la

réalisation d'une analyse modale expérimentale paramétrique en condition opérationnelle est décrite. Cette mesure permet de suivre l'évolution des modes du système en condition de fonctionnement en fonction de la pression. Finalement, le modèle de signal HBV est appliqué à l'analyse de mesures par vibromètre laser 3D à balayage pour la caractérisation détaillée du cycle limite : les formes associées à la fréquence fondamentale et les aux harmoniques supérieures sont obtenues.

A.2 Modèle de signal pour le crissement

Étant donné que le crissement ne se produit que pour certaines configurations de paramètres du frein, il est essentiel de comprendre comment l'évolution de ces paramètres influence le crissement. Quelques paramètres typiquement considérés par l'industrie sont la pression hydraulique appliquée [9], le profil de chargement [19], la température [12], la vitesse de la roue, la position angulaire de la roue [7, 20, 8, 17, 21], et d'autres.

Pour mieux caractériser l'effet des paramètres sur le cycle limite, la section A.2.1 introduit le modèle de signal HBV (*harmonic balance vector*) qui est capable de représenter les vibrations quasi-périodiques du crissement. La section A.2.2 décrit ensuite un algorithme d'estimation des composantes du signal HBV à partir d'une mesure expérimentale.

A.2.1 Définition du modèle de signal HBV (Harmonic Balance Vector)

Pour construire notre modèle de signal pour le crissement, nous allons tout d'abord analyser en détail les principales caractéristiques d'une mesure de crissement. Cette mesure fait partie de la campagne expérimentale sur frein complet décrite au chapitre 3. La figure A.2 montre le spectrogramme de la vibration auto-excitée résultant d'un profil de pression augmentant progressivement de $p = 1,5\text{bar}$ à $p = 9\text{bar}$. Dans cette figure, il est possible de remarquer quatre régions différentes de crissement à différents moments de la mesure, avec des fréquences fondamentales autour de 1560, 6440, 1900, 2950 Hz. Cela montre que le changement de pression de freinage a un effet direct sur la fréquence fondamentale du cycle limite. Il est important de remarquer que le frein utilisé dans les essais a été modifié pour favoriser l'apparition du crissement.

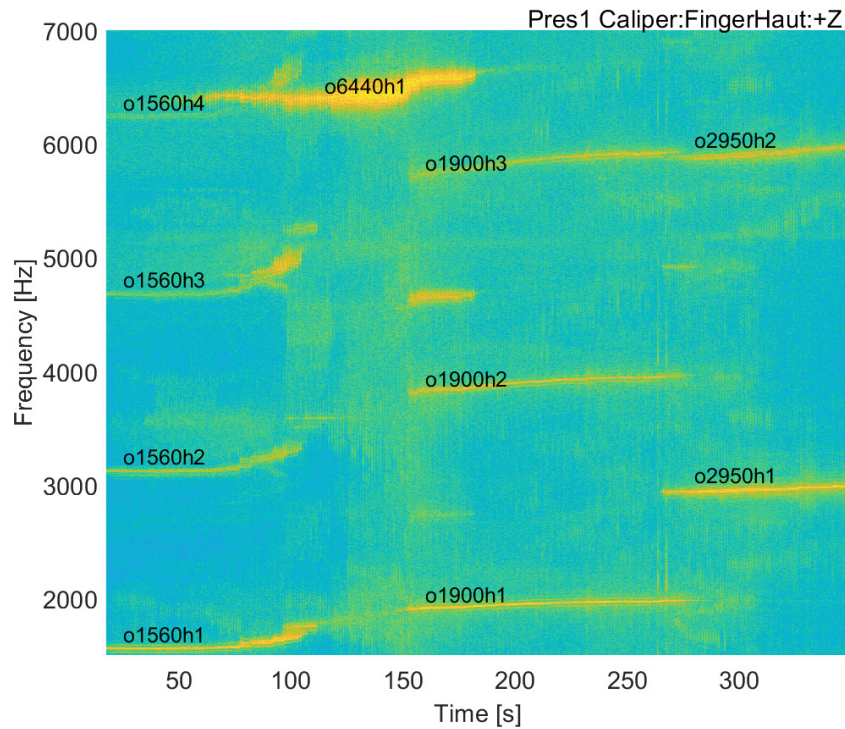


Figure A.2: Exemple de spectrogramme d'une mesure de crissement sur frein complet avec pression lentement variable. Longueur de buffer 3 secondes avec fenêtre de Hanning et overlap de 90 %.

Si la pression engendre les modifications de premier ordre sur le système, ce n'est pas le seul paramètre à prendre en considération. Pour illustrer cela, 2.2 à gauche concentre l'analyse sur la première harmonique de la vibration entre 65 et 80s. Dans cette figure, deux autres effets paramétriques sont visibles dans le spectrogramme, en plus des paliers de pression. L'un de ces effets prend la forme de fluctuations périodiques, dont la période correspond à la révolution de la roue. L'autre effet se traduit par la présence de deux bandes latérales à $\pm 30\text{Hz}$ autour de la fréquence du cycle limite du crissement. Cette modulation correspond à la fréquence de la fluctuation du couple induite par un mode de torsion de l'arbre du banc d'essai (transmettant la rotation entre la sortie de couple du banc et le disque frein).

Afin d'améliorer la résolution temporelle de l'analyse, la figure 2.2 à droite réduit la longueur du buffer du spectrogramme de 1,5 s à 0,15 s et la bande temporelle à l'intervalle entre 75 et 80. À cette échelle de temps, les fluctuations périodiques dues à la rotation des roues sont plus visibles, car la longueur du buffer est faible par rapport aux temps de variation caractéristiques. La modulation de 30 Hz, en revanche, est beaucoup moins visible car la résolution en fréquence est trop faible.

A.2. MODÈLE DE SIGNAL POUR LE CRISSEMENT

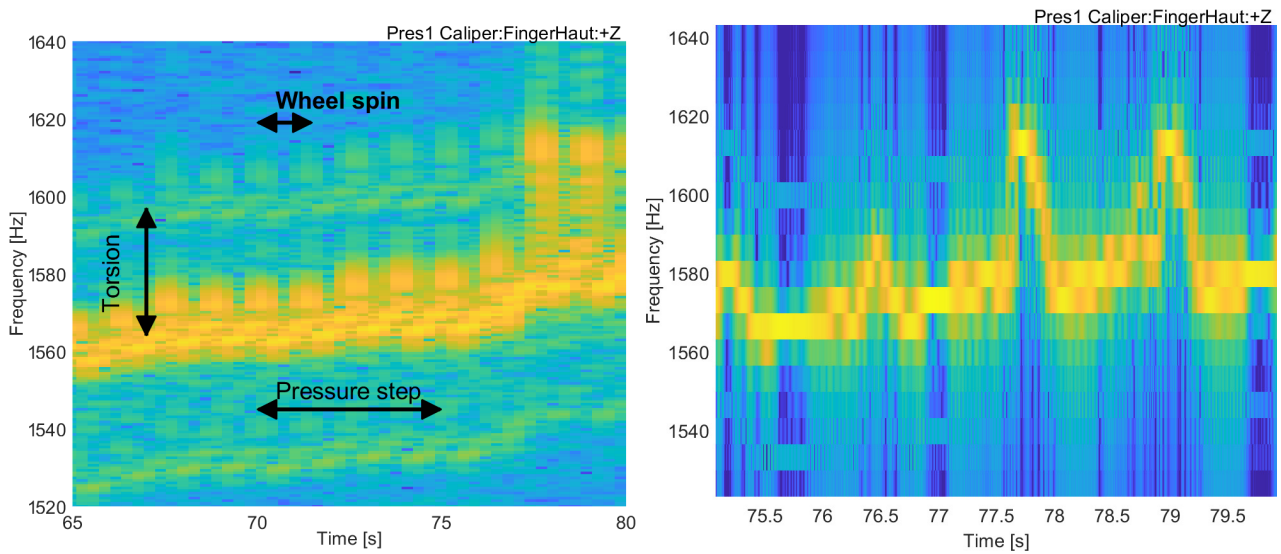


Figure A.3: Spectrogramme d'une mesure de crissement avec différentes fenêtres temporelles et longueurs de buffer, toutes deux utilisant une fenêtre de Hanning et un overlap de 90%. Gauche : entre 65 et 80s, longueur du buffer 1,5s. Droite : Entre 75 et 80s, longueur du buffer 0,15s.

Les temps caractéristiques d'évolution des paramètres dans le système de frein sont illustrés dans la figure A.4 et peuvent être comparés avec la fréquence de vibration du cycle limite. La température varie très lentement (temps caractéristique arbitrairement fixé à 20s). Les pas de pression ont été effectués avec un intervalle d'environ 5s. La période de rotation de la roue est d'environ 1,3s (pour une vitesse de 6km/h). Le mode de torsion dans l'essieu du système induit des fluctuations proches de 30Hz (période de 0.03s). Enfin, le crissement génère des oscillations quasi-périodiques, supérieures à 1,5kHz ici.

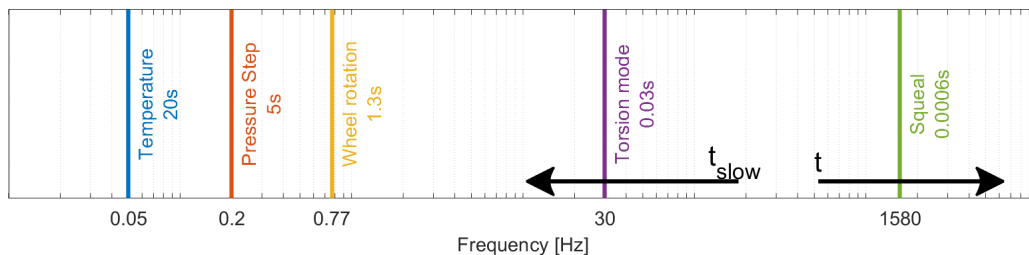


Figure A.4: Comparaison des temps caractéristiques des différentes variations paramétriques et de la vibration du crissement. Les flèches indiquent la séparation entre les échelles de temps rapides et lentes.

On observe une séparation d'échelles de temps de presque deux ordres de grandeur entre la fréquence la plus basse du cycle limite et l'évolution paramétrique la plus rapide. Malgré cette séparation, l'extraction des caractéristiques principales du cycle limite à l'aide d'un spectrogramme comme fait ci-dessus n'est pas si simple avec une dépendance importante aux réglages des tailles de buffers et l'obtention de fréquences discrètes. Un modèle de signal est donc proposé.

Les vibrations issues du crissement peuvent être considérées comme un cycle limite quasi-périodique

A.2. MODÈLE DE SIGNAL POUR LE CRISSEMENT

avec présence d'harmoniques et variation lente de la fréquence fondamentale et de la forme de vibration induite par les paramètres. Pour représenter ce type de vibration, nous avons proposé le modèle de signal (A.1) inspiré du classique modèle de signal analytique [28] auquel ont été ajoutés la notion de formes (fréquence commune à tous les capteurs), les harmoniques supérieures et où la variation lente de la fréquence de des formes harmoniques est explicitées (t_{slow}) On appelle ce modèle de signal HBV (*Harmonic Balance Vector*).

$$\{q_{HBV}(t)\} = Re \left(\sum_h \{q_h(t_{slow})\} e^{ih \int_0^t \omega(t_{slow}) dt} \right). \quad (A.1)$$

Lors des mesures d'essai, il est possible de remarquer la présence d'un bruit large bande introduit par le contact frottant et d'autres écarts entre la mesure et le modèle de signal (saturation des capteurs, effets non représentés pas le modèle de signal,...). Cela signifie qu'un reste d'identification peut être trouvé après avoir extrait le signal HBV d'une mesure. On notera ce reste $\{q_{Rest}\}$.

$$\{q_{Test}\} = \{q_{HBV}\} + \{q_{Rest}\} \quad (A.2)$$

A.2.2 Extraction des composantes du signal HBV

Après avoir défini le modèle de signal HBV (A.1), examinons maintenant comment estimer ses paramètres à partir d'un signal mesuré. Considérant que le modèle de signal HBV est une extension des signaux analytiques qui impose une fréquence fondamentale et ses harmoniques communes à plusieurs capteurs, il est naturel de considérer que les algorithmes utilisés pour estimer un signal analytique peuvent également être utilisés ici. La démodulation synchrone (figure A.5) est une méthode répandue et robuste pour estimer un signal analytique, les applications les plus notables de la démodulation étant certainement l'extraction des modulations de fréquence et d'amplitude dans la radio FM et AM respectivement. Dans le domaine de la mécanique, l'utilisation de la démodulation peut être trouvée par exemple dans les contrôleurs à boucle fermée type PLL utilisés pour la caractérisation expérimentale des systèmes non linéaires [59].

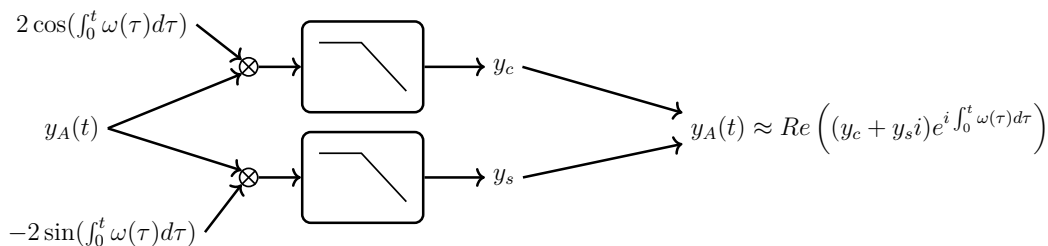


Figure A.5: Diagramme schématisant l'algorithme de démodulation synchrone

Inspirée par ces applications, cette section décrit l'utilisation de la démodulation synchrone pour extraire les différentes composantes du modèle de signal HBV (A.1). La méthode proposée est un processus en trois étapes:

1. Première démodulation à partir d'une fréquence instantanée (harmonique 1) approximée, donnant une estimation grossière de la forme associée à cette fréquence

A.2. MODÈLE DE SIGNAL POUR LE CRISSEMENT

2. Correction de la fréquence instantanée à partir de la dérive de phase de la forme extraite précédemment
3. Deuxième démodulation avec la fréquence instantanée corrigée pour améliorer l'estimation de la forme fondamentale et obtenir (également par démodulation) les formes associées aux harmoniques supérieures

La correction de la fréquence instantanée est basée sur le fait qu'un écart $\delta\omega$ entre la fréquence d'un signal analytique

$$y_A(t) = \text{Re} \left((y_c + y_s i) e^{i(\omega + \delta\omega)t} \right) = \text{Re} \left(y_1 e^{i(\omega + \delta\omega)t} \right) \quad (\text{A.3})$$

et la fréquence de démodulation ω_0 induit une variation lente des composantes sinus et cosinus estimées

$$\begin{aligned} \hat{y}_c &= y_c \cos(\delta\omega t) - y_s \sin(\delta\omega t) \\ \hat{y}_s &= y_c \sin(\delta\omega t) + y_s \cos(\delta\omega t) \end{aligned} \quad (\text{A.4})$$

Cela résulte en une dérive de phase de l'amplitude complexe estimée $\hat{y}_1 = \hat{y}_c + \hat{y}_s i$ qui est proportionnelle à $\delta\omega$

$$\delta\omega = \frac{\partial \hat{\varphi}}{\partial t} = \frac{\partial \arctan \left(\frac{\hat{y}_s}{\hat{y}_c} \right)}{\partial t} \quad (\text{A.5})$$

et peut être utilisée pour obtenir une fréquence corrigée

$$\omega(t) = \omega_0 + \delta\omega(t). \quad (\text{A.6})$$

Pour assurer que la fréquence instantanée corrigée est lentement variable comme prévu par le modèle de signal HBV, un filtre passe-bas est appliqué à $\delta\omega$. Cela aide aussi à réduire le bruit induit par la dérivation numérique de la phase. L'algorithme d'estimation obtenu, illustré dans la figure A.6, est capable d'estimer à la fois la fréquence instantanée et les formes harmoniques d'un signal HBV.

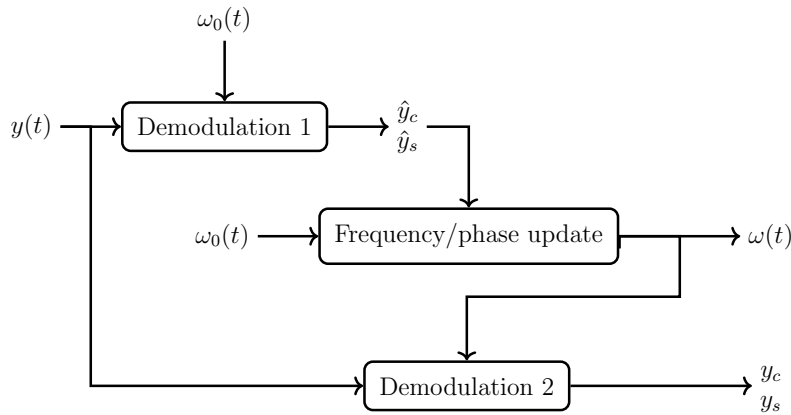


Figure A.6: Diagramme montrant l'algorithme d'estimation d'un signal HBV en 3 étapes (notations pour une mesure à un seul capteur)

Dans le cas de multiples capteurs, la correction de phase est réalisée avec l'amplitude complexe associée à la première forme principale réelle obtenue par SVD.

A.3 Modèle fonctionnel pour le crissement

Des modèles simplifiés ont été largement utilisés dans la littérature afin de caractériser les mécanismes de vibration du crissement de frein. Hoffmann [4] a notamment proposé un modèle simple à deux degrés de liberté qui décrit la formation de l'instabilité. Ce modèle fonctionnel simple a été utilisé pour montrer comment le coefficient de frottement μ et l'amortissement affectent la stabilité du système.

Notre objectif dans cette section est de proposer une version modifiée du modèle fonctionnel de Hoffmann [4] qui représente l'effet de la variation de la charge appliquée (pression) et de l'amplitude de vibration sur l'initiation du crissement et le cycle limite qui en résulte. L'utilisation d'un modèle fonctionnel vise à simplifier au maximum l'analyse tout en reproduisant les évolutions du crissement observées lors des essais. Le nouveau modèle fonctionnel, composé d'un système à deux degrés de liberté soumis à des non-linéarités de contact et de frottement, est décrit dans la section 1.2. En décrivant l'influence de la pression statique et de l'amplitude des vibrations sur les forces de contact (et donc de frottement), le modèle proposé est capable de représenter comment l'évolution des configurations de freinage influe sur couplage des modes et la saturation du cycle limite.

A.3.1 Construction du modèle fonctionnel

L'objectif du modèle fonctionnel est de représenter le mécanisme d'instabilité par couplage de modes et sa dépendance à la charge statique et à l'amplitude du cycle limite. Le modèle fonctionnel proposé, illustré dans la figure A.7, répond à de nombreuses exigences grâce aux différents éléments indiqués dans le tableau A.1. Le résultat est un système à deux degrés de liberté avec une partie linéaire composée d'une masse maintenue par deux paires de ressorts-amortisseurs dans des directions orthogonales. Ce système est censé représenter les deux modes interagissant dans une situation de crissement de frein. Une charge externe F_{Pres} , représentant la pression quasi-statique du piston, est appliquée à la masse. Le contact et le frottement sont introduits par un plan de glissement incliné selon un angle θ par rapport à la direction x . Il couple les deux modes par l'intermédiaire de la force non linéaire F_{NOR} normale au plan de glissement et de la force de frottement (loi de Coulomb) F_{TAN} tangente au plan de glissement. Dans [24], l'angle de contact θ (également appelé angle de frottement) est lié à une condition nécessaire à l'apparition du crissement. Cette condition stipule que le couplage de mode du crissement n'est possible que lorsque $0 < \tan(\theta) < \mu$ où μ est le coefficient de frottement, une condition qui est vérifiée dans le modèle fonctionnel proposé.

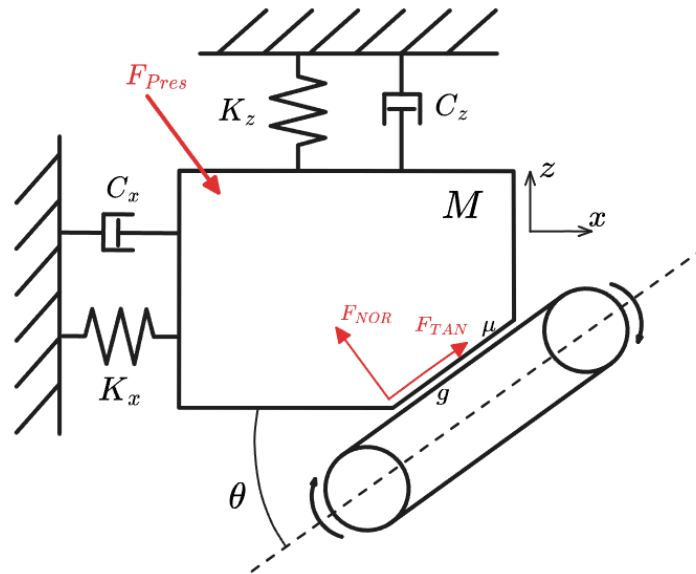


Figure A.7: Schéma du modèle fonctionnel à 2-DDL.

Table A.1: Caractéristiques du modèle fonctionnel (à gauche) et solutions (à droite)

Caractéristiques du modèle	Éléments du modèle
Le crissement est théorisé comme une bifurcation de Hopf [4, 5] et nécessite au moins deux DOF.	2 directions de translation x et z
Ajuster les fréquences modales et les amortissements	<ul style="list-style-type: none"> • Masse M, commune aux deux DDLs • Ressorts/amortisseurs K_x et C_x entre la direction x et le bâti • Ressorts/amortisseurs K_z et C_z entre la direction z et le bâti
Variation de la charge (quasi-)statique	Charge externe F_{Pres}
Force de contact sensible à la charge statique et à l'amplitude	Force de contact $F_{NOR}(g)$ dépend non-linéairement de l'interpénétration g . Cela conduit à une rigidité linéarisée qui dépend de la charge statique et de l'amplitude de vibration.
Couplage de modes par frottement	<ul style="list-style-type: none"> • $F_{TAN} = \mu F_{NOR}$ (Loi de Coulomb) • θ : inclinaison du plan de glissement par rapport à la masse pour régler le couplage

L'équation différentielle décrivant ce modèle est la suivante

$$\underbrace{\begin{bmatrix} M & 0 \\ 0 & M \end{bmatrix}}_{[M]} \begin{Bmatrix} \ddot{x} \\ \ddot{z} \end{Bmatrix} + \underbrace{\begin{bmatrix} C_x & 0 \\ 0 & C_z \end{bmatrix}}_{[C]} \begin{Bmatrix} \dot{x} \\ \dot{z} \end{Bmatrix} + \underbrace{\begin{bmatrix} K_x & 0 \\ 0 & K_z \end{bmatrix}}_{[K]} \begin{Bmatrix} x \\ z \end{Bmatrix} + \{ \tilde{F}_{NOR}(x, z) \} + \{ \tilde{F}_{TAN}(x, z) \} - \{ \tilde{F}_{Pres} \} = 0 \quad (\text{A.7})$$

et nous allons maintenant détailler l'expression complète de F_{Pres} , F_{NOR} et enfin F_{TAN} .

La charge externe \tilde{F}_{Pres} est appliquée pour représenter la pression exercée sur le système de freinage. Cette force est considérée comme statique, ou lentement variable (quasi-statique) : elle représente une évolution lente de la configuration de fonctionnement du frein.

$$\{ \tilde{F}_{Pres} \} = \begin{bmatrix} \sin(\theta) \\ -\cos(\theta) \end{bmatrix} F_{Pres}(t_{slow}) = [\tilde{b}_{Pres}] F_{Pres}(t_{slow}) \quad (\text{A.8})$$

La force F_{NOR} (normale au plan de glissement) représente la réaction de la surface de contact entre le patin et le disque. Pour simplifier, on considère ici que le contact a lieu en un seul point. Dans les modèles de freins réduits plus détaillés, on considère une distribution de la pression sur la surface de contact. Pour une surface donnée S_{Pad} , F_{NOR} est donc simplement lié à la pression de contact par $F_{NOR} = P_c(g)S_{Pad}$. $P_c(g)$ est une loi de contact non linéaire en fonction de g l'interpénétration (l'opposé de l'espace entre les surfaces). g est linéairement relié aux DOFs du modèle par l'équation d'observation.

$$g = [\tilde{c}_{NOR}] \{ q \} = \begin{bmatrix} \sin(\theta) & -\cos(\theta) \end{bmatrix} \begin{Bmatrix} x \\ z \end{Bmatrix} \quad (\text{A.9})$$

L'aspect clé pour la loi de contact est qu'elle est supposée dépendre de l'amplitude, et donc ne pas être linéaire par morceaux, ce qui est vérifié pour les surfaces qui ne sont pas considérées comme idéalement plates [23]. Dans cette thèse, la loi exponentielle utilisée par Hitachi Astemo est conservée

$$P_c(g) = p_0 e^{\lambda_c(g)} \quad (\text{A.10})$$

La force de contact normale F_{NOR} sur les DOFs du modèle est donc la suivante

$$\{ \tilde{F}_{NOR} \} = \begin{bmatrix} \sin(\theta) \\ -\cos(\theta) \end{bmatrix} F_{NOR} = \begin{bmatrix} \sin(\theta) \\ -\cos(\theta) \end{bmatrix} S_{pad} P_c(g) = [\tilde{b}_{NOR}] P_c(g) \quad (\text{A.11})$$

La force F_{TAN} (tangente au plan de glissement) représente le frottement engendré par l'effort normal F_{NOR} . Elle est modélisée à l'aide des lois de Coulomb et son amplitude est donc linéairement liée à F_{NOR} par l'intermédiaire du coefficient de frottement μ

$$F_{TAN} = \mu F_{NOR} \quad (\text{A.12})$$

On considère parfois que F_{TAN} dépend de la vitesse de glissement ([24] par exemple), mais dans le cadre de cette étude, il sera considéré comme indépendant, pour souligner que cela n'est pas nécessaire pour expliquer le mécanisme de stabilisation du cycle limite. Comme pour la force de contact, F_{TAN} peut être décrite à l'aide du formalisme d'observation/commande comme suit

$$\{\tilde{F}_{TAN}\} = \begin{bmatrix} -\cos(\theta) \\ -\sin(\theta) \end{bmatrix} F_{TAN} = - \begin{bmatrix} \cos(\theta) \\ \sin(\theta) \end{bmatrix} \mu S_{pad} P_c(g) = -\mu [\tilde{b}_{TAN}] P_c(g) \quad (\text{A.13})$$

En prenant comme référence le système linéaire obtenu en posant $\mu = 0$, il est alors possible de construire un ensemble de coordonnées modales $\{q\} = [\phi] \begin{Bmatrix} x \\ z \end{Bmatrix}$ telles que $[\phi]^T [M] [\phi] = [I]$ et $[\phi]^T [K] [\phi] = \begin{bmatrix} \omega_x^2 \\ \omega_z^2 \end{bmatrix}$. En utilisant ces coordonnées modales dans les expressions (A.8), (A.8), (A.10), (A.13) et (A.7), nous obtenons l'équation dynamique non linéaire pour le modèle fonctionnel en coordonnées modales

$$[I] \{\ddot{q}\} + \begin{bmatrix} 2\zeta_j \omega_j \end{bmatrix} \{\dot{q}\} + \begin{bmatrix} \omega_j^2 \end{bmatrix} \{q\} + [b_{NOR} - \mu b_{TAN}] P_c([c_{NOR}] \{q\}) - [b_{Pres}] F_{Pres} = 0. \quad (\text{A.14})$$

Où $[b_{NOR}] = [\phi]^T [\tilde{b}_{NOR}]$, $[c_{NOR}] = [\tilde{c}_{NOR}] [\phi]$, $[b_{TAN}] = [\phi]^T [\tilde{b}_{TAN}]$ et $[b_{Pres}] = [\phi]^T [\tilde{b}_{Pres}]$.

Bien que la représentation d'un système de freinage par un simple modèle fonctionnel puisse sembler restrictive à première vue, un développement similaire peut être appliqué à un modèle réduit à deux modes résultant de la linéarisation d'un modèle de frein complet à éléments finis. Les difficultés viennent alors du fait que la pression ne se réduit pas à un point mais est répartie sur une surface et ce champ de pression évolue avec la pression statique et l'amplitude de vibration. Des études de ce type ont été réalisées par SDTools en dehors du cadre de cette thèse.

Le modèle final proposé utilise les valeurs de paramètres indiquées dans le tableau 1.2. Elles ont été sélectionnées manuellement pour obtenir un cycle limite représentatif des résultats expérimentaux.

Table A.2: Paramètres choisis pour le modèle de crissement fonctionnel

m [kg]	ω_x [kHz]	ω_z [kHz]	ζ_x [%]	ζ_z [%]	p_0 [MPa]	λ_c [mm ⁻¹]	θ [°]	S_{Pad} [mm ²]
1	1.5	1.45	0.1	0.2	0.01	750	25	20

A.3.2 Analyse aux valeurs propres dépendant de l'amplitude

La première analyse du modèle fonctionnel est effectuée dans le domaine fréquentiel à l'aide de l'analyse des valeurs propres complexes (CEA). Ce type d'analyse de stabilité est couramment utilisé pour évaluer la présence d'instabilité menant au crissement dans les modèles industriels. La première étape est la linéarisation du système d'équation autour d'une condition de freinage qui dépend ici de la pression statique appliquée F_{Pres} . On résout donc le problème statique pour trouver $\{q_0\}$

$$\begin{bmatrix} \omega_j^2 \end{bmatrix} \{q_0\} + [b_{NOR} - \mu b_{TAN}] P_c([c_{NOR}] \{q_0\}) - [b_{Pres}] \{F_{Pres}\} = 0 \quad (\text{A.15})$$

Et on obtient la raideur linéarisée en fonction de $g_0 = [c_{NOR}] \{q_0\}$

$$K_c(g_0) = \frac{\partial P_c}{\partial(g)}(g_0) = p_0 \lambda_c e^{\lambda_c g_0} \quad (\text{A.16})$$

A.3. MODÈLE FONCTIONNEL POUR LE CRISSEMENT

En remplaçant (A.16) dans (A.14), l'équation du système devient un problème aux valeurs propres complexes dépendant de g_0 avec des solutions du type $\{q\} = \{\psi\} e^{\lambda t}$.

$$\left(\lambda^2 [I] + \lambda \left[2\zeta_j \omega_{j\setminus\lambda} \right] + \left[\omega_{j\setminus\lambda}^2 \right] + [b_{NOR} - \mu b_{TAN}] K_c(g_0) [c_{NOR}] \right) \{\psi\} = 0 \quad (\text{A.17})$$

Les modes de ce système correspondent à des solutions non triviales ($\{\psi_j\} \neq 0$) associées aux pôles $\lambda_j = -\zeta_j \omega_j + i\omega_j \sqrt{1 - \zeta_j^2}$. Un mode est instable si la partie réelle du pôle est positive, c'est-à-dire si son coefficient d'amortissement ζ_j est négatif. Dans l'analyse linéaire invariante dans le temps (LTI) classique, le système est considéré comme instable si au moins un pôle est instable.

L'évolution des fréquences propres et amortissements des pôles est montrée dans la figure A.8 pour des valeurs de charge statique F_{Pres} entre 250N et 550N. La région entre les barres verticales met en évidence la plage de charge statique [375 – 460]N pour laquelle le système est instable (amortissement négatif).

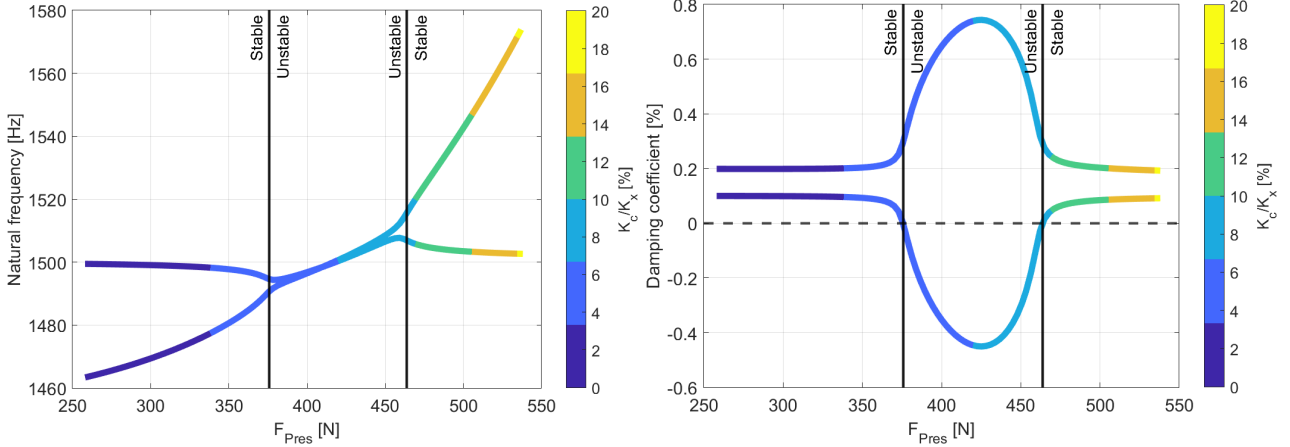


Figure A.8: Evolution des pôles du système linéarisé en fonction de la charge statique F_{pres} . A gauche : fréquence modale. A droite : coefficient d'amortissement modal. La couleur indique la rigidité de contact normalisée K_c/K_x .

Afin d'inclure l'effet d'amplitude sur la CEA, une deuxième stratégie de linéarisation basée sur la méthode de balance harmonique (Harmonic Balance Methode ou HBM) est utilisée. Dans le cadre de la méthode HBM, on calcule le travail virtuel sur une période des efforts selon les trajectoires des harmoniques (composantes des vecteurs $\{q_h\}$). On introduit la notion de rigidité équivalente en égalant le travail virtuel de la pression non linéaire $P_c(t)$ et celui de la pression engendrée par une raideur surfacique équivalente $K_h(g_0, g_1)g(t)$ par la relation

$$\int_0^{2\pi/\omega} P_c(t) e^{-ih\omega t} dt = \int_0^{2\pi/\omega} (K_h(g_0, g_1)g(t)) e^{-ih\omega t} dt. \quad (\text{A.18})$$

Une raideur surfacique de contact linéaire ayant le même travail que l'harmonique un de la pression non-linéaire vérifie donc

$$K_{c,0}(g_0, g_1) = \frac{P_{c,0}(g_0, g_1)}{g_0} \quad K_{c,1}(g_0, g_1) = \frac{P_{c,1}(g_0, g_1)}{g_1}. \quad (\text{A.19})$$

A.3. MODÈLE FONCTIONNEL POUR LE CRISSEMENT

où $P_c^0(g^0, g^1)$ et $P_c^1(g^0, g^1)$ sont le travail virtuel des harmoniques 0 et 1 de la pression de contact, la partie gauche de l'équation (A.18). En utilisant cette relation, on peut alors remplacer la pression de contact non linéaire en son équivalent linéaire dépendant de g_0 et g_1 . On obtient alors un nouveau problème aux valeurs propres

$$\left(\lambda^2 [I] + \lambda \left[\sqrt{2} \zeta_j \omega_{j\setminus} \right] + \left[\omega_{j\setminus}^2 \right] + [b_{NOR} - \mu b_{TAN}] K_c(g_0, g_1) [c_{NOR}] \right) \{ \psi \} = 0. \quad (\text{A.20})$$

La figure A.9 à gauche montre l'évolution de $K_{c,1}(g_0, g_1)/K_x$ en fonction de la charge statique et de l'amplitude. Elle montre que l'augmentation de la rigidité résultant de l'amplitude est significative par rapport à l'écart relatif entre les deux raideurs du modèle fonctionnel $\frac{|K_z - K_x|}{K_x}$, qui est de l'ordre de 6.5%. L'évolution des pôles correspondants est représentée sur la figure A.9 à droite sous la forme d'un lieu des pôles.

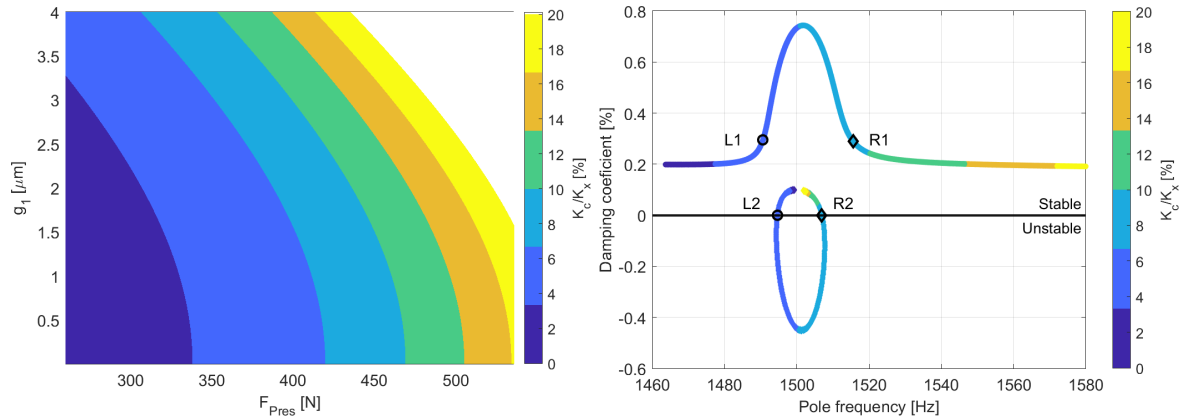


Figure A.9: Gauche: Évolution de la rigidité équivalente en fonction de la charge statique F_{pres} et de l'amplitude de la première harmonique g_1 . Droite: Pôles obtenus à partir de (1.11) pour différentes valeurs de la rigidité de contact K_c (Root Locus). Les paires de pôles correspondant au passage de la ligne $\zeta = 0$ (cycles limites) sont indiquées par L1/L2 et R1/R2.

A partir des pôles obtenus, il est alors possible de tracer l'évolution de l'amortissement modal ζ du pôle instable dans l'espace paramétrique g_0, g_1 , comme le montre la figure A.10. Les régions en rouge à gauche et à droite indiquent un amortissement positif. Ce sont les zones stables où les vibrations sont atténuées. Au milieu, une région bleue correspond à un amortissement négatif (instabilité) qui entraîne une croissance de l'amplitude. À la frontière entre les régions stables et instables, on trouve les cycles limites. Leur emplacement à la frontière signifie que tous les cycles limites possibles peuvent être trouvés en suivant les régions où l'amortissement est égal à zéro (lignes noires dans la figure A.10). Si la rigidité équivalente proposée est pertinente, on s'attend à avoir des cycles limites d'amplitude différente pour une pression statique variable. Ceci sera illustré par des simulations temporelles.

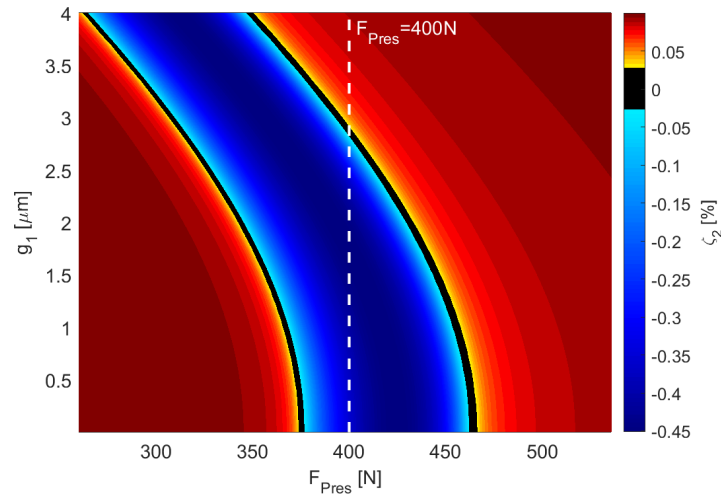


Figure A.10: Coefficient d’amortissement de l’évolution du mode instable ζ_2 en fonction de la charge statique F_{Pres} et de l’amplitude de la première harmonique g_1 . La limite de stabilité LPV est représentée par la ligne noire.

A.3.3 Comparaison entre les domaines temporel et fréquentiel

En se basant sur les résultats de la CEA dépendant de la pression statique et de l’amplitude de vibration précédemment décrits, on considère d’abord une pression appliquée F_{Pres} . Comme le montre la figure 1.9 gauche, F_{Pres} augmente lentement de zéro jusqu’à $370N$ près de la région instable (voir figure 1.7), se stabilise pendant $0.4s$ pour limiter les effets transitoires résultant de la charge initiale, puis augmente jusqu’à $385N$, ce qui déclenche l’instabilité. La figure A.11 à droite montre la réponse statique évoluant lentement avec de petites vibrations induites par le bruit jusqu’à ce que le système entre dans la région instable, où l’amplitude des vibrations augmente soudainement et atteint rapidement un cycle limite qui reste stable jusqu’à la fin de la simulation. Cela montre que le modèle proposé est capable de reproduire les mécanismes responsables de la croissance instable et de la formation d’un cycle limite.

A.3. MODÈLE FONCTIONNEL POUR LE CRISSEMENT

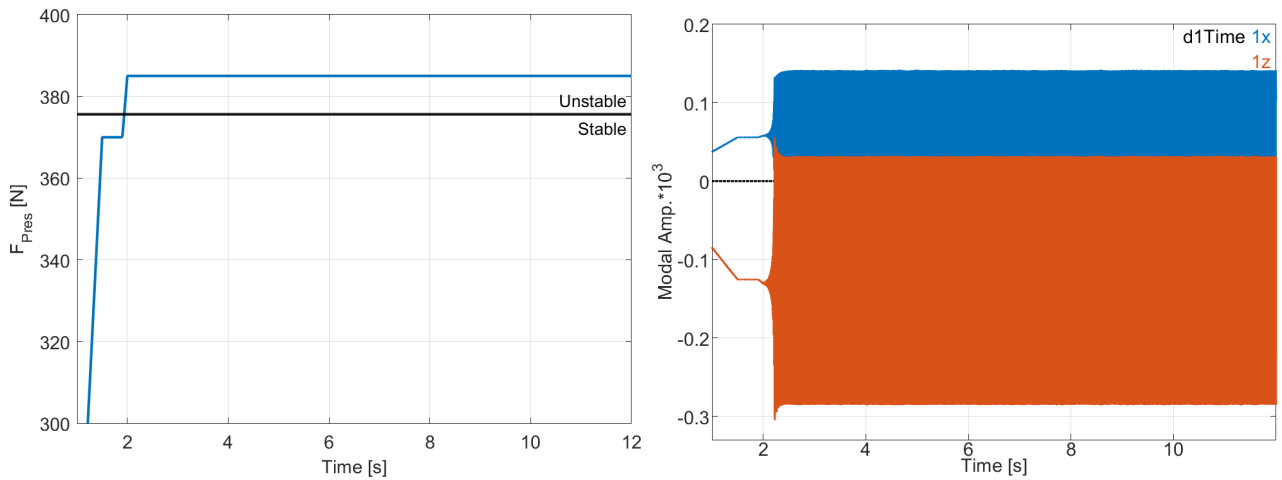


Figure A.11: A gauche : Profil de charge statique constante F_{Pres} et frontière de stabilité. A droite : Évolution des amplitudes modales au cours du temps

Dans l'analyse des valeurs propres dépendantes de l'amplitude du modèle fonctionnel détaillé dans 1.3.4, nous avons considéré que le comportement du système peut être décrit par la trajectoire du contact, plus précisément les amplitudes des harmoniques 0 et 1 de l'interpénétration g_0 et g_1 respectivement. Ces deux valeurs peuvent être extraites de l'interpénétration $g(t)$ (observation de l'interpénétration du contact à chaque échantillon de temps de la simulation temporelle) à l'aide du modèle de signal HBV et de la stratégie de démodulation décrite dans la section (1.12).

La figure 1.10 compare l'amplitude de la première harmonique du cycle limite g_1 extraite de la simulation temporelle et sa valeur attendue à partir de la CEA dépendant de l'amplitude avec $F_{pres} = 385N$. La prédiction obtenue à partir de la CEA est très proche des valeurs obtenues dans la simulation temporelle non linéaire, malgré le fait que la CEA classique ne prend en compte que les harmoniques 0 et 1 pour estimer le cycle limite.

A.3. MODÈLE FONCTIONNEL POUR LE CRISSEMENT

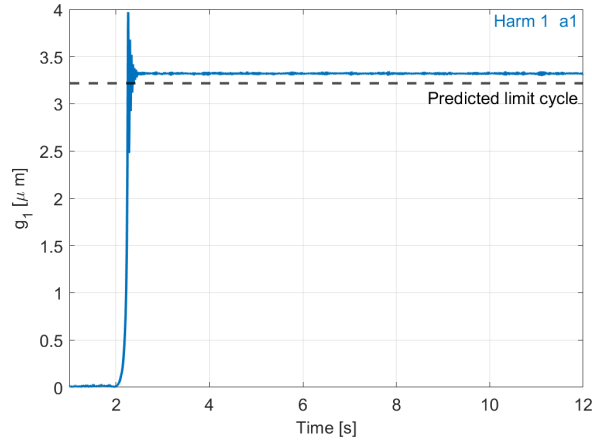


Figure A.12: Évolution de $g_1(t)$ extraite de la simulation transitoire décrite dans la figure 1.9 utilisant la démodulation (-) comparée à l'amplitude du cycle limite prédite en utilisant la CEA dépendante de l'amplitude (- -).

Ensuite, le même type d'analyse est appliqué à des simulation temporelles avec d'autres profils de pression comme le profil de croissance linéaire montré dans la figure A.13. En traçant l'évolution de $g_1(t)$ avec $F_{pres}(t)$ par rapport à la stabilité prévue par l'analyse aux valeurs propres, il est très clair que dès que le système entre dans la plage instable, l'amplitude de vibration augmente rapidement. À mesure que l'amplitude augmente, l'influence des non-linéarités du système s'accroît, induisant une saturation de l'évolution de l'amplitude près de la limite supérieure de stabilité. À partir de ce point, l'amplitude du cycle limite suit de près celle prédite par l'analyse aux valeurs propres jusqu'à la fin de la zone instable. Cette superposition montre que l'utilisation de la première harmonique extraite de la simulation temporelle est comparable aux résultats des valeurs propres dépendant de l'amplitude.

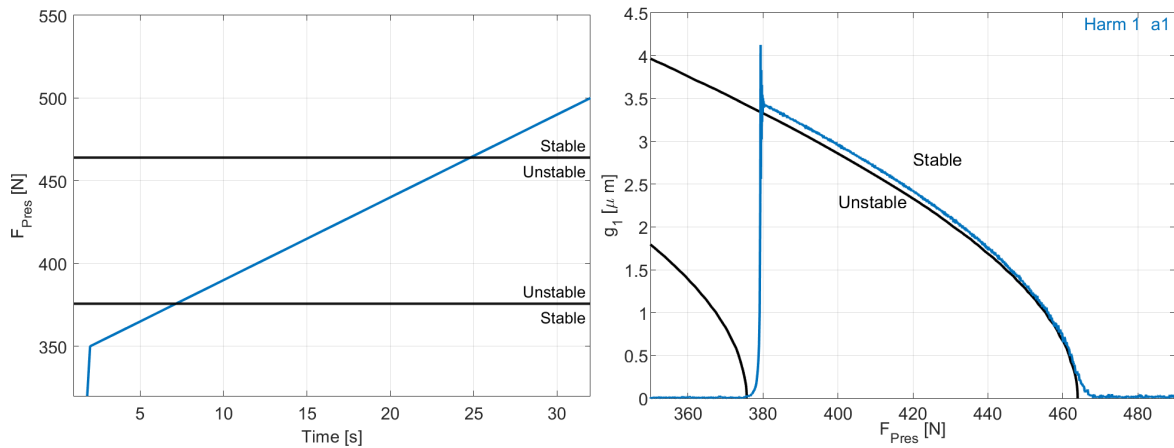


Figure A.13: A gauche : Profil de charge statique F_{Pres} de la rampe lente et frontières de stabilité. A droite : Première composante harmonique de l'interpénétration $g_1(t)$ extraite à l'aide de la démodulation (bleu) et limite de stabilité obtenue à partir de la CEA dépendante de l'amplitude (noir) en fonction de F_{Pres} .

A.4 Essais sur banc complet

Les essais ont été réalisés sur un banc d'essai inertiel de Hitachi Astemo en utilisant un système de frein modifié. Tous les patchs viscoélastiques ont été enlevés et la composition du matériau de friction ainsi que la forme du contact ont été modifiées afin d'augmenter la probabilité d'apparition d'un crissement. Le système de freinage est maintenu par la suspension réelle du véhicule et est relié au banc d'essai par un arbre connecté au côté intérieur du frein. La partie avant du disque est donc orientée vers l'extérieur, comme le montre la figure A.14.



Figure A.14: Système de freinage sur le banc d'essai, setup 2023.

Les mesures réalisées sur ce banc d'essai ont pour objectif de caractériser les dépendances paramétriques du système de frein avec un focus particulier sur l'effet des variations lentes des paramètres. L'analyse de ces essais est divisée en trois parties, chacune correspondant à un type de mesure: mesure de crissement paramétrique, analyse modale en condition opérationnelle, et mesure de forme détaillée par vibromètre laser.

A.4.1 Mesures de crissement paramétrique

Dans les essais paramétriques sans excitation, notre objectif est d'illustrer la sensibilité du crissement aux paramètres de fonctionnement et de décrire leur effet sur les vibrations du cycle limite. Le premier paramètre étudié est la pression. Des rampes lentes de la pression, tout en maintenant une vitesse de roue constante ont été réalisées. Trois de ces mesures sont analysées dans cette section, les profils de pression appliqués étant présentés dans la figure A.15 à gauche. La température, représentée sur la figure A.15 à droite, évolue lentement lors d'un freinage continu. Il s'agit d'un paramètre non contrôlé qui augmente en raison de la dissipation d'énergie. D'autres variations non contrôlées de

paramètres sont la position angulaire de la roue et un mode de torsion de l'arbre en sortie de couple du banc d'essai, qui seront examinés plus loin.

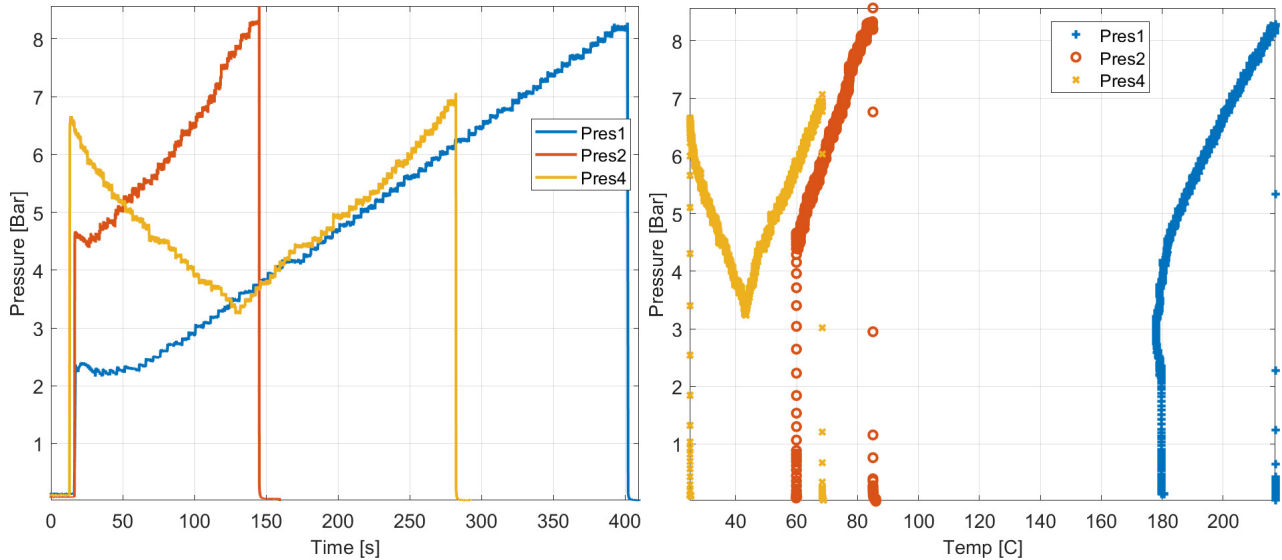


Figure A.15: A gauche : rampes de pression. A droite : profils de pression en fonction de la température.

Comme prévu dans cette expérience, les crissements se produisent très facilement et le changement progressif de pression permet de suivre son évolution. Le premier essai, intitulé **Pres1** dans la figure A.15 à gauche, a été effectué à 6km/h avec une pression augmentant de 1,5 à 9bar . Le spectrogramme de la figure A.16 illustre au moins trois grandes plages de fonctionnement. Au début de la mesure, une instabilité se produit autour de 1560 Hz, avec 4 harmoniques visibles étiquetées **o1560h1** dans le tracé. Vers 100s (3 Bar), une seconde instabilité se développe autour de 6440 Hz, les deux instabilités semblant coïncider. Près de 6 bar (280s), une autre transition se produit et la fréquence du cycle limite est proche de 3 kHz.

Le deuxième essai **Pres2** est une répétition partielle de l'essai **Pres1** dans des conditions légèrement différentes. La vitesse de la roue correspond à 5km/h et la pression est augmentée de 4 à 9bar . L'accent est mis sur le cycle limite de 3 kHz et une transition apparaît plus précisément vers 5,5 bar (65s). La question posée dans ce test est de savoir si **o2710h1** se transforme continuellement en **o3050h1** ou si cela se produit avec un changement notable dans les interactions modales. En d'autres termes, faut-il considérer qu'il s'agit d'une seule occurrence de crissement ou faut-il définir différents groupes ? La réponse, qui sera donnée dans les figures 3.17, 3.18, 3.19, est qu'il existe trois groupes.

Le dernier essai **Pres4** à 5km/h vise à étudier la reproductibilité paramétrique, lors de l'augmentation et de la diminution de la pression. Des cycles limites de grande amplitude sont effectivement trouvés à la fois lors de la diminution et de la ré-augmentation de la pression à des fréquences similaires. Comme dans le cas de l'essai Pres2, les transitions entre des fréquences distinctes sont proches de 3 kHz. Un certain nombre de caractéristiques sont intéressantes : qu'est-ce qui est constant dans les deux occurrences de **o2710h1** qui diffèrent principalement par la température (augmentation continue montrée dans la figure A.15 à droite) ? Faut-il considérer que **o2710h1** et **o2900h1** sont différentes ? Peut-on étudier l'interaction entre **o2710h2** près de 5420 Hz et l'occurrence de **o5200h1** ? Ces deux

cycles limites se produisent-ils en même temps ?

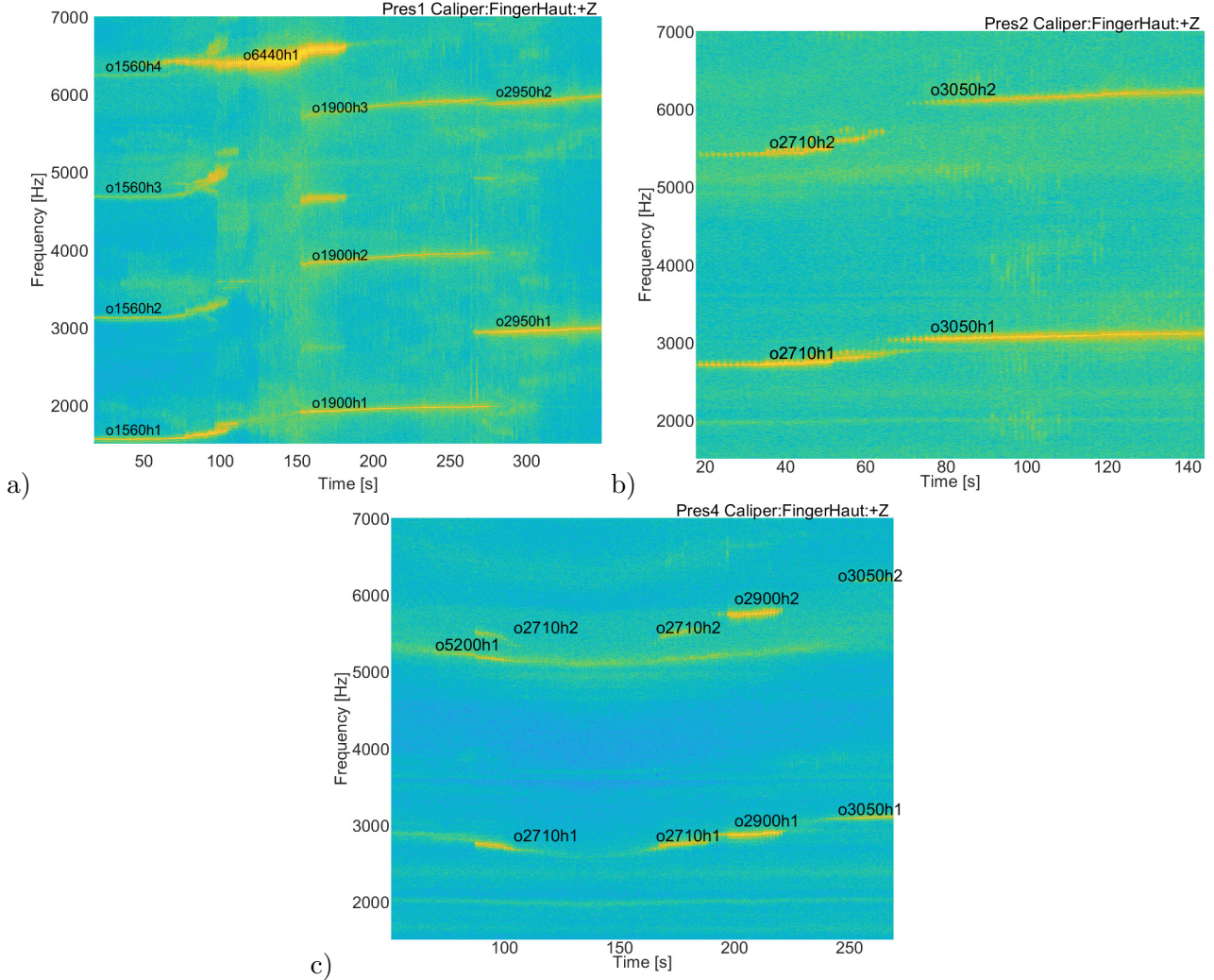


Figure A.16: Spectrogramme utilisant des buffers de temps de 1 tour de roue pour les essais a) **Pres1**, b) **Pres2**, c) **Pres4**. Le texte indique les harmoniques des cycles limites qui seront examinés.

Pour analyser ces mesures, les signaux mesurés sont décomposés par le modèle de signal HBV pour obtenir une fréquence instantanée $\omega(t_{slow})$ un vecteur d'amplitudes $\{q_1(t_{slow})\}$ (formes de l'harmonique fondamentale). Ces caractéristiques extraites de la mesure permettent d'analyser et classifier (clustering) les occurrences de crissement.

La figure A.17 illustre cette classification pour la mesure **Pres2**. La figure A.17 à gauche montre l'évolution de la fréquence du crissement sur un spectrogramme obtenu avec une taille de buffer de 1,5 s. Dans le spectrogramme, on observe trois zones distinctes de forte amplitude qui évoluent lentement avec la pression. Le signal HBV extrait une fréquence commune à tous les capteurs montrée dans la figure A.17 au milieu. Cette fréquence combinée avec l'amplitude globale (norme hermitienne, montrée par la couleur et la transparence) permet de distinguer trois groupes (notés A, B et C). Le tracé de l'amplitude globale en fonction de la fréquence instantanée dans la figure A.17 à droite fait apparaître

les groupes comme des pics. L'ajout de la pression en couleur permet de montrer la dépendance des ces groupes à la pression.

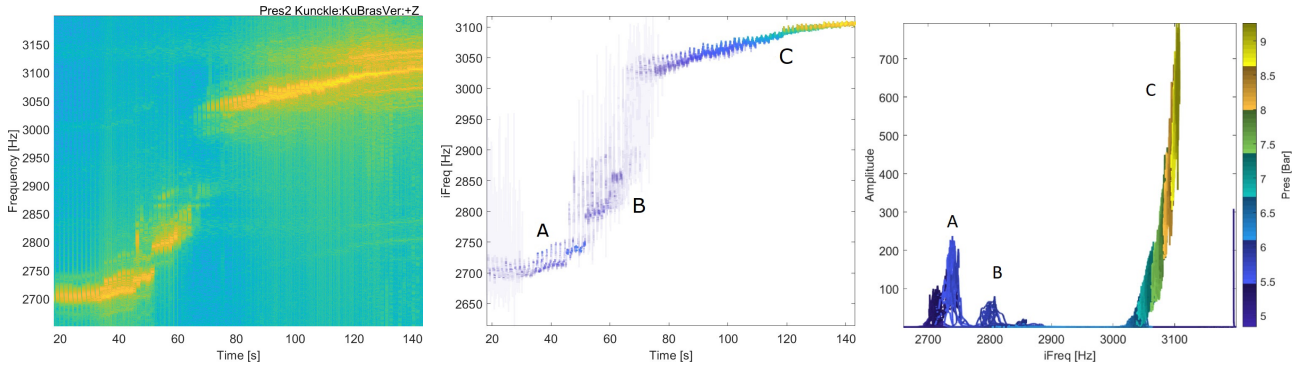


Figure A.17: A gauche : spectrogramme pour l'essai [pres2](#). Au milieu : fréquence instantanée en fonction du temps et de l'amplitude globale (en couleur et transparence). A droite : amplitude globale en fonction de la fréquence instantanée et de la pression (en couleur).

La section 3.3.3 décrit plus en détail cette classification des trois groupes de crissement, en particulier comme on peut considérer dans cette classification l'évolution des formes.

A.4.2 Analyse modale en condition opérationnelle

Afin d'obtenir une caractérisation de l'évolution du système proche du crissement, cette section décrit une analyse modale expérimentale paramétrique réalisée en condition de fonctionnement (glissement). Un pot vibrant est fixé au système pour l'exciter de façon contrôlée. Une excitation de type balayage sinus est utilisée pour caractériser le comportement du système autour des fréquences où le crissement est susceptible d'apparaître.

La figure A.18 montre le spectrogramme de l'effort imposé (à gauche) ainsi que l'évolution de la pression de freinage (à droite). Les lignes d'apparence verticales (qui sont en réalité diagonales) correspondent à l'excitation par balayage sinus. Outre ces lignes, on peut noter la présence de trois plages temporelles "inattendues" dans le signal de force où de fortes amplitudes parasites apparaissent : l'effort réel ne correspond pas à la consigne souhaitée. Ces taches apparaissent aux mêmes moments et aux mêmes fréquences que le crissement (zones grises dans la figure A.18 à droite), ce qui indique qu'à ces fréquences la vibration de la structure engendre un effort injecté par le pôt vibrant supérieur à la consigne souhaitée : on ne contrôle plus l'effort imposé. Cette combinaison d'effets accroît la difficulté de l'analyse car, dans les systèmes non linéaires, la réponse à une somme de charges n'est pas la somme des réponses individuelles à chacune de ces charges.

La première zone de crissement correspond à la pression la plus élevée avec une occurrence du crissement autour de 3100Hz. Les deuxième et troisième régions montrent que les deux occurrences autour de 2900 Hz se produisent à des plages de pression similaires. Les points sur la figure A.18 à droite indiquent les configurations de pression desquels les transferts sont extraits pour réaliser l'analyse modale expérimentale.

A.4. ESSAIS SUR BANC COMPLET

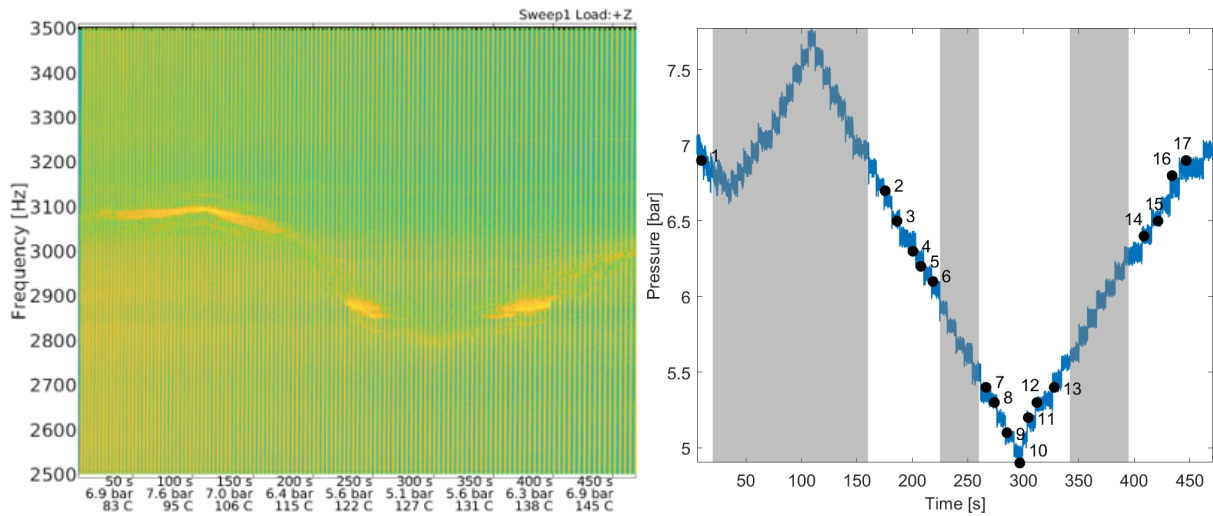


Figure A.18: Gauche : spectrogramme de l'effort appliqué dans l'essai de balayage paramétrique sur toute la durée de la mesure, avec indication de la pression et de la température. Droite : Évolution de la pression appliquée avec indication des zones de crissement de forte amplitude (zones grises) et des points de pression sélectionnés pour l'analyse modale expérimentale dans la section 3.4.3 (points).

Afin de mieux analyser les fonctions de transfert, les points sélectionnés ont été divisés en trois groupes. Par simplicité, seul le premier sera analysé ici. Ce premier groupe de fonctions de transfert, montré en figure A.19, contient les cinq balayages sélectionnés entre les deux premières occurrences de crissement. Les résonances, hors de la zone grise centrale, entre 2900Hz et 3050Hz, ne sont pas très sensibles à la variation de pression. Dans la zone grise, une tendance au déplacement vers la gauche peut être clairement observée lorsque la pression diminue. Ce pic d'amplitude se déplace entre les deux occurrences de crissement observées dans la figure A.18 près de 3050Hz pour 6,7 bar et près de 2900Hz pour 6,1 bar. on note que dans la bande fréquence correspondant à la zone grise dans la figure A.19, la cohérence associée au couple entre/sortie sur transfert est faible, ne permettant pas une analyse en terme de modes.

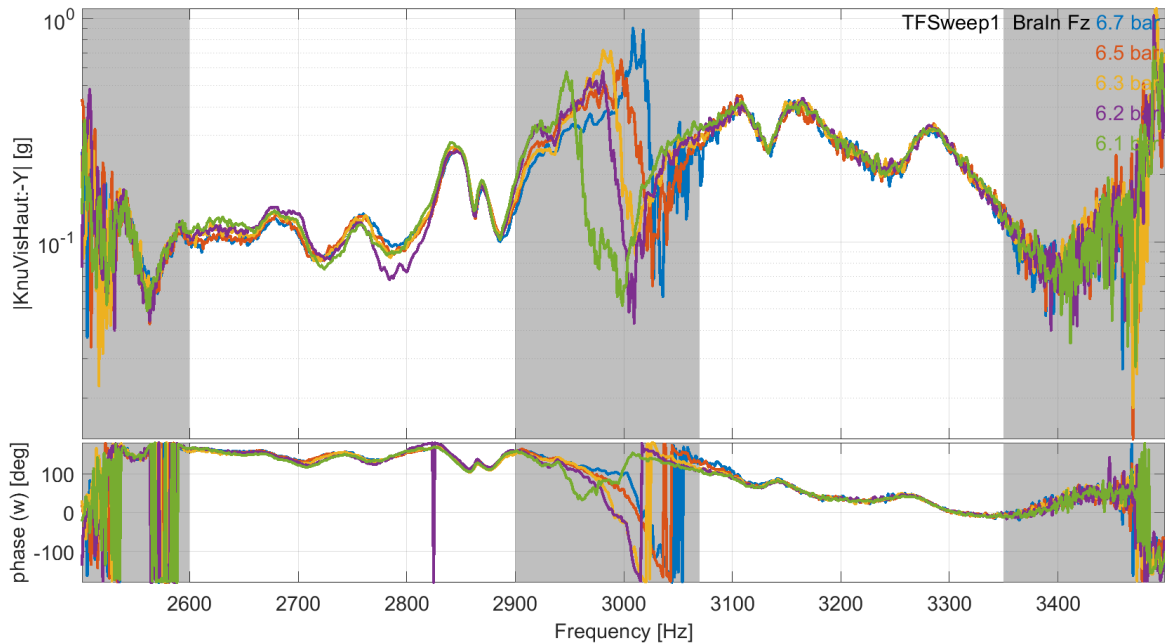


Figure A.19: Superposition des fonctions de transfert décrivant la réponse du système en réponse à un balayage sinus, pour les événements sélectionnés dans le groupe 1. Les zones grises indiquent les régions où une faible cohérence a été détectée.

Pour chaque transfert, les modes du système sont identifiés à l'aide de l'algorithme IDRC (implémenté dans le logiciel SDT [54]), en utilisant autant de modèles pôles résidus locaux que de résonances (1 mode complexe + termes résiduels haut et bas dans une bande étroite autour des résonances). L'identification modale pour la première pression est réalisée manuellement en fournissant les fréquences de résonance. Ensuite, les modèles locaux sont optimisés de pression en pression pour minimiser l'écart entre la synthèse du transfert et le transfert mesuré, permettant d'obtenir fréquence, amortissement et forme de chaque mode et pour chaque pression.

Deux facteurs différents font que cette identification n'est pas simple. La difficulté la plus notable est la présence de forces non linéaires internes de frottement de contact. Ces forces internes agissent comme une source secondaire d'énergie et provoquent la perte de cohérence observée.

Les pôles identifiés sont affichés dans la figure A.20, il est possible de voir que les pôles situés en dehors de bande grise présentent une très faible variation à la fois de la fréquence et de l'amortissement. Les pôles 4 et 6 présentent une variation plus importante de l'amortissement que de la fréquence. Il est cependant difficile de dire si ces variations d'amortissement résultent des difficultés de mesure (cohérence faible) ou des variations de pression. Les effets de la pression sont beaucoup plus clairement visibles sur le pôle 5, qui reproduit le décalage de fréquence observé précédemment sur la figure A.19.

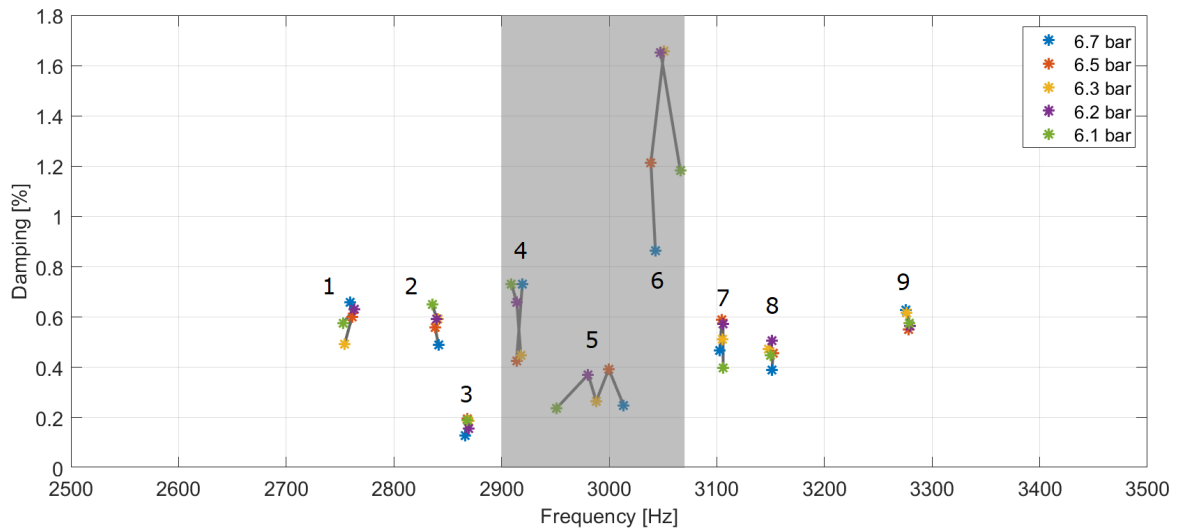


Figure A.20: Évolution des pôles identifiés pour la fonction de transfert du groupe 1. Les zones grises indiquent les régions où une faible cohérence a été détectée dans au moins une mesure.

A.4.3 Mesure de forme détaillée par vibromètre laser

Finalement, cette section exploite les mesures du vibromètre laser utilisées pour obtenir des caractérisations spatiales détaillées des cycles limites. L'extraction des formes détaillées des cycles limites constitue une base importante pour proposer des mesures correctives sur la conception d'un frein. Dans les mesures 3D-SLDV, la vitesse de vibration est mesurée séquentiellement pour une série de points sur la surface du système avec quelques accéléromètres de référence fixes. Deux vues différentes (frontale et miroir) sont utilisées pour capturer les vibrations dans une large zone du disque de frein, de l'étrier, de la chape et de la plaquette extérieure. Les deux vues sont indiquées dans la figure A.21.

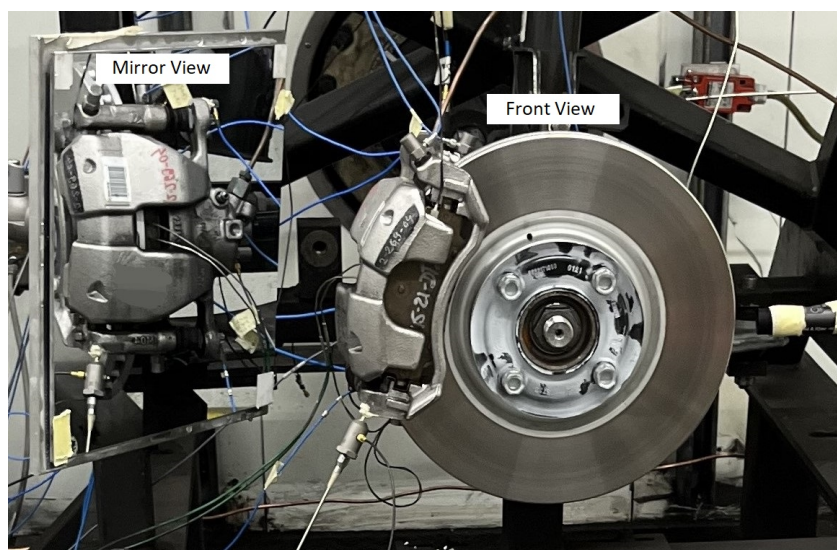


Figure A.21: Système de frein avec vues frontale et miroir

A.4. ESSAIS SUR BANC COMPLET

Le modèle de signal HBV est utilisé pour extraire les formes complexes de vibration à partir des mesures temporelles du vibromètre. La figure A.22 montre l'animation de la forme complexe obtenue pour une occurrence de crissement proche de 2kHz.



Figure A.22: Images de l'animation (différentes phases de la forme complexe) montrant la forme de la première harmonique obtenue à partir des signaux HBV séquentiels recombinaés

En plus de la forme correspondant à la première harmonique, la méthode utilisée pour extraire la forme de la figure A.22 nous donne accès aux formes des harmoniques supérieures. Les figures A.23 et A.24 montrent les formes correspondant respectivement aux harmoniques 2 et 3 du cycle limite. Les formes obtenues sont raisonnablement lisses. Il est possible de constater qu'avec l'augmentation de la fréquence, le nombre de lobes dans le disque passe progressivement de 3 pour la première harmonique à 5 pour la troisième harmonique. La différence entre les formes des harmoniques met en évidence le fait que chaque harmonique répond différemment au harmoniques des efforts non-linéaires à la surface du contact frottant.

A.5. CONCLUSION

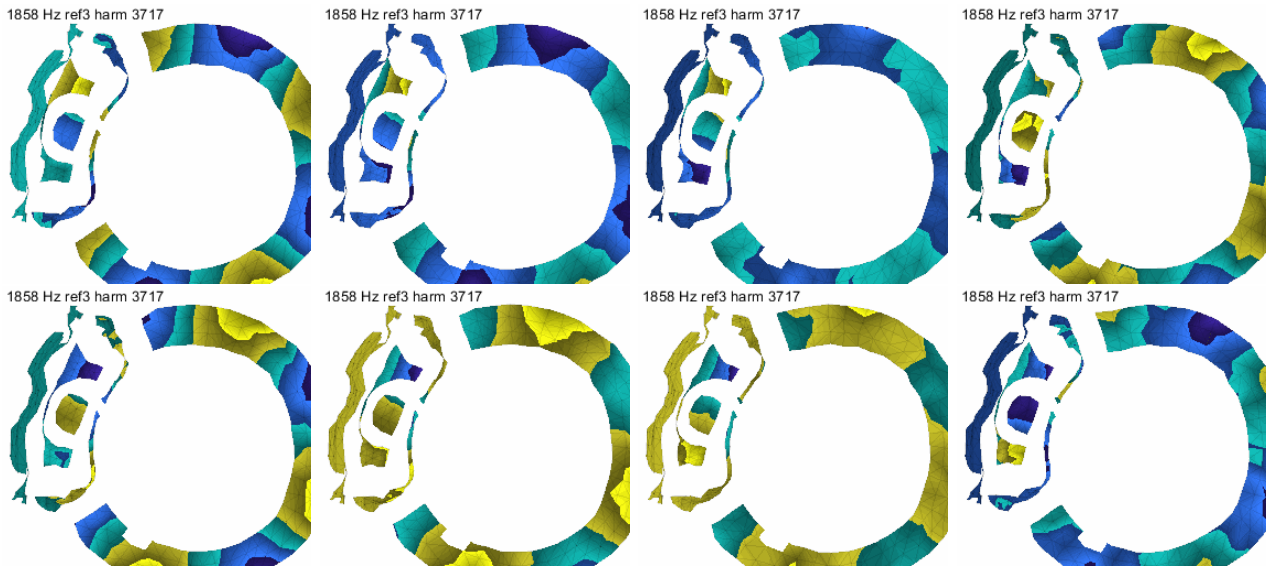


Figure A.23: Images de l'animation montrant la forme de la seconde harmonique obtenue à partir du signal du HBV

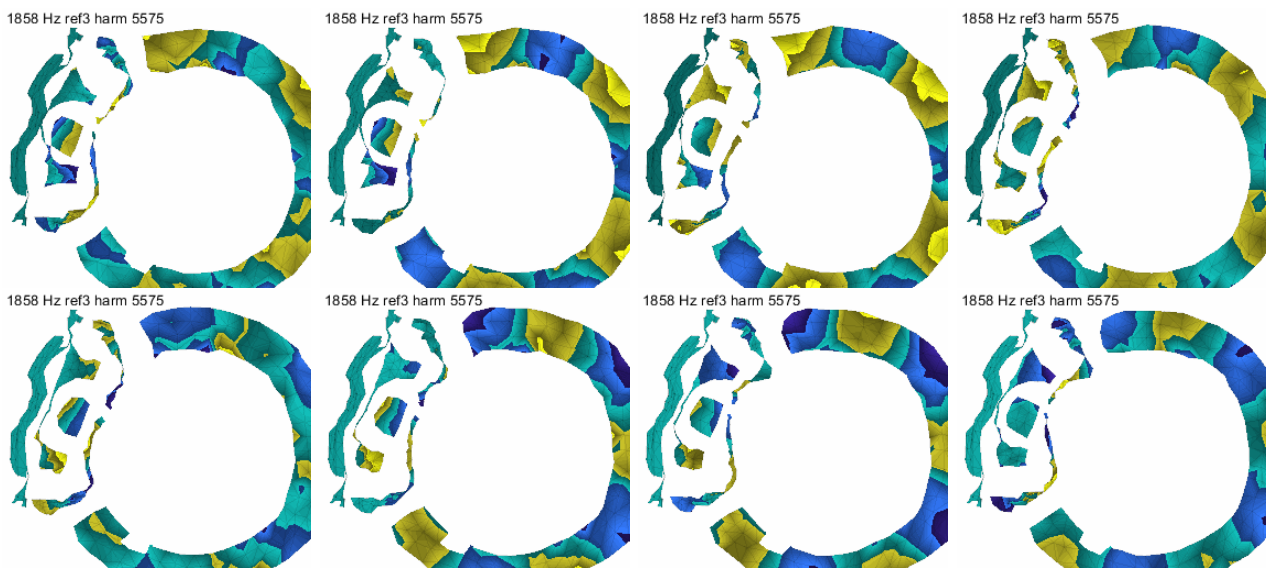


Figure A.24: Images de l'animation montrant la forme de la troisième harmonique obtenue à partir du signal du HBV

A.5 Conclusion

Le crissement de frein est un phénomène complexe qui fait l'objet d'études depuis de nombreuses années. Malgré cela, il n'existe pas de méthode de conception robuste pour le prévenir. Les mesures correctives reposent en grande partie sur le prototypage et la validation, ce qui est long et coûteux.

Ce travail a donc cherché à proposer et à analyser de nouvelles méthodes d'essais.

L'utilisation du modèle de signal HBV s'est avérée être un outil efficace pour analyser les variations paramétriques du crissement des frein. Son application aux mesures de crissement nous a permis d'obtenir une meilleure caractérisation et classification des occurrences de crissement. L'application du modèle de signal HBV pour caractériser le crissement s'est révélée être un processus robuste capable de traiter de grands ensembles de données en un temps raisonnable. Cela confirme que la stratégie proposée pourrait être automatisée et intégrée dans des procédures industrielles.

Afin de mieux comprendre l'influence des paramètres du système de frein sur crissement, un nouveau modèle fonctionnel pour le crissement est proposé. Comme dans le modèle bien connu de Hoffmann [4], deux translations d'une masse permettent de représenter le crissement comme résultant d'un couplage de mode. La nouveauté réside dans le remplacement de l'hypothèse de coefficient de frottement variable par une loi de contact non linéaire, qui introduit une sensibilité à la pression appliquée (puisque l'état statique est modifié par elle) et à l'amplitude (par son effet sur le contact non linéaire).

La réalisation sur banc d'essai industriel d'une analyse modale paramétrique en condition de fonctionnement a montré que, loin de la fréquence de crissement (au moins 100 Hz ou 3%, ce qui est encore assez proche), les modes sont bien identifiés et ne sont pas très sensibles aux petites variations de pression. Dans les régions proches du crissement, les faibles valeurs de cohérence indiquent que l'interprétation des résonances ou des pôles identifiés est difficile et se limite à dire que les fréquences des pôles suivent les mêmes tendances que les fréquences du crissement. Cela suggère que, près des fréquences de crissement, d'autres méthodes telles que l'excitation en résonance de phase sont nécessaires.

Dans l'analyse des mesures par vibrométrie laser, l'application du modèle de signal HBV caractérise la vibration comme une somme d'harmoniques. Cela nous permet de définir et d'extraire des formes spatialement détaillées correspondant aux harmoniques supérieures, en plus de la forme obtenue pour l'harmonique fondamentale. Les formes extraites ont permis de mettre en évidence la manière dont les non-linéarités excitent la structure aux harmoniques supérieures à 1.

Bibliography

- [1] A. Akay, “Acoustics of friction,” *The Journal of the Acoustical Society of America*, vol. 111, pp. 1525–1548, Apr. 2002.
- [2] R. T. Spurr, “A Theory of Brake Squeal,” *Proceedings of the Institution of Mechanical Engineers: Automobile Division*, vol. 15, pp. 33–52, Jan. 1961.
- [3] F. Moirrot, *Etude de La Stabilité d’un Équilibre En Présence de Frottement de Coulomb*. PhD thesis, Ecole Polytechnique, 1998.
- [4] N. Hoffmann and L. Gaul, “Effects of damping on mode-coupling instability in friction induced oscillations,” *ZAMM*, vol. 83, pp. 524–534, Aug. 2003.
- [5] H. Hetzler, “Bifurcation Analysis for Brake Squeal,” in *ASME 2010 10th Biennial Conference on Engineering Systems Design and Analysis*, pp. 253–262, American Society of Mechanical Engineers Digital Collection, Dec. 2010.
- [6] J. D. Fieldhouse and P. Newcomb, “The Application of Holographic Interferometry to the Study of Disc Brake Noise,” SAE Technical Paper 930805, SAE International, Warrendale, PA, Mar. 1993.
- [7] A. Akay, O. Giannini, F. Massi, and A. Sestieri, “Disc brake squeal characterization through simplified test rigs,” *Mechanical Systems and Signal Processing*, vol. 23, pp. 2590–2607, Nov. 2009.
- [8] S. Besset, D. Lenoir, and J.-J. Sinou, “Brake Squeal Investigations Based on Acoustic Measurements Performed on the FIVE@ECL Experimental Test Bench,” *Applied Sciences*, vol. 13, p. 12246, Jan. 2023.
- [9] F. Renaud, G. Chevallier, J.-L. Dion, and G. Taudière, “Motion capture of a pad measured with accelerometers during squeal noise in a real brake system,” *Mechanical Systems and Signal Processing*, vol. 33, pp. 155–166, 2012.
- [10] S. Huemer-Kals, J. Kappauf, M. Zacharczuk, H. Hetzler, K. Häsler, and P. Fischer, “Advancements on bifurcation behavior and operational deflection shapes of disk brake creep groan,” *Journal of Sound and Vibration*, vol. 534, p. 116978, Sept. 2022.
- [11] S. Koch, H. Gödecker, and U. von Wagner, “On the interrelation of equilibrium positions and work of friction forces on brake squeal,” *Archive of Applied Mechanics*, vol. 92, pp. 771–784, Mar. 2022.

BIBLIOGRAPHY

- [12] N. Strubel, *Brake Squeal : Identification and Influence of Frictional Contact Localizations*. These de doctorat, Université de Lille, Dec. 2023.
- [13] G. Vermot Des Roches, *Frequency and Time Simulation of Squeal Instabilities. Application to the Design of Industrial Automotive Brakes*. PhD thesis, Ecole Centrale Paris, CIFRE SDTools, 2011.
- [14] S. Besset and J. J. Sinou, “Modal reduction of brake squeal systems using complex interface modes,” *Mechanical Systems and Signal Processing*, vol. 85, pp. 896–911, Feb. 2017.
- [15] S. Nacivet and J.-J. Sinou, “Modal Amplitude Stability Analysis and its application to brake squeal,” *Applied Acoustics*, vol. 116, pp. 127–138, Jan. 2017.
- [16] S. Koch, N. Gräbner, and U. von Wagner, “A minimal model for the influence of equilibrium positions on brake squeal,” *GAMM-Mitteilungen*, vol. 46, no. 1, p. e202300001, 2023.
- [17] G. Martin, *Méthodes de Corrélation Calcul/Essai Pour l’analyse Du Crissement*. Ph.D. thesis, CIFRE SDTools, Arts et Metiers ParisTech, Paris, Mar. 2017.
- [18] G. Martin, E. Balmes, T. Chancelier, S. Thouviot, and R. Lemarie, “A Structural Dynamics Modification Strategy based on Expanded Squeal Operational Deflection Shapes,” in *EuroBrake 2022 - Technical Content*, FISITA, May 2022.
- [19] K. Soobbarayen, S. Besset, and J.-J. Sinou, “Influence of physical parameters and operating conditions for structural integrity of mechanical system subjected to squeal noise,” *Key Engineering Materials*, vol. 569–570, pp. 1076–1084, 2013.
- [20] L. Zhang, J. Wu, and D. Meng, “Transient Analysis of a Flexible Pin-on-Disk System and Its Application to the Research Into Time-Varying Squeal,” *Journal of Vibration and Acoustics*, vol. 140, Sept. 2017.
- [21] G. Martin, E. Balmes, G. Vermot Des Roches, and T. Chancelier, “Squeal measurement using operational deflection shape. Quality assessment and analysis improvement using FEM expansion,” in *Eurobrake*, (Dresden, Germany), pp. VDT–018, 2017.
- [22] N. Peyret, J.-L. Dion, and G. Chevallier, “A framework for backbone experimental tracking : Piezoelectric actuators, stop-sine signal and Kalman filtering,” *Mechanical Systems and Signal Processing*, vol. 78, pp. 28–42, Oct. 2016.
- [23] L. Pesaresi, J. Armand, C. Schwingshackl, L. Salles, and C. Wong, “An advanced underplatform damper modelling approach based on a microslip contact model,” *Journal of Sound and Vibration*, vol. 436, pp. 327–340, Aug. 2018.
- [24] P. A. Meehan and A. C. Leslie, “On the mechanisms, growth, amplitude and mitigation of brake squeal noise,” *Mechanical Systems and Signal Processing*, vol. 152, p. 107469, May 2021.
- [25] S. Oberst and J. C. S. Lai, “Chaos in brake squeal noise,” *Journal of Sound and Vibration*, vol. 330, pp. 955–975, Feb. 2011.

BIBLIOGRAPHY

- [26] B. A. Wernitz and N. P. Hoffmann, “Recurrence analysis and phase space reconstruction of irregular vibration in friction brakes: Signatures of chaos in steady sliding,” *Journal of Sound and Vibration*, vol. 331, pp. 3887–3896, July 2012.
- [27] M. Stender, M. Tiedemann, and N. Hoffmann, “Characterization of complex states for friction-excited systems,” *PAMM*, vol. 17, no. 1, pp. 45–46, 2017.
- [28] M. Feldman, “Hilbert transform in vibration analysis,” *Mechanical Systems and Signal Processing*, vol. 25, pp. 735–802, Apr. 2011.
- [29] G. M. Alves, E. Balmes, and G. Martin, “Analysis of a brake squeal functional model using a linear parameter varying perspective.,” in *INTER-NOISE and NOISE-CON Congress and Conference Proceedings*, vol. 270, pp. 473–484, 2024.
- [30] G. Malacrida Alves, E. Balmes, G. Martin, T. Chancelier, and E. Kassa, “Parametric modal testing using slow but continuous variation of operating conditions. Illustration on a contact bench.,” in *Surveillance, Vibrations, Shock and Noise*, 2023.
- [31] R. Penas, E. Balmes, and A. Gaudin, “A unified non-linear system model view of hyperelasticity, viscoelasticity and hysteresis exhibited by rubber,” *Mechanical Systems and Signal Processing*, vol. 170, p. 25, 2022.
- [32] G. Malacrida Alves and E. Balmes, “A time varying system perspective on rubber mount tests.,” in *ISMA*, (Leuven, Belgium), KUL, 2022.
- [33] G. Malacrida Alves, E. Balmes, G. Martin, G. Vermot Des Roches, D. Zhang, and T. Chancelier, “An harmonic balance vector signal model to study slow parametric sensitivity of brake squeal occurrences,” 2023.
- [34] P. A. Meehan, “Prediction of wheel squeal noise under mode coupling,” *Journal of Sound and Vibration*, vol. 465, p. 115025, Jan. 2020.
- [35] J.-J. Sinou and S. Besset, “Simulation of Transient Nonlinear Friction-Induced Vibrations Using Complex Interface Modes: Application to the Prediction of Squeal Events,” *Shock and Vibration*, vol. 2017, pp. 1–10, 2017.
- [36] K. Soobbarayen, J.-J. Sinou, and S. Besset, “Numerical study of friction-induced instability and acoustic radiation - Effect of ramp loading on the squeal propensity for a simplified brake model,” *Journal of Sound and Vibration*, vol. 333, pp. 5475–5493, Oct. 2014.
- [37] M. Stender, M. Tiedemann, L. Hoffmann, and N. Hoffmann, “Determining growth rates of instabilities from time-series vibration data: Methods and applications for brake squeal,” *Mechanical Systems and Signal Processing*, vol. 129, Apr. 2019.
- [38] T. Karaağaçlı and H. N. Özgüven, “A frequency domain nonparametric identification method for nonlinear structures: Describing surface method,” *Mechanical Systems and Signal Processing*, vol. 144, p. 106872, Oct. 2020.
- [39] H. Ouyang, W. Nack, Y. Yuan, and F. Chen, “Numerical analysis of automotive disc brake squeal: A review,” *International Journal of Vehicle Noise and Vibration*, vol. 1, pp. 207–231, Jan. 2005.

BIBLIOGRAPHY

- [40] X. Lorang, *Instabilité Vibratoire Des Structures En Contact Frottant: Application Au Crissement Des Freins de TGV*. PhD thesis, Ecole Polytechnique, 2007.
- [41] G. Kerschen, M. Peeters, J. C. Golinval, and A. F. Vakakis, “Nonlinear normal modes, Part I: A useful framework for the structural dynamicist,” *Mechanical Systems and Signal Processing*, vol. 23, pp. 170–194, Jan. 2009.
- [42] N. Coudeyras, J. J. Sinou, and S. Nacivet, “A new treatment for predicting the self-excited vibrations of nonlinear systems with frictional interfaces: The Constrained Harmonic Balance Method, with application to disc brake squeal,” *Journal of Sound and Vibration*, vol. 319, pp. 1175–1199, Jan. 2009.
- [43] L. Guillot, A. Lazarus, O. Thomas, C. Vergez, and B. Cochelin, “A purely frequency based Floquet-Hill formulation for the efficient stability computation of periodic solutions of ordinary differential systems,” *Journal of Computational Physics*, vol. 416, p. 109477, Sept. 2020.
- [44] L. Lentz and D. Hochlenert, “Nonlinear analysis of disk brake squeal by normal form theory,” in *11th International Conference on Vibration Problems*, (Lisbon), Sept. 2013.
- [45] I. Mehdipour, D. D. Ganji, and M. Mozaffari, “Application of the energy balance method to nonlinear vibrating equations,” *Current Applied Physics*, vol. 10, pp. 104–112, Jan. 2010.
- [46] J. Kappauf and H. Hetzler, “A comparison of methods for approximating periodic limit cycles in nonlinear systems with joint friction,” *PAMM*, vol. 18, no. 1, p. e201800341, 2018.
- [47] J. Brunetti, F. Massi, W. D’Ambrogio, and Y. Berthier, “A new instability index for unstable mode selection in squeal prediction by complex eigenvalue analysis,” *Journal of Sound and Vibration*, vol. 377, pp. 106–122, Sept. 2016.
- [48] T. Thenint, E. Balmes, and M. Corus, “Stabilization effect of shock non linearity on the dynamics of a steam generator tube,” in *Proceedings of COMPDYN 2011*, p. 262, 2011.
- [49] R. Rosenberg, “On nonlinear vibrations of systems with many degrees of freedom,” *Advances in Applied Mechanics*, 1966.
- [50] S. W. Shaw and C. Pierre, “Non-linear normal modes and invariant manifolds,” *Journal of Sound and Vibration*, vol. 150, pp. 170–173, Oct. 1991.
- [51] S. W. Shaw and C. Pierre, “Normal Modes for Non-Linear Vibratory Systems,” *Journal of Sound and Vibration*, vol. 164, pp. 85–124, June 1993.
- [52] T. Karaağaçlı and H. N. Özgüven, “Experimental modal analysis of nonlinear systems by using response-controlled stepped-sine testing,” *Mechanical Systems and Signal Processing*, vol. 146, p. 107023, Jan. 2021.
- [53] R. J. Allemang, “The modal assurance criterion—twenty years of use and abuse,” *Sound and vibration*, vol. 37, no. 8, pp. 14–23, 2003.
- [54] *Structural Dynamics Toolbox (for Use with MATLAB)*. Paris: SDTools, 1995/2020.

BIBLIOGRAPHY

- [55] G. Martin, E. Balmes, G. Vermot Des Roches, and T. Chancelier, “Squeal measurement with 3D Scanning Laser Doppler Vibrometer: Handling of the time varying system behavior and analysis improvement using FEM expansion,” in *ISMA*, KUL, Sept. 2018.
- [56] C. Farhat, P. Avery, T. Chapman, and J. Cortial, “Dimensional reduction of nonlinear finite element dynamic models with finite rotations and energy-based mesh sampling and weighting for computational efficiency: Non-linear model reduction and energy conserving sampling and weighting,” *International Journal for Numerical Methods in Engineering*, vol. 98, pp. 625–662, June 2014.
- [57] E. Balmes, C. Chapelier, P. Lubrina, and P. Fargette, “An evaluation of modal testing results based on the force appropriation method,” in *International Modal Analysis Conference*, pp. 47–53, 1995.
- [58] G. Raze, G. Abeloos, and G. Kerschen, “Experimental continuation in nonlinear dynamics: Recent advances and future challenges,” July 2024.
- [59] M. Scheel, S. Peter, R. I. Leine, and M. Krack, “A phase resonance approach for modal testing of structures with nonlinear dissipation,” *Journal of Sound and Vibration*, vol. 435, pp. 56–73, Nov. 2018.
- [60] M. Scheel, “Nonlinear modal testing of damped structures: Velocity feedback vs. phase resonance,” *Mechanical Systems and Signal Processing*, vol. 165, p. 108305, Feb. 2022.
- [61] J.-L. Dion, C. Stephan, G. Chevallier, and H. Festjens, “Tracking and removing modulated sinusoidal components: A solution based on the kurtosis and the Extended Kalman Filter,” *Mechanical Systems and Signal Processing*, vol. 38, pp. 428–439, July 2013.
- [62] C. Li and M. Liang, “A generalized synchrosqueezing transform for enhancing signal time–frequency representation,” *Signal Processing*, vol. 92, pp. 2264–2274, Sept. 2012.
- [63] S. Kiser, P. Margerit, M. Rébillat, M. Guskov, and N. Ranc, “FFT-ESPRIT: A kernel-based subspace estimator for frequency super-resolution at quasi-linear time complexity,” Mar. 2023.
- [64] S. L. Kiser, M. Rébillat, M. Guskov, and N. Ranc, “Real-time sinusoidal parameter estimation for damage growth monitoring during ultrasonic very high cycle fatigue tests,” *Mechanical Systems and Signal Processing*, vol. 182, p. 109544, Jan. 2023.
- [65] C. Stephan, H. Festjens, F. Renaud, and J.-L. Dion, “Poles tracking of weakly nonlinear structures using a Bayesian smoothing method,” *Mechanical Systems and Signal Processing*, vol. 84, pp. 136–151, Feb. 2017.
- [66] M. D. Coats and R. B. Randall, “Single and multi-stage phase demodulation based order-tracking,” *Mechanical Systems and Signal Processing*, vol. 44, pp. 86–117, Feb. 2014.
- [67] D. Peng, W. A. Smith, R. B. Randall, K. Feng, Z. Peng, W. Teng, and Y. Liu, “Iterative improvement in tacholeless speed estimation using instantaneous error estimation for machine condition monitoring in variable speed,” *Mechanical Systems and Signal Processing*, vol. 216, p. 111488, July 2024.

BIBLIOGRAPHY

- [68] W. Heylen and P. Sas, *Modal Analysis Theory and Testing*. Katholieke Universteit Leuven, Departement Werktuigkunde, 2006.
- [69] S. Davis and I. Bucher, “Automatic vibration mode selection and excitation; combining modal filtering with autoresonance,” *Mechanical Systems and Signal Processing*, vol. 101, pp. 140–155, Feb. 2018.
- [70] M. Volvert and G. Kerschen, “Phase resonance nonlinear modes of mechanical systems,” *Journal of Sound and Vibration*, vol. 511, p. 116355, Oct. 2021.
- [71] E. Balmes, “New results on the identification of normal modes from experimental complex modes,” *Mechanical Systems and Signal Processing*, vol. 11, no. 2, pp. 229–243, 1997.
- [72] B. Fraejis de Veubeke, “A variational approach to pure mode excitation based on characteristic phase lag theory,” Tech. Rep. AGARD report 39, 1956.
- [73] E. Balmes, *Methods for Vibration Design and Validation*. Course notes ENSAM/Ecole Centrale Paris, 1997/2023.
- [74] J. Bianchi, E. Balmes, G. Vermot des Roches, and A. Bobillot, “Using modal damping for full model transient analysis. Application to pantograph/catenary vibration,” in *ISMA*, (Leuven, Belgium), KUL, Sept. 2010.
- [75] Q. Zhang, R. Allemang, and D. Brown, “Modal Filter: Concept and Applications,” in *International Modal Analysis Conference*, pp. 487–496, 1990.
- [76] D. Kammer, “Sensor Placement for On Orbit Modal Identification and Correlation of Large Space Structures,” *J. Guidance, Control, and Dynamics*, vol. 14, no. 2, 1991.
- [77] E. Balmes, “Orthogonal Maximum Sequence Sensor Placements Algorithms for modal tests, expansion and visibility,” *IMAC*, vol. 145, p. 146, 2005.
- [78] G. Martin, E. Balmes, and T. Chancelier, “Characterization of identification errors and uses in localization of poor modal correlation,” *Mechanical Systems and Signal Processing*, vol. 88, pp. 62–80, May 2017.
- [79] American Society for Testing and Materials, “ASTM E756-98 : Standard Test Method for Measuring Vibration-Damping Properties of Materials,” in *Annual Book of Standards*, vol. 14.02, ASTM International, 1998.
- [80] R. Penas, *Models of Dissipative Bushings in Multibody Dynamics*. PhD thesis, Ecole Nationale Supérieure d’Arts et Métiers Paris, Nov. 2021.
- [81] F. Massa, *Contributions à l’intégration Des Variabilités En Dynamique Des Structures*. PhD thesis, UVHC, 2022.
- [82] G. Vermot Des Roches and E. Balmes, “Understanding friction induced damping in bolted assemblies through explicit transient simulation,” in *ISMA*, p. ID360, KUL, Sept. 2014.
- [83] E. Balmes, “Frequency domain identification of structural dynamics using the pole/residue parametrization,” in *International Modal Analysis Conference*, pp. 540–546, 1996.

- [84] E. Balmes, *Modèles Analytiques Réduits et Modèles Expérimentaux Complètes En Dynamique Des Structures*. Habilitation à diriger des recherches, Université Pierre et Marie Curie, 1997.
- [85] G. Altshul, M. Guskov, E. Balmes, and P. Lorong, “Milling robot modal analysis using spindle-driven unbalanced excitation in context of its response nonlinearity,” in *ISMA*, (Leuven, Belgium), KUL, 2024.

BIBLIOGRAPHY

Résumé : Le crissement des freins est un phénomène complexe résultat d'une instabilité induite par couplage de modes. Bien qu'il fasse l'objet d'études depuis de nombreuses années, il n'existe pas de méthode de conception robuste pour le prévenir et les mesures correctives reposent largement sur le prototypage et la validation, ce qui est long et coûteux. Les essais de crissement peuvent être séparés en trois activités principales : la classification des occurrences de crissement en fonction des niveaux acoustiques, la caractérisation spatiale détaillée des cycles limites et la caractérisation modale des composants et des assemblages. Ce travail a donc cherché à proposer et à analyser l'utilité de différents changements méthodologiques dans les méthodes d'essai. Une spécificité du crissement est que la vibration dépend de multiples paramètres de fonctionnement : pression, vitesse de roue, température, ... qui varient dans le temps relativement lentement par rapport aux fréquences des cycles limites de crissement. Il est donc nécessaire de tenir compte de cette spécificité pour concevoir des méthodes d'essai et analyser leurs résultats. Afin de mieux comprendre les effets des conditions de fonctionnement qui changent lentement, un nouveau modèle fonctionnel pour le crissement est proposé sur la base du modèle d'Hoffmann bien connu. La nouveauté réside dans le remplacement de l'hypothèse de frottement variable par une loi de contact non linéaire, qui introduit une sensibilité à la pression appliquée (car l'état statique est modifié) et à l'amplitude (par son effet sur la pression moyenne). L'analyse et la comparaison de la réponse de ce modèle dans le domaine fréquentiel et temporel permettent de comprendre les relations entre les vibrations et les paramètres du cycle limite de crissement. La définition d'un modèle de signal de balance harmonique vectoriel (HBV) et l'utilisation de la démodulation pour son estimation permettent ensuite de suivre les signaux quasi-périodiques issus du crissement sans les limites de résolution de la transformée de Fourier. Pour les tests de crissement paramétriques, cette méthode a amélioré la classification des événements en extrayant les évolutions des caractéristiques telles que la fréquence instantanée, l'amplitude globale de la vibration, les coordonnées généralisées et la forme. Pour l'analyse détaillée de la forme à l'aide de mesures 3D-SLDV, les estimations du signal HBV ont permis d'améliorer les résultats par rapport aux méthodes actuelles basées sur les transformées de Fourier à court terme. Les applications sont illustrées dans un banc d'essai de contact pour obtenir l'évolution des formes en fonction de la pression, et dans des essais de freinage sur frein complet pour obtenir les formes du cycle limite. L'estimation du signal HBV peut également extraire des formes spatialement détaillées pour les harmoniques supérieures. Deux indicateurs (modulation harmonique et perturbation harmonique) sont ensuite proposés, sur la base de la notion de rigidité instantanée, comme moyen d'évaluer à quel moment d'une période le système est plus ou moins rigide. Enfin, pour l'analyse modale expérimentale (EMA) paramétrique en fonctionnement, les essais en vraie grandeur ont montré que les modes éloignés du crissement peuvent être identifiés et suivis de manière cohérente. À proximité du crissement, cependant, la présence d'une perte de cohérence indique que d'autres méthodes sont nécessaires, telles que le suivi de la résonance de phase par anticipation proposé dans l'analyse du banc d'essai de contact simplifié.

Mots clés : Crissement de frein, Vibrations non-linéaires, Cycle limite, Systèmes à paramètre variable, Modèle de signal, Analyse modale expérimentale, 3D-SLDV, Raideur instantanée, Clustering.

Abstract : Brake squeal is a complex phenomenon resulting from a mode coupling instability. Despite being a subject of study for many years, no robust design method exists for its prevention and correcting measures are heavily based on prototyping and validation, which is time-consuming and expensive. Squeal testing can be separated into three main activities: classification of squeal occurrences based on acoustic levels, detailed spatial characterization of limit cycles, and modal characterization of components and assemblies. This work thus seeks to propose and analyze the usefulness of different methodological changes to testing methods. A specificity of squeal is that vibration depends on multiple operating parameters pressure, wheel speed, temperature, ... which vary in time relatively slowly compared to the frequencies of squeal limit cycles. It is thus necessary to take this specificity into consideration to design testing methods and analyze their results. As a mean to gain further insight on the effects of slowly changing operating conditions, a new functional model for squeal is proposed based on the well-known Hoffmann model. The novelty lies in replacing the variable friction assumption by a nonlinear contact law, which introduces a sensitivity to the applied pressure (as the static-state is modified), and amplitude (through its effect on the mean pressure). Analyzing and comparing the response of this model in frequency and time domain provides a path to understanding the relations between squeal limit cycle vibration and parameters. The definition of a Harmonic Balance Vector (HBV) signal model and the use of demodulation for its estimation, then allows tracking of quasi-periodic squeal signals without resolution limitations of the Fourier transform. For parametric squeal tests, this method improved occurrence classification by extracting the evolutions of features such as instantaneous frequency, global vibration amplitude, generalized coordinates and shape. For the detailed shape analysis using 3D-SLDV measurements, the HBV signal estimates led to results improved over current methods based on short time Fourier transforms. Applications are illustrated in a contact test bench to obtain the evolution of shapes with pressure, and in a full scale brake tests to obtain the limit cycle shapes. The HBV signal estimation can also extract spatially detailed shapes for higher harmonics. Two indicators (harmonic modulation and harmonic perturbation) are then proposed, based on the notion of instant stiffness, as a mean of evaluating where in a period the system is stiffer or softer. Finally, for in operation parametric Experimental Modal Analysis (EMA), full scale tests showed that modes away from squeal can be consistently identified and tracked. Near squeal, however, the presence of a coherence loss indicates that other methods are required such as the feedforward phase resonance tracking proposed in the analysis of the simplified contact test bench.

Keywords : Brake squeal instability, Nonlinear vibrations, Limit cycle, Parameter-varying systems, Signal model, Experimental modal analysis, 3D-SLDV, Instant stiffness, clustering.